AN INVESTIGATION OF LOW ENERGY X-RAY SPECTRA

by

Michael H. Unsworth, B.Sc.

Thesis presented for the Degree of Doctor of Philosophy of the University of Edinburgh, August 1968.

EX BIBL. UNIV. EDINBURGH

CONTENTS

Chapter			Page
	ABSTRACT		vi
1.	INTRODUCTION		
	1.1	Production of X-rays	1
	1.2	Scope of the investigation	2
	1.3	Methods available for spectral analysis	3
		1.3.1 Theoretical calculations	3
		1.3.2 Attenuation analysis	5
		1.3.3 Balanced Filters	8
		1.3.4 Pulse height analysis	9
		1.3.4.1 Gas proportional counter	10
		1.3.4.2 Scintillation counter	12
		1.3.4.3 Semiconductor detector	14
		1.3.5 Crystal diffraction spectrometry	16
2.	THEORETICAL CALCULATIONS OF SPECTRAL DISTRIBUTIONS		
	2.1	Discussion of calculations required	18
	2.2	Continuous X-ray distribution	19
	2.3	Modification to allow for target and tube window attenuation	20
	2.4	Alternative models for continuum production	23
	2.5	Directly produced tungsten L characteristic radiation	27
	2.6	Indirectly produced characteristic radiation	30
	2.7	Summary of results	32
3.	DETERMINATION OF PROPORTION OF CHARACTERISTIC RADIATION IN X-RAY BEAMS USING ROSS FILTERS		
	3.1	Filter thickness	34
		3.1.1 Thickness for balance	34
		3.1.2 Balance at high or low energy side of pass-band	35
		3.1.3 Optimum thickness of filters	36
	3.2	Choice of filter materials	37
	3.3	Effect of L_{a_2} line-width	38
	3.4	Manufacture of thin filters	39
		3.4.1 Thicknesses required	39
		3.4.2 Electrodeposition process for copper and nickel films	40
	3.5	Choice of detectors	41

Chapter | Page

3.5.1 Basic considerations 41
3.5.2 Calorimeter 41
3.5.3 Gas ionization chamber 43
3.5.4 Solid state ionization detector 43
3.5.5 Experimental situation 44

3.6 Balancing the filters 46
3.6.1 Use of continuous distributions 46
3.6.2 Use of characteristic radiation 48

3.7 Measurements of pass-band and total beam intensity 49

3.8 Corrections for filter attenuation 51
3.8.1 Theory 51
3.8.2 Experimental measurements of filter transmission 52

3.9 Total pass-band intensity, continuum corrections and L_α intensity 56

3.10 Total characteristic intensity 58

3.11 Discussion 59

4. ATTENUATION ANALYSIS

4.1 Introduction 63

4.2 Choice of absorption material 64

4.3 Detection system 65

4.4 Experimental situation 66
4.4.1 Scintillation detector in the current mode 66
4.4.2 Absorption system 66
4.4.3 Comparison of detection systems for a 15kV, 30mA X-ray beam 67

4.5 Measurement of attenuation curves 70

4.6 Analysis of attenuation curves 71
4.6.1 Introduction 71
4.6.2 Review of attenuation measurements of beams from beryllium window X-ray tubes 73
4.6.3 Characteristic radiation 73
4.6.4 Attempts at fitting simple Laplace transforms to data 75
4.6.5 Fitting of $f(x) = CK_o\ B(x + d)^{1/2}$ 78
4.6.6 Calculation of spectral distributions .. 82

4.7 Discussion of results 83

Chapter			Page
5.	PULSE HEIGHT ANALYSIS		
	5.1	Introduction	86
	5.2	Discussion of requirements for a pulse height analysis system	86
		5.2.1 Detector	86
		5.2.2 High voltage supplies	87
		5.2.3 Preamplifier	87
		5.2.4 Amplifier	88
		5.2.5 Pulse height analyser	88
	5.3	Method of calibration	89
	5.4	Expected count rate	91
	5.5	Possible methods of count rate reduction	92
		5.5.1 Reduction of tube current	92
		5.5.2 Inverse square law	92
		5.5.3 Apertures	92
		5.5.4 Filtration	93
		5.5.5 Detector efficiency	93
		5.5.6 Summary	94
	5.6	Survey of X-ray scattering	94
		5.6.1 Introduction	94
		5.6.2 Optimum angle of scatter	95
		5.6.3 Choice of scattering material	97
		5.6.4 Composition of the scattered radiation.	97
	5.7	Estimation of the count rate due to a 90° scattered spectrum	99
	5.8	Description of scattering spectrometer	101
	5.9	Investigation of the performance of the scattering spectrometer	101
	5.10	Summary	103
6.	CORRECTION FOR DETECTOR RESOLUTION		
	6.1	Introduction	105
	6.2	Formulation of the problem	105
	6.3	Survey of suggested methods of resolution correction	107
		6.3.1 Numerical integration	107
		6.3.2 Matrix inversion	108
		6.3.3 Matrix iteration	108
		6.3.4 Numerical analysis	108
	6.4	Literature survey	109
	6.5	Descriptions of computer programmes for resolution correction	111

Chapter			Page
	6.5.1	Matrix inversion	111
	6.5.2	Iteration	112
	6.5.3	Numerical analysis	112
	6.6	Conclusion	113
7.	MEASUREMENTS OF X-RAY SPECTRA USING THE PROPORTIONAL COUNTER		
	7.1	Introduction	115
	7.2	Detection system	115
	7.3	Experimental situation	116
	7.4	Calibration	116
	7.5	Quantum efficiency of the detector	117
	7.6	Air attenuation	119
	7.7	Estimation of proportion of tungsten L radiation	119
	7.8	Corrected spectral distributions	121
	7.9	Summary	123
8.	MEASUREMENTS OF X-RAY BEAMS BY SCATTERING SPECTROMETRY		
	8.1	Introduction	124
	8.2	Detection system	124
	8.3	Experimental situation	125
	8.4	Calibration	125
	8.5	Measurement of spectra	125
	8.6	Further corrections	126
	8.7	Summary	127
9.	COMPARISON AND DISCUSSION OF RESULTS AND METHODS		
	9.1	Introduction	128
	9.2	Comparison and discussion of results	128
	9.3	Discussion of the merits of methods used	131
	9.4	Weighted mean spectra	133
	9.4.1	Characteristic radiation	133
	9.4.2	Continuous distributions	134
	9.4.3	Variation of the intensity of characteristic and continuous radiation with tube voltage	136

Chapter			Page
	9.5	Comparison with the results of other workers ...	137
	9.6	Summary	138
	9.7	Points for further study	139
Appendix			
1.		ESTIMATION OF ENERGY LOSSES FROM DETECTORS	
	A1.1	Introduction	141
	A1.2	General theory	141
	A1.3	Energy losses from the sodium iodide detector ..	143
	A1.4	Energy losses from other detectors	143
2.		STATISTICAL CONSIDERATIONS GOVERNING THE RESOLUTION OF SCINTILLATION SPECTROMETERS	
	A2.1	Introduction	145
	A2.2	Statistical definitions	145
	A2.3	Crystal package	146
	A2.4	The photomultiplier tube	147
	A2.5	System resolution: Comparison of theory with experiment	149
	A2.6	Discussion	151
		ACKNOWLEDGEMENTS	152
		REFERENCES	153

ABSTRACT

Spectral distributions of X-ray beams generated at 10 - 30kV have been determined by three experimental methods and by theoretical calculations. The X-ray unit used consists of a Machlett tungsten target tube with a beryllium window, and a constant potential generator. Special attention has been paid to the measurement of the proportion of beam intensity due to tungsten L radiation since this important factor has not previously been accurately determined.

Continuous distributions have been calculated on the basis of Kramers' theory. Filtration by the target has been shown to be very important in modifying the distributions near the tungsten L absorption edges. This leads to a new concept of "pseudo-characteristic" radiation, which is important in low resolution spectrometry. Calculations of the true L characteristic intensity have also been made and are discussed in relation to experimental results.

Balanced "Ross" filters of nickel and copper have been used to isolate an X-ray pass-band containing the tungsten L_α line. Totally absorbing detectors have been used to give absolute measurements of the intensities in the filter pass-band and of total beam intensities. By using the theoretical continuous distributions and accepted values of the relative intensities of tungsten L lines, the proportions of the total intensities which are due to characteristic radiation have been found.

Continuous distributions have also been determined by attenuation analysis, using results obtained with aluminium filters and totally absorbing detectors. Computer programmes have been written to estimate the proportion of characteristic radiation present and to make

a fuller investigation of the applicability of several Laplace transforms than has previously been feasible. The transform finally used does not appear to have been employed in any previously published work. Three-component representations of each beam have also been presented, and are adequate for many applications. Simple transforms for the analysis of filtered spectra have been suggested.

Further measurements of continuous spectra and characteristic radiation have been made by two pulse height analysis methods, specially designed to give acceptable count rates from a very high photon fluence. The first used an argon gas flow proportional counter. The second employed a new scattering technique in conjunction with a high resolution sodium iodide scintillation counter. The latter method has enabled spectra to be defined at lower energies than has previously been possible by pulse height analysis. With both systems, a new experimental method of estimating the proportion of characteristic radiation present has been used.

A thorough investigation of correction methods for detector resolution broadening has been made by the use of digital computing. Previous workers have been unable to restore detail at low energies. A new programme, using numerical analysis, has been developed, which enables corrections to be made accurately at all energies.

Spectra obtained by the three experimental methods and by theory have been compared, and are generally in very good agreement. Small discrepancies have been discussed. Weighted mean results, both of continuous distributions and proportions of characteristic radiation have been derived, and the relationship between intensity of L characteristic

radiation and X-ray tube voltage has been investigated. The results obtained in this study represent a significant improvement in the definition of low energy X-ray spectra.

CHAPTER 1

I N T R O D U C T I O N

1.1 Production of X-rays

Electromagnetic radiation is produced whenever electrons are rapidly accelerated or decelerated. In particular, if the deceleration involves a large loss of energy in a short time, the ensuing radiation may be of high enough energy to ionise matter and is then called X-radiation. The majority of the interactions of an electron beam with the atoms of a target result in the production of heat; at energies up to 50keV, less than 1% of the incident energy may produce X-rays which can be formed in two types of interaction.

Firstly, electrons can lose their energy by collisions with the target atoms. Those electrons which are most rapidly decelerated by the atoms of the surface layer of the target will give rise to X-rays of energy equal to that of the incident electrons; the majority of electrons will however be decelerated less rapidly and will be stopped deeper in the target, at distances depending on the initial energy of the electrons. These will give rise to X-rays of lower energy than that of the incident electrons. Hence this first type of interaction produces a continuum of X-rays, of energies ranging from zero up to the energy of the incident electrons.

The second type of interaction may occur if the energy of the incident electrons is sufficient to release an electron from an internal, closed, shell of a target atom. The subsequent rearrangement of electrons produces quanta of X-radiation, photons, the energies of which depend on the levels between which the transitions take place, and are

"characteristic" of the target element. This characteristic spectrum takes the form of series of lines, called the K, L, or M lines depending on the shell to which the transition takes place; K-radiation is therefore the most energetic.

There is also a probability that suitably energetic photons of the continuum can interact with the target atoms, producing characteristic radiation "indirectly".

Thus, in general, an X-ray spectrum consists of a continuous distribution with a line spectrum characteristic of the target superimposed on it.

1.2 Scope of the Investigation

The purpose of the investigation was to provide information about the spectral distributions of low energy X-ray beams below 30kV. In order to specify completely the radiation at any point due to an X-ray beam, it is necessary to measure two quantities: i) the energy flux, ii) the spectral distribution (most usefully the photon energy spectrum). The former has been measured by Redpath (1967); this investigation concerns the measurement of the latter by various methods and the evaluation of the usefulness of these methods. For many purposes the complete specification of the radiation is not necessary. For example, in therapeutic X-ray work a sufficient indication of the quality of the radiation may often be given by the half-value layer in some standard material, and this can be used further to specify an "effective energy", i.e. the energy of monoenergetic radiation which exhibits the same half-value layer. However, in the determination of chemical or biological effects it is often necessary to calculate the

numbers and energies of secondary ionising particles produced by the beam, and for this the complete specification of the beam is necessary. In determining the spectral distributions for the majority of these uses, the extremely high resolution of a crystal diffraction spectrometer is not necessary, since such high resolution is only required near discontinuities of the distribution function, e.g. characteristic lines. In this study, since the tube target is known, (and therefore the characteristic lines) it will be sufficient to use lower resolution methods to measure the continuous distribution and in addition to determine the proportion of the total energy flux which is due to the characteristic lines.

1.3 Methods Available for Spectral Analysis

Several methods are available for X-ray spectrometry. These will be surveyed for their usefulness in determining continuous distributions and line intensities.

1.3.1 Theoretical Calculations

Calculations of spectral distributions from a thick target X-ray tube are complicated by the difficulty in defining the electron paths in the target, and the problem of self-absorption of the radiation produced. Kramers (1923) applied the Thomson-Whiddington law to take into account the electron paths and derived the well known formula $I(E) = CZ(E_o - E)$, where I is the intensity per unit energy interval, Z is the target atomic number and E_o is the energy of the incident electrons. This confirmed Kuhlenkampff's empirical relationship (1922) apart from a small additional term, although the experimental results were only taken for $\frac{1}{2}E_o < E < E_o$ to eliminate multiple order diffraction effects. His work was also at low

accelerating potential (10.47kV) and with low atomic weight targets; in a tungsten tube the low energy radiation will suffer more absorption in the target before escape. For this reason the calculations of Jager and Soole (1965) and Jennings (1953) must be treated with caution, since they do not appear to have taken the nature of the target into account. More recently (I.C.R.U. 1964), Kramer's formula has been found to agree with experimental determinations over a wide energy range when target and tube window attenuation is taken into account.

We will also require an estimate of the intensity of tungsten L-characteristic radiation produced. This subject appears to have been largely ignored although a considerable amount of work has been done on the intensity of K-radiation of lower atomic number elements. Burhop (1940) has calculated the cross-section per electron for L-ionization, and his results are used by Spielberg (1959), in calculating line intensities. Spielberg's results, however, over-emphasise self-absorption and are not made for the same angle of take off as we are interested in.

By using a digital computer, it would be possible to allow for the random electron paths in the target in calculations, using a "Monte Carlo" type of calculation. This has been done by Green (1963), for a copper target and 29keV electrons, but the writing and "debugging" of such a programme for the present case would be a very lengthy business and seems scarcely justified in view of the variety of experimental methods available.

Simplified calculations have been made, and are described in Chapter 2.

1.3.2 Attenuation Analysis

This method determines the spectral distribution from an analysis of accurately determined transmission data in an absorber. It requires much simpler apparatus than other experimental methods; a set of suitable filters for placing in the beam and a detector with a known response over the energy range are sufficient. The transmission curve is fitted to one of several functions which have been suggested, each having two or three adjustable constants for this purpose. Having obtained these constants, they are substituted into corresponding functions, bearing a known relationship to the transmission curve function and satisfying certain physical assumptions, and the spectral distribution is calculated.

Silberstein (1933) in a mathematical analysis of X-ray attenuation was apparently the first to make use of a Laplace transform to solve the integral equation which describes the absorption of a continuous X-ray distribution. Jones (1940) and Greening (1947, 1950, 1952) have further developed the method, and the latter, in his paper of 1950, has put the technique on a more sound physical and theoretical basis.

The use of the technique is best seen from the mathematical equations.

If I_o is the original intensity of an X-ray beam and I_x is the intensity after traversing x cm of absorber.

$$I_x = I_o \int_{\lambda_o}^{\infty} \exp(-\mu(\lambda)x) \quad f(\lambda)d\lambda \quad \ldots\ldots\ldots 1.1$$

where $\mu(\lambda)$ is the linear attenuation coefficient of the absorber at wavelength λ, and $f(\lambda)$ is the distribution function required. The

short wavelength cut-off λ_o is given by the Duane-Hunt Law, viz.

$$\lambda_o = \frac{hc}{Ve} = \frac{12.4}{V_o} \text{ Å}$$

where V_o is the maximum applied voltage in kV. Since μ is a function of wavelength, we can make the transformation

$$f(\lambda)d\lambda = \phi(\mu)d\mu \quad \ldots\ldots\ldots 1.2$$

Hence equation 1.1 becomes

$$I_x = I_o \int_{\mu_o}^{\infty} \exp(-\mu x)\, \phi(\mu)d\mu \quad \ldots\ldots\ldots 1.3$$

This is the stage that Silberstein reached in 1933, but he then concentrated on one specific solution of equation 1.3 which suited his data, and it was not until Greening developed the solution in terms of Laplace transforms as follows that the method was useful for lightly filtered radiation.

Equation 1.3 is strongly similar to one form of the Laplace transform equation, viz.

$$f(x) = \int_{o}^{\infty} \exp(-\mu x)\ \psi(\mu)d\mu \quad \ldots\ldots\ldots 1.4$$

where f(x) is the Laplace transform of $\psi(\mu)$. Now from the properties of Laplace transforms, if $f(x) \leftarrow \psi(\mu)$ then $\exp(-ax)\, f(x) \leftarrow \phi(\mu)$ where $\phi(\mu) = 0$ when $0 < \mu < a$ and $\phi(\mu) = \psi(\mu - a)$ when $\mu > a$. Writing $a = \mu_o$ where μ_o is the absorption coefficient at λ_o, we have from equation 1.4,

$$\exp(-\mu_o x)\, f(x) = \int_{o}^{\infty} \exp(-\mu x)\, \phi(\mu)d\mu = \int_{\mu_o}^{\infty} \exp(-\mu x)\ \psi(\mu - \mu_o)d\mu$$

$$\ldots\ldots\ldots 1.5$$

since $\int_0^{\mu_o} \exp(-\mu x)\, \phi(\mu) d\mu$ is zero.

Thus equations 1.5 and 1.3 are identical with

$$\exp(-\mu_o x)\, f(x) = \frac{I_x}{I_o}$$

Hence if one can find a function f(x) such that f(x) $\exp(-\mu_o x)$ will fit experimental values of the fractional transmission, then $\psi(\mu - \mu_o)$ can be calculated and the required spectral distribution $f(\lambda)$ is given by:-

$$f(\lambda) = \phi(\mu) \frac{d\mu}{d\lambda} = \psi(\mu - \mu_o) \frac{d\mu}{d\lambda} \quad \text{for } \mu > \mu_o$$

Suitable Laplace pairs have been suggested by Greening (1950), and most have found use e.g. Norman and Greenfield (1955), Wang et al. (1957), Burke and Pettit (1958). Cases where the method has appeared to fail, e.g. Greenfield et al. (1952) can usually be attributed to unsuitable physical assumptions (see Greening 1952).

The majority of spectral investigations by attenuation analysis have used ionization chambers as the detectors and if these are air equivalent then the resultant $f(\lambda)$ is a dose rate distribution. It is more desirable, if energy effects are to be investigated, to measure the intensity distribution by using a total absorption detector. Wang et al. (1957) used a sodium iodide crystal in this mode, but this is likely to be insensitive to very low energies due to the non-linearity of NaI response. It has been possible to intercompare attenuation curves obtained from various detectors and these results are described in Chapter 4.

Figure 1

X-ray mass attenuation coefficients
for elements of adjacent atomic number

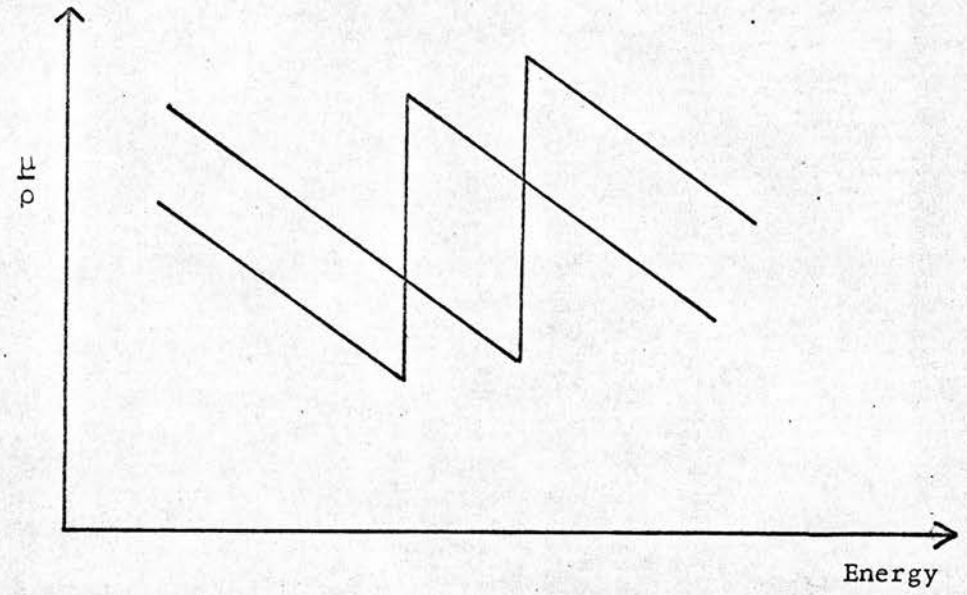

Figure 2

Effect of Ross filters on an X-ray spectrum

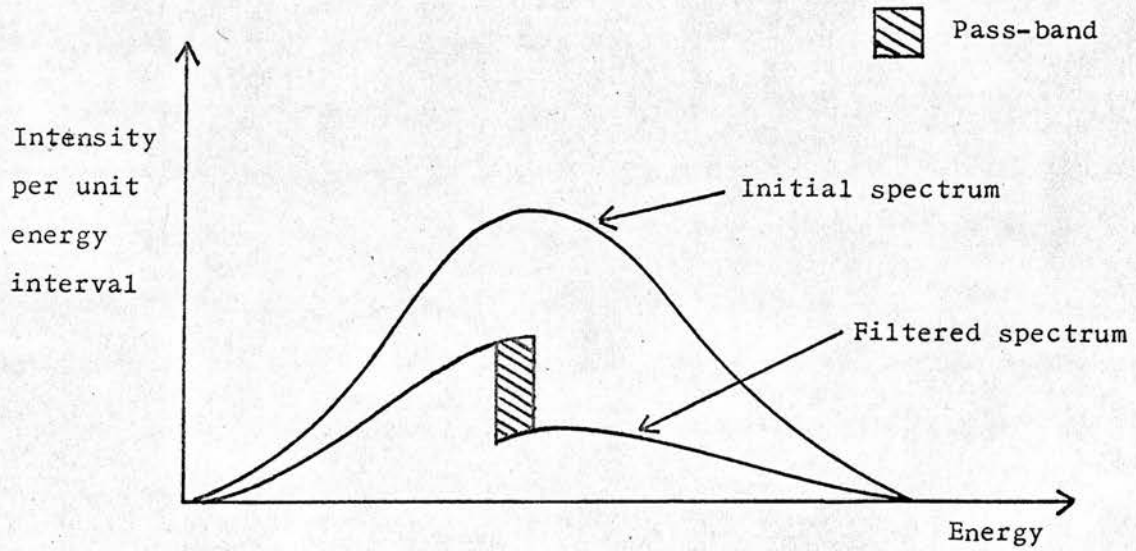

Because attenuation analysis requires a smooth continuum, it is unable to deal with spectra containing characteristic radiation; the correct proportion of this must be subtracted from the total intensity before analysis can proceed.

1.3.3. Balanced Filters

By the use of balanced filters made of elements of adjacent (or nearly adjacent) atomic numbers, narrow energy bands of the X-ray spectrum can be isolated. By a suitable choice of elements it is possible to isolate the characteristic radiation in an X-ray spectrum and hence to measure the proportion of characteristic to total intensity, or the efficiency of production of characteristic radiation. The method was first suggested by Ross (1926, 1928) and has been developed by Kirkpatrick (1939, 1944). The principle depends on the similarity of the variation of attenuation coefficient with energy of elements of adjacent atomic number except in the immediate vicinity of an absorption edge. Figures 1 and 2 illustrate this; in Fig. 1 attenuation coefficient is plotted against energy for two adjacent atomic number elements, with the differences exaggerated for clarity. It will be seen from Fig. 2 that if filter thicknesses are chosen correctly, a transmitted spectrum will be identical at all energies except those lying in the pass-band. Hence by subtracting measurements taken with each filter in the beam, any difference must be due to the energy in the pass-band. This technique is widely used to obtain nearly monochromatic radiation e.g. Spiers (1946), since the "monochromatic" radiation produced, although not as pure as that by crystal diffraction, is of much higher intensity. The use of the

method to filter out characteristic lines has been described by Metchnik (1963), Bendit (1958) for Cu K_α, Tothill (1964) for Tungsten K, and Hink (1965) for Tungsten L.

Hink's paper on tungsten L-radiation aims at the measurement of the efficiency of production of the characteristic radiation and he uses a tube with a tungsten film as the combined target and window. In our case, with a thick target with take off angle of 20°, and a beryllium window tube, we cannot make any great use of his results, although some qualitative conclusions will be drawn when the use of balanced filters is discussed in Chapter 3.

The "resolution" of the balanced filter method is only bettered by crystal diffraction and possibly semiconductor spectrometry, both of which require expensive apparatus and sophisticated measurement techniques.

1.3.4 Pulse Height Analysis

In this method of spectrometry, electrical output pulses are obtained from the detector, the size of the pulses being proportional to the energy of the incident X-ray photons. By investigating the distribution of pulse heights it is possible to work back to the distribution of photon energies. We were fortunate to have the use of a 100-channel pulse height analyser; this makes the collection of pulse height distributions a very much quicker task than with a single channel instrument, although certain early work was done with a single channel set-up.

There are three types of proportional counter available at present; each is characterised by its resolution and efficiency, both

Figure 3

Effect of detector resolution on monoenergetic X-rays

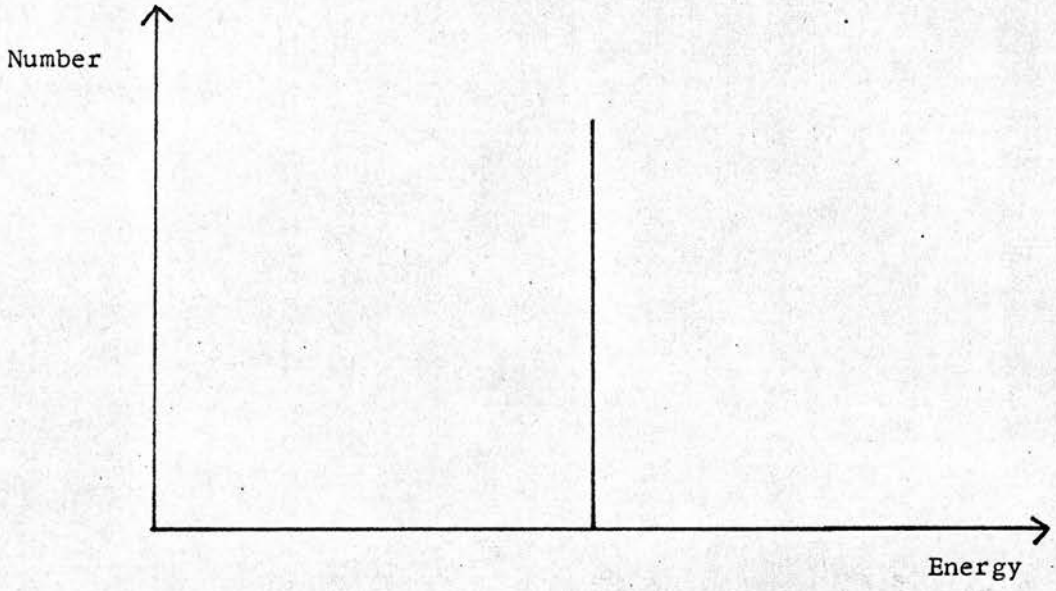

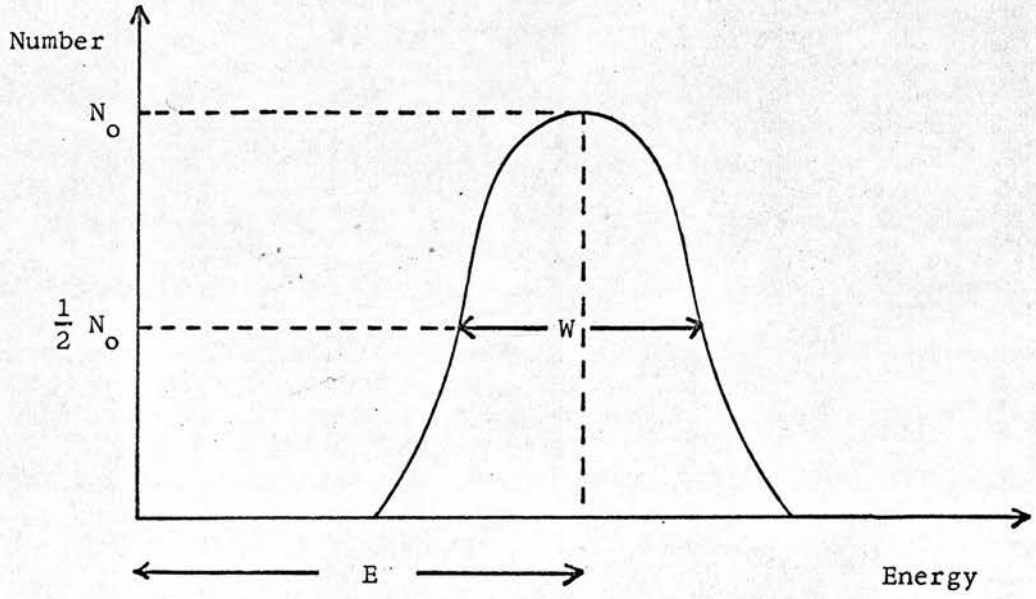

of which will necessitate corrections. The effect of the resolution of a detector on a monoenergetic X-ray line is shown in Fig. 3: although the incident photons are all of the same energy, the output pulses form a distribution of pulse heights. We define percentage resolution R by

$$R = \frac{\text{Full width at half-maximum height (energy units)}}{\text{Photon Energy}} \times 100$$

The efficiency of a detector refers to the probability of detecting a photon of given energy. This will vary with energy due to variations of transmission, backscattering and sidescattering of the X-ray beam in the detector.

We will consider each type of counter for resolution and efficiency.

1.3.4.1 Gas Proportional Counter

In this device, often referred to simply as the "proportional counter", primary ionization in the gas filling is amplified by gas multiplication, and an output pulse of the order of 3 - 10 millivolts is produced which is proportional in size to the initial ionization, i.e. to the X-ray quantum energy. Proportional counters are usually filled with inert gas, often with a small proportion of organic gas, such as methane, added to check the random velocity of the electrons and give a sharp pulse. For low background, good gain stability and resolution, the gas mixture is usually allowed to flow through the counter at atmospheric pressure so that electron capturing impurities do not accumulate.

Mulvey and Campbell (1958) have studied the gas multiplication process and their work shows that the optimum

resolution for a gas proportional counter is given by

$$R = 2.36\left[\frac{1}{N}\left\{\frac{1}{F}+1\right\}\right]^{\frac{1}{2}}$$

where N is the number of primary ions, and F is the Fano factor for the gas (See Fano, 1947). For comparison with other proportional detectors we may note that good resolution for Copper K_α radiation is 14 - 16% (e.g. Lukirskii et al., 1964).

Disadvantages of the proportional counter are its low detection efficiency at energies greater than 15keV due to the low density of the filling gas, and its inability to deal with count rates of $> 10^4$ without loss of linearity. An additional problem is the occurrence of "escape peaks"; these will be discussed later.

Gas proportional counters have seldom been used to measure spectral distributions above 15kVp, although spectral measurements at lower energies have been reported by Dyson (1959) and Bowen et al. (1964). Zedler (1964) has described a proportional counter for the 5 - 35keV energy range but appears to have sacrificed resolution for detection efficiency. Tothill (1964) used a gas flow counter to study tungsten K-radiation and was able to use an isotope source to calibrate the detector so as to get a direct comparison between characteristic and total radiation. It was felt that the use of a similar method to look at the continuum from 20 - 50keV would not be justified in view of the calibration problems and the fact that since there are no characteristic lines in this region the extra resolution is scarcely necessary.

At lower energies the low efficiency of the proportional counter has proved useful due to the high photon fluxes from the

beryllium window tube although the correction factor becomes large for energies >20keV. Results taken by this method are discussed in Chapter 7.

1.3.4.2 Scintillation Counter

Historically, the first detection system for individual nuclear particles was a scintillation screen as used by Rutherford; modern detectors use a photomultiplier tube to detect the scintillations. In the detection of X-rays the absorption of an X-ray photon produces a trail of ionization in the phosphor. In doped inorganic phosphors de-excitation occurs by radiative transitions rather than mechanical interaction with the crystal lattice. The emitted photons are converted by the photomultiplier to a pulse of charge which is usually integrated and amplified as a voltage pulse. In a well designed system, pulse height is proportional to the energy of the incident photon. For good resolution of low energy X-rays the choice of a suitable phosphor and photomultiplier tube is important. This subject is treated in Appendix 2, but we may note here that sodium iodide is usually chosen as the phosphor since it has the highest conversion efficiency (i.e. the efficiency with which the initial energy deposited in the scintillator is converted into light radiation; this is approximately 20% for NaI).

A great advantage of a scintillation counter is its high detection efficiency. A crystal of sodium iodide 3mm deep will stop 99.9% of 50keV X-rays although subsequently some of the iodine K-radiation due to the photo-electric absorption process will escape; this escape fraction only occurs for energies >33keV.

The scintillation counter has its disadvantages; resolution is worse than a gas proportional counter, and varies greatly for different combinations of crystal and photomultiplier. The best results published give the resolution for Copper K_α as approximately 40% (Bisi and Zappa, 1958; Epp and Weiss, 1966) but it is by no means uncommon for resolution figures to be quoted of 60% or greater for the same energy (Wang et al., 1957; Ehrlich, 1955). By a careful study of the processes involved in defining resolution it has been possible to obtain a detector with a Cu K_α resolution of 40%. A further disadvantage with sodium iodide is that it is hygroscopic and so must be enclosed in a can with reflecting or diffusing walls. For low energy X-ray work a beryllium window can be fitted which permits measurements down to 4keV with reasonable transmission efficiency. At this sort of energy thermal noise from the photomultiplier can cause problems, but with the system referred to above this did not exceed a level corresponding to 2keV.

Scintillation counters have been used to measure spectral distributions by many workers, e.g. Epp and Weiss (1966), Ehrlich (1955), Liden and Starfelt (1954), Rawson and Cormack (1958). The greatest difficulty is the correction of the results for detector resolution and escape peaks. At higher energies, these corrections have been possible by both iterative and matrix inversion methods (e.g. Liden and Starfelt; Rawson and Cormack) although Dixon and Aitken (1958) have pointed out that the latter method is only applicable in certain cases. Spectra from beryllium window tubes operated at up to 50kV have been measured by Wang et al. (1957) and

Ehrlich (1955) by scintillation spectrometry. It is unfortunate that both these studies employed poor resolution detectors and so their results must be ill-defined at the low energy end. In addition, Wang et al. dealt with the photon flux problem by using a very narrow collimator which only viewed part of the target; this procedure seems unsatisfactory since Epp and Weiss (1966) have demonstrated variations of spectral distribution from different points of the target. Ehrlich tackled the problem by reducing the tube current and using a tube-detector distance of 1 metre. Epp and Weiss have shown that reduction of tube current alters the shape of the spectral distribution and the large correction for air filtration makes Ehrlich's results extremely uncertain at low energies. Ehrlich's correction method used a large channel width and matrix inversion; the large channel width enables the inversion to be made easily, although it is apparently not very effective in improving resolution. In the present study a more acceptable method of coping with high photon fluxes has been developed and the correction process has been analysed and improved (Chapters 5 and 6).

1.3.4.3 Semiconductor Detector

Over the past seven or eight years, the increasing availability of high purity semiconductor materials has led to the development of solid-state analogues of gas filled detectors. The principles of semiconductor detectors are discussed in several recent review papers (Dearnaley, 1966; Gunnersen, 1967). An incident X-ray photon, when absorbed in the detector, produces electron-hole pairs; the energy required for the production of one electron-hole pair is about 3eV

whereas the corresponding figure for a gas proportional counter is about 30eV. Hence the resolution of semiconductor detectors is intrinsically about three times better than that of a gas filled detector. To achieve good detection efficiency for X-rays germanium detectors are used, and these are lithium drifted to obtain large sensitive volumes. Because the energy band gap of germanium is only .67eV at 300°K, it is necessary to operate the system at liquid nitrogen temperature to reduce the noise and to use cooled field effect transistors in the preamplifier to achieve optimum resolution. Germanium also has the advantage that below 100keV the photoelectric effect is the principal absorption process and so the Compton background is small. It is possible to obtain commercial systems giving an energy resolution of 1keV, i.e. 12% for Cu $K_{\alpha+\beta}$ and figures have been published giving a resolution of 9% for Cu $K_{\alpha+\beta}$ (T.M.C., 1967).

Unfortunately the high cost of a suitable system ruled this method out in the present work, but there is no doubt that such a detector would have been extremely useful not only for spectral distributions, but also for the accurate measurement of characteristic line intensities and of spectral purity.

Table 1 summarises the difference in resolution available with various types of proportional detector.

Table 1

Detector	Optimum Resolution for Copper K_α (8.05keV)
Gas proportional Counter	~ 14%
Scintillation Counter	~ 40%
Li-drifted Germanium Counter	< 9%

Figure 4

Illustrating elementary deriation of Bragg Law

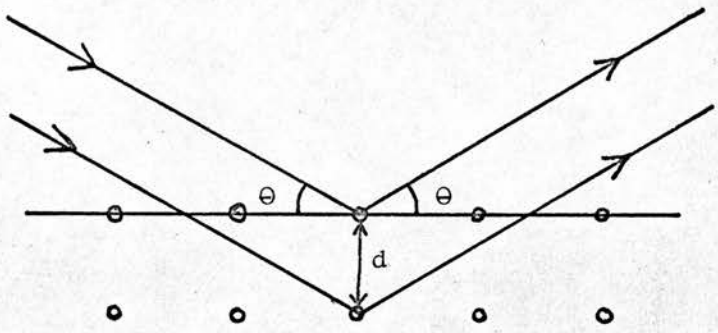

Apparently, at the time of writing, no continuous X-ray spectral determinations have been made using semiconductor spectrometry although there have been applications in the field of non-destructive materials analysis (Bowman et al, 1966), and neutron activation analysis (Dearnaley, 1966).

1.3.5 Crystal Diffraction Spectrometry.

This method provides the highest resolution possible and may be used to determine the intrinsic width of spectral lines. The theory of crystal diffraction was developed by Bragg and may be found in many text books on X-rays (e.g. Compton and Allison, 1954). It can be shown that if a beam of X-rays is incident on a suitably prepared crystal at an angle Θ (see Fig. 4) then only X-rays whose wavelengths satisfy the equation

$$n\lambda = 2d \sin \Theta \qquad \ldots\ldots\ldots 1.6$$

where n is an integer, λ is the wavelength and d is the spacing of the lattice, planes in the crystal will be reflected. Hence provided Θ can be accurately measured the variation of spectral intensity with wavelength can be found. Ulrey (1919) measured spectral distributions in this way, but his measurements taken with an ionization chamber are not corrected for variation of crystal reflectivity with energy nor for window attenuation. Disadvantages of crystal spectrometry are the need for the reflectivity correction, the low intensity of the resultant beam, and the problem of "multiple orders". The latter is due to the fact that equation 1.1 can be satisfied by first order diffractions of wavelength λ ($n = 1$) or second order diffractions of wavelength $\lambda/2$ ($n = 2$) etc. Thus for all wavelengths greater than $2\lambda_o$ there is the need for a

detector which can discriminate between orders; this is usually a proportional counter (gas or scintillation). A further disadvantage in our case was the high cost of crystal diffraction apparatus. It is probable that a semiconductor detector would have more applications in Medical Physics if high resolution is required. It is interesting for comparison with Table 1 to note that the intrinsic line width of the Copper K_{α_1} line has been measured by crystal spectrometry as 2.78eV and only required a 1 - 2% correction for instrumental broadening.

CHAPTER 2

THEORETICAL CALCULATIONS OF SPECTRAL DISTRIBUTIONS

2.1 Discussion of Calculations Required

As described in Chapter 1, it will be necessary to calculate continuous distributions at several tube voltages, and also to calculate the number of tungsten L-characteristic quanta produced at these voltages. Continuum calculations will be made using Kramers' formula (Kramers 1923) and making corrections for target self-absorption and window attenuation. This approach has been used by Jennings (1953) who used a beryllium window X-ray tube, and Jager and Soole (1965), but both initially ignored the important self-absorption correction. In comparing theoretically and experimentally determined attenuation curves in aluminium, Jennings found it necessary to assume an extra inherent filtration in the theoretical beam equivalent to 0.03mm Aluminium to improve agreement between the two curves, and he attributes this filtration to self-absorption effects. Jager and Soole found good agreement between theoretical and experimental attenuation, but their X-ray tube also had inherent filtration of glass, epoxy resin and oil, which attenuated 10keV X-rays by a factor exp(-14), hence their neglect of self-absorption will not be significant. In the present investigation we are interested in the amount of continuous radiation in the region of the tungsten L lines so that the self-absorption correction will be necessary, and it will be apparent that for an accurate description of this effect tungsten filtration must be considered rather than aluminium as assumed by Jennings.

The calculations of characteristic radiation will follow the lines of the work of Green and Coslett (1961) on K-quanta production and will make use of Burhop's calculations of L-ionization cross-sections (Burhop, 1940) to estimate the number of L-quanta produced. Green and Coslett did not allow for self-absorption but show that this is unnecessary for atomic numbers < 40 and excitation potentials greater than $3\ E_k$ where E_k is the ionization potential of the K shell. Their results for copper agree well with experimental determinations, and these are the results which we shall use in calculating 'L' intensity. Having calculated the number of L-quanta produced directly it will be necessary to correct for self-absorption in tungsten. Calculations of L-radiation produced by the continuum in its passage through the target (indirect characteristic radiation) can be very complicated due to the modification of the continuum at various depths and we will attempt to draw some qualitative conclusions from the work of Hink (1964, 1965) to see whether such calculations are necessary.

2.2 Continuous X-ray Distribution

In terms of energy in an energy interval dE per incident electron, Kramers' formula is

$$I(E)dE = CZ(E_o - E)dE \quad \text{keV/electron} \quad \ldots\ldots\ldots 2.1$$

where Z is the atomic number of the target, E_o is the maximum energy of the continuum in keV, and C is a constant which Dyson has measured as 2.76×10^{-6}.

Hence the intensity distribution I(E) is given by:-

$$I(E) = 1.02 \times 10^{11} (E_o - E) \quad \text{keV/keV interval-mA-sec-sterad.} \quad \ldots\ldots\ldots 2.2$$

Figure 5

Energy distributions by Kramers' formula

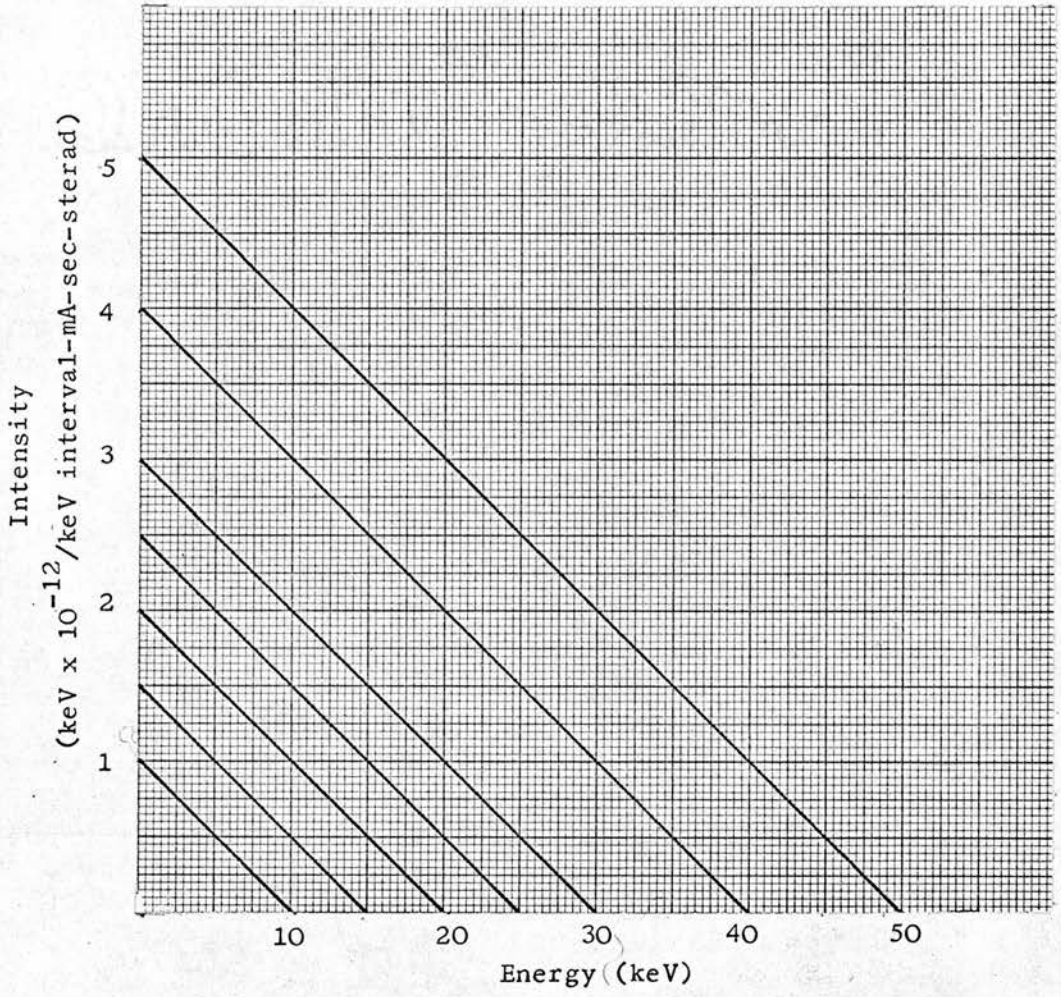

Figure 6

Photon distributions by Kramers' formula

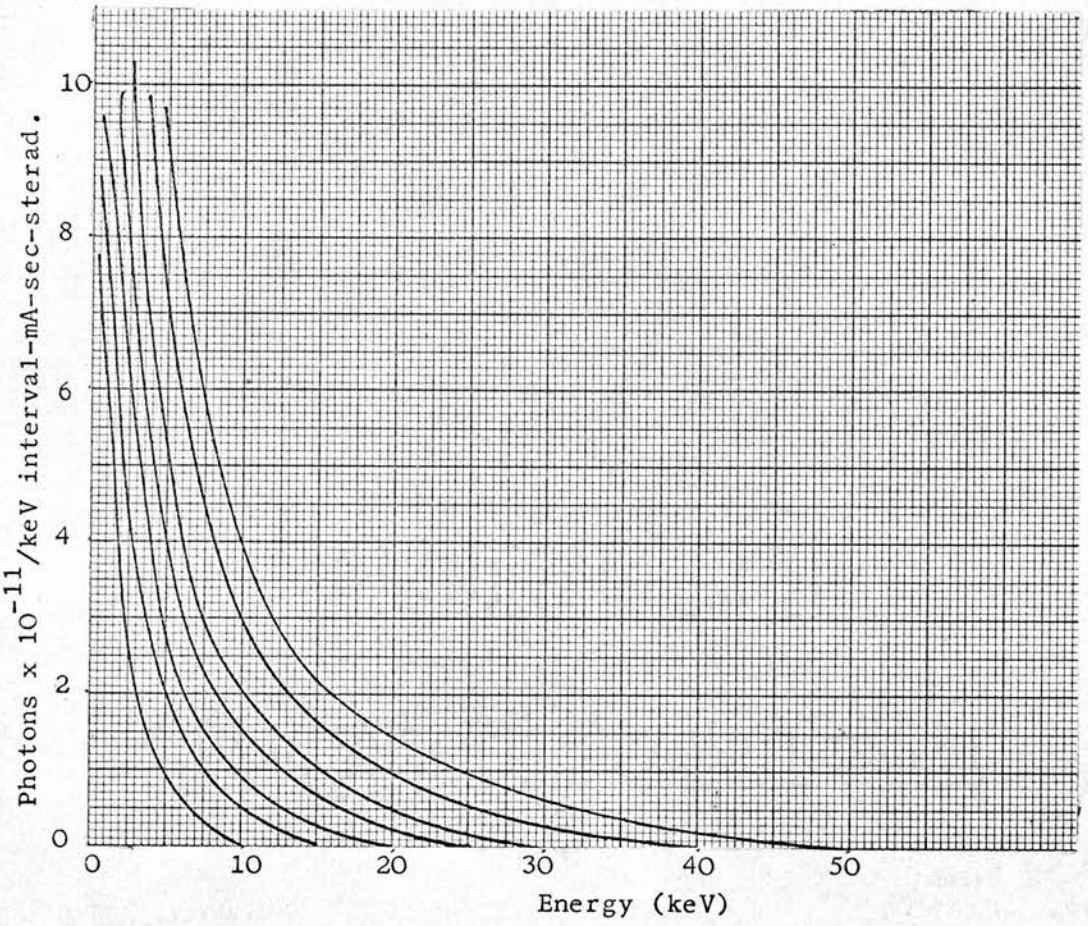

Figure 7

Transmission of 1mm beryllium

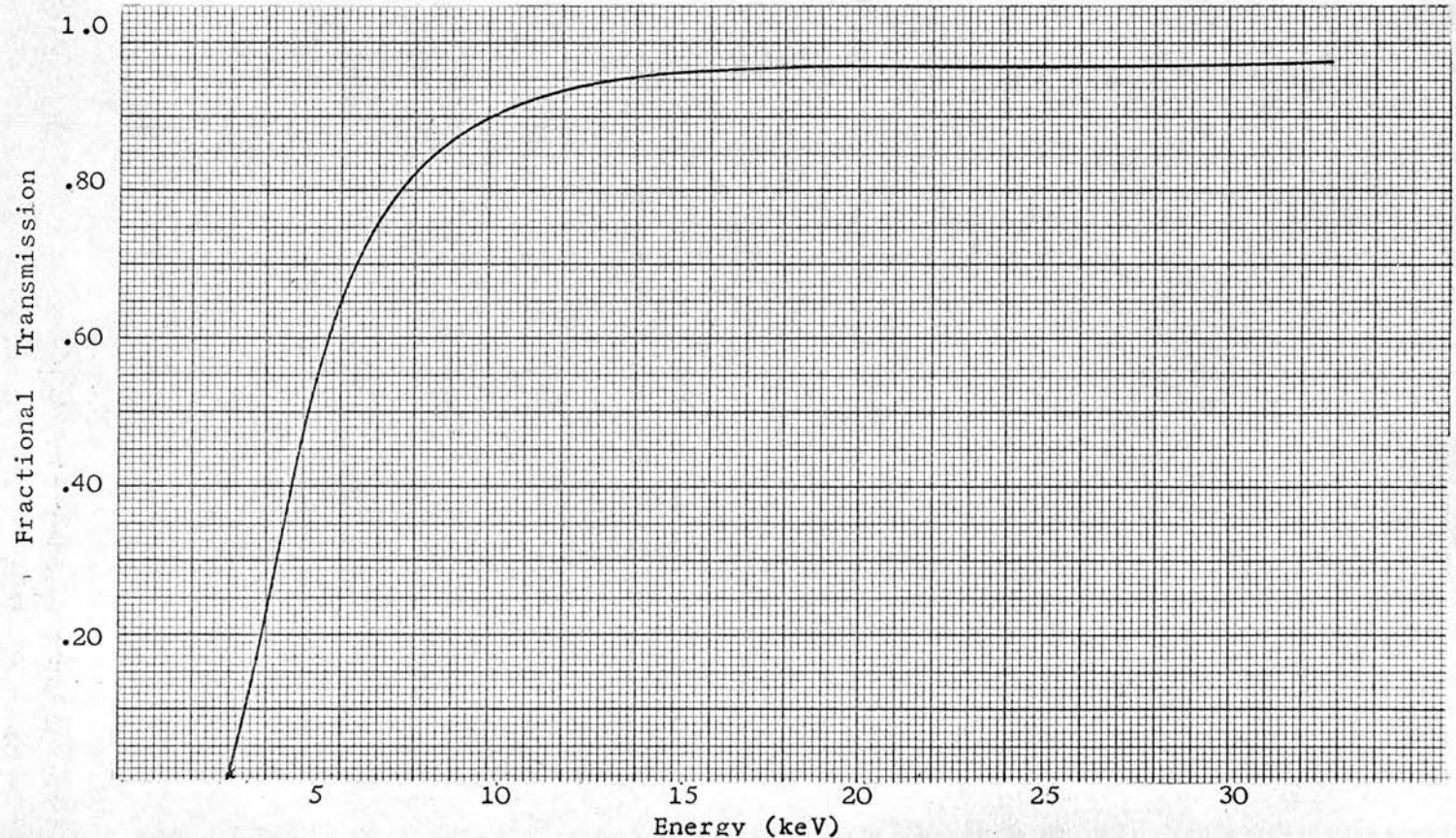

Figure 8

Electron interactions

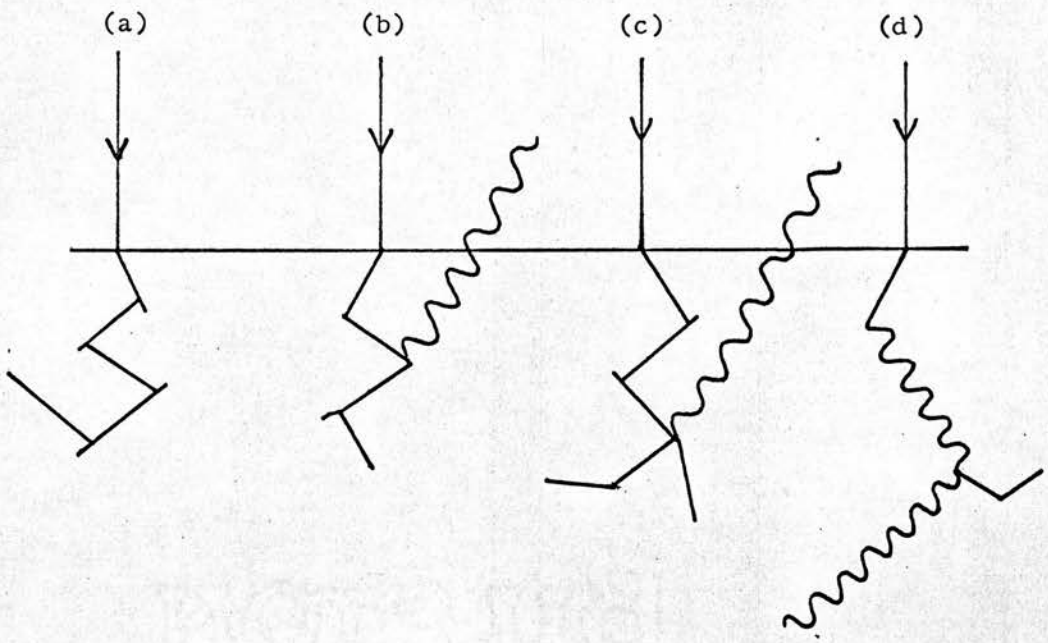

Figure 9

X-ray target angle

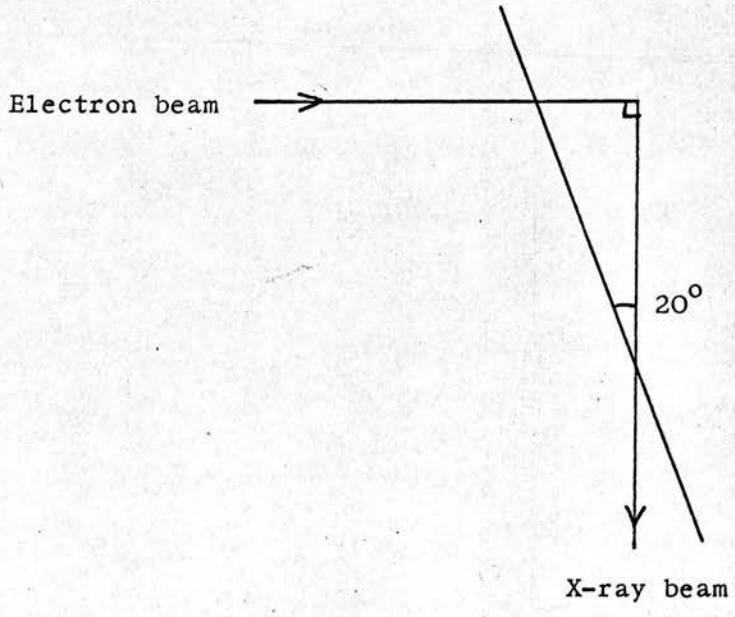

for a tungsten (Z = 74) target.

Similarly N(E), the number of photons in the energy interval dE is given by

$$N(E) = 1.02 \times 10^{11} \left(\frac{E_o}{E} - 1 \right) \text{ photons/keV interval-mA-sec-sterad.}$$

This indicates the high photon flux at low energies although this will of course be heavily attenuated. We may note that the total energy flux is given by

$$\int_o^{E_o} I(E)dE = 0.51 E_o^2 \times 10^{11} \text{ keV/mA-sec-sterad.} \quad \ldots\ldots\ldots 2.3$$

Energy distributions for tube voltages from 15 - 50kV are shown in Fig. 5 and the corresponding photon distributions in Fig. 6.

2.3 Modification to allow for Target and Tube-window Attenuation

The raw spectra derived in 2.2 will be subject to attenuation both within the target and in the tube window. The fractional intensity transmitted through the window, which is beryllium, 1mm thick, is easily calculated using the attenuation coefficients from McMaster et al. (1967). This transmission is shown in Fig. 7.

Attenuation in the target is more difficult to assess, since ideally it requires the knowledge of the path in the target of each electron and hence the production depth of each photon. Some of the possible ways in which the energy of the electrons may be dissipated are illustrated in Fig. 8. The most common case is shown in (a) where the electron loses its energy as heat in many non-radiative interactions. There is a possibility that in following a zig zag path the electron may be scattered out of the target. Secondly, at some point on its path the electron may pass close to a nucleus and give up part of its

Table 2

Ranges of Electrons in Tungsten
(from Berger and Seltzer, 1964)

Electron Energy (keV)	Electron Range (g/cm^2)
50	.0097
40	.0067
30	.0042
25	.0031
20	.0022
15	.0014
10	.0008

energy to produce bremsstrahlung. Thirdly, an electron may ionise an atom of the target and produce a characteristic photon, and finally a photon of bremsstrahlung may ionise a target atom and produce characteristic radiation 'indirectly'. Green (1963) has simulated the multiple electron paths by a "Monte Carlo" type calculation, and concludes that most direct K-shell ionizations in copper occur within less than $^1/4$ of the effective electron range. Farr (1955), and Stoddard (1935), have shown that the effective depth for production of continuous X-rays in high atomic number targets is about $^1/4$ of the electron range for energies from 150 - 250keV. The most common simplification in theoretical calculations of this type is to assume that the electrons penetrate the target in a straight line. This method was adopted by Worthington and Tomlin (1956) who report good agreement with experimental results, although they conclude that more quanta appear to be emitted close to the surface than their calculations predict.

Calculations of target attenuation would be most easily made if a single effective production depth for a given spectrum can be defined. Clearly this is an approximation, since in fact a high energy bremsstrahlung is formed near the target surface, and that of low energy is more likely to be formed deeper in the target when the electrons have lost most of their energy. The largest self-absorption correction will be in the case of a 50kV spectrum, so it will be useful to calculate such a spectrum on the basis of a single effective production depth and to compare it with spectra based on more realistic models.

Electron ranges in tungsten are shown in Table 2.

Figure 10

50kV X-ray intensity distribution

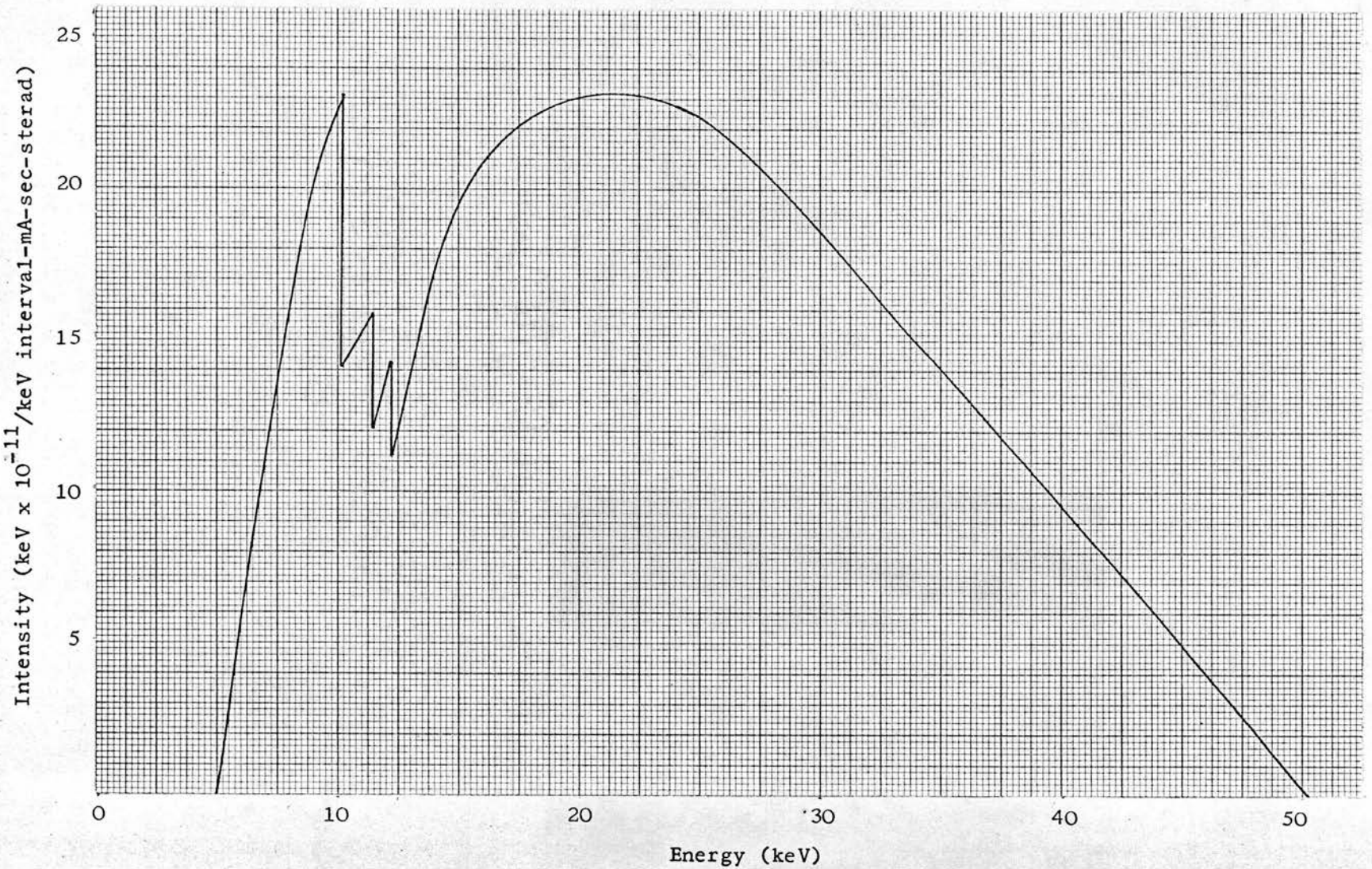

Figure 11

Mass attenuation coefficients of tungsten
(from McMaster et al., 1967)

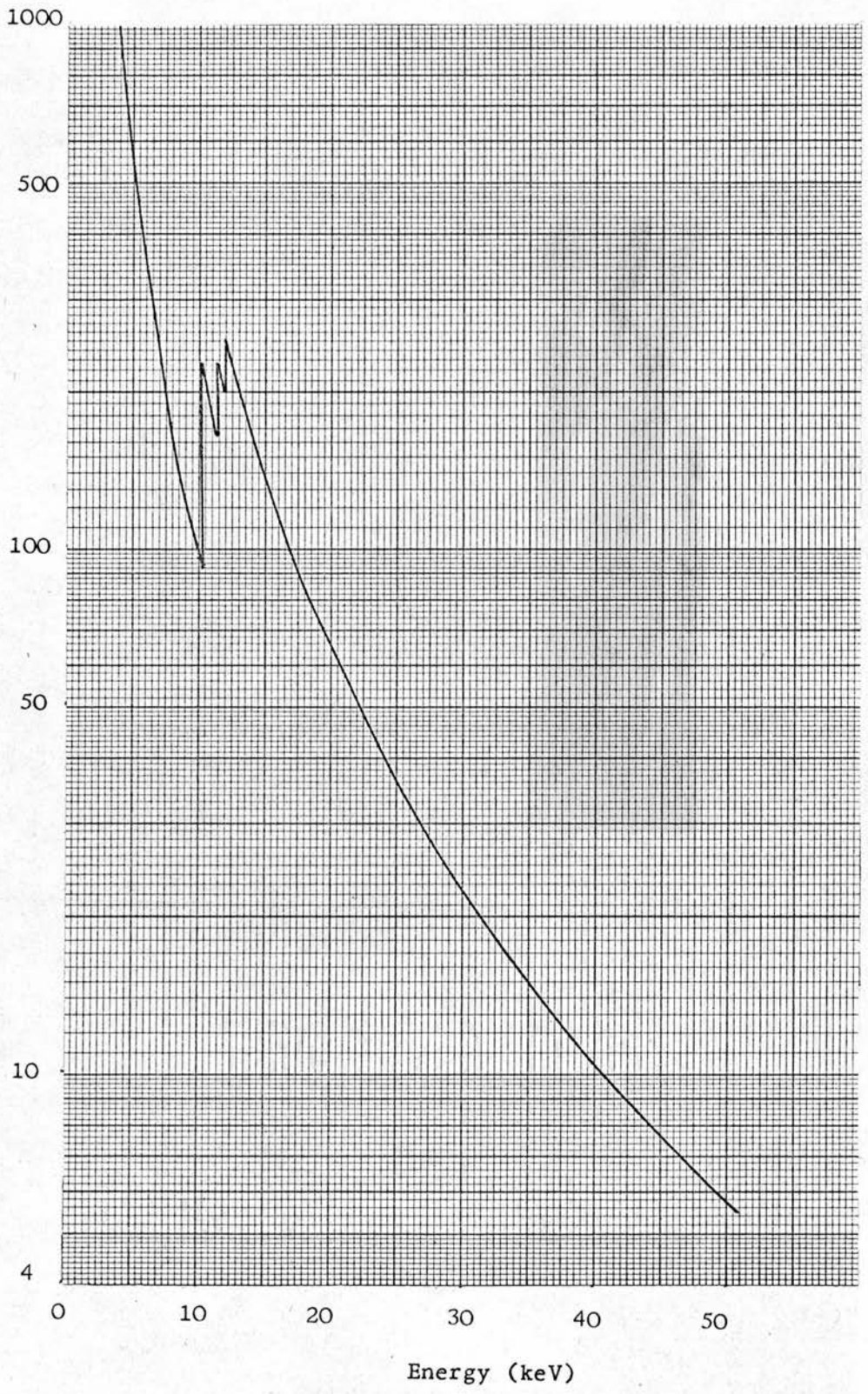

Table 3

50kV intensity distribution
corrected for target and tube window filtration

A - Intensity I, by Kramer's Formula, keV x 10^{-11}/keV interval-mA-s-sterad.
B - Target attenuation, $\exp(-(\mu t)_W \cot 20^\circ)$
C - Window attenuation, $\exp(-(\mu t)_{Be})$
D - Corrected intensity, I $\exp -((\mu t)_W \cot 20^\circ + (\mu t)_{Be})$
keV x 10^{-11}/keV interval-mA-s-sterad.

X-ray Energy (keV)	A	B	C	D
50	0	0.98	0.97	0
40	10.2	0.97	0.97	9.9
30	20.4	0.95	0.97	18.8
20	30.6	0.79	0.96	23.2
15	36.0	0.58	0.95	19.8
12.1	38.5	0.31	0.93	11.2
12.1	38.5	0.40	0.93	14.2
11.5	39.0	0.34	0.92	12.2
11.5	39.0	0.44	0.92	15.8
10.2	40.5	0.39	0.90	14.2
10.2	40.5	0.63	0.90	23.0
9.5	41.0	0.59	0.89	21.6
8	42.5	0.45	0.84	16.1
5	45.6	0.02	0.44	0.4

Table 4

Principal L characteristic lines of Tungsten
(from Blokhin, 1961)

Line	Energy (keV)
α_1	8.40
α_2	8.33
β_1	9.67
β_2	9.96
γ_1	11.28

In the Machlett X-ray tube which was used throughout this investigation, the target is inclined at 20^{o} to the electron beam, and is viewed at 90^{o} as in Fig. 9. Hence the escape path for quanta produced at depth x is x cot 20^{o}. Following the previous discussion of the results of Farr and Stoddard an effective production depth for a 50kV spectrum of 0.002 g/cm^2 (i.e. $^1/4$ electron range, assuming straight line target penetration) has been assumed. Hence the 50kV Kramers energy distribution is filtered by 0.002 x cot 20^{o} g/cm^2 of tungsten, and by 1mm beryllium, the tube window. The resultant distribution is shown in Fig. 10 and tabulated in Table 3. Its most striking features are the three steps at 10.2, 11.5 and 12.1keV. These correspond to the absorption jumps at the tungsten L edges which result in a higher transmission of energies below these edges than would be expected if the attenuation coefficient varied smoothly with energy. Attenuation coefficients for tungsten (McMaster, 1967) are shown in Fig. 11. Some consideration reveals that this 'preferential transmission' must always be present if a non-zero production depth is assumed: by choosing more realistic models of the production process the magnitude of this effect may alter, but it cannot be entirely eliminated. The effect in a practical spectrum will be complicated by the addition of tungsten L-characteristic radiation at energies given in Table 4.

Non-dispersive spectrometry as used throughout this study is unable to resolve the characteristic lines from the preferential transmission steps, so that the overall effect will be to broaden and increase the height of the single peak which is due to all the characteristic lines. This is shown in Fig. 12. If no instrumental broadening is

Figure 12

(i) No broadening

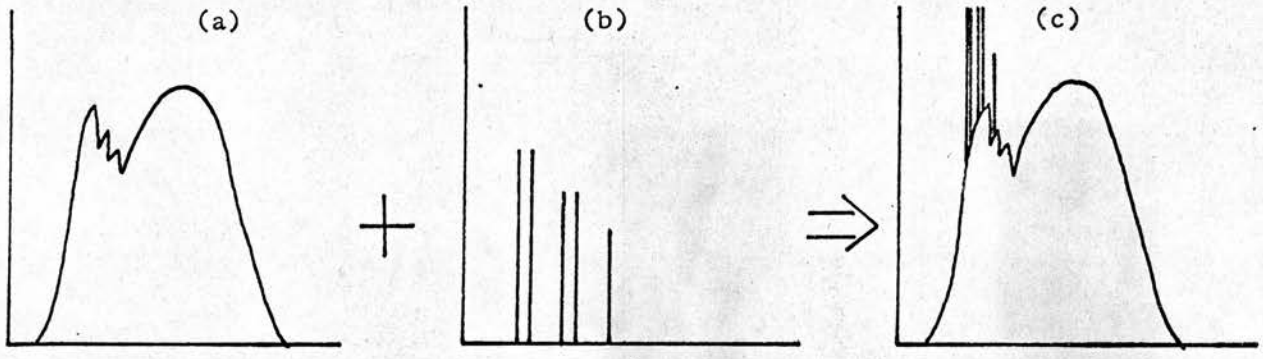

(ii) With broadening

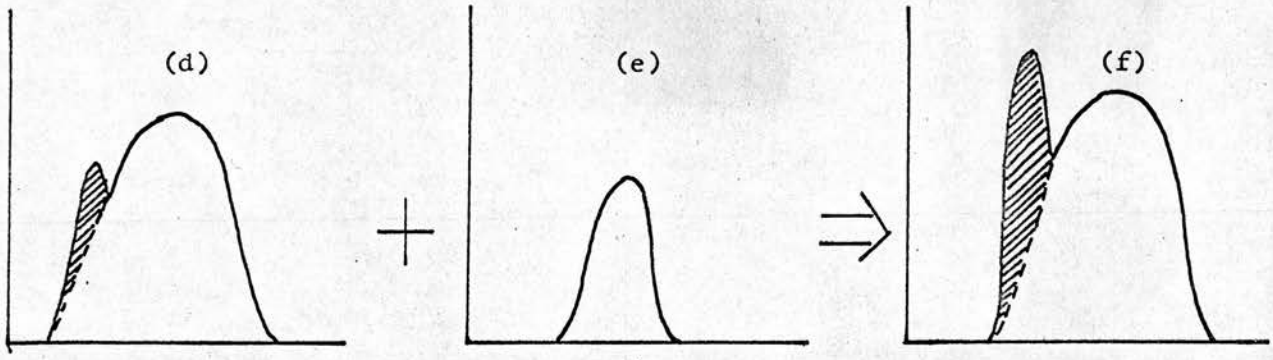

present, the continuous distribution (a) has the characteristic distribution (b) superimposed upon it to give (c). Typical instrumental broadening (e.g. by a scintillation counter) would give (d), (e) and their resultant (f). Once fine structure has been lost it cannot be recovered by subsequent resolution corrections, hence for low resolution spectrometry we can say that the shaded area in (f) represents that part of the total energy radiated which is due to characteristic effects in the target and the unshaded area represents a truly continuous distribution. The proportion of the "characteristic" energy due to preferential transmission (i.e. the shaded area in Fig. 12(d)) is most likely to depend on the model of X-ray production chosen, so we will consider two other models to see how they affect this.

2.4 Alternative Models for Continuum Production

As a first improvement, suppose that the photon production depth varies linearly with photon energy, i.e.

$$\rho d_E = \rho d_o \left(1 - \frac{E}{E_o}\right)$$ where E_o is the energy of the incident electrons, 50keV and take ρd_o as the production depth assumed before. This removes the earlier objection that high energy photons are being overfiltered, but does not allow for the possibility of production of low energy photons near the surface. The distribution is shown in Fig. 13.

An alternative approximation which allows for the production of low energy radiation near the surface of the target can be made by considering the rate of energy loss of the incident electrons.

Consider an incident beam of electrons with energy 50keV. By assuming a continuous slowing down approximation, the depths at which the mean energy of the electrons is 40, 30, 20, 10, 0 keV can be calculated. These are shown in Table 5. The electron ranges as tabulated by Berger and Seltzer (1964) were used in these calculations.

Table 5

Variation of Mean Energy with Depth for incident 50keV Electrons

Mean Electron Energy (keV)	Depth (Tungsten g/cm^2)
50	-
40	.0030
30	.0055
20	.0075
10	.0089
0	.0097

It will be assumed that a 50kV Kramers' distribution is formed at one half the depth required for the mean energy to drop from 50keV to 40keV; that a 40kV distribution is formed at one half the depth for the mean energy to drop from 40 to 30keV, and so on. Production depths for spectra from 50 to 10kV and their photon escape paths are shown in Table 6.

Table 6

Production depths and escape paths for components of 50kV spectrum

Peak Energy (keV)	Assumed Production Depth (g/cm^2 Tungsten)	Photon Escape Path (g/cm^2 Tungsten)	Weighting Factor
50	.0015	.004	.556
40	.0043	.011	.444
30	.0065	.018	.333
20	.0082	.023	.222
10	.0093	.026	.111

Table 7

Component beams for 50kV Intensity distribution

Energy (keV)	Intensity (keV x 10^{-11}/keV interval-mA-sec-sterad)				Window Filtration	Corrected Intensity
	I_{50}	I_{40}	I_{30}	I_{Total}	$\exp(-\mu t_{Be})$	
50.0	-	-	-	-	0.97	-
40.0	5.5	-	-	5.5	0.97	5.3
30.0	10.4	3.5	-	13.9	0.97	13.5
20.0	13.0	4.3	1.1	18.4	0.96	17.7
15.0	11.5	2.4	0.5	14.4	0.95	13.7
12.1	8.0	0.9	0.1	9.0	0.93	8.4
12.1	9.7	1.4	0.2	11.3	0.93	10.5
11.5	9.0	1.0	0.1	10.1	0.92	9.3
11.5	11.4	2.2	0.4	14.0	0.92	12.9
10.2	9.3	1.1	0.1	10.5	0.90	9.5
10.2	15.7	4.8	1.4	21.9	0.90	19.7
9.5	14.7	4.1	1.0	19.8	0.89	17.6
8.0	11.9	2.1	0.4	14.4	0.84	12.1
5.0	2.3	-	-	2.3	0.44	1.0
4.0	-	-	-	-	0.19	-

Figure 13

50kV X-ray Intensity Distributions

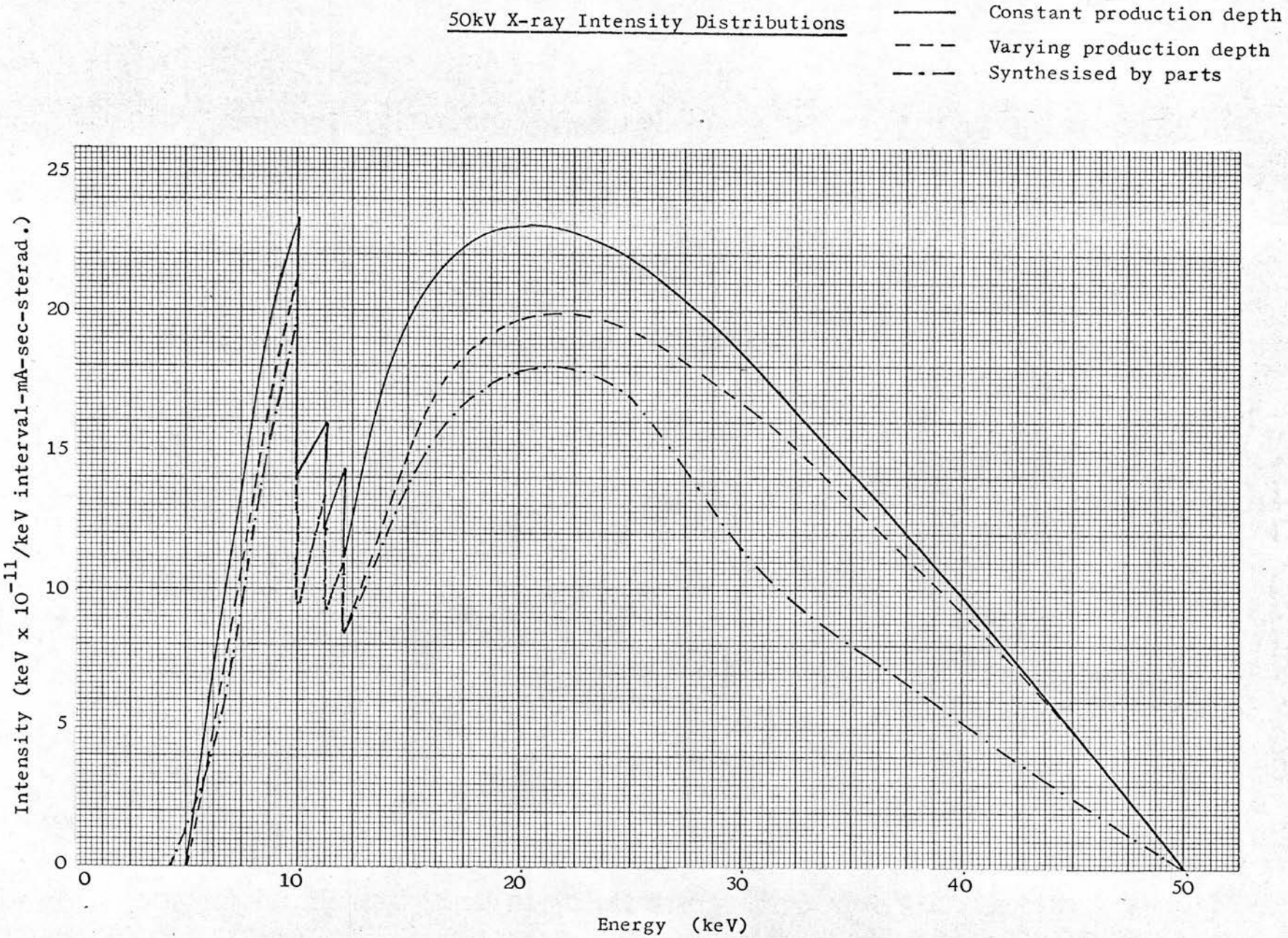

Table 8

Division of 50kV spectra into smooth continuum and peak area

Spectrum Type	Total Intensity x 10^{-11} (keV/mA-sec-sterad.)		Ratio (Peak/Continuum)
	Continuum	Peak	%
Constant production depth	484	48	10.0
Varying production depth	416	44	10.6
Synthesised in 5 parts	380	40	10.5

The resultant spectrum will be the sum of these five components, each weighted according to its production efficiency. Production efficiency can be taken as proportional to the peak X-ray energy (Compton and Allison, 1954) and the total unfiltered energy of the sum spectrum must be given by the energy in a 50kV Kramers' distribution. Hence the weighting factors in column 4 of Table 6 are calculated. Due to their production depth the contributions of the 20kV and 10kV component beams are negligible; the other three weighted spectra, corrected for their varying target attenuations are shown in Table 7 where the resultant spectrum beforeand after window attenuation is tabulated.

The intensity distribution corrected for window filtration is plotted in Fig. 13, with the previous two distributions shown for comparison. Considering the uncertainties introduced in choosing the weighting coefficients and production depths the three spectra do not appear radically different. It might be expected that the synthesised spectrum of Table 7 would be the lowest at high energies due to the difficulty of defining a suitable production depth for the 50kV part, and similarly the spectrum assuming varying production depth with energy might be expected to over-filter at the low energy end due to the large escape path, and it will be seen that these effects do indeed occur. Further, if each spectrum is divided into a "peak" portion (see Fig. 14) and a continuum portion, and the total energy due to each is found by measuring the areas with a planimeter, the results shown in Table 8 are obtained.

It therefore appears that there is no large error introduced in the ratio of peak to continuum intensity by assuming a constant X-ray

Figure 14 (i)

40kV and 30kV Intensity distributions

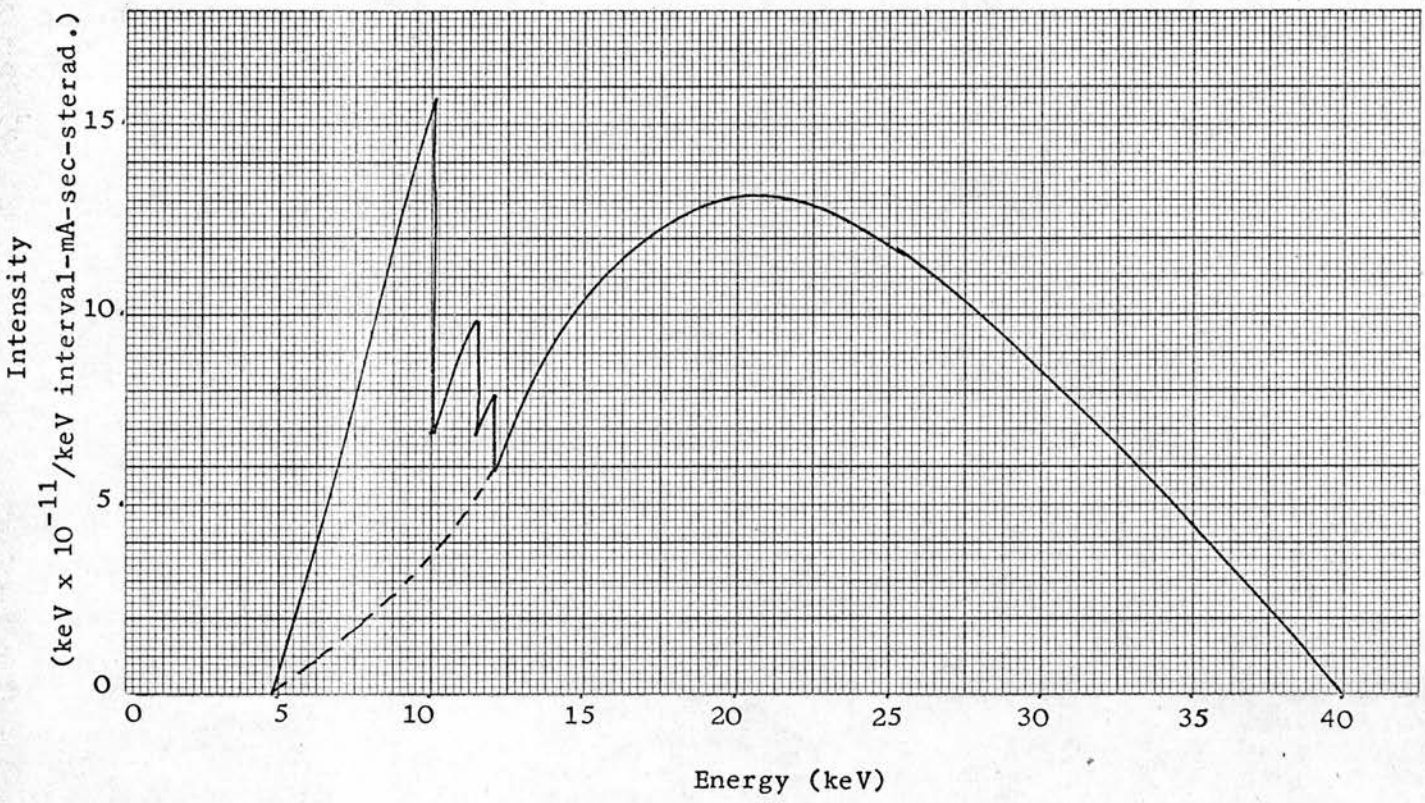

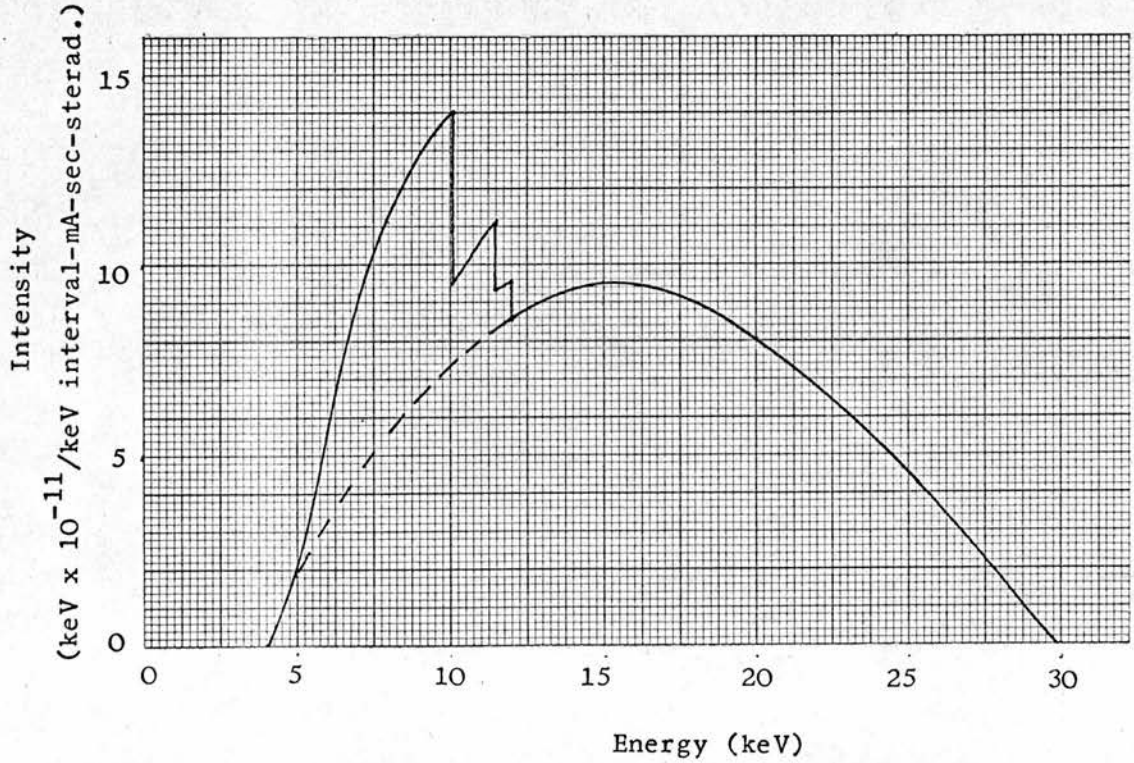

Figure 14(ii)

25kV Intensity distribution

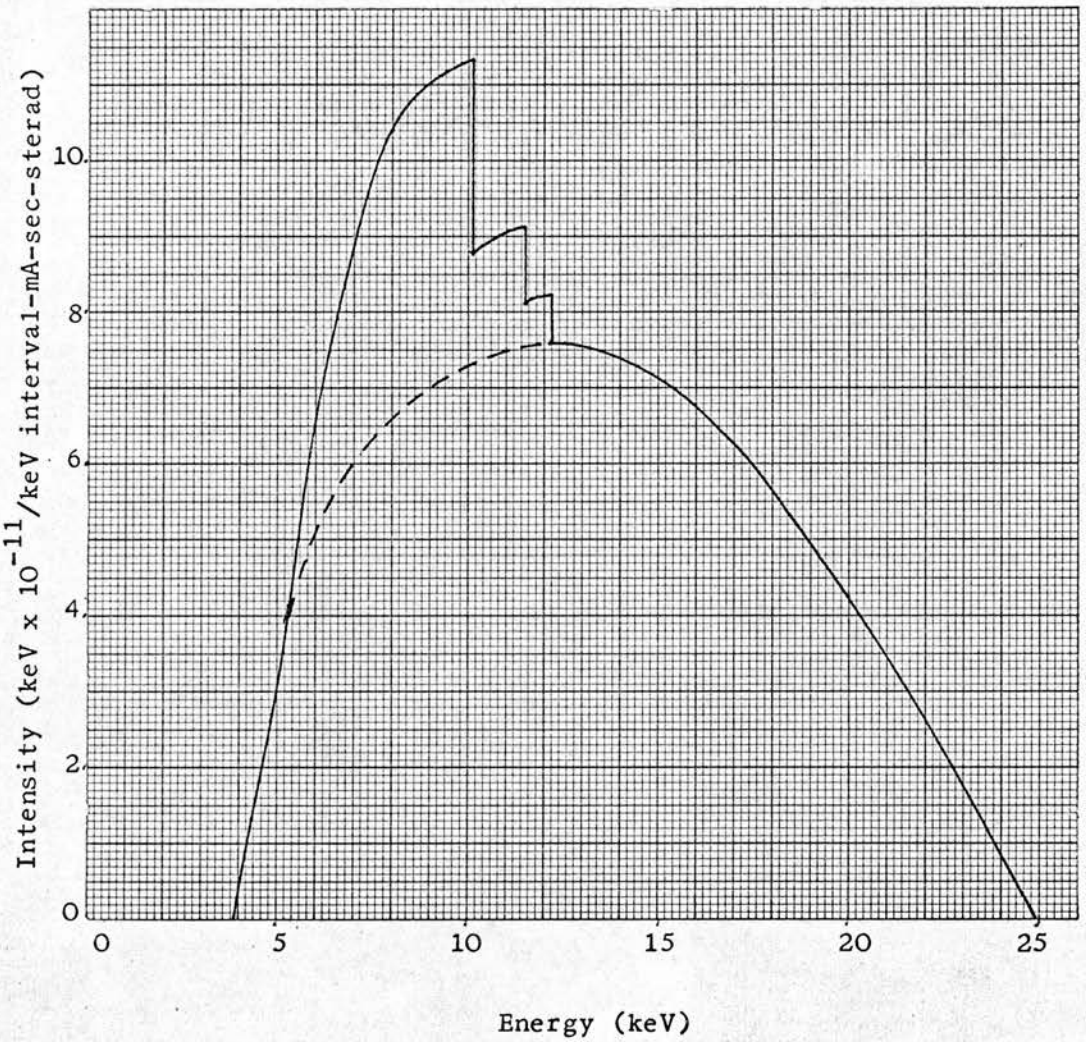

Figure 14(iii)

20, 15 and 10kV Intensity distributions

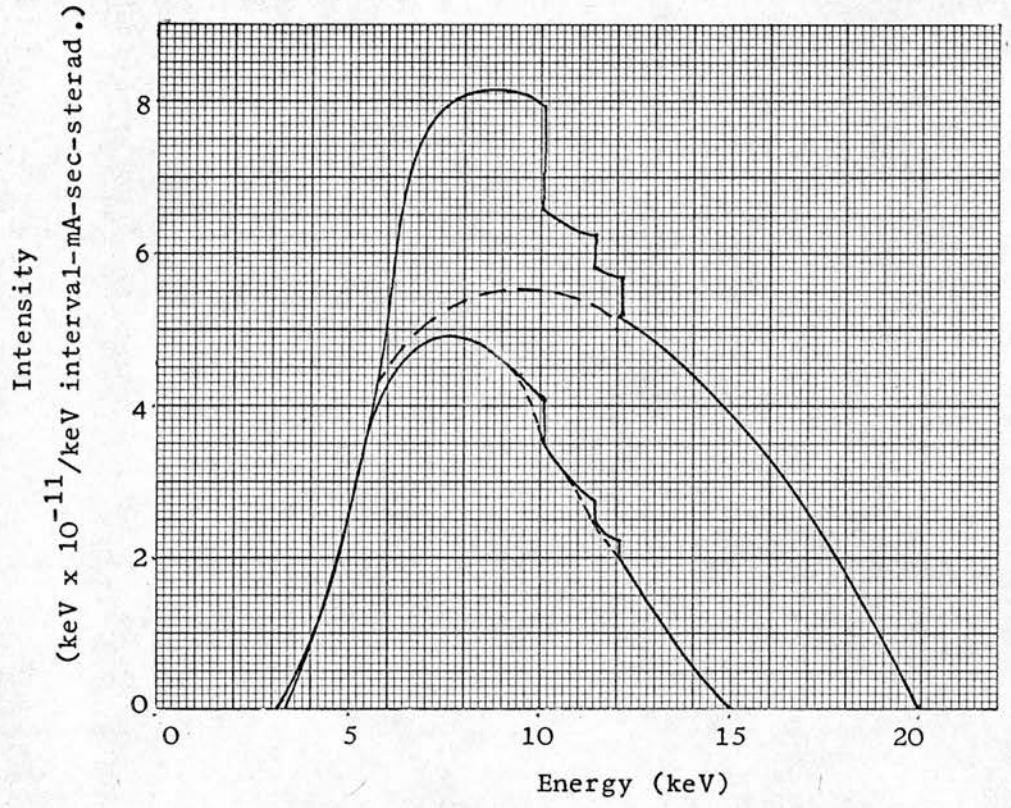

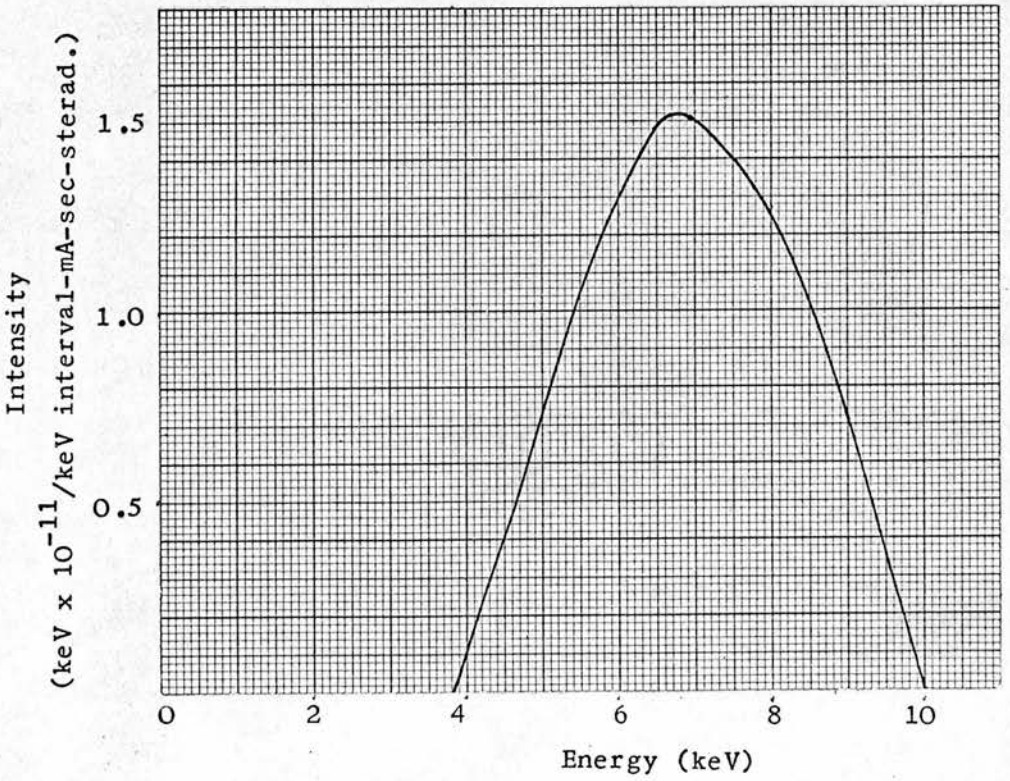

production depth, and that in view of the uncertainties the total intensities are also in reasonable agreement. Spectra for peak energies from 40 - 10keV have been calculated, assuming a constant production depth of $^1/4$ electron range in tungsten. Calculations are on the same lines as that in Table 3, and the resultant distributions corrected for target and window filtration are shown in Fig. 14.

As before, the spectra have been divided into a continuous portion and a portion which is due to characteristic target effects. It can be seen that the choice of the characteristic area becomes increasingly arbitrary as the peak of the continuum coincides with it. This is most apparent for the 20keV spectrum. The total intensities due to each part have been measured using a planimeter and are shown together with the ratio of peak/continuum intensity in Table 9.

Table 9

Division of spectra into smooth continuum and peak areas

Peak Energy (keV)	Production Depth (mg/cm^2)	Total Intensity x 10^{-11} (keV/mA-sec-sterad.)		Ratio (Peak/Continuum) %
		Continuum	Peak	
40	2.0	262	36	14
30	1.0	152	28	18
25	0.7	108	18	17
20	0.5	64	9.5	15
15	0.3	33	0.2	0.6
10	0.2	8.6	-	-

These intensity distributions can be converted to photon distributions using the relationship

Figure 15(ii)

15 and 10kV photon distributions

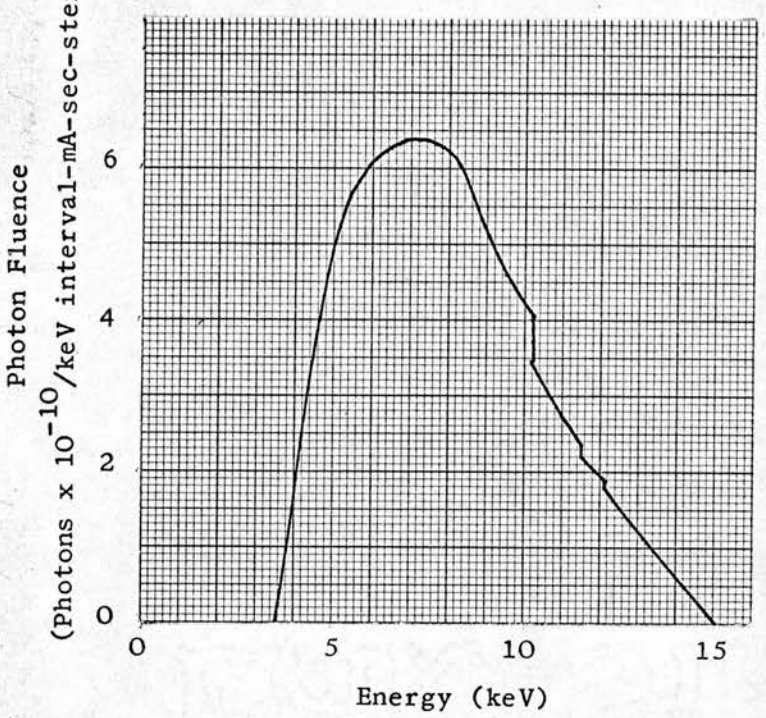

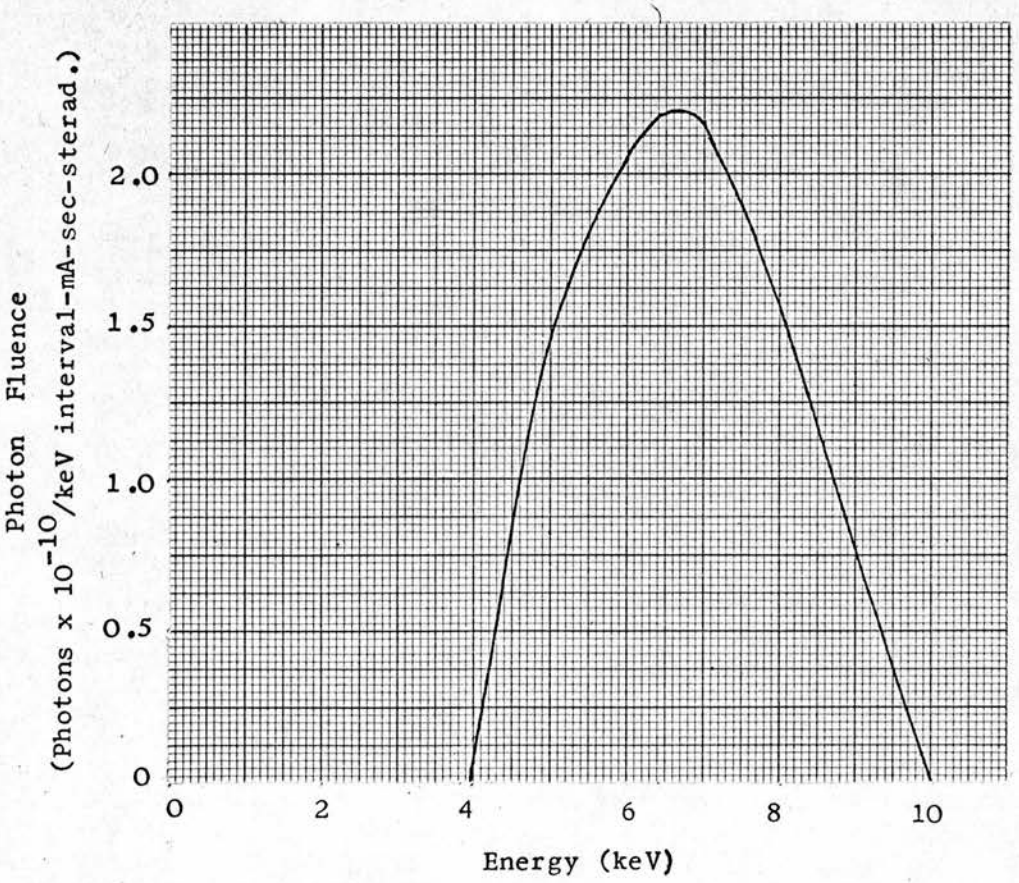

Figure 15(i)

50, 40, 30, 25 and 20kV photon distributions

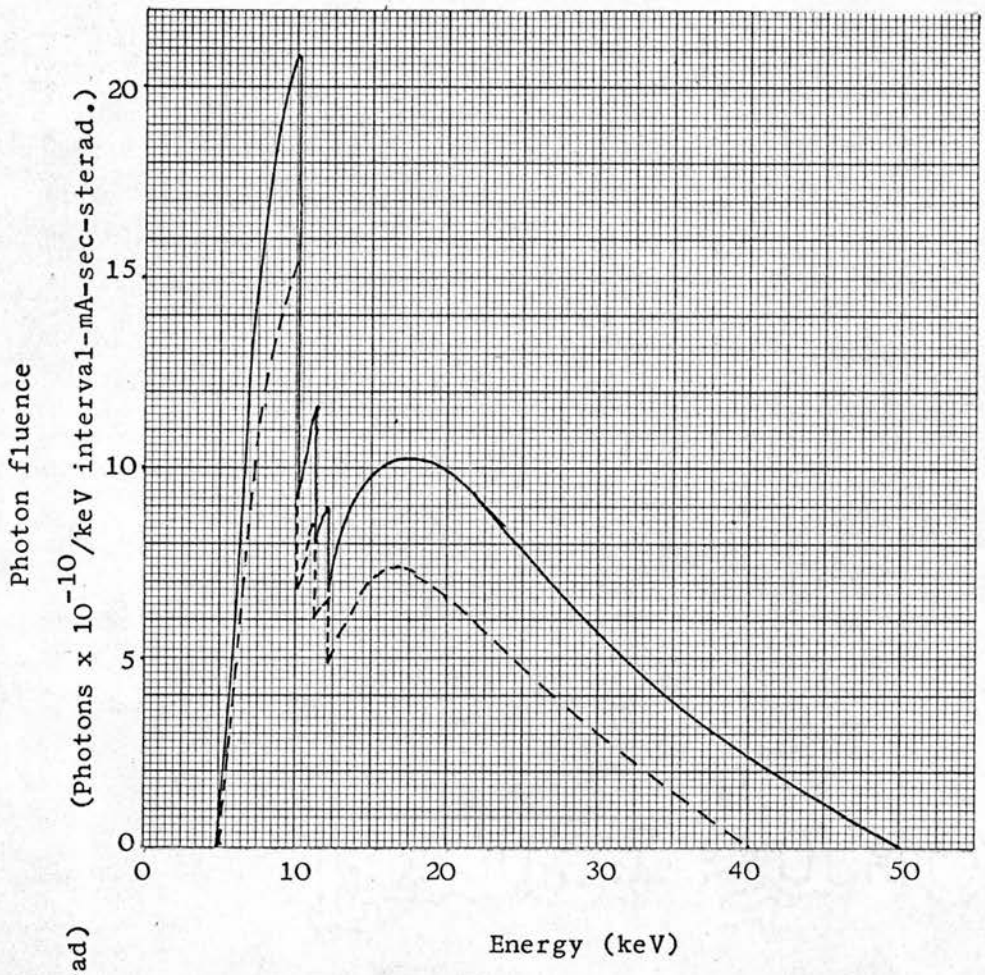

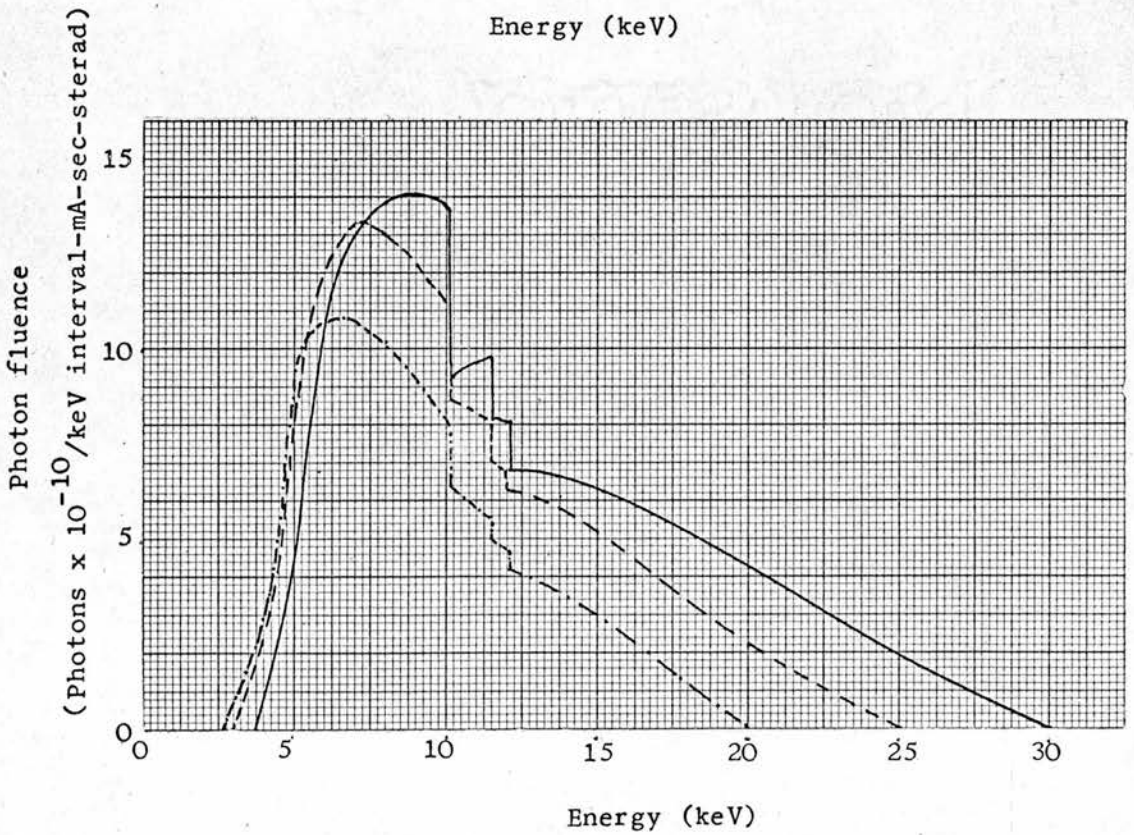

$$I(E) = N(E) \times E$$

where N(E) is the number of photons with energy E and I(E) is the corresponding intensity. Photon distributions corrected for window attenuation are shown in Fig. 15.

2.5 Directly Produced Tungsten L-Characteristic Radiation

Green and Cosslett (1961) have derived an analytic expression for the number of direct K shell ionizations in a thick target per incident electron, namely

$$n_k \text{ (direct)} = 9.535 \times 10^4 \frac{R}{Ac} \left[U_o \ln U_o - (U_o - 1) \right] \quad \ldots\ldots 2.4$$

where A = Atomic weight of target

R = A factor to allow for the backscatter of electrons

c = the constant in the Thomson-Whiddington energy loss equation

$U_o = \frac{E_o}{E_k}$ the ratio of the energy of the incident electron to the K excitation energy of the target material.

From Burhop's calculations (Burhop, 1940), for the ionization cross-section of L-shells Spielberg (1959) has derived the expression

$$n_L \simeq (8/3) (E_k/E_L)^2 \, n_k \quad \ldots\ldots 2.5$$

where n_L is the total number of L-shell ionizations per incident electron for an element with an L-series excitation energy E_L and n_k, E_k are as defined above for either the same target element or another target element being operated at the same over-voltage (defined as V/V_k for K-ionization where V is the tube voltage and V_k the K-ionization potential). Spielberg also quotes fair agreement with this expression from experimental work comparing Selenium K quanta with Lead L quanta. Hence we will proceed to n_L for tungsten by calculating n_k for copper.

Since we are not concerned with the absolute efficiency of X-ray production, we can take R = 1, i.e. assume no backscattering loss of

Figure 16

c, the constant in the Thomson-Whiddington energy losses equation, versus energy

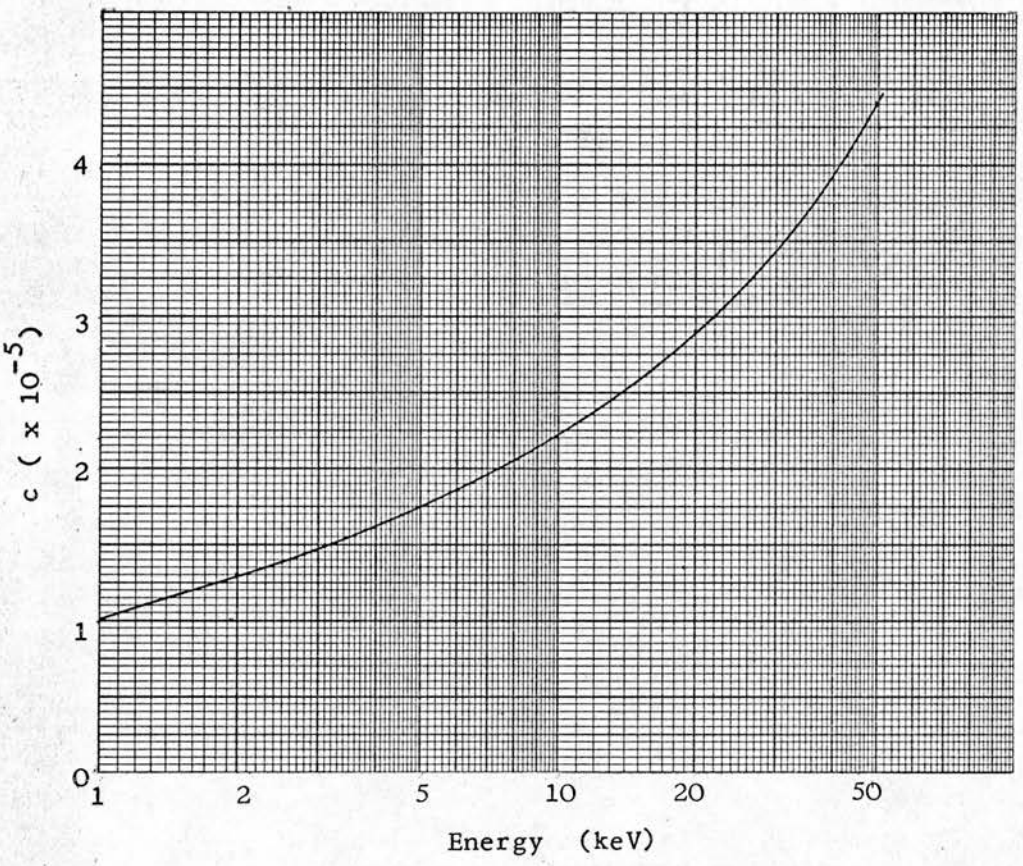

electrons. This was also assumed in the continuum calculation, so that the ratio of characteristic to continuum intensity will not be affected. (In fact Hink (1964, 1965) concludes that R for copper $\simeq$ .90 and for tungsten $\simeq$ .80, so that the calculations here will only be a slight overestimate of the absolute case).

Empirical values of the constant c versus energy (from Green and Cosslett, 1961) are shown in Fig. 16. Hence values of n_k for different values of electron energy have been calculated, and are shown in Table 10.

Table 10

n_k, the number of K-shell ionizations in Copper per Incident Electron

E_k = 9.0keV A = 63.6 R = 1

Energy (keV)	$c \times 10^{-5}$	$n_k \times 10^2$
50	4.4	1.70
40	4.0	1.19
30	3.5	0.712
25	3.2	0.497
20	2.9	0.286
15	2.6	0.104
10	2.3	0.003

The number n_L, of L shell ionizations per electron in tungsten can now be calculated from equation 2.5, taking E_L as 11.5keV. The number of L photons produced per unit solid angle per mA per sec. is then given by

$$\frac{6.26\ \omega n_L \times 10^{15}}{4\pi}$$

where ω is the L fluorescence yield which will be taken as 0.29 (Blokhin, 1961).

Results are shown in Table 11.

Table 11

$(N_{\alpha\beta})_t$, the number of L photons produced in Tungsten before filtration

Energy (keV)	n_L $\frac{\text{ionizations} \times 10^2}{\text{electron}}$	$(N_{\alpha\beta})_t$ $\frac{\text{photons} \times 10^{-11}}{\text{mA-sec-sterad.}}$
50	2.80	40.3
40	1.95	28.2
30	1.17	16.9
25	0.82	11.8
20	0.48	6.9
15	0.17	2.5

Having obtained the direct L characteristic production rate it is necessary to correct for target and window attenuation. The same production depths will be assumed as in the continuum calculations, but since the tungsten attenuation coefficients vary rapidly between 8 - 10keV separate corrections will be made for the L_α and L_β radiation (8.4 and 9.7keV). (The L_γ has been excluded by choosing E_L = 11.5keV). Escape fractions for L_α, L_β radiation for production potentials from 50 - 15kV are shown in Table 12. (Values of μ/ρ for tungsten are from Fig. 11. Extra filtration due to the beryllium window is also shown using

$$\left[\frac{\mu}{\rho} B_e\right]_{L_\alpha} = 1.20 \text{ g/cm}^2$$

(McMaster et al., 1967)

$$\left[\frac{\mu}{\rho} B_e\right]_{L_\beta} = 0.84 \text{ g/cm}^2$$

It remains to find the ratio $\left(\frac{N_\beta}{N_\alpha}\right)_t$, the ratio of the photon flux in the L_β and L_α components when produced at the production depth t, and to correct this for the various escape paths. This can be derived from the results of Jönsson (1926) who found that the ratio of the intensities at the surface of a tungsten target when the tube was operating at 20kV was

Table 12

Fraction f_α, f_β of characteristic radiation escaping from Tungsten Target and Beryllium Window using production depths from Table 9.

Production Potential (kVp)	Target Escape Fraction exp(-μt cot 20°)		Window Transmission		Total Escape Fraction	
	α	β	α	β	f_α	f_β
50	0.372	0.545	0.80	0.86	0.298	0.469
40	0.372	0.545	0.80	0.86	0.298	0.469
30	0.609	0.740	0.80	0.86	0.487	0.637
25	0.730	0.826	0.80	0.86	0.584	0.710
20	0.790	0.869	0.80	0.86	0.633	0.746
15	0.847	0.903	0.80	0.86	0.678	0.776

Table 13

Characteristic Intensity and Photon Flux, corrected for Target and Window Attenuation

Production Potential (kVp)	N (photon x 10^{-11}/mA-sec-sterad.)				I (keV x 10^{-11}/mA-sec-sterad.)		
	$(N_{\alpha\beta})_t$	N_α^*	N_β^*	$N_{\alpha\beta}^*$	I_α^*	I_β^*	$I_{\alpha\beta}^*$
50	40.3	7.95	6.40	14.40	66.8	62.0	129.0
40	28.2	5.56	4.47	10.00	46.7	43.3	90.0
30	16.9	5.45	3.64	9.09	45.8	35.4	81.2
25	11.8	4.56	2.83	7.39	38.4	27.5	65.9
20	6.9	2.89	1.74	4.63	24.3	16.9	41.2
15	2.5	1.12	0.66	1.78	9.4	6.4	15.8

$\frac{I_\beta}{I_\alpha} = 0.646$

From Table 12 $\left(\frac{I_\beta}{I_\alpha}\right)_t \times \frac{0.869}{0.790} = 0.646$

Hence $\left(\frac{I_\beta}{I_\alpha}\right)_t = 0.588$ and $\left(\frac{N_\beta}{N_\alpha}\right)_t = \left(\frac{I_\beta}{I_\alpha}\right)_t \cdot \frac{E_\alpha}{E_\beta} = 0.510$

and if $(N_{\alpha\beta})_t$ is the total characteristic photon flux at depth t,

$(N_\alpha)_t = 0.662\ (N_{\alpha\beta})_t$ and $(N_\beta)_t = 0.338\ (N_{\alpha\beta})_t$

Hence the photon fluxes in the α , β components outside the tube window are given by

$$N_\alpha' = (N_\alpha)_t \times f_\alpha \qquad N_\beta' = (N_\beta)_t \times f_\beta \qquad N_{\alpha\beta}' = N_\alpha' + N_\beta'$$

Values of $(N_{\alpha\beta})_t$ have been calculated in Table 11, hence the total characteristic photon flux and intensity outside the tube window can be calculated. Results are shown in Table 13.

2.6 Indirectly Produced Characteristic Radiation

Green and Cosslett in considering lower atomic number targets were able to assume that continuous radiation is emitted isotropically from a layer very close to the surface of the target so that one half of the continuous quanta are absorbed in the target and may produce indirect characteristic radiation. By considering an example it will be shown that this approach is not applicable in the present study.

It has been assumed that the effective production depth for bremsstrahlung excited at 50kV is $\simeq 2$ mg/cm^2, giving an escape path of $\simeq 6$ mg/cm^2. We can consider indirect ionization for two separate cases:-

a) Ionization taking place at a depth >2mg/cm^2

In this case the characteristic radiation formed has a large escape path through the target, and will almost all be absorbed. (An

escape path of 12 mg/cm^2 of tungsten absorbs ~90% of 9keV radiation).

b) Ionization taking place at a depth < 2 mg/cm^2

It is from ionizations of this type that indirect quanta which may escape can be produced. Hink (1965) has undertaken the extensive work necessary to calculate the indirect component for tungsten targets operated in the transmission mode; these calculations are very sensitive to production depth and so it does not seem worthwhile undertaking them for the present case. Hink considers 2 targets of thickness 13.7 mg/cm^2 and 25.4 mg/cm^2, using these also as the tube windows (i.e. viewing angle = 0°); we will draw qualitative conclusions from his results. He measures P, the ratio of the number of direct L photons to the number of indirect L photons; his results for the two targets are shown in Table 14.

Table 14

P, the ratio of the number of direct to indirect L photons escaping from tungsten transmission targets (from Hink, 1965).

kV	P	
	13.7 mg/cm^2	25.4 mg/cm^2
50	8.1	5.3
40	8.1	5.5
30	9.0	6.7
20	10.0	9.0

Consider the 50kV results. We have assumed an effective production depth of ~2 mg/cm^2, hence the escape paths are ~12, 23 mg/cm^2 for the two targets which Hink used, and it will be seen that there is less indirect radiation produced for the shorter escape path. In our case, with an escape path of ~6 mg/cm^2 we will expect still less indirect radiation, probably in the region of 5 - 10% of the direct at 50kV, and even less at lower potentials.

In view of the approximations in the calculation of the number of direct photons, this small proportion of indirect radiation will be neglected.

2.7 Summary of Results

Results can now be tabulated in terms of the intensities due to (a) the smooth continuum, as defined in 2.3,

(b) the characteristic part of the continuum,

(c) the true characteristic radiation.

These are shown in Table 16.

Table 15

X-ray Intensity Distributions
corrected for target and window filtration

Production Potential (kV)	Intensity (keV x 10^{-11}/mA-sec-sterad.)			
	Continuum	"Characteristic" Continuum	True Characteristic	Total
50	484	48	130	662
40	262	36	90	388
30	152	28	81	261
25	108	18	66	192
20	64	9.5	41	115
15	33	0.2	16	49
10	8.6	-	-	8.6

A comparison with experiment can be drawn from the results of Redpath (1967), who measured the energy fluence of various beams through a $^{3}/16$" aperture at a focus-aperture distance of 9cm and corresponding air path of 12cm, with an additional filtration of 0.0015" Melinex film. Theoretical X-ray distributions corrected for this extra filtration are

shown in Table 16, where they are compared with the experimental results.

Table 16

X-ray Intensity Distributions
with an additional 12cm Air and 0.0015" Melinex filtration

Production Potential (kV)	Intensity (keV x 10^{-11}/mA-sec-sterad.)					
	Continuum	"Charact" Continuum	Characteristic α	Characteristic β	Total (Theory)	Total (Expt.)
30	148	22	39	32	241	260
25	97	17	33	25	172	175
20	50	12	20	15	97	97
15	30		8	6	44	36
10	5.7		-	-	5.7	6.2

The very good agreement must be regarded as somewhat fortuitous in view of the many approximations in the theory, but it certainly appears that spectra derived in this way are consistent with experimental intensity measurements. These calculations show the importance, which does not appear to have been fully recognised by previous workers, of self-absorption effects in modifying the spectra of beryllium window X-ray tubes so that low resolution spectrometry will show apparently more characteristic radiation than is in fact present. Results presented here should prove useful in the calculation of intensities and dose rates from similar beryllium window tubes under a variety of experimental conditions.

Figure 1 (repeated)

Attenuation coefficients for materials of adjacent atomic number

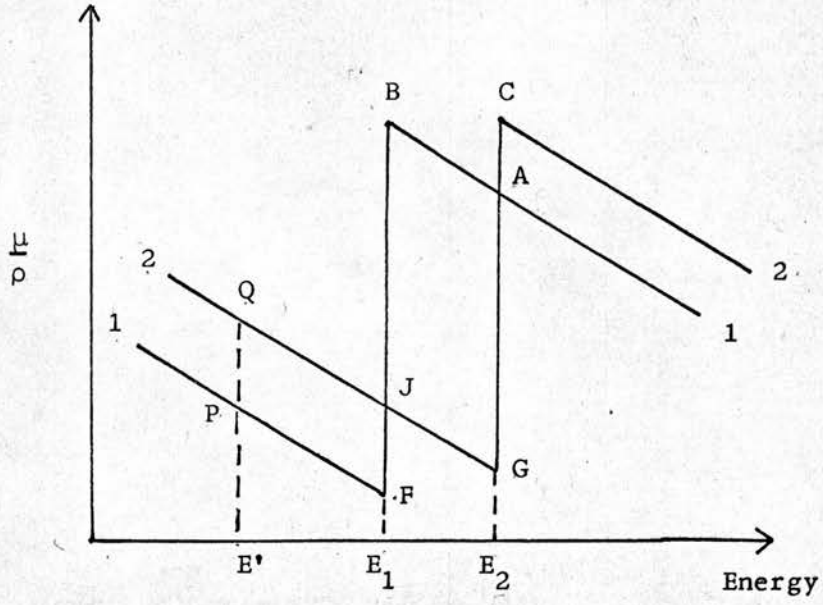

CHAPTER 3

DETERMINATION OF PROPORTION OF CHARACTERISTIC RADIATION IN X-RAY BEAMS USING ROSS FILTERS

3.1 Filter thickness

3.1.1 Thickness for balance

In Chapter 1 the use of Ross filters for isolating a narrow energy band of a spectral distribution has been briefly discussed. Kirkpatrick (1939, 1944) has considered the balancing of such filters in two useful papers; some of his results will be used here. Fig. 1(repeated) illustrates the variation of attenuation coefficient with energy for two elements of adjacent atomic number. Suppose that we require filters of these elements which transmit equal intensities of a monoenergetic beam of energy E' and initial intensity I_o. Then, denoting the attenuation coefficient of the filter of material (1) at energy E' by μ_P, etc., the ratio of the filter thicknesses t_1 and t_2 are given by:-

$$I_o \exp(-\mu_P t_1) = I_o \exp(-\mu_Q t_2)$$

$$\text{i.e. } \mu_P t_1 = \mu_Q t_2$$

If μ_P/μ_Q were constant eith energy, then these filters would be balanced at all energies. However, between energies E_1 and E_2 (Fig. 1) this proportionality is not valid due to the K-absorption edges, which vary in magnitude (e.g. μ_B/μ_F) and energy for different elements. Thus between energies E_1 and E_2 the filter of thickness t_2 will transmit a much higher intensity than the filter of thickness t_1. Above energy E_2, the filters will again be balanced if μ_P/μ_Q is constant with energy. The energy

band $E_2 - E_1$ is called the pass band.

Because of the variations of K jump (μ_B / μ_F) with element, it is convenient to balance filters just above or below the pass-band energy and to consider the lack of balance at all energies other than those in the pass-band as contributing to the "error area". This error area will also take into account the fact that the variation of μ with energy is not identical even for adjacent atomic number elements at energies away from the absorption edges.

Kirkpatrick (1939) shows that the addition of a third filter which has no K edge in the region of interest will reduce this error area; the ratios of the thicknesses t_1, t_2 and t_3 of the filters are then given by:-

$$\mu_{3L} t_3 = \mu_J t_2 \frac{|(r_1 - r_2)|}{r_1 - 1} \quad \ldots\ldots 3.1$$

$$\mu_F t_1 = \mu_J t_2 \frac{(r_2 - 1)}{(r_1 - 1)} \quad \ldots\ldots 3.2$$

where μ_{3L} is the attenuation coefficient of the third filter at E_1, the low energy side of the pass band, μ_J and μ_F are the attenuation coefficients at the points J, and F in Fig. 1, and r_1 and r_2 are the K-jumps $\frac{\mu_B}{\mu_F}$ and $\frac{\mu_C}{\mu_G}$ respectively.

3.1.2 Balance at High or Low Energy side of Pass Band

It will be seen later that the use of a third filter to improve balance is difficult at low energies, hence it is important to decide at which side of the pass band to balance for minimum error. We will consider the error as represented by the lack of balance $\Delta(\mu t)$ at the opposite side of the passband to that at which balance took place. Kirkpatrick shows

that if balance is made at the low energy side, the error p_2 (= $\Delta(\mu t)$ at high energy side) is approximately given by

$$p_2 = \mu_J t_2 \left(\frac{E_1}{E_2}\right)^3 (r_1 - r_2)$$

and it can also be shown that balancing at high energy gives an error

$$p_1 = \mu_A \left(\frac{E_2}{E_1}\right)^3 \left[\frac{1}{r_1} - \frac{1}{r_2}\right] t_1'$$

and with some manipulation

$$\frac{p_1}{p_2} = \frac{1}{r_2} \left(\frac{E_2}{E_1}\right)^3 \frac{t_1'}{t_1} \qquad \ldots\ldots 3.3$$

where t_1', t_1 refer to the thicknesses of filter 1 necessary for balance when effected at high and low energy sides respectively. In cases to be considered the last two factors in equation 3.3 are $\simeq 1$, hence

$$\frac{p_1}{p_2} \simeq \frac{1}{r_2} \qquad \text{and} \qquad r_2 \simeq 10$$

for materials with K edges in the region of tungsten L radiation so that the error will be least if filters are balanced at the high energy side of the pass band.

3.1.3 Optimum Thickness of Filters

The expressions quoted in 3.1.1 merely define the ratio of filter thicknesses necessary for balance; the actual values chosen for the thicknesses depend on the intensity of transmission required. For a high percentage accuracy, the intensity of the pass band must be maximised. Reference to Fig. 2 shows that this intensity is approximately given by

$$I = I_o \Delta E (\exp(-\mu_L t) - \exp(-\mu_H t))$$

where $I_o \Delta E$ is the initial intensity in the energy band ΔE, and μ_L, μ_H are the absorption coefficients of the filter thickness E at the low and high energy sides of the band.

Hence $t(\text{optimum}) = \frac{\ln r}{\mu_L(1 - r)}$ $\qquad r = \frac{\mu_H}{\mu_L}$

For copper, a typical element with a K-edge near the tungsten L lines, $\mu_H \simeq 2700\ cm^{-1}$ $\mu_L \simeq 360\ cm^{-1}$, hence $t(\text{optimum}) \simeq 9\ \mu m$. Thus it will be seen that manufacturing problems are likely to influence the choice of filter materials.

3.2 Choice of filter materials

In order to isolate the tungsten L lines, filters with K-edges on either side of the line or lines of interest will be required. Suitable materials, with their K-edges are shown in Table 17.

Table 17

K edges of elements considered for Ross Filters

Element	K-edge (keV)	Tungsten Line (keV) α	β	γ
27 Co	7.71			
28 Ni	8.33	8.33		
29 Cu	8.98	8.40		
30 Zn	9.66		9.67	
31 Ga	10.37		9.96	
32 Ge	11.10			11.28
33 As	11.86			

Figure 17

Line shape of tungsten $L\alpha_2$ line

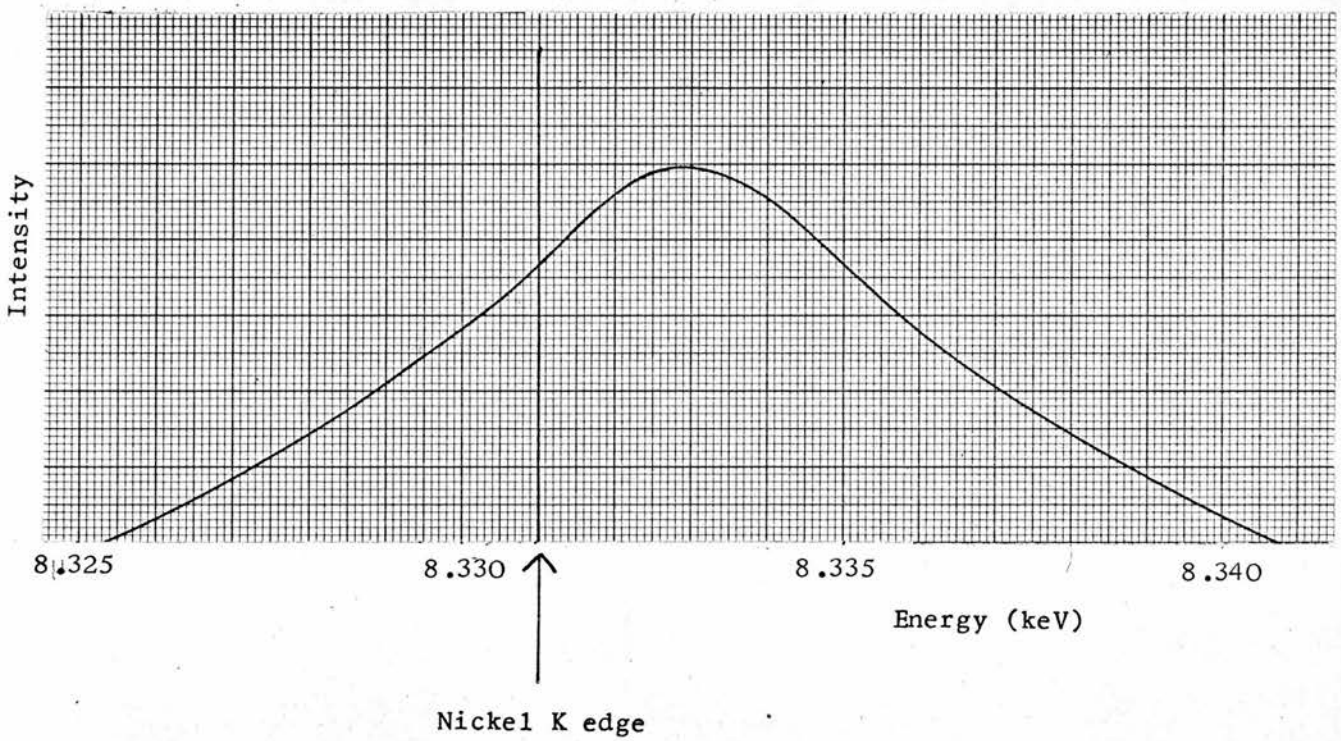

Of this list, only nickel and copper can easily be made into thin uniform films, e.g. by electrodeposition. It would also be useful to isolate the β component but germanium sheet does not appear to be manufactured. The possibility of using liquid filters (as used by Tothill (1964) to isolate the tungsten K-lines) was investigated, but analysis showed that at low energies the attenuation due to the liquid and other elements in the compound used would be comparable to the attenuation due to the element, and so sensitivity would be greatly reduced. Hence nickel and copper were chosen as filter materials and from measurements of the α component, the intensity of the β component was deduced using the results of Chapter 2.

3.3 Effect of L_{α_2} Line-width

The K-absorption edge of nickel is quoted as 8.331 keV (all results here are from Blokhin, 1961) and the tungsten L_{α_2} line is at 8.333 keV. Hence there is a possibility that part of the intensity of the α_2 line will not be transmitted by the filter, due to the finite width of the line and the absorption edge.

The L_{α_2} line is due to the transition from the M_{IV} to the L_{III} shell, and the line width ΔE is given by the sum of the widths of the atomic levels (extrapolating from the values for gold).

$$\Delta E = 7.1 \text{ eV} \pm 0.6$$

The effect of this line width is shown in Fig. 17. Approximately 75% of the intensity falls above the nickel edge if this is assumed infinitely sharp. In fact the edge does have a width, from 8.329 - 8.332 keV. The intensity of the α_2 line is 10.3% of the total α intensity (Blokhin,

1961). Hence, between 2.5 - 7.5% of the total α intensity will be lost. A correction will be made for this.

3.4 Manufacture of Thin Filters

3.4.1 Thicknesses required

For maximum pass band intensity, and balance at the high energy side, taking attenuation coefficients from (McMaster, 1967) the thickness of the copper filter is given by

$$t_{Cu} = \frac{\ln \frac{307}{37}}{(307 - 37)\ 8.9} = 8.8\ \mu m$$

i.e. $\rho t_{Cu} = 7.9\ mg/cm^2$

and the nickel filter mass cross-section for balance is

$$\rho t_{Ni} = 9.0\ mg/cm^2$$

Then the mass cross-section of the low atomic number filter is given by

$$\rho t_3 = 18.0 / \left(\frac{\mu}{\rho}\right)_{3L}$$

Aluminium has been suggested (Kirkpatrick, 1939) for this filter, although the scatter component of its attenuation coefficient at 20keV is significant, and so the total attenuation coefficient will not have the same dependence with energy as that of the other filters. For aluminium $\left(\frac{\mu}{\rho}\right)_{3L} = 4.3 cm^2/gm.$

therefore $\rho t_3 = 0.45\ mg/cm^2$ $t_3 = 1.7 \times 10^{-4} cm$

which would present great manufacturing difficulties. Melinex film is available commercially in thicknesses down to 6.3×10^{-4}cm. For Melinex

$\left(\frac{\mu}{\rho}\right)_{3L} = 6.0\ cm^2/gm.$

therefore $\rho t_3 = 3.3\ mg/cm^2$ $t_3 = 24 \times 10^{-3} cm$

However (μ/ρ) for Melinex depends mostly on scatter at energies greater than 15 keV, so it was decided to use a single sheet of 6.3×10^{-4}cm

Figure 18

Electroplating situation

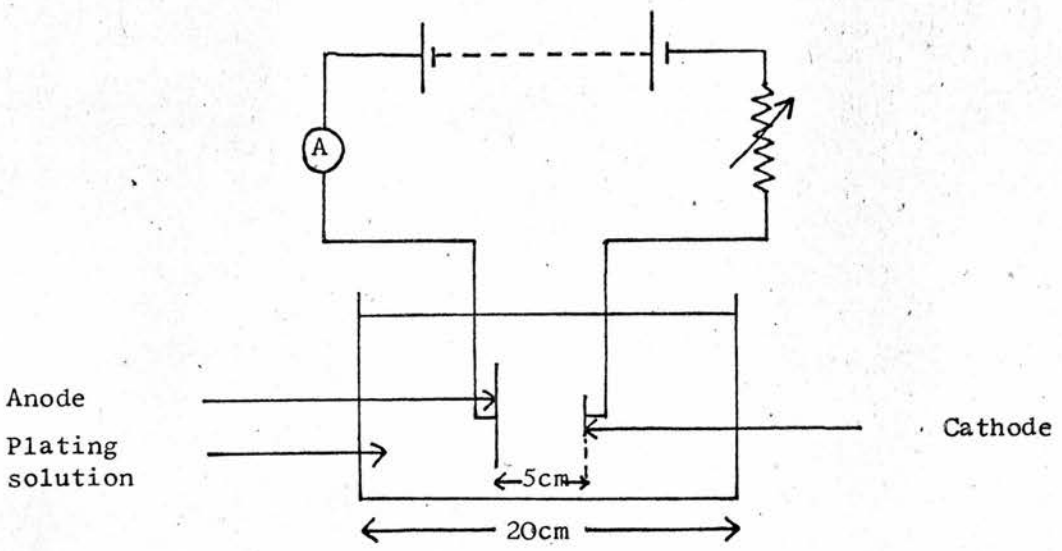

	Copper Plating	Nickel Plating
Plating Solution	$CuSO_4$ 60gm/l H_2SO_4 (conc) 6ml/l	$NiSO_4$ 72g/l $MgSO_4$ 24g/l HBO_3 9g/l NH_4Cl 6g/l $C_6H_{12}O_6$ 6g/l
(used at room temperature)		
Cathode	Stainless Steel 2 x 2cm	Stainless Steel 2 x 2cm
Anode	Cu, 8 x 8cm	Ni, 8 x 8cm
Current Density	10-15mA/cm^2	5mA/cm^2
Agitation	15-20rpm.	5-10rpm.

film combined with the copper filter. This should improve the balance at low energies whilst not affecting high energies, and we will further improve this by balancing at high energies.

3.4.2 Electrodeposition Process for Copper and Nickel Films

After a certain amount of trial and error, a suitable system was found for making the thin films. The apparatus is illustrated in Fig. 18 with details of the materials used. To ensure even deposition large anodes had to be used, and rate of stirring (done magnetically) and current density were critical. The cathode was scrupulously cleaned and polished and masked with plastic tape so that only an area 2cm square was exposed for plating. (It was found that larger areas did not plate uniformly). Nickel plating produced most problems since the film was brittle and tended to split at thicknesses greater than $5mg/cm^2$. Eventually two suitable films were made and sandwiched together. The approximate time to plate films of the required thickness could be found from a knowledge of the electrochemical equivalents. After plating, the cathode was washed in distilled water and alcohol, and dried in warm air; the metal film could then be peeled off, trimmed to size, and measured and weighed to calculate its thickness. From the many films thus made, those with thicknesses most near to those calculated in 3.4.1 were mounted on firm card frames. The measured thicknesses are:-

Filter 1. $\rho t_{Cu} = 8.50 \pm 5\%\ mg/cm^2$; $\rho t_{Melinex} = 0.87\ mg/cm^2$

Filter 2. $\rho t_{Ni} = 4.81 + 4.94 = 9.75 \pm 7\%\ mg/cm^2$

The accuracy of these thickness measurements has been improved by attenuation measurements described later (section 3.8.2) but even so, fine adjustment is made experimentally by rotating the copper and Melinex filter about an axis perpendicular to the beam, so that a very accurate

balance of the two filters can be achieved.

3.5 Choice of Detectors

3.5.1 Basic considerations

Since it is required to measure intensities, the most convenient form of detection system will employ a total absorption device since this is energy independent in response. Three suitable systems have been developed by Redpath (1967) and have been fully described in his thesis. The following is a brief survey to choose the most suitable system or systems for measuring the low intensities expected whilst balancing the filters, and for measuring the total intensities of unfiltered X-ray beams.

3.5.2 Calorimeter

This provides an absolute method of determining the energy deposited by an X-ray beam, by absorbing the beam in a suitable material and measuring the temperature rise produced. If the beam is totally absorbed, then the total energy fluence is measured, although in practice there are small corrections to be made for the loss of energy due to scattered radiation. The calorimeter used is of the constant temperature environmental type, employing twin gold absorbers, each containing a thermistor temperature sensor. One absorber is an unirradiated "dummy". The other irradiated absorber contains a heating coil so that known calibration energies can be introduced electrically. The temperature difference between the absorbers is detected by connecting the thermistors in opposing arms of an a.c. Wheatstone bridge circuit. The advantage of using twin absorbers of equal heat capacity, both in the same environment is that the effect of external temperature variation is reduced.

Figure 19

SCHEMATIC DIAGRAM OF CALORIMETER

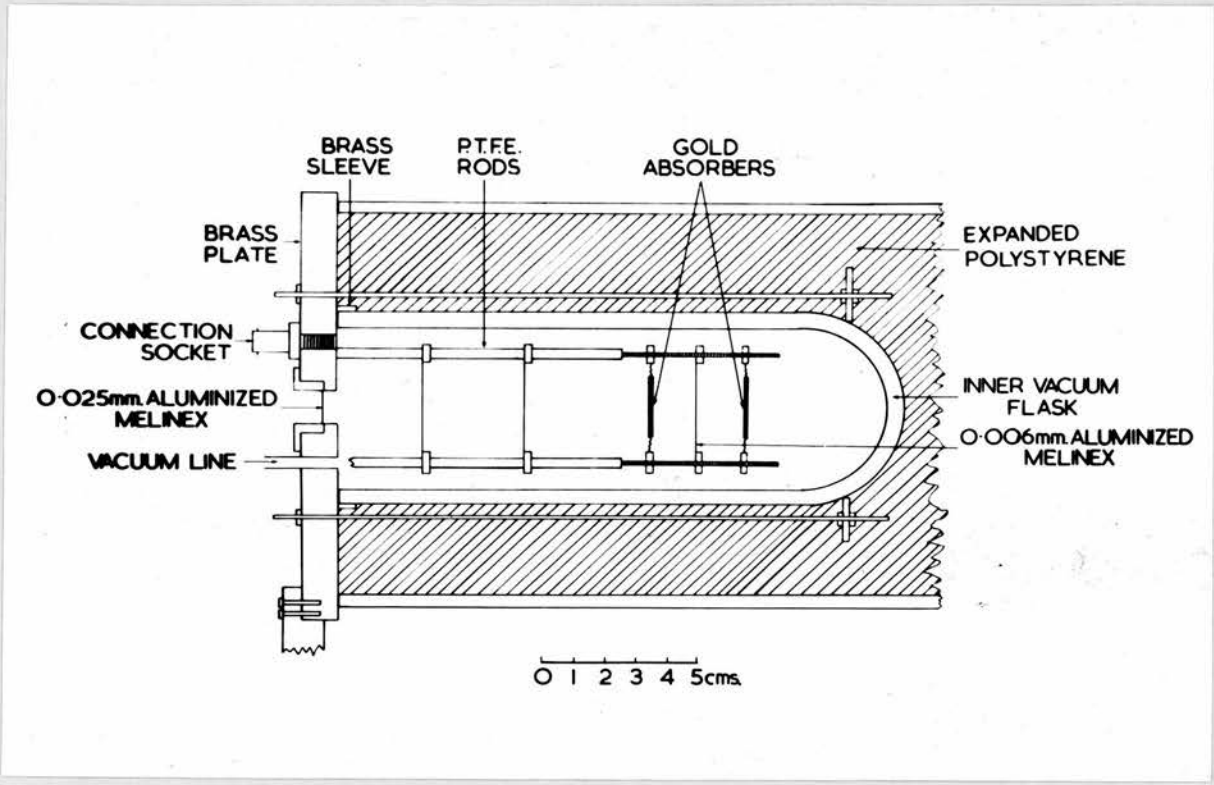

The out-of-balance signal is amplified, passed through a phase sensitive detector to improve the signal to noise ratio, and displayed on a chart recorder. Redpath discusses several methods of operation and condludes that from the point of view of convenience, lack of subjectivity and accuracy, thermal cycling is best. This method was used for calorimetry throughout the present study.

Thermal cycling consists of allowing the absorber to cool from a temperature Θ_1 to a temperature Θ_2 and then heating it with the X-ray beam from Θ_2 to Θ_1 again, the cooling and heating periods t_1 and t_2 being measured. Then it can be shown that the power, P, of the beam is given to a close approximation by

$$P = k(\Theta_1 - \Theta_2)\left(\frac{1}{t_1} + \frac{1}{t_2}\right) \qquad \text{where k is a constant.}$$

By repeating the measurements with known electrical powers the constant term $k(\Theta_1 - \Theta_2)$ can be found, and the X-ray power calculated.

The design of the calorimeter is shown schematically in Fig. 19 and the large amount of thermal insulation ensures the constant temperature environment. Since the interior is evacuated, the total filtration introduced is merely that due to the Melinex window and heat shields amounting to 0.038mm in all.

Using the calorimeter, Redpath has calibrated secondary standards, the responses of which depend on ionization by the X-ray beam and he has used these for intensity measurements. This calibration required the accurate measurement of $\overline{W}$, the average energy required to form an ion pair in the materials, and for a useful dosimeter $\overline{W}$ must not vary with energy. No variation was found for the secondary standards used. The use of secondary instruments gives some advantages in simplicity and ease of

operation, but as will be seen, they are most useful only up to 15keV.

3.5.3 Gas Ionization Chamber

This secondary instrument has been designed to achieve 99.9% absorption of X-ray beams of up to 15kV when filled with Argon at pressures of up to 3 atmospheres, and to be of sufficient diameter to reduce the energy loss due to side-scatter to small proportions. Entrance and exit windows are of Melinex, total filtration being the same as that used in the calorimeter. In order to achieve saturation it is necessary to operate with a potential of up to 4kV across the plates. To allow for fluctuations in the power output of the X-ray tube, the current from the ionization chamber is integrated for a fixed time on a capacitor and compared with the charge collected over the same time from a monitor chamber. The advantage of the ionization chamber is that the background current is very low and hence the sensitivity high for low power beams. This system has been used for attenuation measurements on the Ross Filters.

3.5.4 Solid State Ionization Detector

This consists of a silicon surface barrier detector approximately 3mm thick and 2 sq.cm in sensitive area. Such detectors are manufactured by exposing pure N-type silicon to the air; this results in a thin layer of P-type material being produced on the surface by oxidation. Electrodes are made by depositing a thin layer of gold, 80$\mu g/cm^2$ on to the surfaces. The region close to the P-N junction is called the depletion layer since it is almost carrier free. It is radiation sensitive, and analogous in operation to a gas ionization chamber, with the advantage of having a higher stopping power. By applying reverse bias to the junction the depth of the depletion layer can be increased although a relatively high leakage current,

mostly due to surface leakage, now exists. In operation the detector is mounted in an evacuated can with an opaque aluminised Melinex window since the device is light sensitive. Total filtration is the same as that used in the calorimeter. Since the leakage current is comparable with the ionization currents to be measured it is backed off with a high impedance current source. Saturation takes place at greater than 10V reverse bias, and breakdown is stated to occur at 120V; all readings were taken with a bias of 48V. Collected charge is stored on the same capacitor system as before and compared with the monitor reading. Energy losses for this detector become substantial at 15keV due to transmission and at low energies the absorption of the gold window is significant. Even so, it is the most convenient device to use for total intensity measurements of 10 and 15kV beams. For higher energies the calorimeter has been used, but transmission through the absorbers limits the maximum energy accurately measurable to 30keV.

3.5.5 Experimental Situation

The X-ray tube used is a Machlett, type OEG-50-A, with a beryllium window 1mm thick and a focal spot 1.5mm square in projection. The target is high purity tungsten. The tube is operated at constant potential, kilovoltage being continuously variable between 0-50kV and tube current between 0-30mA with the limitation that the maximum power dissipation is 800 watts. The HT output of the constant potential unit is stabilised within $\pm$ 50V over a period not exceeding 4 hours at full load, and HT ripple is quoted as $\simeq$ 70V/mA. Kilovoltage is measured on a variable scale "Scalamp" galvanometer which measures the current through a high resistance leak across the tube. There are two ranges

Figure 20

OPTICAL BENCH WITH CALORIMETER IN POSITION

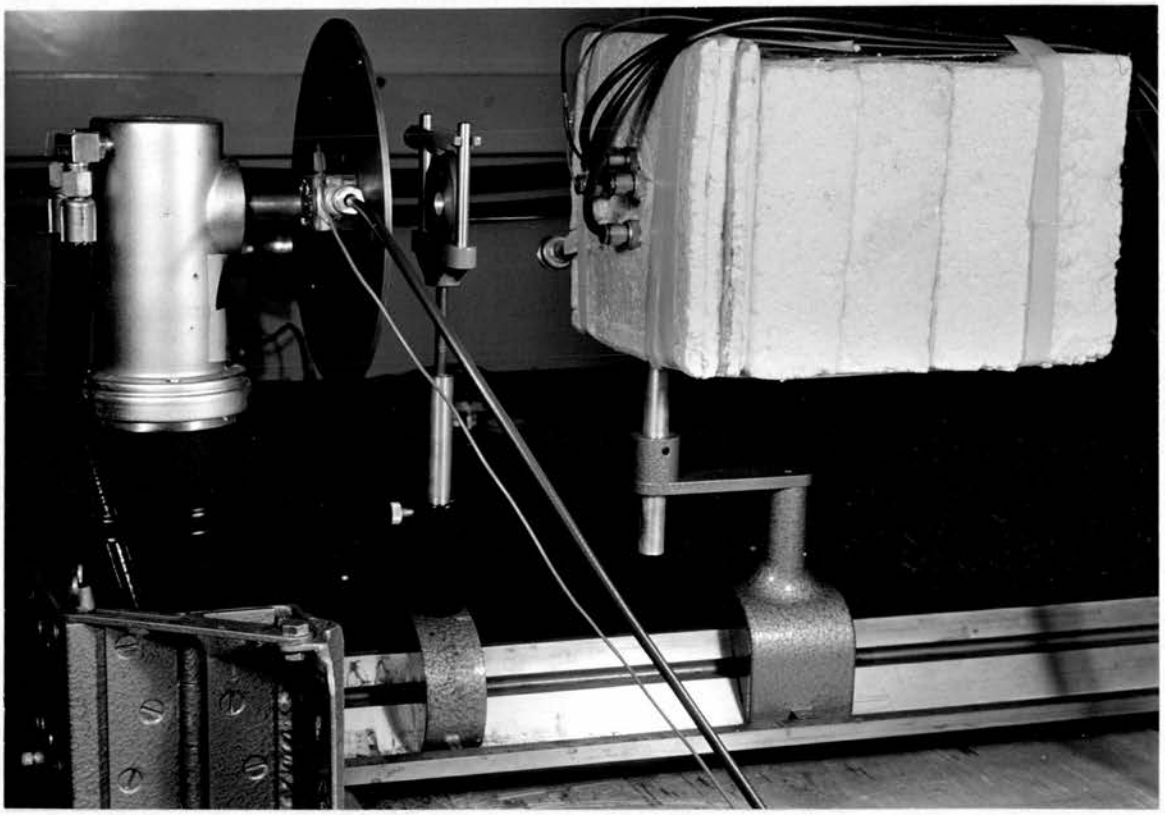

Figure 21

Monitor Chamber Assembly

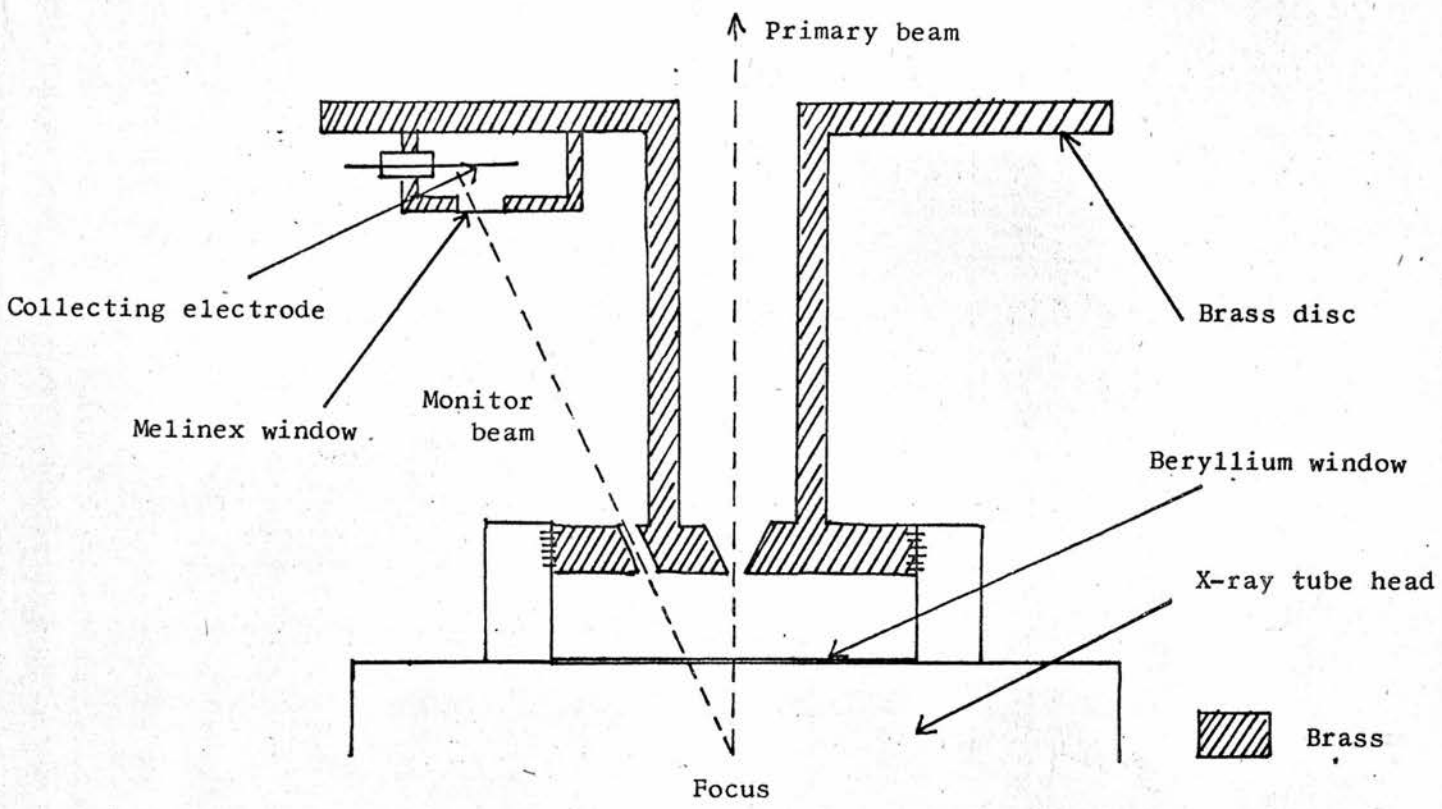

Figure 22

Integrating Circuit

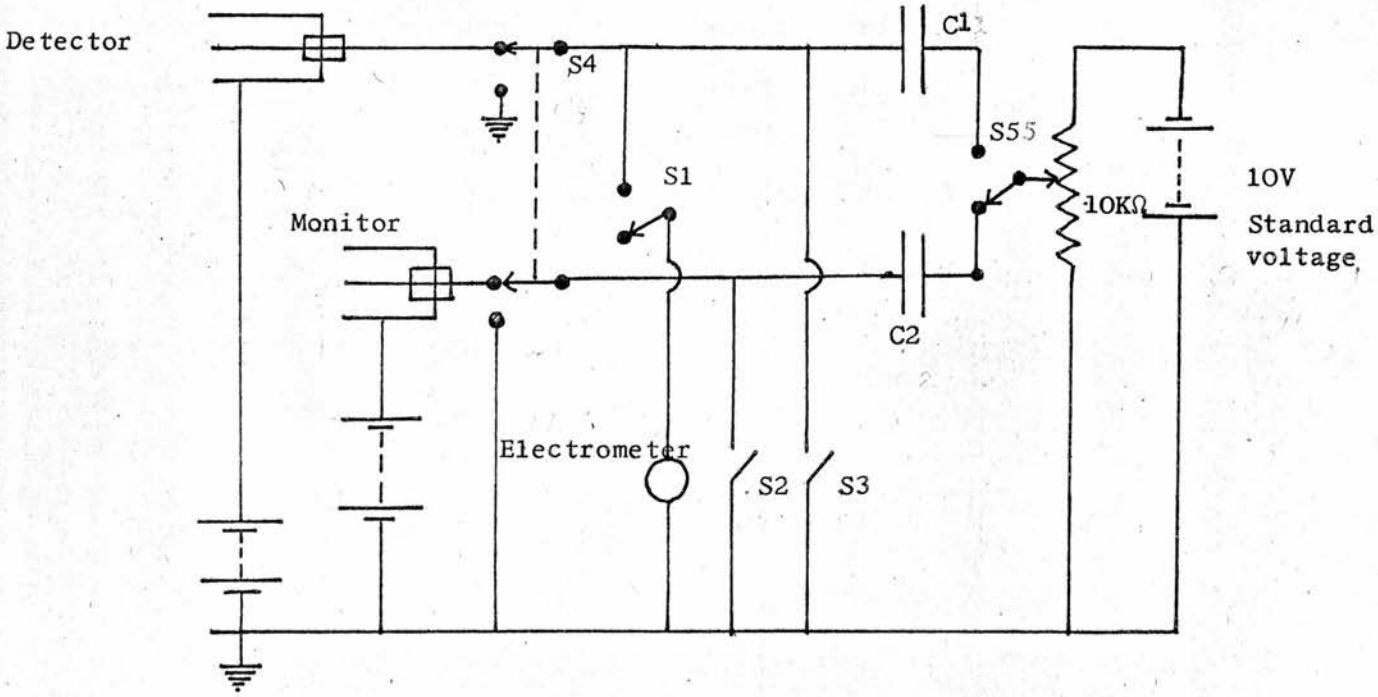

used

1. 0-10kV: sensitivity 1mm = 0.1kV
2. 0-50kV: sensitivity 1mm = 0.5kV

Although a given kV setting is reproducible to better than 1%, the manufacturers can only quote the accuracy of the absolute kV measurement to ±5%. However, indicated readings have been measured by the method of Greening (1955) and found to be accurate to ± 0.5kV (Law, 1966).

The X-ray tube is mounted vertically so that the beam axis is horizontal. An optical bench lies parallel to and below the primary beam. All detection devices and defining apertures are mounted on this bench and are positioned by means of a reference pointer which is placed at a known position on the bench and the device moved up until the pointer touches a mark on the front face. All detectors are designed so that the distance from the front face to the entrance window is constant, hence this method ensures the same geometrical position for each detector with respect to the X-ray beam. Fig. 20 shows the calorimeter lined up on the optical bench. This accurate lining up has also been checked with radiographs. The X-ray beam accepted is defined by a single aperture placed at a known position on the bench. The Ross filters, mounted on stands, are placed in the beam after this defining aperture, which is chosen sufficiently small to ensure that the entire beam passes through the filters. The copper filter can be rotated through small angles about the vertical axis for balancing.

The monitor chamber arrangement is shown in Fig. 21. The chamber is mounted on a brass disc which screws into the front of the

Figure 23

20kV spectrum filtered with 0.01cm tin

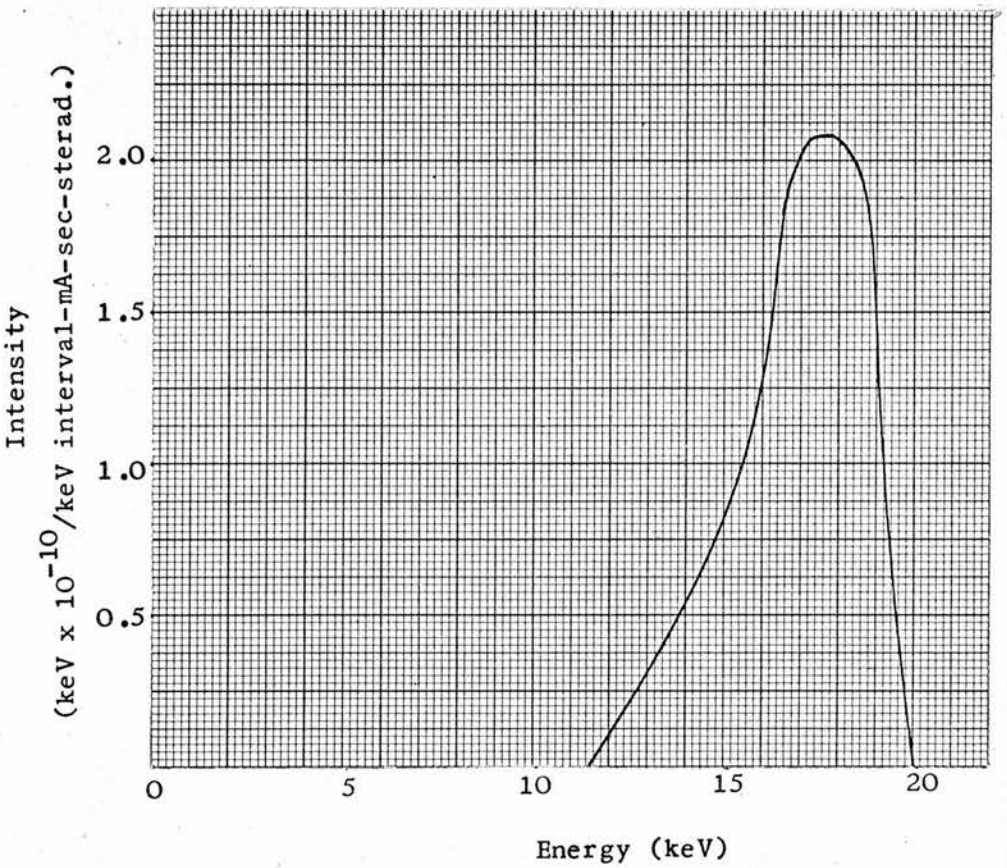

X-ray tube, and receives, via a small angled aperture, a beam of X-rays of the same quality as that being measured. The chamber is made of brass with a Melinex entrance window and is operated with a potential difference of -600V (sufficient to achieve saturation) between the chamber and the central electrode. Currents from the chamber and the ionization detector in use are separately integrated by the circuit shown in Fig. 22. The chamber charges a 0.5μF capacitor C2, the voltage developed being backed off from a standard 10V source using a 10kΩ decade dividing box. The electrometer is then used as a null detector. This system allows measurement to better than 0.1%. Similarly by operating the switches S1 and S5, the voltage developed by the detector on capacitor C1 can be measured. A value of C1 is selected to give voltages which can be measured accurately. The switch S4 is ganged so that both monitor and device can be connected to their collection capacitors at the same moment, ensuring equal integrating times. The voltage developed across C2 is a measure of the total X-ray output, and when divided by the integration time will be referred to as the "monitor unit" (m.u.).

3.6 Balancing the Filters

3.6.1 Use of Continuous Distributions

To balance at a higher energy than the pass band, a beam with no energy in the pass band was produced by adding 0.01cm tin filtration to a 20kV 25mA beam. The effect of this filtration on the distribution calculated in Chapter 2 is shown in Fig. 23. The solid state system was used for detection, charge being integrated on a 10μF capacitor. The intensity transmitted by the nickel filter was first measured, the mean

of several readings being taken. The copper filter was then placed in the beam in place of the nickel, and rotated through small angles about a vertical axis until the intensity transmitted agreed with that of the nickel to within the experimental error.

To estimate the lack of balance at low energies, intensity measurements were repeated for each filter using a beam produced at 8kV 30mA, i.e. with all its energy below the pass band energy. Results are shown in Table 18.

Table 18

Transmission of balanced filters using continuous distributions.

Beam	Transmitted Intensity (volts/m.u.)	
	Nickel filter	Copper filter
20kV 25mA + 0.01cm tin	2.119 ± .002	2.121 ± .003
8kV 30mA	1.899 ± .002	1.938 ± .005

To see whether this could be improved, a sheet of 6.3×10^{-4} cm Melinex was added to the copper filter to reduce its transmission at low energies, and the measurements were repeated. Results are shown in Table 19.

Table 19

Transmission of modified balanced filters using continuous distributions

Beam	Transmitted Intensity (volts/m.u.)	
	Nickel filter	Copper + Melinex filter
20kV 25mA + 0.01cm tin	2.120 ± .003	2.122 ± .005
8kV 30mA	1.895 ± .002	1.892 ± .007

Figure 24

Schematic diagram of fluorescent X-ray source

(designed by Randle, 1966,
Department of Medical Physics, Univ. of Edinburgh)

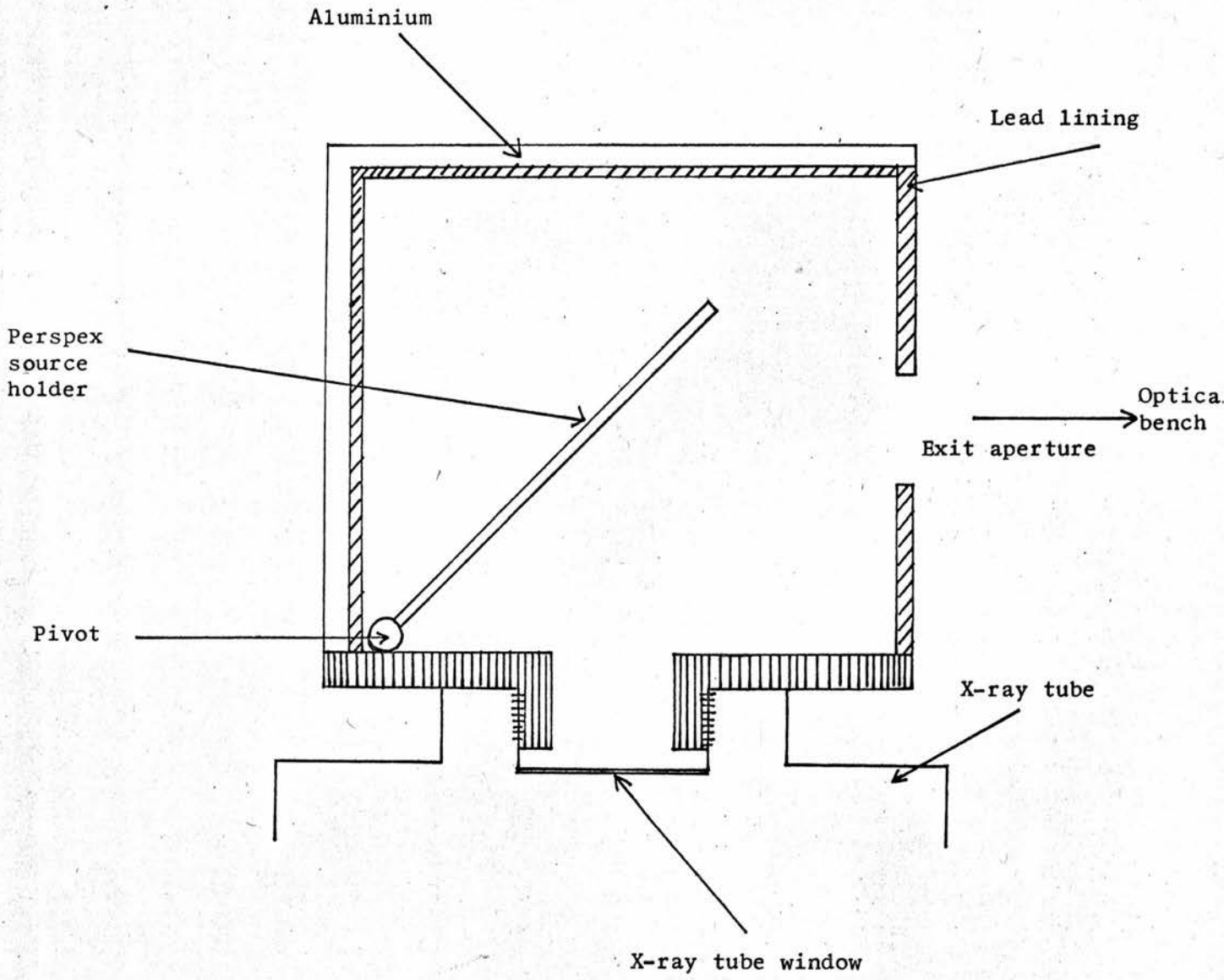

So that the balance is improved by the addition of this third filter.

3.6.2 Use of Characteristic radiation

The balancing of filters by the use of continuous distributions may be criticised, since it is possible that a lack of balance may occur at specific energies with one filter and yet be cancelled out by a similar imbalance at different energies with the other filter. If monoenergetic radiation is used for balancing, this effect could not occur. A suitable source of this radiation is provided by the characteristic K-radiation produced when a pure element is irradiated with X-rays. By suitable design of apparatus and choice of the incident spectrum, the amount of scattered continuum radiation may be very small. The fluorescent radiation is not of course purely monoenergetic since it consists of K_α and K_β lines (and possibly L lines) but for low atomic number elements the K line separation is small, and the radiation can be considered monoenergetic for many purposes, although we will see later (3.8.2) that corrections must be applied for the K_β lines in certain cases. It is sometimes possible to preferentially filter out the K_β radiation by inserting a thin filter of material with a K absorption edge lying between the α and β lines, but this method also attenuates the K_α radiation.

A box to hold fluorescent sources has been designed by Randle (1966). Fig. 24 shows the construction. The box is lead-lined to eliminate transmission and reduce scattered radiation. The fluorescent sources are mounted on thin glass slides and placed in a Perspex holder, the angle of which to the primary beam can be varied to produce maximum intensity. Sources are mostly in the form of sheets of pure elements although other forms have been used and are described in Chapter 6. The

thickness of the sheet is sufficient to absorb 50keV photons. Preliminary experiments have shown that maximum intensities of characteristic radiation are produced when the angle of the fluorescent source to the incident beam is $\simeq 35^{o}$. The characteristic beam escapes through a $\frac{1}{2}$" aperture which also serves to reduce the solid angle for the escape of lead fluorescent radiation from the box lining; no such radiation is observed.

Because of the low intensity of the characteristic radiation, the argon-filled ionization chamber was used as a detector, and collected charge was integrated on a 1μF condenser. The radiation of several elements was used to check the balance obtained in 3.6.1. Results are shown in Table 20.

Table 20

Fractional transmission of modified balanced filters, using characteristic radiation

Element	K-radiation energy (keV)		Fractional transmission I/I_o	
	α	β	Nickel filter	Copper filter
Cadmium	23.2	26.1	0.825 ± .003	0.831 ± .004
Zirconium	15.8	17.7	0.598 ± .004	0.605 ± .004
Iron	6.4	7.1	0.432 ± .002	0.424 ± .003

In spite of the very low intensities being measured here, the filters balance within experimental error. The slight disagreement for iron may possibly be due to the source not being of high purity in this case.

3.7 Measurements of Pass-band and Total beam Intensity

With the filters balanced, measurements were taken of the intensity

transmitted by each filter and the total intensity of beams produced at 10 - 30kV. The solid state detector was used for the 10 and 15kV measurements and the calorimeter for the higher energies. For all measurements the total filtration was 12cm Air + .0038cm Melinex. Results have not been converted to absolute units since only the proportion of characteristic radiation in the total beam is required. Table 21 shows the raw results and also indicates the pass-band intensity, i.e. the difference in the intensities transmitted by the filters. Uncertainties quoted are the standard deviations on the mean of the several readings taken for each configuration.

Table 21

Pass-band and Total Beam Intensities - Raw Results

Beam Type	Intensity transmitted Cu filter	Intensity transmitted Ni filter	Pass-band Intensity	Total beam Intensity
10kV 30mA	3.133 ± .004	2.617 ± .007	0.516 ± .008	6.653 ± .003
15kV 30mA	5.299 ± .007	3.824 ± .004	1.475 ± .008	12.57 ± .01
20kV 25mA	3.316 ± .023	2.473 ± .010	0.843 ± .025	7.28 ± .02
25kV 25mA	4.365 ± .014	3.434 ± .008	0.931 ± .016	8.64 ± .05
30kV 25mA	5.466 ± .012	4.515 ± .013	0.971 ± .018	10.08 ± .04

Units:- V/m.u. for 10, 15kV: ergs x 10^{-4}/m.u. otherwise

These figures must be corrected for energy losses due to scatter and transmission by the detector. This subject is treated in Appendix I, where graphs of the percentage intensity loss versus energy are shown. Corrections to the pass-band intensity are easily made since it may be regarded as monoenergetic at 8.6keV. Corrections to the total intensity have been made using the results which will be described in Chapter 4. By analysis of the attenuation curves, each beam can be considered as

Table 22

Initial and Scatter-Corrected Intensity, for Pass-band and Total Beam

Beam Type	Pass-band Intensity	% Energy lost	Corrected Pass-band Intensity	Total Intensity	% Energy lost	Corrected Total Intensity
10kV 30mA	0.516	1.80	0.526	6.65	3.00	6.85
15kV 30mA	1.475	1.80	1.500	12.57	1.80	12.80
20kV 25mA	0.843	0.41	0.850	7.28	0.69	7.33
25kV 25mA	0.931	0.41	0.940	8.64	1.44	8.77
30kV 25mA	0.971	0.41	0.980	10.08	1.27	10.21

(Units as in Table 21)

Figure 25

Illustrating filter attenuation

(After Tothill, 1964)

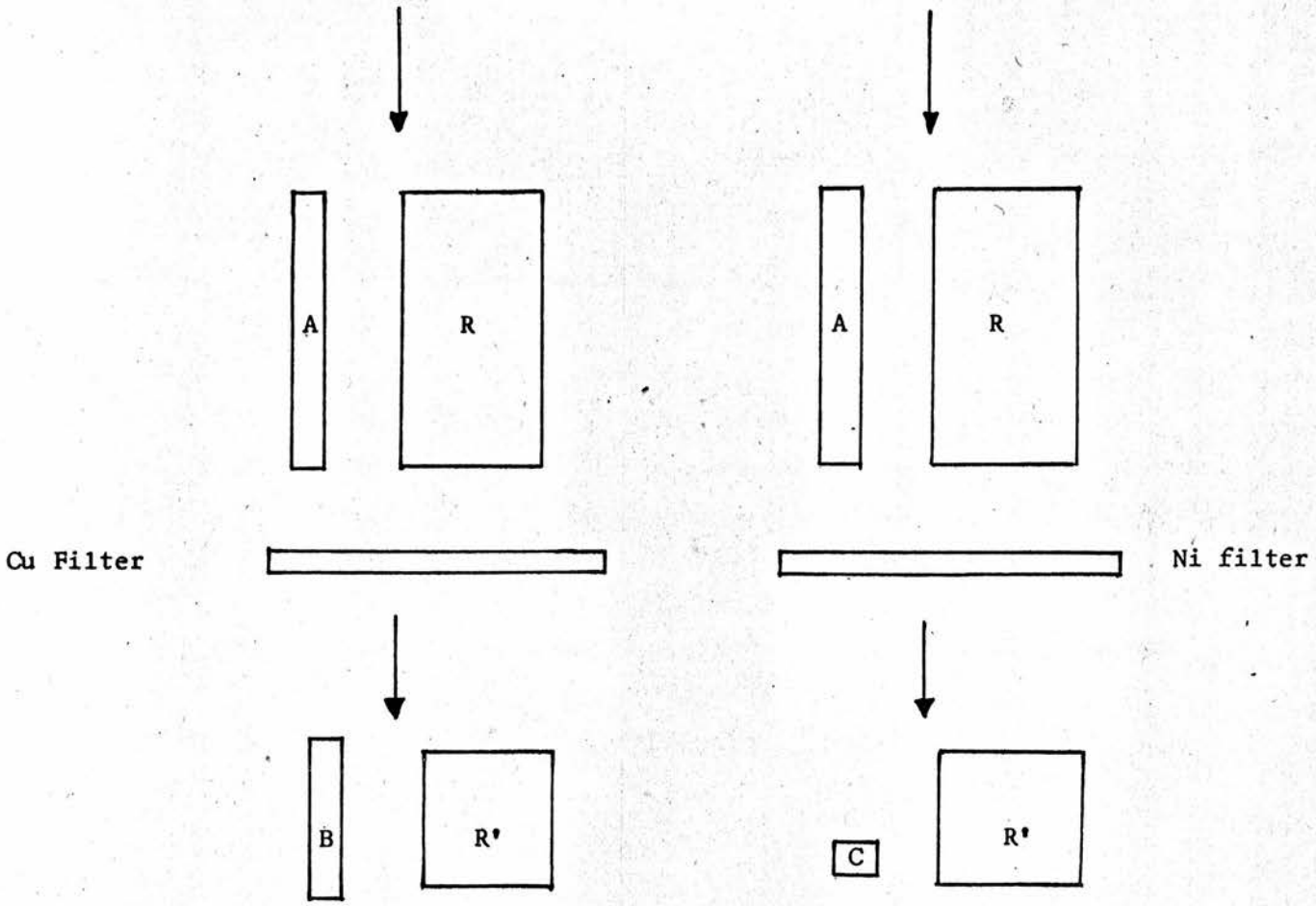

being composed of three monoenergetic components and hence the corrections can be calculated. Initial and corrected results for total intensity and pass-band intensity are shown in Table 22.

The correction factors rely on a large number of approximations and are probably only accurate to 20%, but since the corrections are small, values of corrected intensity have an uncertainty of $\pm$ 2%

3.8 Corrections for Filter Attenuation

3.8.1 Theory

Further corrections are now necessary for the attenuation due to the Ross filters themselves. Following the analysis of Tothill (1964) we can consider the situation as illustrated in Fig. 25. The intensity of the beam incident on the filters may be thought of as an intensity proportional to area A representing the incident pass-band intensity plus the intensity due to the rest of the beam lying outside the pass-band, i.e. the "remainder" (R). After transmission through the filters the pass-band intensities become B and C, and the remainder is attenuated equally in each filter to become R'. Measurements taken are:-

1) Total Initial Intensity $A + R$

2) Cu filtered Intensity $B + R'$)
) i.e. 2) - 3) = B - C
3) Ni filtered Intensity $C + R'$)

and we wish to find A

Now if the attenuation coefficients of the copper, Melinex, and nickel filters for the pass-band energy are μ_c, μ_m and μ_n, then

$$A \exp -(\mu_c t_c + \mu_m t_m) = B$$

$$A \exp -(\mu_n t_n) = C$$

$$\text{Therefore } A = \frac{B - C}{\exp -(\mu_c t_c + \mu_m t_m) - \exp -(\mu_n t_n)} \qquad \ldots\ldots 3.4$$

where t_c, t_m and t_n are the thickness of each filter. Values of B - C, the pass-band intensity, have already been tabulated.

Because of the fairly large uncertainties in measuring the filter thicknesses by weighing techniques it was decided to try to evaluate the denominator of the above expression experimentally.

3.8.2 Experimental Measurements of Filter Transmission

Ideally one would like to measure experimentally the transmission of an 8.6keV X-ray beam through each filter. The apparatus described in 3.6.2 provides a suitable source, but corrections will be required for any radiation lying outside the pass-band. Unfortunately tungsten L-radiation cannot be produced with sufficient intensity for accurate transmission measurements owing to the low fluorescent yield, but the K-radiation of zinc (K_α at 8.6keV, K_β at 9.6keV) provides a good substitute. However some consideration of the production process for characteristic radiation will show that there are considerable difficulties in the interpretation of transmission measurements of zinc radiation.

To obtain a high intensity of characteristic radiation, a 30kV 25mA beam must be used for excitation, and we must consider the intensity of this incident beam that is scattered from the zinc and reaches the detector. Most of the scattering is by the coherent process, and we will ignore the small energy loss entailed in Compton scattering. The geometry is identical for both scattered and zinc characteristic radiation to reach the detector, hence the intensities I_s and I_c of scattered and characteristic radiation produced by a monoenergetic beam of energy E and intensity I are

given by:-

$$I_s(E) \propto I(E) \times \sigma(E)/\rho$$

$$I_c(E_K) \propto I(E) \times \omega\, \tau(E)/\rho$$

where σ/ρ and τ/ρ are the total scattering and photoelectric components of the mass attenuation coefficient of zinc, and ω is the zinc fluorescent yield. The spectral distribution derived in Chapter 2 provides an estimate of I(E) and values of σ/ρ and τ/ρ are given by McMaster et al. (1967). Values of ω are tabulated by Blokhin (1961). Thus the total scattered continuum intensity is given by:-

$$I_s(\text{total}) \propto \int_0^{E_o} I(E) \quad \sigma(E)/\rho \; dE \quad \ldots\ldots\ldots \; 3.5$$

where E_o is the maximum energy in the beam and the total zinc characteristic radiation is given by:-

$$I_c(\text{total}) \propto \omega \int_{E_K}^{E_o} I(E) \; \tau(E)/\rho \; dE \quad \ldots\ldots\ldots \; 3.6$$

Since the geometry is the same, and assuming equal absorption in the zinc and an isotropic distribution for scattered and characteristic radiation, the constant of proportionality is the same for equations 3.5 and 3.6. The integrations can be made using a planimeter.

The intensity of the scattered radiation transmitted by the filter is approximately given by:-

$$I_s' \quad \propto \int_0^{E_o} I(E) \; \frac{\sigma(E)}{\rho} \quad \exp -(\mu(E)t) \; dE$$

where $\mu(E)$ is the linear attenuation coefficient of the filter and t is its thickness as calculated in 3.4.2.

The zinc characteristic intensity can be split into the α and β components (using the relative intensities as given by Blokhin), and to these we must add the scattered tungsten L intensity. The transmission of these components through the filter is easily calculated.

Thus this simplified analysis yields an estimate of the fractional transmission through each filter which would be measured using a zinc radiation source. This is

Nickel filter transmission	$\simeq$	10%
Copper filter transmission	$\simeq$	60%

The nickel filter result is very sensitive to variations in the scattered intensity. These results are in reasonable agreement with experimental measurements which yielded transmissions of 14% and 63%. However, the transmissions of a pure 8.6keV beam would be $\simeq$4% and $\simeq$69%. Hence it is apparent that the use of zinc radiation to derive the filter transmissions involves large corrections for radiation outside the pass-band, especially for the nickel filter, and so the method is inherently inaccurate.

The most uncertain correction is that due to the scattered radiation, and the effect of this can be minimised if a higher energy characteristic beam is used to deduce the filter thicknesses from fractional transmission measurements. The Zirconium results of 3.6.2 can be used here. Advantages of working at higher energy are:-

1. Larger fluorescent yield (0.71 for zirconium, 0.45 for zinc).
2. More accurate values of attenuation coefficients of nickel and copper are available away from the K edges.
3. Less attenuation of characteristic radiation in the filters.

If the effect of the scattered radiation can be allowed for, the zirconium α and β radiation can be treated as follows:

Denote the relative intensities of the α and β radiation by f_α and f_β, and denote the attenuation coefficients of the filter to α and β radiation by μ_α and μ_β. Then the transmitted intensity I through a filter of thickness t is given by:-

$$I = f_\alpha I_o \exp(-\mu_\alpha t) + f_\beta I_o \exp(-\mu_\beta t) \quad \ldots\ldots\ldots 3.7$$

For copper, $f_\alpha = 0.88$

$f_\beta = 0.12$ (Blokhin, 1961)

$\mu_\alpha/\rho = 64 \text{ cm}^2/\text{g}$

$\mu_\beta/\rho = 47 \text{ cm}^2/\text{g}$ (McMaster et al. 1967)

I/I_o is the fractional transmission of a pure K_α and K_β beam. The mean result of 3.6.2 gives $I/I_o = 0.602 \pm .006$. However this contains some scattered radiation. An analysis similar to that described for zinc indicates that a correction of + 3% must be applied. This correction is derived from the theoretical spectrum, but this will be shown to be a valid representation, and the correction is probably correct to $\pm$ 20%.

Hence $I/I_o = 0.620 \pm .007$

Equation 3.7 can now be solved by substitution; this yields, for the copper filter

$$\rho t = 7.75 \text{ mg/cm}^2 \pm 2\%$$

and hence the mass cross-section of the nickel filter is

$$\rho t = 8.85 \text{ mg/cm}^2 \pm 2\%$$

At 8.6keV, the attenuation coefficients are:-

Copper: $\mu/\rho = 43 \pm 1 \text{ cm}^2/\text{g}$

Nickel: $\mu/\rho = 325 \pm 10 \text{ cm}^2/\text{g}$

Hence the fractional filter transmissions are:-

Copper: 0.717 ± 0.010

Nickel: 0.057 ± 0.004

Throughout this calculation the attenuation of the Melinex is less than 0.05% and so has been neglected.

3.9 Total pass-band intensity, continuum corrections, and L_α intensity

Values of A, the true pass-band intensity in equation 3.4 can now be calculated. Results expressed as percentages of the total intensity are shown in Table 23.

Table 23

True pass-band intensity as a percentage of total intensity

Beam	Pass-band Intensity (% of total intensity)
30kV 25mA	$14.5 \pm 5\%$
25kV 25mA	$16.2 \pm 5\%$
20kV 25mA	$17.5 \pm 5\%$
15kV 30mA	$17.7 \pm 5\%$
10kV 30mA	$11.7 \pm 5\%$

The peak pass-band intensity at 15-20kV may be indicative of the continuum peak lying near the pass-band at these energies. This pass-band intensity contains the tungsten L_α radiation and part of the continuum. In order to estimate the contribution of the continuum we will consider the theoretical spectra derived in Chapter 2. Details of these spectra attenuated by the required air and Melinex filtration are shown in Table 16. By plotting the spectra the intensity in the pass-band due to the continuum can be found by planimeter measurements. This intensity, expressed as a percentage of the total

Table 25

Comparison of measured L_α intensity with theoretical predictions

Production Potential (kV)	L_α intensity (% total intensity)	
	Experiment	Theory
30	12.3	16.2
25	13.3	19.2
20	13.6	19.4
15	11.8	18.2

theoretical intensity is then subtracted from the measured pass-band intensity. The remainder is the intensity due to $L\alpha$ radiation in the pass-band. These results are shown in Table 24.

Table 24

Percentage of total beam intensity due to $L\alpha$ radiation in the pass-band

Production Potential (kV)	Intensity in pass band (% total intensity)		
	Total (experiment)	Continuum (theory)	$L\alpha$
30	14.5	2.8	11.7
25	16.2	3.5	12.7
20	17.5	4.6	12.9
15	17.7	6.6	11.1
10	11.7	10.5	1.2

The 10kV result may be regarded as $\simeq 0$ in view of the large uncertainties, and this is as expected since the tungsten L_I edge occurs at 10.2keV.

The correction can now be made for the loss of part of the $L\alpha_2$ line intensity due to finite line width (See 3.3). This correction has been taken as 5%. The resultant, the percentage of the total beam intensity which is due to $L\alpha$ radiation can now be compared with the predictions of the theoretical distributions of Chapter 2, Table 16. The comparison is shown in Table 25.

Experimental values all lie below the theoretical figures, although the variation of intensity with production potential is as predicted. Uncertainties in the experimental measurements may amount to 10%. Consideration of the theoretical calculations (Chapter 2, section 4) reveals two possible sources of error. The value of c in

equation 2.4 is uncertain at low electron energies, and in fact, the validity of the Thomson Whiddington form of the energy loss equation is also uncertain at low energies (Green and Cosslett, 1961). Secondly, Spielberg's expression, equation 2.5, is an approximation, and the two experimental results with which he substantiates it (Spielberg, 1959) both suggest that the factor 8/3 may be an overestimate and that a factor 2.0 may be more accurate. This would bring the theoretical calculations within the experimental error.

3.10 Total Characteristic Intensity

The percentage of the total intensity which is due to L_β and the "characteristic continuum" radiation can now be estimated by assuming that the relative proportions are as shown in Table 16. Hence the percentage of the total intensity which is due to true characteristic and to true plus "pseudo"-characteristic radiation can be tabulated. This is shown in Table 26.

Table 26

Percentage of total intensity due to characteristic radiation

Production Potential (kV)	L_α	L_β	"Characteristic" Continuum	Total (L_α + L_β)	Total (L_α + L_β + "Characteristic")
30	12.3	10.0	6.9	22.3	29.2
25	13.3	10.0	6.8	23.0	30.1
20	13.6	10.2	8.2	23.8	32.0
15	11.8	8.8	-	20.6	20.6

It must be pointed out that the division of the continuous distributions into smooth and characteristic parts is largely arbitrary, but the differences in the two "total" columns indicate that one might expect large differences in the measurement of the amount of L-radiation in X-ray beams by less sensitive methods, e.g. by curvature criteria in attenuation analysis.

3.11 Discussion

There is little published work with which to compare the results of 3.9 and 3.10. Hink (1965) has used the Ross filter method to measure tungsten L-radiation intensity, but used a transmission target tube. It has not been possible to find any published measurements of this type on on a tungsten target beryllium window tube, a fact which is somewhat surprising in view of the high proportion of characteristic radiation in beams from such tubes, and the insensitivity of other methods of measurement of this proportion (see 3.10).

Norman and Greenfield (1955) measured exposure-rate distributions of a beryllium window tube by attenuation analysis and were able to analyse their results without subtracting any characteristic radiation. They compare their derived exposure rate distribution with distribution calculated from Kramer's formula with added filtration for the beryllium window, the air path, and an extra .04mm aluminium to allow for target filtration (following the empirical result of Jennings, 1953). The agreement is not particularly good at any energies, but is poorest between 7 - 12keV where the experimental curve is considerably higher than that predicted by theory. This seems most likely to indicate the presence of characteristic radiation. If the beam does contain characteristic radiation (i.e. the

spectrum is not smooth) then attenuation analysis cannot yield the true spectral distribution, and this will account for the poor agreement between experiment and theory in Norman and Greenfield's work. This provides a good example of the need for measurements as presented in this chapter before attenuation analysis can be used for very low filtration X-ray beams. Wang et al. (1957) in their attenuation measurements of 50kV constant and pulsating potential spectra from a beryllium window tube estimated the amount of characteristic radiation present by Greening's modification (1947) of Jones' analysis (1940). This method is not considered very sensitive. Using a 50kV 35mA beam they found that 65% of the exposure rate was due to characteristic radiation, and operating the tube at pulsating potential with 8cm air plus 0.0127mm aluminium filtration, 40% of the intensity was due to characteristic radiation. The exposure rate figure cannot easily be converted to intensity with the information given, but one might expect more characteristic radiation from constant potential production than from pulsating potential since the tube voltage is above the L edges permanently. The 40% figure was obtained from measurements with a scintillation counter. This form of detector will be shown to be insensitive to low energies (in Chapter 4), hence this figure is possibly rather low.

Burke and Pettit (1958) have published spectra obtained by absorption analysis of X-ray beams from beryllium window tubes operated at potentials of 20-50kVp. They argue that the form of the continuous distribution should not depend on the target material, and deduce from the spectra of chromium and molybdenum target tubes the proportion of

characteristic radiation in a tungsten target spectrum. The results which we have reached in Chapter 2 must cast doubt on their initial premise, but even so, a large number of intermediate steps are required and therefore the method lacks sensitivity. They have measured exposure rate distributions but have converted them to intensity distributions at the target surface. They also quote the exposure rate at the detector due to characteristic radiation. This can be converted to intensity using

$$I = \frac{\dot{X} \times 86.9}{\left(\frac{\tau + \sigma_a}{\rho}\right)_{Air}} \quad ergs/cm^2\text{-}s$$

where I is the intensity, $\dot{X}$ is the exposure rate in roentgen/s, and $(\tau + \sigma_a)/\rho_{Air}$ is the true absorption coefficient of air for L-radiation. The characteristic intensity can then be corrected for filtration and expressed as a percentage of the total intensity at the target. This yields figures of 21% for a 30:kVp beam and 16% for a 20kVp beam, whereas our figures when corrected for filtration indicate that the corresponding values should be 36% and 31%. Burke and Pettit's results were obtained with the tube operating from a full wave rectified generator, and it seems likely that a constant potential situation would produce a higher percentage of characteristic radiation.

The measurements described in this chapter define the contribution of characteristic radiation in the specification of the spectral distribution. They indicate the high proportion of characteristic radiation in X-ray beams from tungsten target beryllium window tubes when operated at constant potential under low filtration conditions. It is essential that this is taken into account in

calculations of mean energies and half-value layers, and results presented here will also be useful if similar tubes are to be used for fluorescence analysis studies.

CHAPTER 4

ATTENUATION ANALYSIS

4.1 Introduction

The theory underlying attenuation analysis has been discussed in Chapter 1. Accurate measurements are required of the transmission of various X-ray beams through different thicknesses of a suitable absorbing material. These measurements must be taken under conditions of good geometry, and the detector used should have a response which is not energy dependent. The greatest amount of information is contained in the high transmission measurements, but to specify the beam accurately, results should be taken to less than 10% transmission. The detectors described in Chapter 3 all have energy-independent responses and so will be very useful for transmission measurements, although they may not be sufficiently sensitive for accurate measurements when the X-ray beam transmission is low. Most previous attenuation analysis studies of the spectra of beryllium window tubes have used ionization chambers as detectors of the transmitted beam (Emigh and Megill, 1953; Norman and Greenfield, 1955; Wang et al., 1956; Burke and Pettit, 1958). However, although ionization chambers permit measurements to very low transmission values, the calculation of intensity distributions is rather indirect, and a totally absorbing detector is preferable. Wang also obtained attenuation curves using a scintillation counter which totally absorbed the beam. His method was extremely indirect, involving obtaining pulse height distributions, converting to intensity distributions and integrating under the graph to derive the total intensity in the beam. A far more

straightforward method would be to use the counter in the current mode. Provided the response is energy independent the signal current would be proportional to the X-ray intensity incident on the crystal. The sensitivity of scintillation counters suggests that their use in the current mode may be more suitable than calorimetry for the measurement of attenuation curves. However, Wang did not ensure that the detector response was energy independent. We will be able to use the calorimeter (or previously calibrated secondary detectors) to investigate this response. The first requirement however is the choice of a suitable absorbing material.

4.2 Choice of Absorption Material

The primary requirement in the choice of absorber is that the material must have no absorption edge in the energy region of interest. In our case this limits the choice to a low atomic number material. Further, accurate attenuation data must be available for the material used. The part of the attenuation curve containing the most information is that part where the transmission is high. Consequently absorber thickness must be accurately known if this part is to be well defined. The material must also be available in high purity form and preferably cheaply. Aluminium satisfies all these criteria and has been used for all measurements described here. Burke and Pettit (1958) have conveniently tabulated absorption data.

An alternative absorption system could be provided by a gas-filled chamber with Melinex windows, where the mass cross-section could be continuously variable by varying the pressure. However for small transmission values a suitable gas (e.g. argon or neon) would have to be

at high, and accurately measured, pressure. For example, for 98% absorption of 15keV X-rays an argon filled chamber 60cm long would require operation at a pressure of ≃3 atmospheres. Furthermore, the length of the chamber would reduce the beam intensity by the inverse square law and hence the sensitivity required of detectors would be increased. Therefore solid absorbers were preferred. Initial measurements were made using high purity foils of thicknesses 0.0010" and 0.0053" (measured by weighing). To produce larger absorber thicknesses the foils were sandwiched together. However the 0.001" foil absorbs about 25% of a 15kV beam so that the low absorption region of the attenuation curve is ill-defined. In addition the foils are easily damaged. A set of commercially available absorbers[1] is more convenient to use and provides a wider range of thicknesses which are believed accurate to better than $\pm$ 5%. The attenuation curves of a 15kV beam measured with these absorbers and with the pure foils are in excellent agreement hence the commercial system was used for all further measurements.

4.3 Detection System

The purpose of the experiment is to provide accurate measurements of I_x/I_o, the ratio of the intensity transmitted through an absorber of thickness x to the total unattenuated intensity, hence a total absorption form of detection is most useful. It has been suggested in 4.1 that a scintillation detector operated in the current mode might provide a highly sensitive system capable of measuring very low transmission values. Since such a technique does not seem to have been considered by any previous

---

1. Marketed by Panax Equipment Ltd.

Figure 26

Photomultiplier operated in current mode

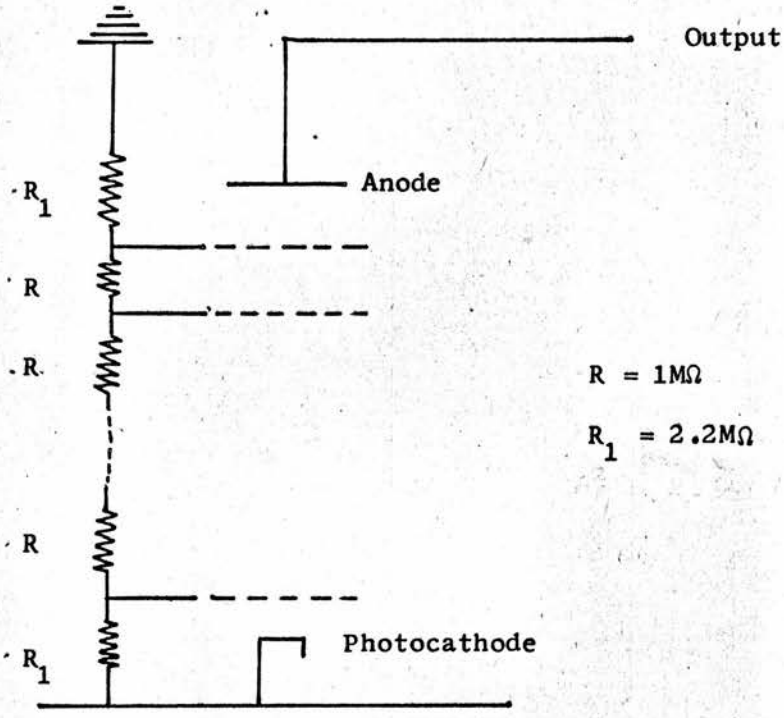

workers we must first investigate the energy dependence of a scintillation detector by comparison with the calorimeter and other secondary dosimeters.

4.4 Experimental Situation

4.4.1 Scintillation Detector in the Current Mode

The scintillation detector used is an integral assembly made by Nuclear Enterprises consisting of a 1" x 0.080" sodium iodide crystal mounted on a 1", 11 stage E.M.I. photomultiplier tube. The entrance window is beryllium, 0.008" thick. The dynode chain is set up as in Fig. 26, with the cathode operated at a negative high voltage of 600V. Curent output from the anode is integrated on the capacitor system shown in Fig. 22. Dark current of $\sim 6 \times 10^{-9}$ Amp is backed off from a high impedance current source. To keep the dark current and gain constant it is necessary to keep the signal to less than 1% of the dynode chain current. The E.H.T. on the tube is also monitored potentiometrically to ensure gain stability. Signal current is integrated on a 0.01μF capacitor.

4.4.2 Absorption System

The beam defining system has been described in Chapter 3 (Figs. 20, 21). This gives an air path of 12cm and defines the accepted beam by an aperture of 0.16cm diameter placed in the primary beam before this aperture so that energy removed by scattering processes is not likely to reach the detector. Melinex filtration of 0.0038cm is the same for all detectors. The calorimeter, solid-state detector, and ion chamber are operated in the same way as in Chapter 3. The ion chamber contains argon at a pressure of 42.5 lb/in^2 and a plate potential of 3.5kV is used. The scintillation detector requires a very fine

Table 27

Uncorrected Data for Fractional Transmission of 15kV 30mA X-ray beam through Aluminium

Filter Thickness cm x 10^{-3}	Fractional Transmission, I_x/I_o, as measured by			
	Calorimeter	Solid State	Ion Chamber	Scintillation
0.96	0.899 ± 0.012	0.883 ± 0.002	0.8837 ± 0.0011	0.911 ± 0.002
1.89	0.791 ± 0.010	0.792 ± 0.002	0.7935 ± 0.0007	0.833 ± 0.001
4.63	0.646 ± 0.011	0.645 ± 0.001	0.6441 ± 0.0006	0.692 ± 0.004
10.1	0.381 ± 0.006	0.372 ± 0.001	0.3832 ± 0.0006	0.440 ± 0.001
19.5	0.191 ± 0.002	0.1803 ± 0.0007	0.1863 ± 0.0003	0.2280 ± 0.0004
29.3	0.109 ± 0.002	0.1092 ± 0.0005	0.1117 ± 0.0002	0.1420 ± 0.0003
44.8	-	0.0492 ± 0.0006	0.0492 ± 0.0001	0.0642 ± 0.0001

Figure 27

Three component analysis
of 15kV attenuation results

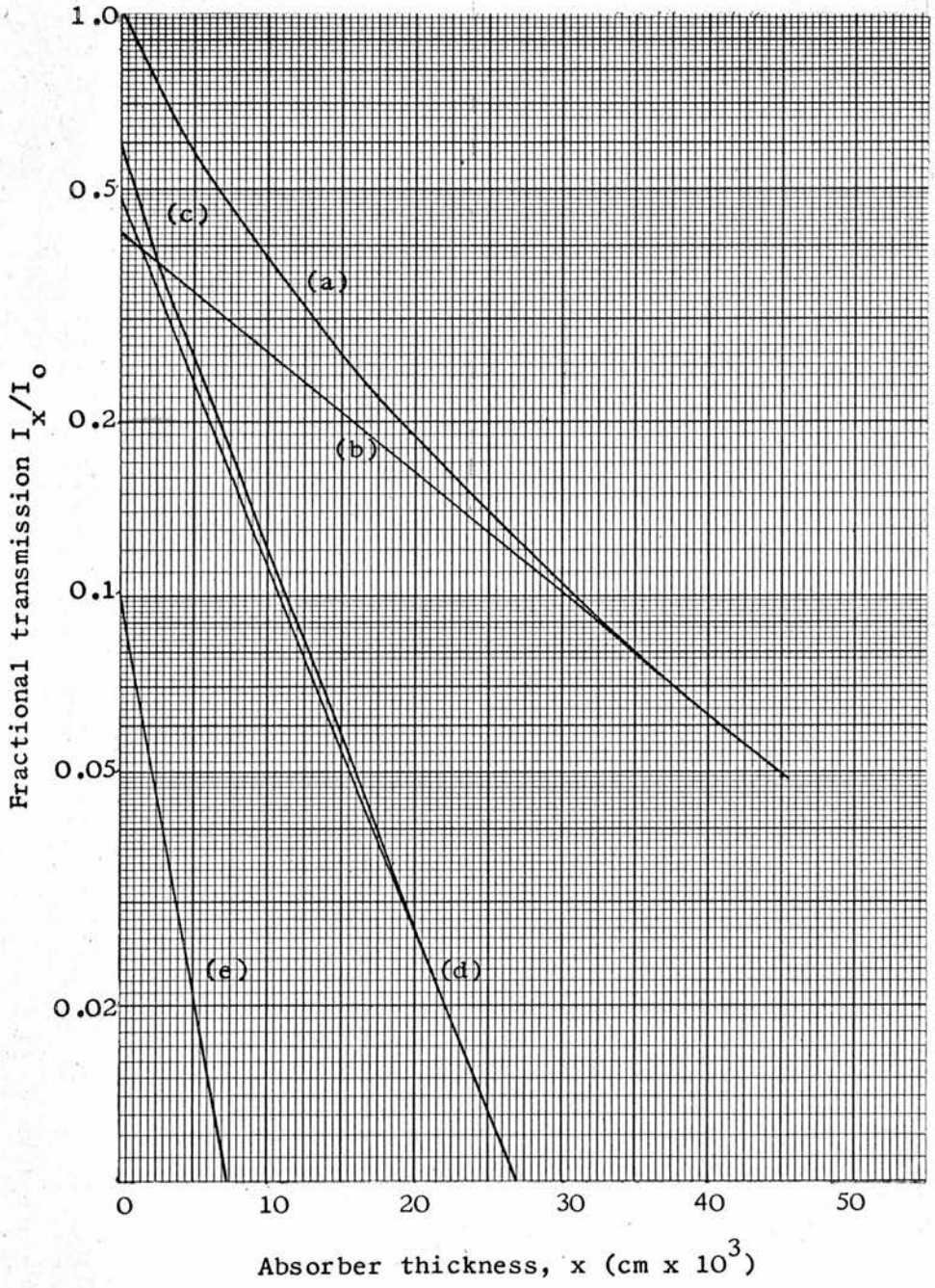

defining aperture of 0.010cm diameter (lead construction) to reduce the signal current and avoid fatigue effects. The monitor chamber described in Chapter 3 is used with all the detectors to remove scatter in the readings due to variations in the X-ray tube output.

4.4.3 Comparison of Detection Systems for a 15kV, 30mA X-ray beam.

For comparison of the detectors a 15kV 30mA beam was used since corrections are small for all systems for energies up to 15keV. Results are shown in Table 27. The uncertainties quoted are standard deviations on mean results.

It can be seen that the greatest precision of measurement is provided by the ion chamber, but before any conclusions about the relative responses can be drawn these results must be corrected for scatter and transmission losses from the detector. Graphs of the percentage of intensity lost from each detector by monoenergetic beams are shown in Appendix 1. To apply corrections for a heterogeneous X-ray beam requires a knowledge of the spectral distribution, the determination of which is the aim of the experiment. However since corrections to the attenuation curve obtained with the calorimeter are expected to be small, they can be derived with sufficient accuracy for the present application by analysing the curve graphically into three monoenergetic component beams. This graphical analysis has been described by Greening (1963). Fig. 27 illustrates the method. The smooth curve (a) has been drawn through the experimental results obtained with the calorimeter (the final point determined by the solid state detector has been included to aid definition of the curve at large absorber thicknesses). When the absorber thickness is large, the transmitted beam is approximately

monoenergetic, and its attenuation in aluminium can be represented by the straight line (b) which is fitted to curve (a) at large thicknesses. Differences between (a) and (b) are replotted to give curve (c) and, using a similar argument, the straight line (d) is fitted at large absorber thickness. Finally (a)-(b)-(c) is plotted and these results can be fitted by the straight line (d). Each straight line represents the attenuation of a monoenergetic X-ray beam in aluminium. The intercepts of (b), (c) and (d) on the ordinate axis give the fraction of the initial intensity contained in each component. The slopes of (b), (c) and (d) yield their linear attenuation coefficients in aluminium using $\mu = 0.693/\text{half-value-thickness}$. Hence the energy corresponding to each component can be found from tables of attenuation coefficients against energy (McMaster et al., 1967). Results are shown in Table 28.

Table 28

Analysis of 15kV data into three monoenergetic components

Component	Percentage of Initial Intensity	Energy (keV)
(b)	42.4	11.3
(c)	48.0	7.8
(d)	9.6	6.1

The percentage of intensity lost by each component beam by scatter and transmission can be read off from the graphs of Appendix 1. These intensity losses are shown in Table 29.

Table 30

Corrected Data for Fractional Transmission of 15kV 30mA X-ray beam through Aluminium

Filter Thickness cm x 10^{-3}	Fractional Transmission, I_x/I_o, as measured by			
	Calorimeter	Solid State	Ion Chamber	Scintillation
0.96	0.899 ± 0.012	0.883 ± 0.002	0.8837 ± 0.0011	0.910 ± 0.002
1.89	0.791 ± 0.010	0.791 ± 0.002	0.7936 ± 0.0007	0.831 ± 0.002
4.63	0.647 ± 0.011	0.644 ± 0.001	0.6443 ± 0.0006	0.689 ± 0.005
10.1	0.381 ± 0.006	0.371 ± 0.001	0.3835 ± 0.0007	0.436 ± 0.003
19.5	0.191 ± 0.002	0.180 ± 0.001	0.1866 ± 0.0004	0.225 ± 0.002
29.3	0.109 ± 0.002	0.109 ± 0.001	0.1119 ± 0.0003	0.140 ± 0.001
44.8	-	0.0489 ± 0.0006	0.0491 ± 0.0001	0.0630 ± 0.0004

Table 29

Percentage of Intensity lost by scatter and transmission from various detectors

Component	Energy (keV)	% Intensity Lost			
		Calorimeter	Silicon detector	Ionization chamber	Scintillation detector
(b)	11.3	0.74	1.2	1.5	2.1
(c)	7.8	0.36	2.0	1.1	4.5
(d)	6.1	0.24	3.4	1.4	9.1

The fraction of each component remaining, as absorber thickness is increased, can be read off from Fig. 27. Hence corrections can be calculated. For example, for the calorimeter, when the absorber thickness is 4.6×10^{-3} cm, the fractional intensity of each of the components (b), (c) and (d) can be read from Fig. 27. These fractions are 0.34, 0.255 and 0.025 respectively. Hence the correction required to the measured fractional transmission (curve (a)) at this thickness is:-

$$(0.34 \times 0.74 + 0.255 \times 0.36 + 0.025 \times 0.24) \times 10^{-2} = 0.0035$$

i.e. 0.5%

Corrected values of the transmission data are shown in Table 30. In the first three cases the corrections are less than experimental uncertainties, but for the scintillation system they are of comparable magnitude. These corrections rely on many approximations and have been taken as accurate to $\pm$ 20%. Estimated uncertainties for these corrected results are also shown in the table.

Most of the results for the first three detectors agree well. Cases where there was disagreement were rechecked, and it appears likely that these are due to slight non-uniformities in the absorber thickness.

Figure 28(i)

Attenuation of 30kV X-ray beam in aluminium

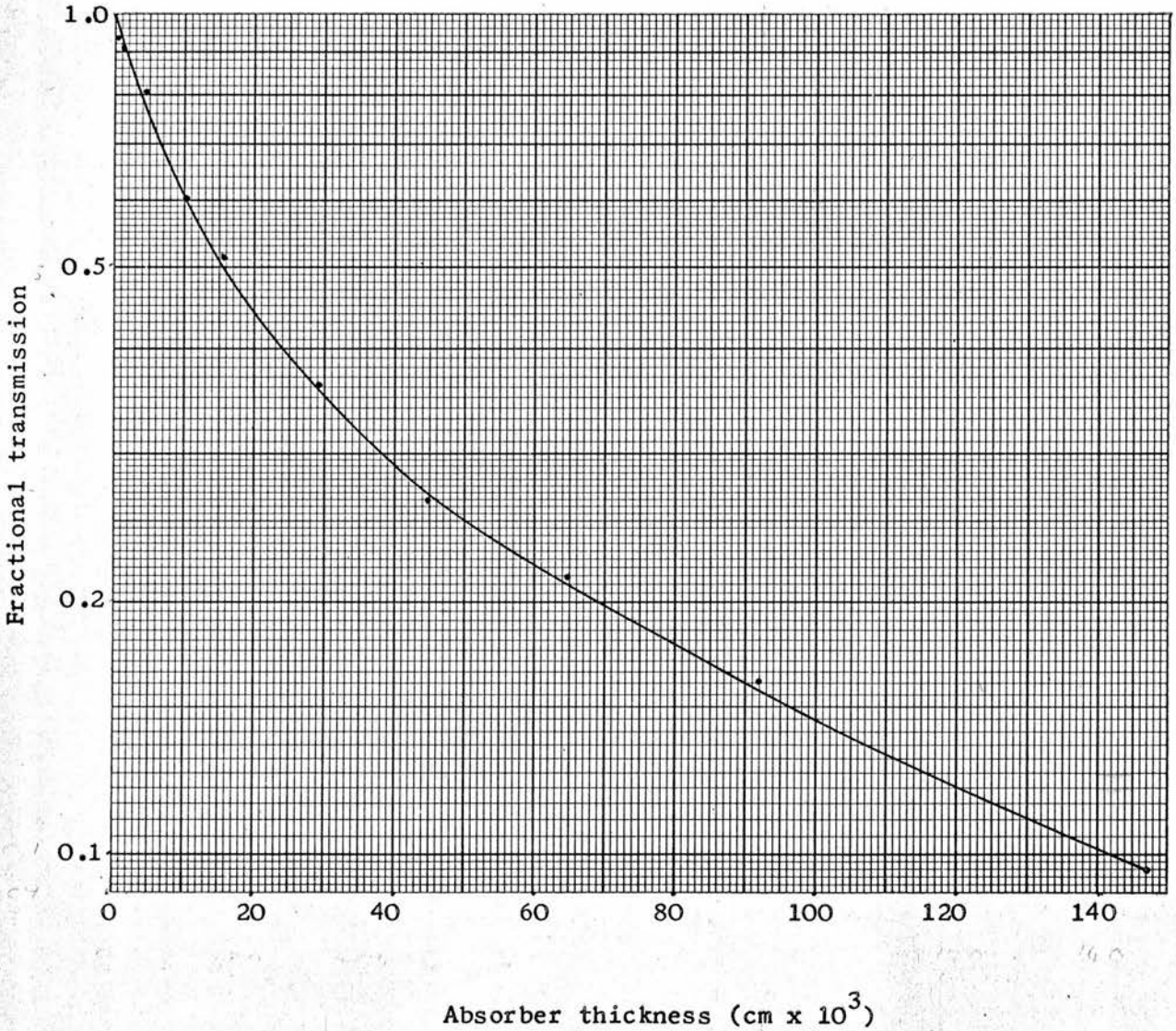

Figure 28(ii)

Attenuation of 25kV X-ray beam in aluminium

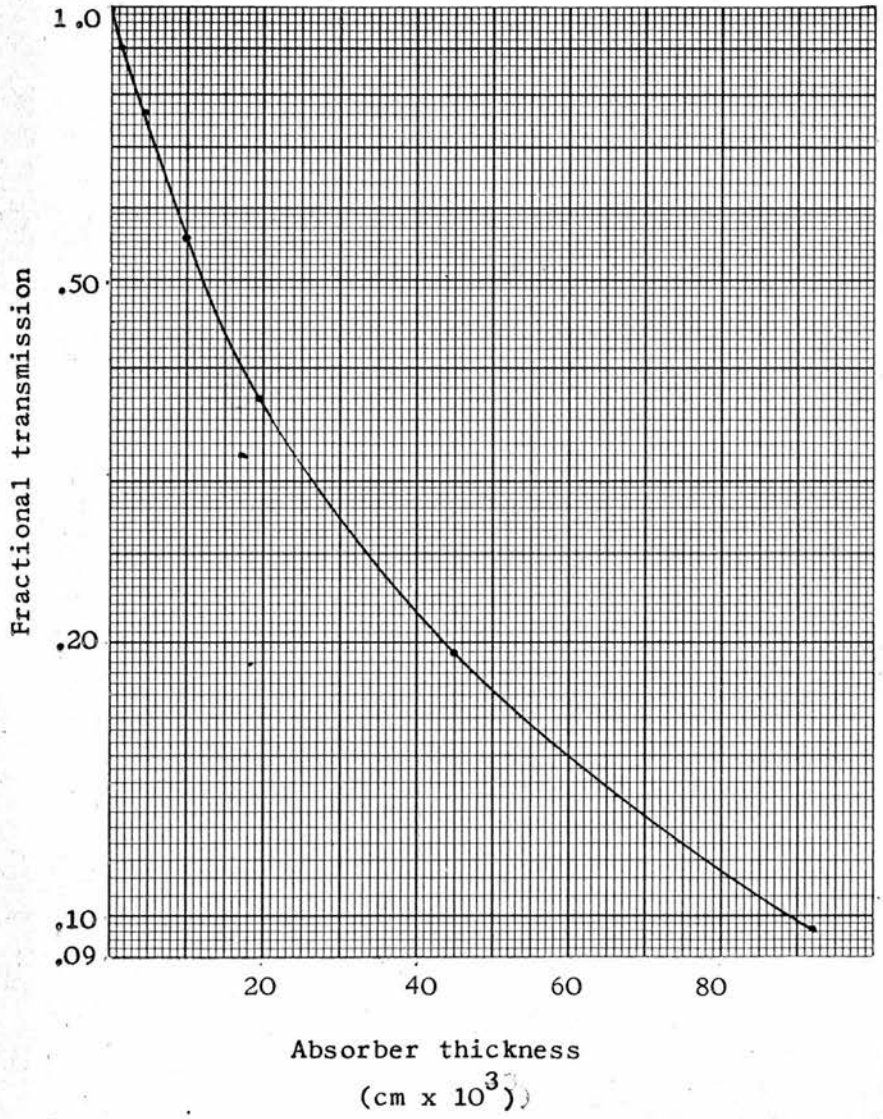

Figure 28(iii)

Attenuation of 20kV X-ray beam in aluminium

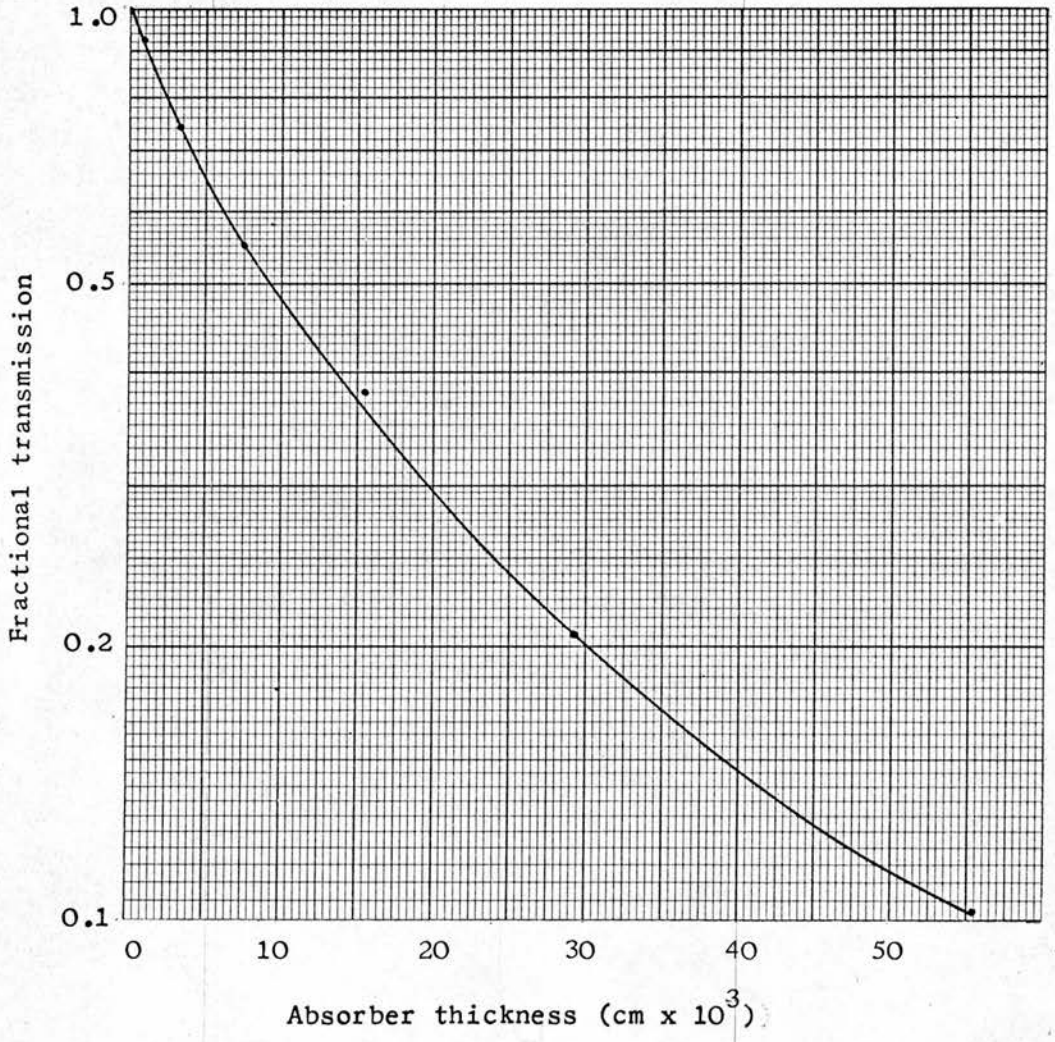

Figure 28(iv)

Attenuation of 15kV X-ray beam in aluminium

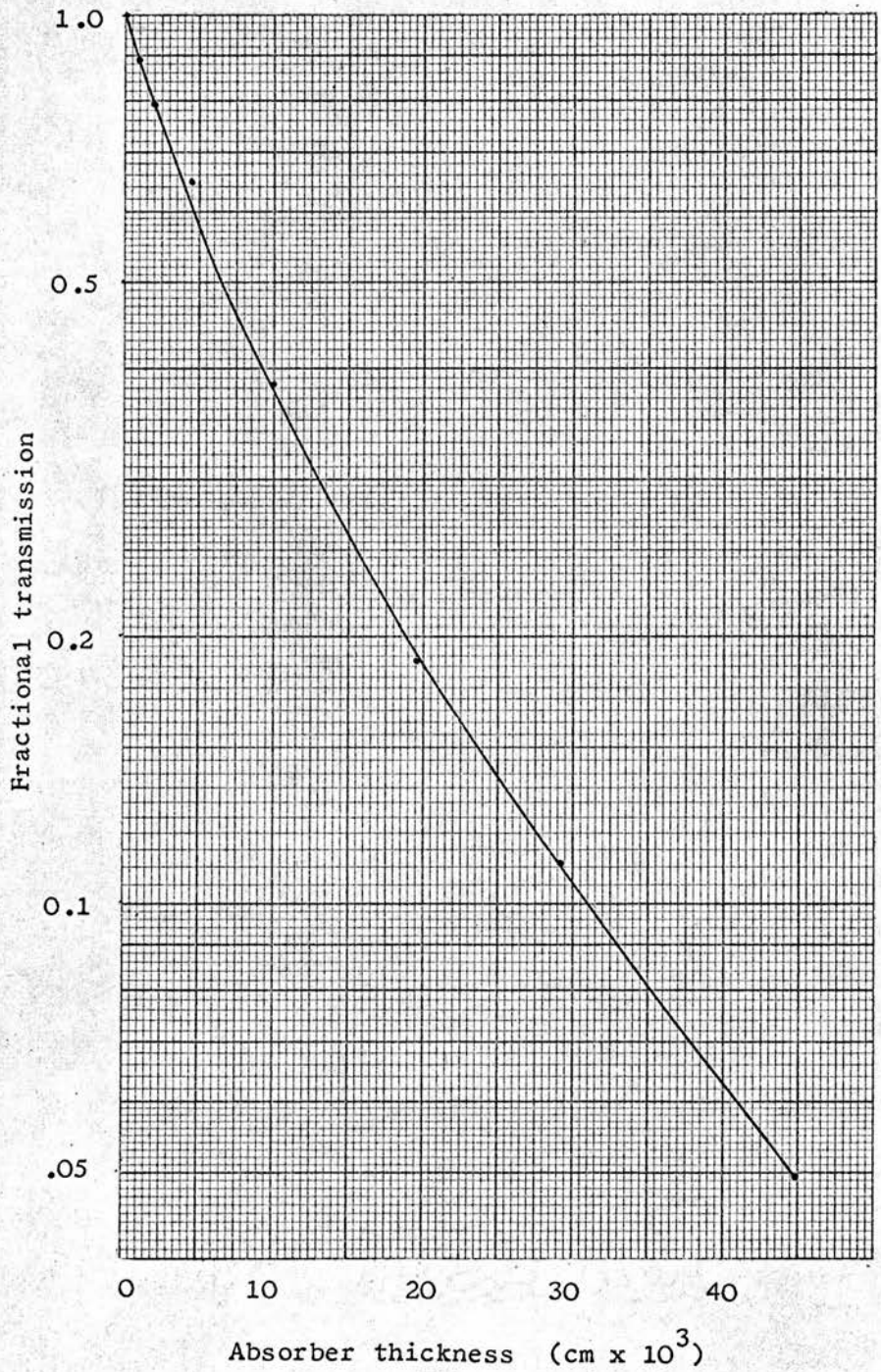

It is apparent that the scintillation detector does not give a valid response to this beam. However, if the ratio of the intensities at the two highest filtrations is considered, all four detectors are in agreement. Thus it appears that the scintillation detector is not responding to very low energy radiation and so is not suitable for the total absorption of beams from a beryllium window tube although it could be used for a tube with a larger inherent filtration. This non-linearity of response has been noted in pulse height analysis by Engelkemeir (1956). In view of the above some of the results of Wang et al., (1957) taken with low filtration and a scintillation detector must be regarded as suspect. To ensure that this effect was not peculiar to the 15kV spectrum the responses of the calorimeter and scintillation detector were also compared for a 30kV spectrum and the same pattern was found with the scintillation detector registering a higher fractional intensity than the calorimeter at high filtrations.

From this comparison of systems it appears that the ion chamber is most accurate for the 15kV results, but for higher energies the calorimeter requires the smallest correction.

4.5 Measurement of Attenuation Curves

Attenuation curves of several X-ray beams have been measured and corrected results are shown in Figs. 28(i - iv). The 15kV results were measured with the ion chamber; all others were measured with the calorimeter. Inherent filtration was 12cm air plus 0.0038cm Melinex. Corrections were made in the same way as before by analysing each curve into mono-energetic components. The results of this analysis are shown

in Table 31.

Table 31

Representation of X-ray beams
in terms of Mono-energetic Components

X-ray beam	% of total Intensity	Energy (keV)
30kV 25mA	38	20.0
	53	9.9
	9	6.1
25kV 25mA	33	17.6
	67	9.4
20kV 25mA	45	13.6
	38	8.4
	17	6.8
15kV 30mA	42	11.3
	48	7.8
	10	6.1

It is interesting to note that for each beam more than 50% of the initial intensity can be represented by components of less than 10keV energy.

This method of describing the X-ray beams can be very useful in situations where the precise spectral distribution is not necessary, since quality is specified more accurately than by simple measurements of half-value-layer and kilovoltage (Greening, 1963).

4.6 Analysis of Attenuation Curves

4.6.1 Introduction

Details of the theory of attenuation analysis have been given in Chapter 1. To apply the method it is necessary to find a function

Table 32

Functions for the analysis of attenuation curves

No.	f(x)	$\psi(\mu - \mu_o)$	Reference
(a)	$\exp(-Bx^{1/2})$	$\frac{B}{2\sqrt{\pi}} \frac{\exp\{-B^2/4(\mu - \mu_o)\}}{(\mu - \mu_o)^{3/2}}$	Bell, 1936.
(b)	$\exp[-B\{(x + d)^{1/2} - d^{1/2}\}]$	$\frac{B \exp B\sqrt{d}}{2\sqrt{\pi}} \frac{\exp\{-(\mu - \mu_o)d\}\exp -\{B^2/4(\mu - \mu_o)\}}{(\mu - \mu_o)^{3/2}}$	Jones, 1940.
(c)	$\frac{d^n}{(x + d)^n}$	$\frac{d^n}{\Gamma(n)} (\mu - \mu_o)^{n-1} \exp\{-(\mu - \mu_o)d\}$	Greening, 1950.
(d)	$\frac{\Gamma(n)}{(x/k + d)^n}$	$k^2 (\mu - \mu_o)^{n-1} \exp\{-k(\mu - \mu_o)d\}$	Norman and Greenfield, 1955.
(e)	$\frac{\sqrt{d} \exp[-B\{(x + d)^{1/2} - d^{1/2}\}]}{(x + d)^{1/2}}$	$\frac{\sqrt{d} \exp B\sqrt{d}}{\sqrt{\pi}} \frac{\exp\{-(\mu - \mu_o)d\}\exp\{-B^2/4(\mu - \mu_o)\}}{(\mu - \mu_o)^{1/2}}$	Greening, 1950
(f)[1]	$C K_o\{B(x + d)^{1/2}\}$	$\frac{C}{2} \frac{\exp\{-(\mu - \mu_o)d\} \exp\{-B^2/4(\mu - \mu_o)\}}{(\mu - \mu_o)}$	Greening, 1950

1. K_o is the modified Bessel function of the second kind.

f(x) such that f(x) exp($-\mu_o x$) fits the experimentally determined values of the fractional transmission I_x/I_o. (μ_o is the linear attenuation coefficient of the absorption material for photons of the maximum energy in the X-ray beam). Several suitable functions have been suggested, some being easier to apply than other. Macey (1948) has described a method of deducing a suitable function from consideration of the way in which simpler functions fail to fit the data. This method is discussed in 4.7.4. Greening (1950) has pointed out that combinations of more than one transform can be used, since Laplace transforms are additive. Functions f(x) which will be discussed in 4.7.2 are shown in Table 32 together with their Laplace transforms $\psi(\mu - \mu_o)$. Apart from the work of Wang (1957), which is criticised in 4.5, there have been no previously reported measurements of attenuation curves of beryllium window X-ray tube spectra by a totally absorbing form of detector. Hence there is no direct guidance available in the choice of a suitable Laplace transform. The method which will be adopted here is to consider first some simple functions which have previously been used for the analysis of exposure rate measurements of beryllium window X-ray tube spectra, and even if these are not applicable the method of Macey (1948) can then be used to suggest a more suitable function.

Function (b), which is a generalisation of (a) is the simplest expression to fit, since Jones (1940) has described a graphical method of determining the constants B and d. This will be used later in this section. In all the other expressions trial and error must be used to determine the constants.

4.6.2 Review of attenuation measurements of beams from beryllium window X-ray tubes

Emigh and Megill (1953) were apparently the first to use attenuation analysis to derive the spectra of beryllium window X-ray tubes. They used an ionization chamber to measure exposure rate, and were able to analyse their results by using a two term combination of functions (b) and (c) (Table 32). Wang et al. (1955) using similar apparatus found that they were unable to use function (b) alone or the two term combination to analyse the beam when no added filtration was present. However by adding 0.05cm aluminium filtration they could fit the two term expression to results obtained with an ionization chamber and with a scintillation counter. Burke and Pettit (1958) have suggested that the need for a two term expression arises from failing to take account of the characteristic radiation from the target. By allowing for this characteristic radiation in a rather indirect manner they were able to fit expression (c) alone to their exposure rate measurements. Norman and Greenfield (1955) used expression (d) to analyse their ionization chamber measurements but made no allowance for characteristic radiation.

Although not referring specifically to beryllium window X-ray tubes, Greening (1950) has suggested that functions (e) and (f) are suitable for the analysis of low energy and lightly filtered beams, but there do not appear to be any reports of their use in the literature.

4.6.3 Characteristic Radiation

In Chapter 1 it has been noted that attenuation analysis can only be used to determine smoothly-varying spectral distributions. The attenuation curves of Fig. 28 are for X-ray beams under conditions of

Figure 29

Attenuation of tungsten L-radiation in aluminium

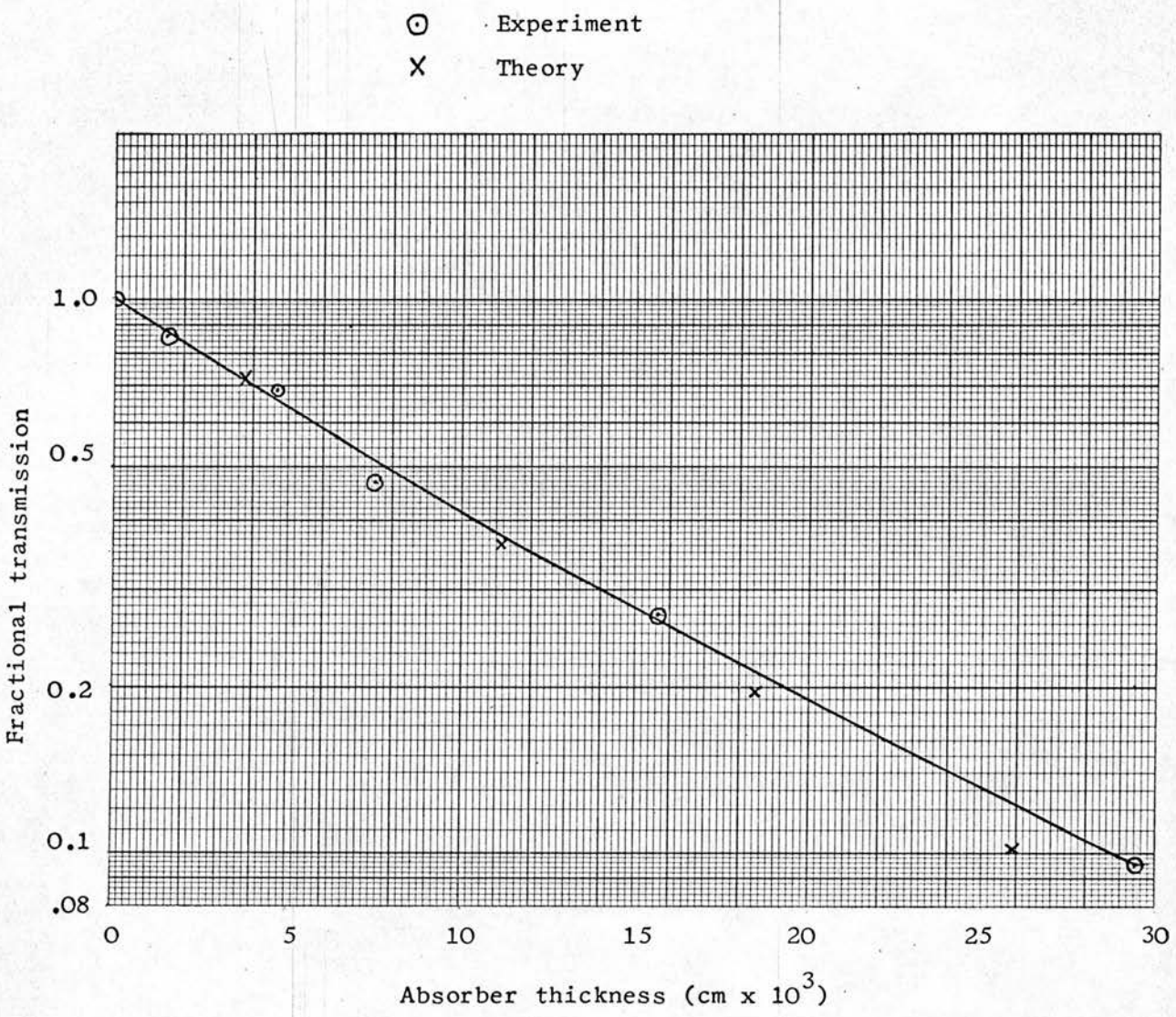

low inherent filtration and hence some tungsten L characteristic radiation will be present. The effect of this characteristic radiation must be removed from the absorption curves before any of the Laplace transforms can be useful over the whole range of data. To do this we will use the results of Chapter 3, giving the proportion of the initial intensity which is due to characteristic radiation, and we will also need to know the attenuation of tungsten L radiation in aluminium. This can be derived theoretically but is rather uncertain for reasons discussed below.

Using a 20kV X-ray beam to excite characteristic radiation from a tungsten sheet, it is possible to measure the attenuation of the characteristic radiation in aluminium, although the low intensity available makes the measurements rather uncertain. There will be variations between the relative intensities produced in this way and by electron excitation, but the results of Chapter 2 indicate that these will not be large. Similarly the attenuation of the beryllium window need not be duplicated since the variation of its transmission over the range of tungsten L radiation is only about 5%. The argon filled ionization chamber was used for detection, and the attenuation curve corrected for scattered continuum radiation and detector energy losses, is shown in Fig. 29. Theoretical attenuation calculated from the results of Jönsson (1926) is also shown. Compton and Allison (1954) discuss Jönsson's results and also review similar measurements by other authors. There are large discrepancies between measurements of the relative intensities of the α, β, γ components, and these lead to uncertainty in the theoretical attenuation curve at large values of absorber thickness. Hence the experimental results which are in good agreement with theory at low

absorber thicknesses give a more reliable representation of the attenuation at large absorber thicknesses. The experimental curve will be used in further calculations.

4.6.4 Attempts at fitting simple Laplace transforms to data

This section describes attempts to fit the absorption data with functions (a), (b), (c) and (e) of Table 32. These functions all have only two constants which may be determined fairly simply. These attempts, although only partially successful, provide useful information on the analysis of filtered spectra, and from the manner in which these transforms fail to satisfy the data it will be shown that it is possible to see in which direction to continue the search for a suitable transform. The results of Chapter 3 indicate that in addition to subtracting from the attenuation curves a proportion of the intensity which is due to "true" characteristic radiation, it will in general be necessary to subtract a further proportion representing the "characteristic continuum" before the resultant curve represents a smooth continuum. This extra proportion cannot be simply determined, and indeed there may be a range of suitable values which will give a smooth continuum. Therefore it was decided to subtract various proportions of tungsten L radiation from the absorption curves, using the results of Chapter 3 for guidance, and to investigate whether this resulted in one or more of the functions of Table 5 fitting the experimental data over the entire range of absorber thickness. This approach is only made possible by the use of a digital computer. A simple programme has been written which subtracts any specified fraction of characteristic radiation from the experimental data, renormalises, and calculates the function $(I_x/I_o)\exp \mu_o x$.

Figure 30

Jones' plot of $\frac{x}{y}$ vs y for 30kV data

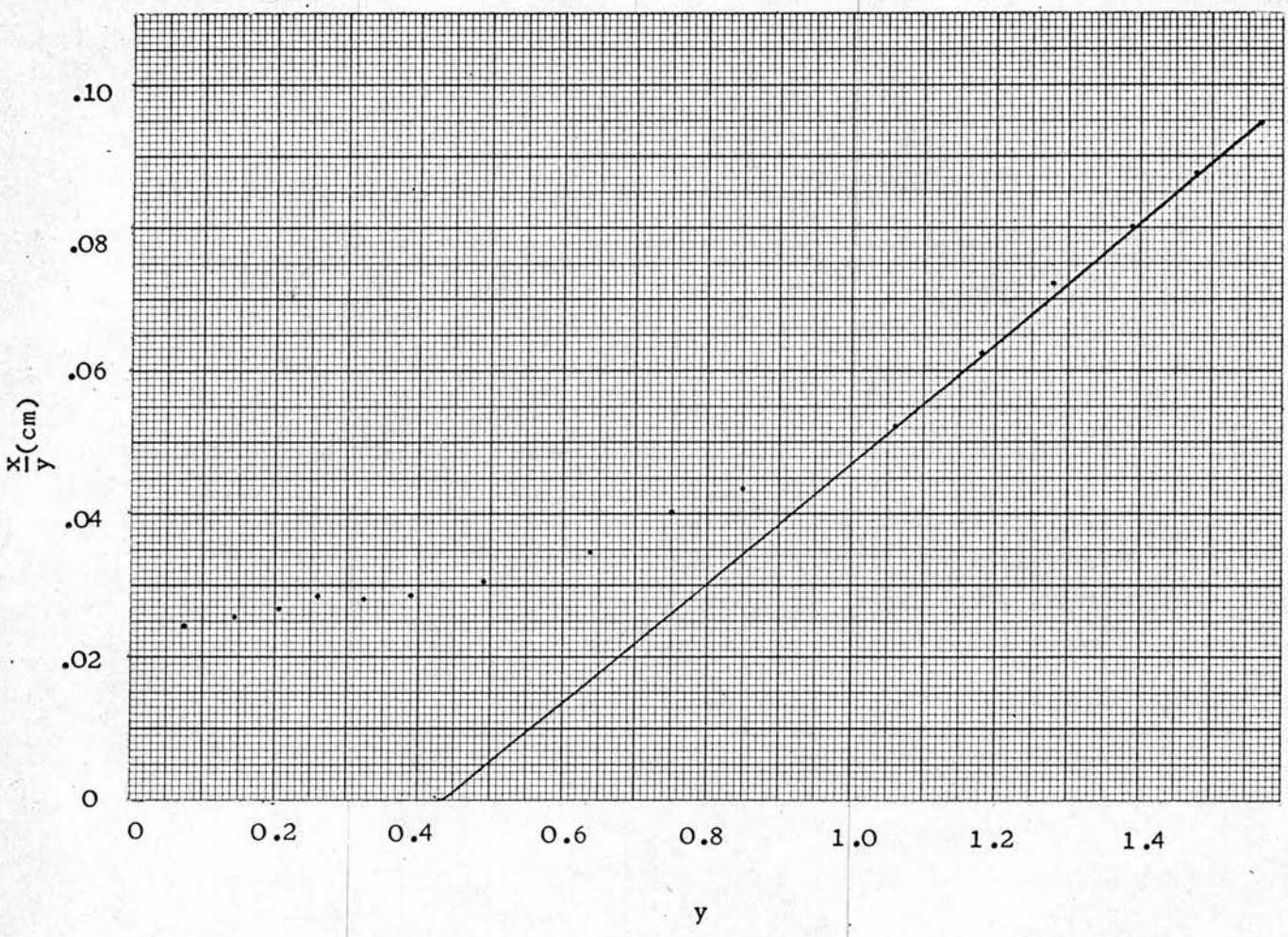

Other programmes can then be used to investigate the suitability of the functions in Table 32.

Computer analysis of function (c) indicates that there is no choice of the constants d and n which will enable this expression to be fitted to the attenuation curves of Fig. 28.

The programme which is used to investigate function (b) uses the method of Jones (1940). The application of this method is most easily seen by consideration of its use on the simple function (a).

We require $(I_x/I_o) \exp \mu_o x = \exp(-Bx^{1/2})$

i.e. $\ln \{(I_x/I_o) \exp \mu_o x\} = - Bx^{1/2}$

and putting $\ln \{(I_x/I_o) \exp \mu_o x\} = -y$

we have $B\sqrt{x} = y$

therefore $\frac{x}{y} = \frac{y}{B^2}$

Hence a plot of x/y against y should give a straight line through the origin. It can be seen that a similar plot for case (b) will give a line of the form $x/y = y/B^2 + C$ (where C is a constant) and it can easily be shown that the constant d in expression (b) is given by $d = B^2C^2/4$. The computer programme calculates values of x/y and y after subtracting various specified percentages of characteristic radiation and results may be displayed in digital or analogue form. This analysis indicates that function (b) cannot be fitted to the experimental data over the entire range of absorber thickness. However we can draw some conclusion which would be useful for the analysis of filtered spectra. Fig. 30 shows an x/y against y plot for the 30kV attenuation data with no characteristic radiation subtracted. The results can be fitted with a straight line for values of x/y greater

than 0.05, which corresponds to x >0.05cm. Thus the addition of 0.05cm of aluminium filtration to the tube produces an X-ray beam which can be analysed by expression (b). In 4.7.2 we have seen that Wang et al. needed to add 0.05cm aluminium filtration before they were able to analyse attenuation results. They do not seem to have appreciated that it is of course impossible to recover the unfiltered spectrum since low energy X-rays have been heavily attenuated e.g. 98% of 9keV photons are removed from the beam by 0.05cm aluminium. The analysis of the other attenuation curves gives the same type of result. Table 33 shows the amount of aluminium filtration which must be added to the various beams before function (b) can be applied without subtracting any characteristic radiation.

Table 33

Added filtration required to X-ray beams for expression (b) (Table 6) to be applicable

Beam (kV)	Added filtration (cm)
30	0.050
25	0.035
20	0.030
15	0.015

The decrease in the filtration thickness required with decreasing beam energy may indicate the decline in the percentage of characteristic radiation present as the tube voltage is decreased. These results will be useful if the analysis of filtered spectra is required since they show that the use of more complex transforms is not necessary for such X-ray beams.

Figure 31

Graphs of $I_x/I_o \exp \mu_o x$ (•), and $\sqrt{x}\, I_x/I_o \exp \mu_o x$ (×), against $\sqrt{x}$

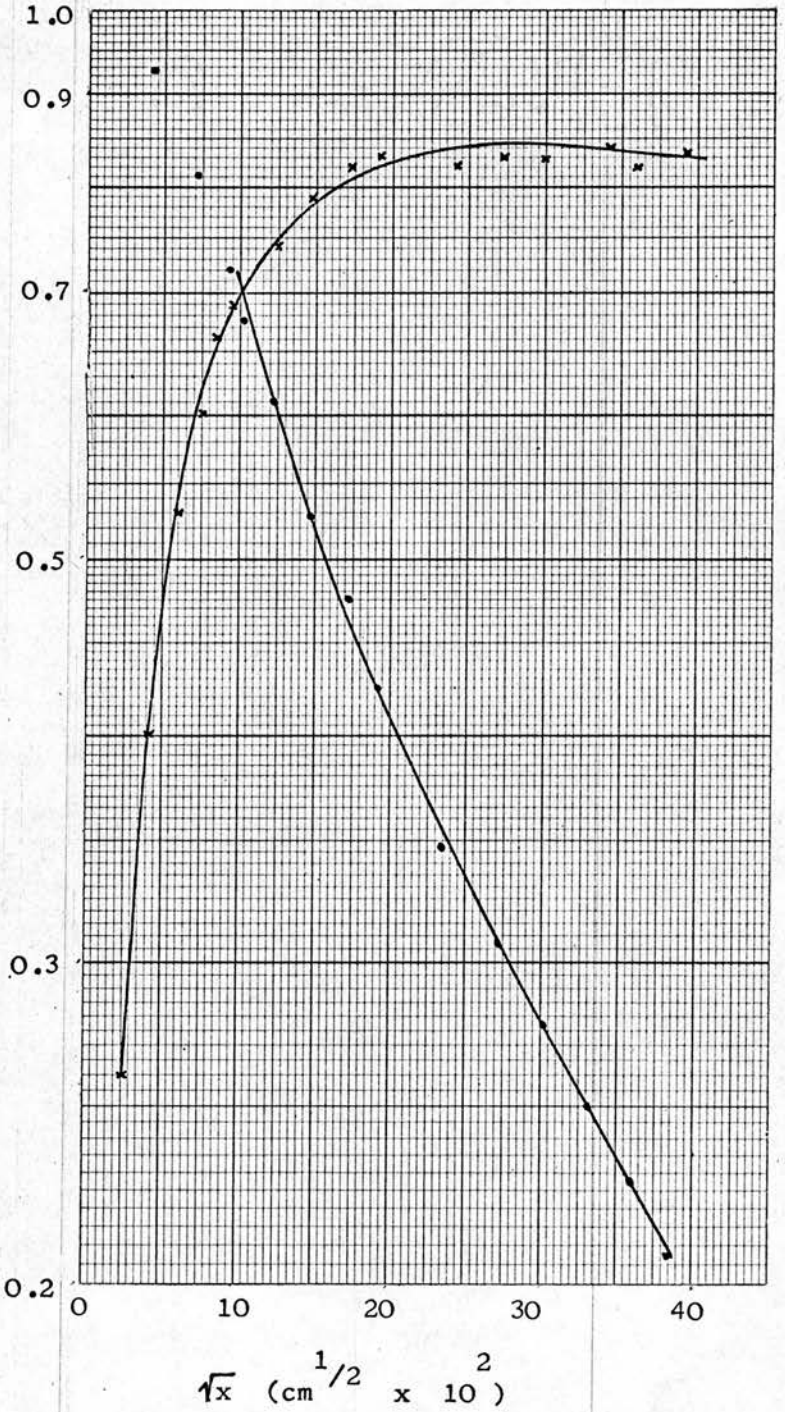

In spite of this unsuitability of (b) for unfiltered beams, we can now apply the method of Macey to suggest a suitable function. This is best seen by a graphical approach. An alternative method of obtaining a linear graph if (b) were suitable would be by plotting $\ln \left\{ (I/I_o) \exp \mu_o x \right\}$ against $\sqrt{x}$. Similarly, if (e) were suitable, a straight line graph would be obtained by plotting $\ln \left\{ \sqrt{x}(I/I_o) \exp \mu_o x \right\}$ against $\sqrt{x}$. These two graphs are shown in Fig. 31 for the 30kV results with no characteristic radiation subtracted. Function (b) gives a curve which is concave upwards (except at very low values of x) and (e) gives a concave downwards curve. The inverse transforms ψ for (b) and (e) are very similar apart from the factor $(\mu - \mu_o)^{-3/2}$ in (b) and $(\mu - \mu_o)^{-1/2}$ in (e). Thus it seems likely that a more suitable transform will contain the factor $(\mu - \mu_o)^{-n}$ where $^3/2 > n > {}^1/2$. Three transforms have been suggested which can satisfy this criterion, namely (c), (d) and (f). We have already shown that (c) is unsuitable and it can be seen that the inverse transforms of (c) and (d) are very similar. Therefore function (f) appears to present the best possibility of success, and we will show that it has proved very satisfactory for all the results.

4.6.5 Fitting of $f(x) = CK_o \left\{ B(x + d)^{1/2} \right\}$

Tables of K_o, the modified Bessel functions of the second kind have been published by Flügge (1954). An estimate of the constant B can be obtained from the value of the constant B in function (b) (which nearly fits the data). An estimate of the value of C can then be found from results for large values of x, assuming $x \gg d$, and finally the value of d is found which fits the function to the curve at low absorber thicknesses. This procedure is tedious but with practice suitable values

can quite quickly be found although the process of optimising the fitting of the curve can still be a lengthy procedure.

The results of the attempts to fit function (b) to the 15 and 20kV data indicate that the least curvature is obtained when it is assumed that 18% and 22% respectively of the initial intensities are due to characteristic radiation. This curvature method has been used by Greening (1947) and others since then but is not believed to be sensitive. However, the 15kV result agrees well with the figure of 21% obtained in Chapter 3, and in view of the results to follow, it seems reasonable to accept these figures.

When characteristic radiation has been subtracted the experimental results J(x), where $J(x) = (I_x/I_o) \exp \mu_o x$, can be fitted by function (f), Table 32, with the following values for the constants:-

15kV: C = 0.986 B = 8.5 d = 0.003cm

20kV: C = 0.660 B = 5.0 d = 0.003cm

Experimental values J(x) and the corresponding calculated values f(x) are shown in Table 34.

Table 34

Comparison of experimental and calculated results for 15kV and 20kV attenuation curves

x (cm)	15kV		20kV	
	J (x)	f(x)	J(x)	f(x)
0.075	-	-	0.160	0.161
0.057	0.100	0.102	0.203	0.203
0.037	0.166	0.165	0.274	0.278
0.020	0.285	0.285	0.384	0.396
0.010	0.460	0.440	0.532	0.540
0.005	0.630	0.600	0.685	0.674
0	1.00	0.980	1.00	0.970

Figure 32

Sum Laplace Analysis of 30kV data

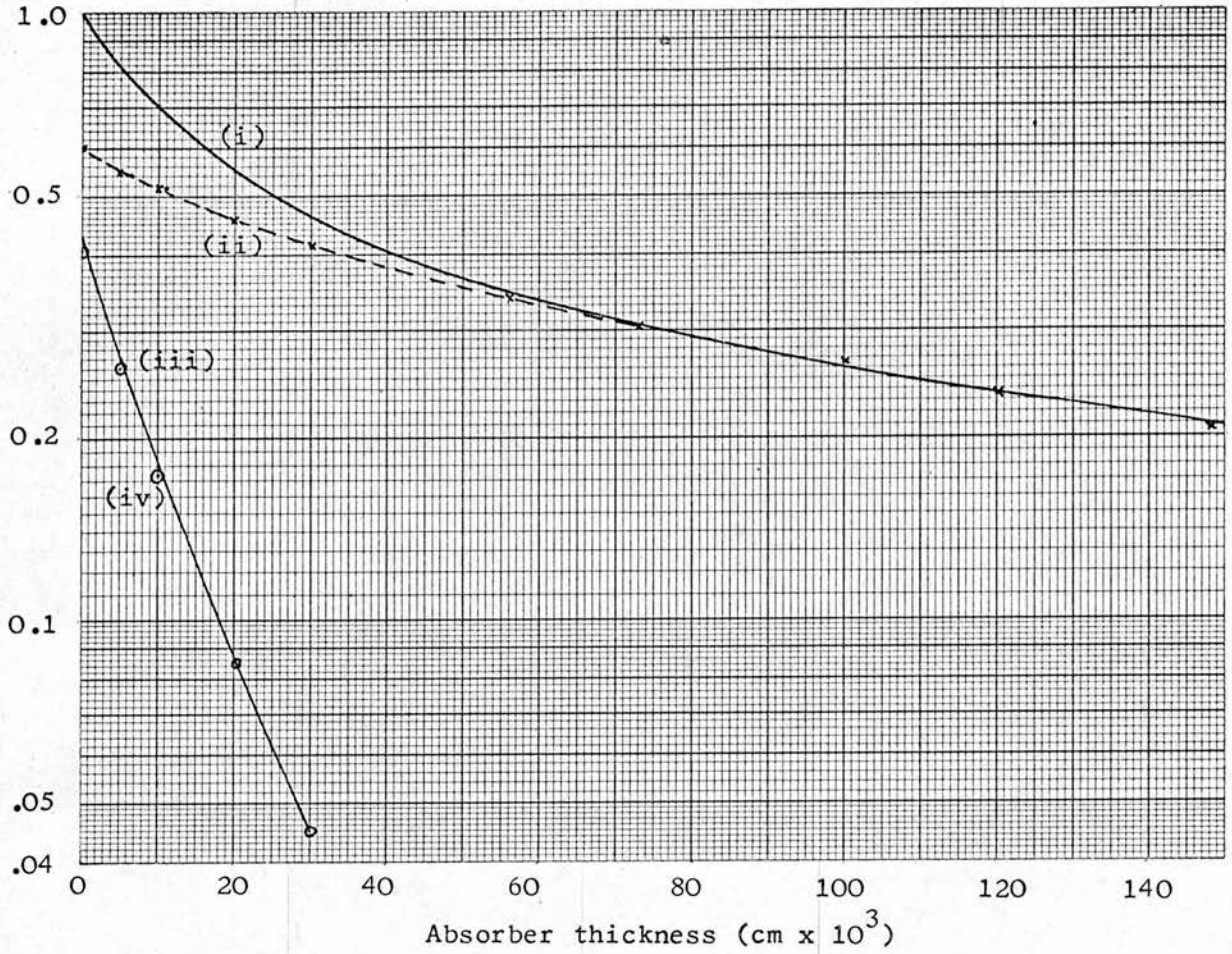

Figure 33

Intensity distributions by sum Laplace method

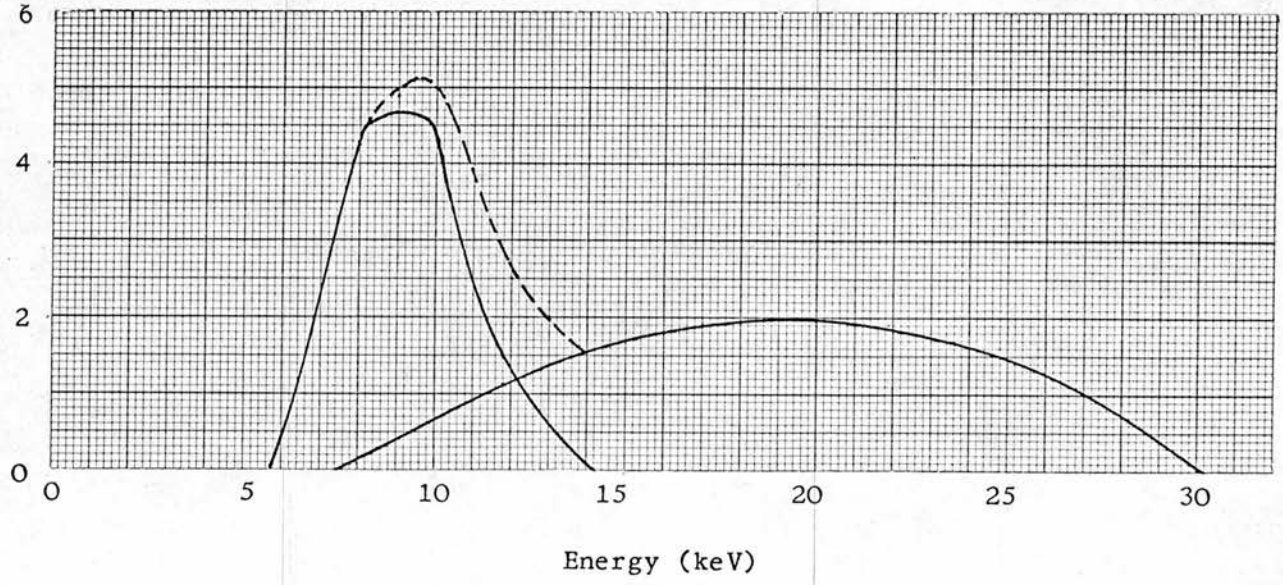

Agreement is good at large x, and is within 5% at low values of x where the experimental accuracy is also in doubt due to uncertainty in absorber thickness.

Computer analysis of the 30kV data in the attempt to fit (b) did not yield an accurate estimate of the proportion of characteristic radiation, but since the results of Chapter 3 indicate that variation in this proportion between 20kV and 30kV should not be very great, for a first approximation a figure of 22% (i.e. the same proportion as was used to analyse the 20kV results) was chosen. It proved impossible to fit the data with a single function, but recourse to the multiple Laplace transform method produced useful information. This method (see Greening, 1950) uses the fact that Laplace transforms are additive. Thus we may write:

$$J(x) = (I_x/I_o) \exp \mu_o x = a\,T_1 + b\,T_2 \ .....$$

where T_1 and T_2 are Laplace transforms. The first transform is fitted for large values of x and should extend over as large a range of x as possible. The second term (two terms usually suffice) is then fitted to the difference $J(x) - a\,T_1$ and is essentially a small correction to the first. In fitting the first term, it is important to use physical considerations so that the attenuation curve of the remainder has a feasible physical shape, i.e. is concave upwards. Fig. 32 illustrates this for the 30kV data with 22% characteristic radiation assumed. Curve (ii) is fitted to the data (i) at large values of x. Differences between (i) and (ii) are then plotted giving the curve (iii) and this is closely fitted by curve (iv). Both (ii) and (iv) are functions of the type $CK_o\left\{B\,(x + d)^{1/2}\right\}$ with constants given below:-

Curve (ii): C = 0.60 B = 2.7 d = 0.030

Curve (iv): C = 26.1 B = 25 d = 0.022

Intensity distributions can now be calculated (see later), and these are shown in Fig. 33. The sum distribution is seen to have a secondary peak at ~9keV. This immediately suggests that insufficient tungsten L radiation has been allowed for initially, and areal measurement suggests that an extra 20 - 30% of characteristic radiation should be subtracted from the beam, i.e. between 35 - 45% of the initial beam intensity should be due to characteristic radiation.

When 40% characteristic intensity is assumed for the 30kV beam the results can be fitted with a single function and similarly if 35% characteristic intensity is assumed for the 25kV results, again a single function fits the data. The function is the same as before, $CK_o \{B(x + d)^{1/2}\}$ with constants:

25kV: C = 0.665 B = 3.7 d = 0.005

30kV: C = 0.595 B = 2.4 d = 0.008

Table 35 illustrates the agreement between experimental values J(x) and calculated values f(x).

Table 35

Comparison of experimental and calculated results for 25kV and 30kV attenuation curves

x (cm)	25kV		30kV	
	J(x)	f(x)	J(x)	f(x)
0.14	-	-	0.280	0.280
0.09	0.230	0.230	0.343	0.345
0.07	0.270	0.275	0.406	0.410
0.05	0.330	0.337	0.478	0.480
0.02	0.530	0.530	0.657	0.657
0.01	0.675	0.670	0.780	0.775
0	1.00	1.00	1.00	1.00

4.6.6 Calculation of Spectral Distributions

Intensity distributions can now be calculated, using the inverse transform $\psi(\mu - \mu_o)$ since the intensity distribution $F(\lambda)$ is given by:-

$$F(\lambda) = \psi(\mu - \mu_o)\, d\mu/d\lambda$$

where λ is the wavelength in Angstroms and

$$\psi(\mu - \mu_o) = \frac{C}{2} \frac{\exp\left\{-(\mu - \mu_o)\, d\right\} \exp\left\{-B^2/4\,(\mu - \mu_o)\right\}}{(\mu - \mu_o)}$$

Values of $d\mu/d\lambda$ and μ have been tabulated by Burke and Pettit (1958), and values of μ_o were also taken from their figures.

The initial intensity with no absorber in the beam was measured with the calorimeter, and this therefore provides a measure of the total energy fluence. The power in keV/mA-s-sterad. through the $^3/_{16}$" aperture at a focus to aperture distance of 9.2cm is shown for each of the beams in Table 36. For comparison, the power calculated from the theoretical distributions (Chapter 2, Table 16) is also retabulated.

Table 36

Powers of X-ray beams used in Absorption Analysis

Beam	Power (keV x 10^{-13}/mA-s-sterad.)	
	Experiment	Theory
30kV 25mA	2.60	2.41
25kV 25mA	1.72	1.75
20kV 25mA	0.94	0.97
15kV 30mA	0.38	0.44

From the results of attenuation analysis we know the percentage of intensity which is due to characteristic radiation, thus the intensity

Figure 34(i)

30kV Intensity distribution

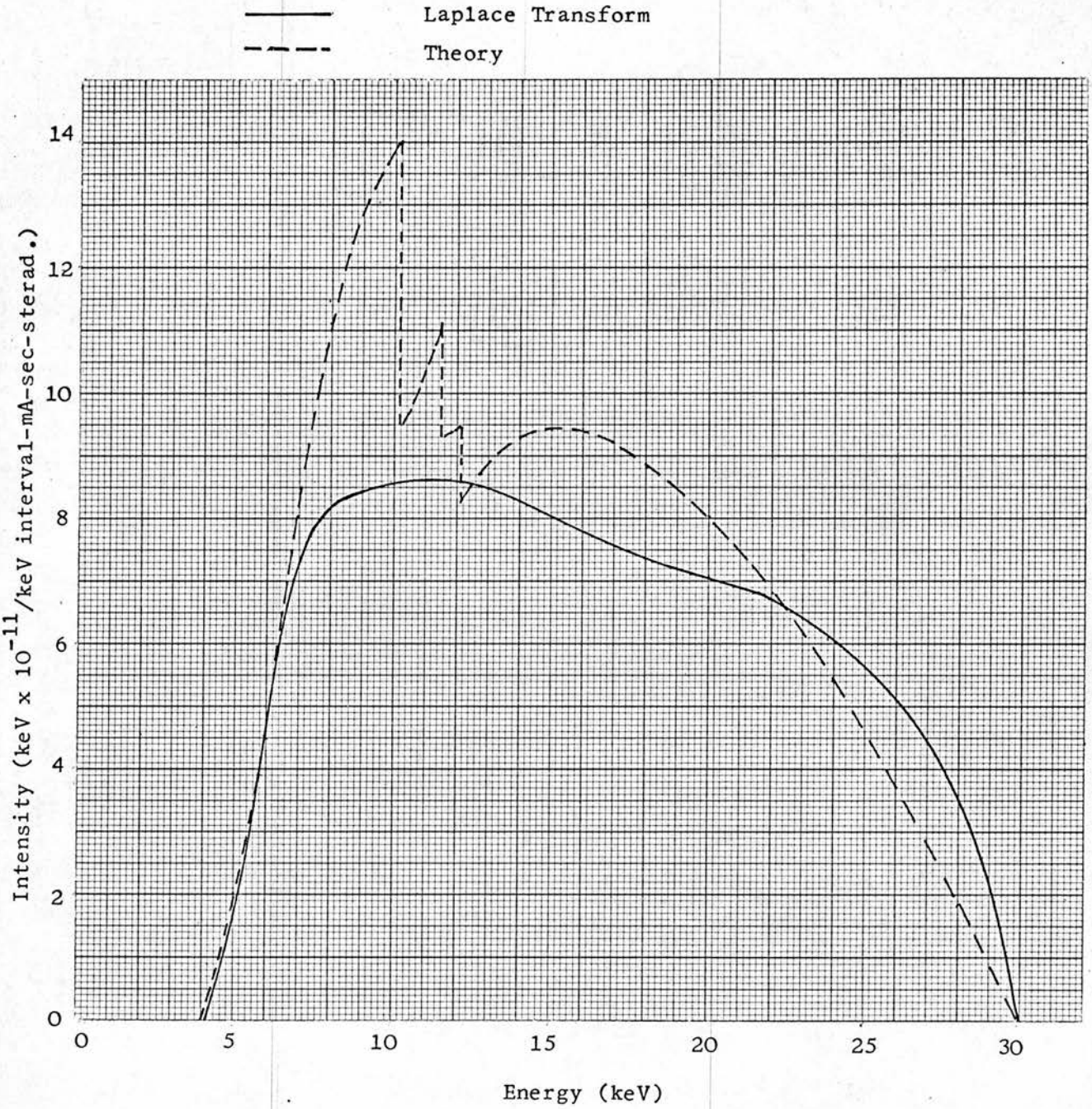

Figure 34(ii)

25kV Intensity distribution

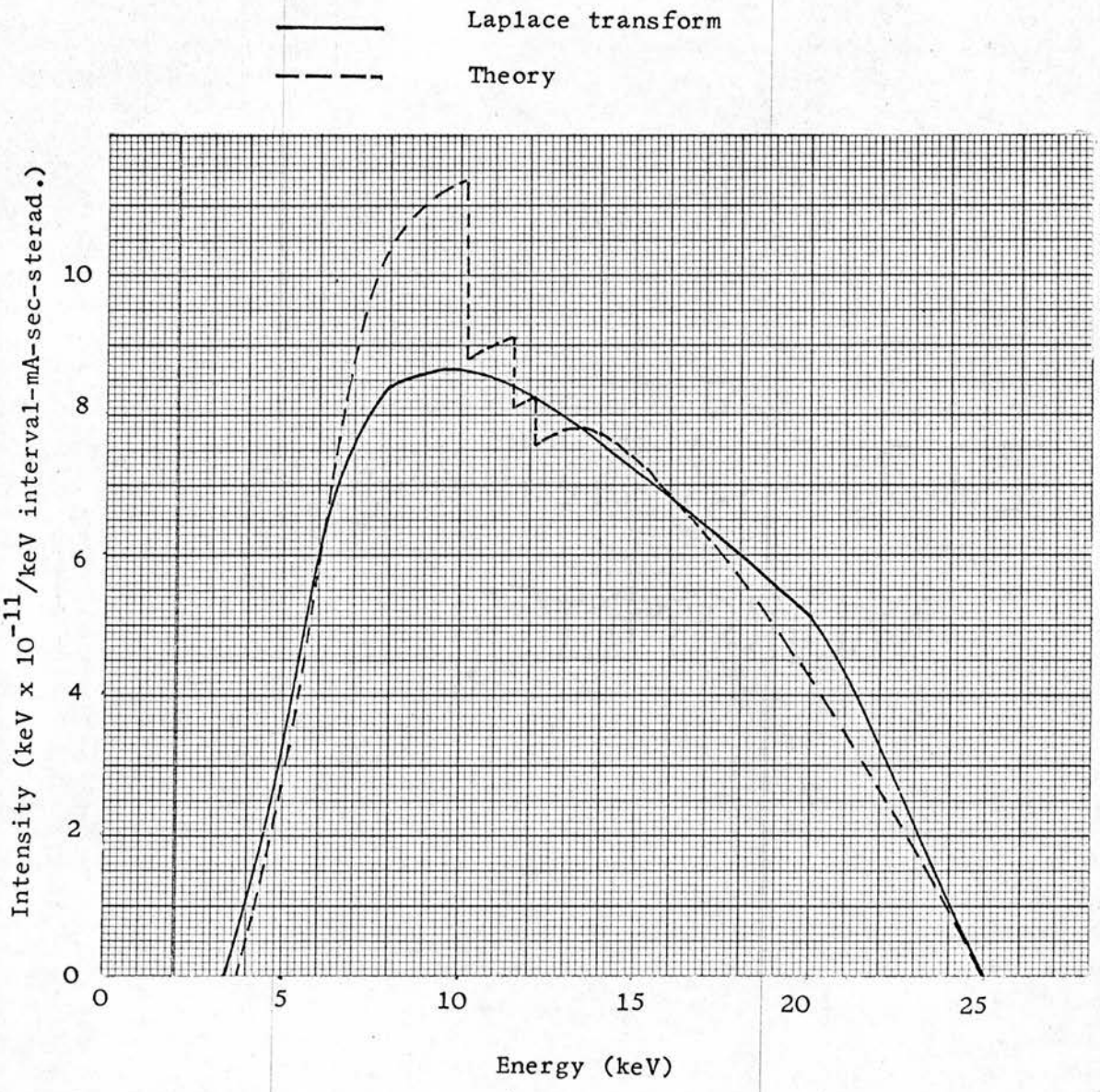

Figure 34(iii) and (iv)

20 and 15kV Intensity distributions

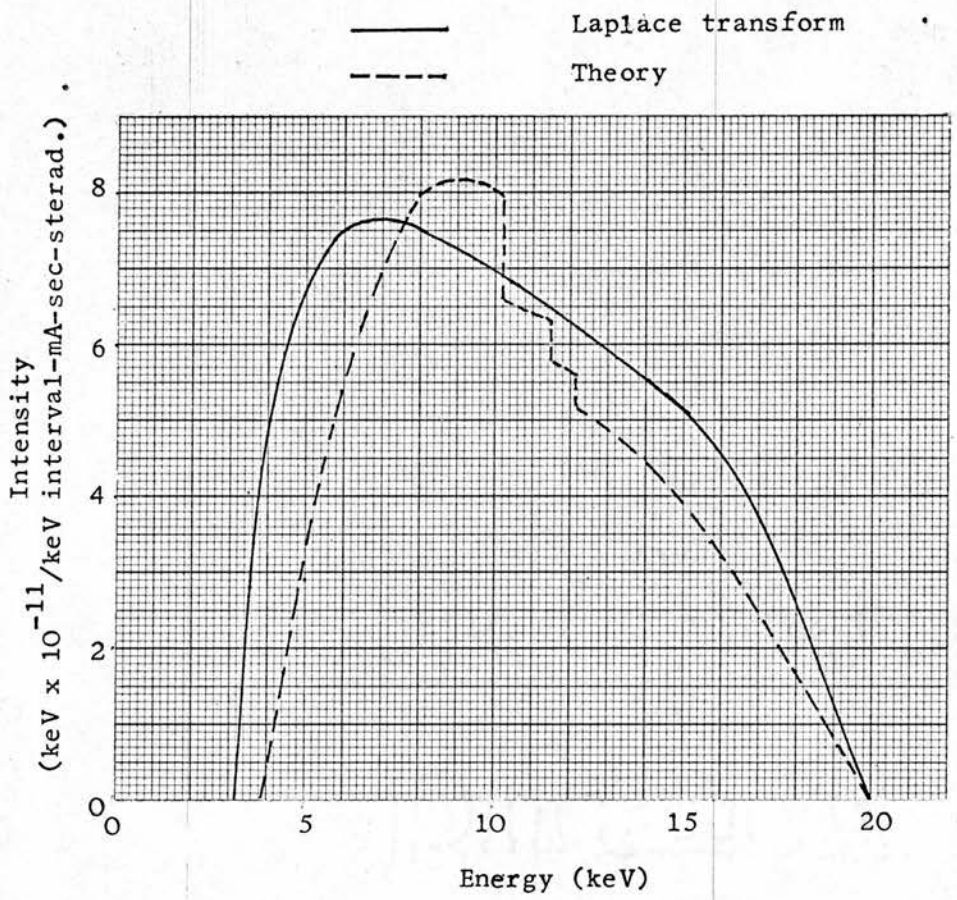

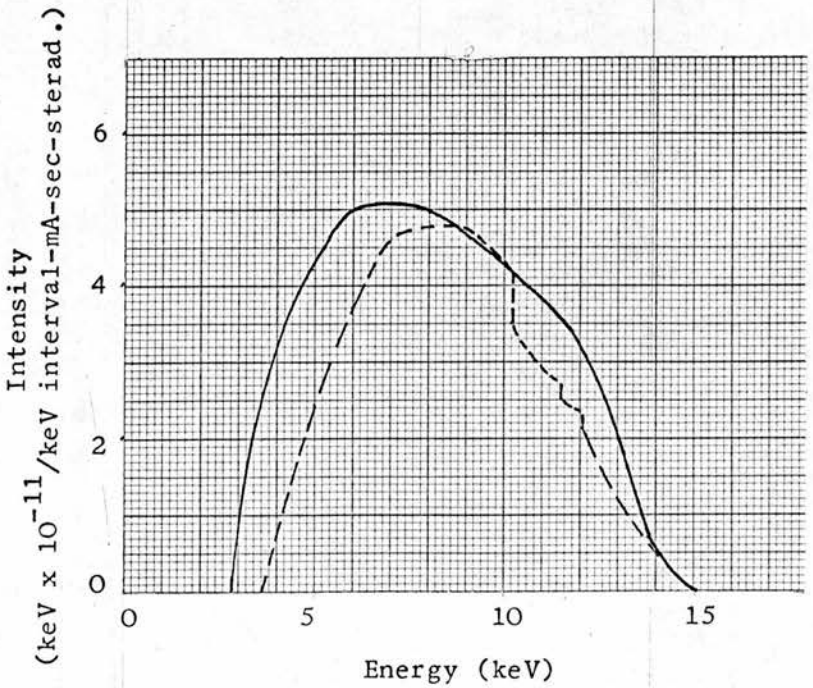

Figure 35(i)

30 and 25kV photon distributions
by attenuation analysis

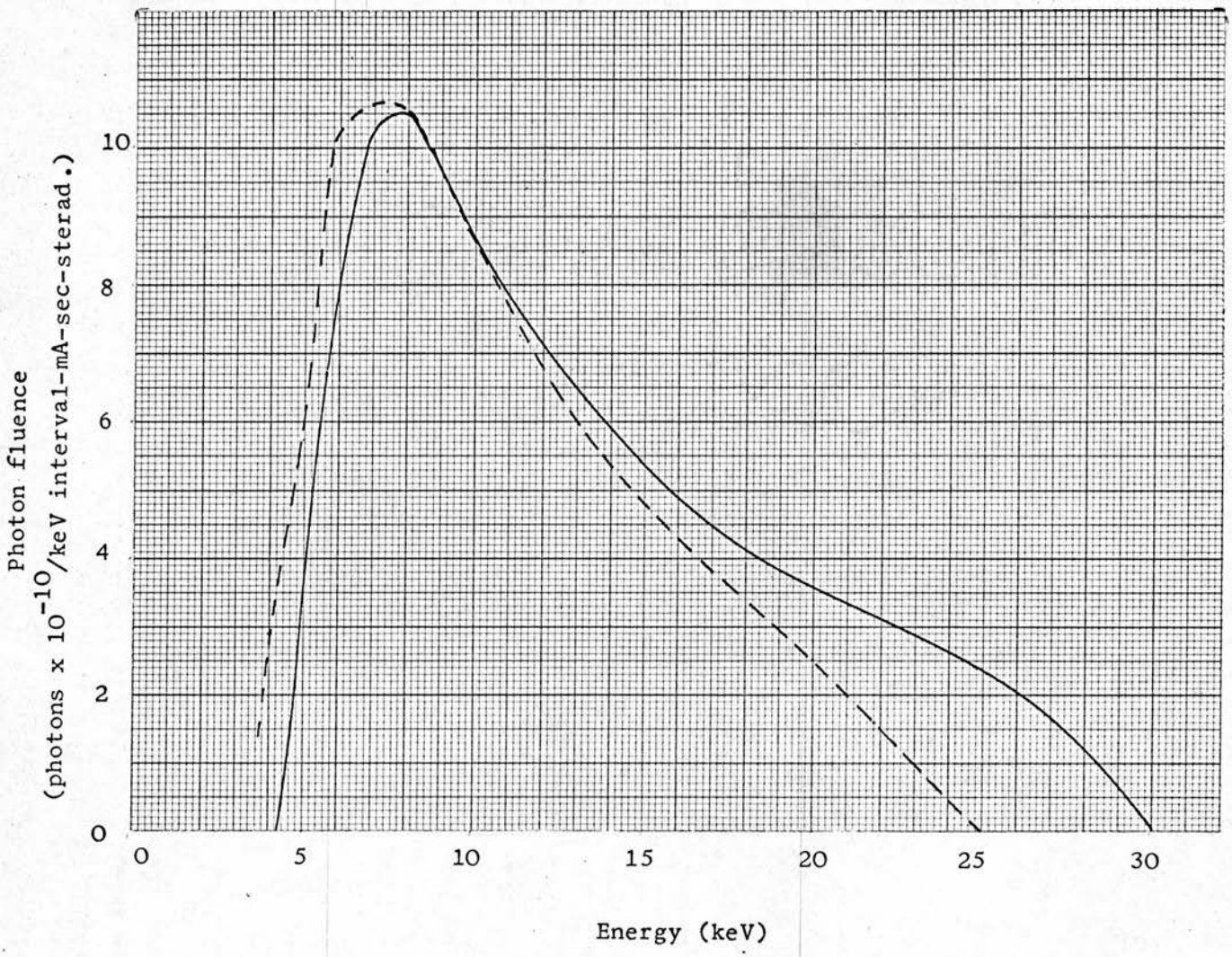

Figure 35(ii)

20 and 15kV photon distributions
by attenuation analysis

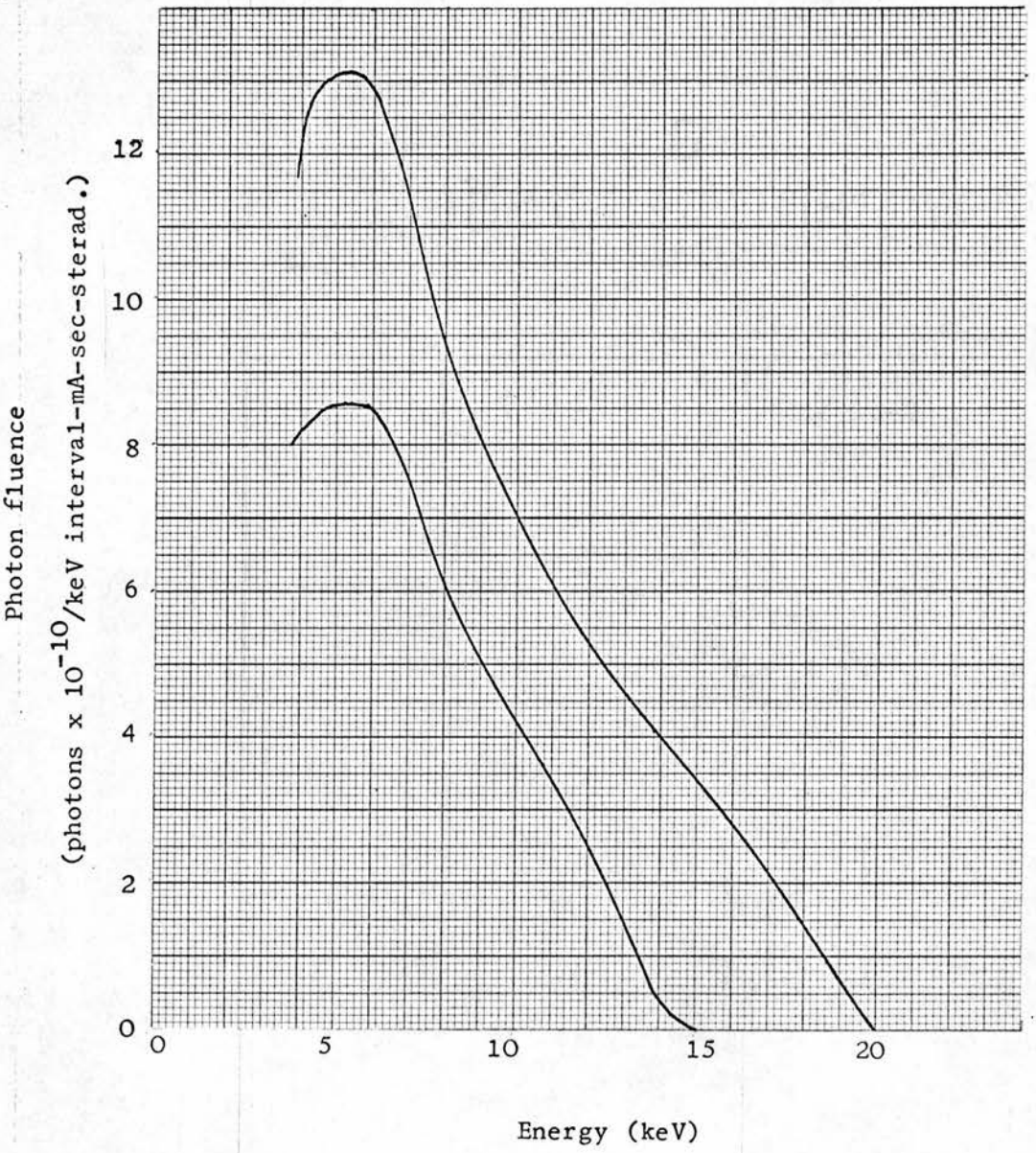

in each beam due to characteristic and continuum radiation can be tabulated as in Table 37.

Table 37

Characteristic and Continuum Intensities of X-ray beams

Beam (kV)	Intensity (keV x 10^{-13}/mA-s-sterad.) Characteristic	Continuum
30	1.04	1.56
25	0.60	1.12
20	0.21	0.73
15	0.07	0.31

The total intensities contained in the calculated continuous distributions must be given by the results of Table 37. Thus absolute intensity distributions can be calculated and corrections can then be made for the attenuation due to the air path and Melinex. These distributions are most usefully plotted against energy. The conversion of the wavelength distribution $f(\lambda)$ to an energy distribution $f(E)$ is easily made since $f(\lambda)\, d\lambda = -f(E)\, dE$ and if E is in keV and λ in Angstroms,

$$\lambda = \frac{12.4}{E} \quad \text{hence} \quad f(E) = \frac{12.4}{E^2} f(\lambda)$$

Intensity distributions at the tube window are shown in Fig. 34(i - iv) with the corresponding distributions from the theoretical calculations of Chapter 2 shown for comparison. Photon distributions can also be calculated and are shown in Fig. 35(i,ii)

4.7 Discussion of Results

The agreement between the experimental and theoretical values of the total intensity in the various X-ray beams is very good. Differences between results in Table 36 and those from Redpath (1967) are due to the

slightly different air path.

There is also good agreement between the experimental and theoretical intensity distributions. It has already been remarked that the choice of a smooth continuum from the theoretical distributions is somewhat arbitrary in view of the preferential transmission peaks, and it is upon this choice that the percentage of characteristic radiation in the beam depends. The spectra obtained by attenuation analysis have all taken in more of the preferential transmission peaks than those arbitrarily suggested in Chapter 2. This will account for the 15kV and 20kV spectra containing less characteristic radiation than had been suggested in Chapter 3. In the case of the 25kV and 30kV spectra it seems possible that there may be a contribution due to indirect characteristic radiation which has not been allowed for in the theory.

Both intensity and photon distributions are well defined down to 5keV. Below this energy the large correction factor for filtration and the uncertainty in values of μ and $d\mu/d\lambda$ for aluminium make the results rather unreliable.

It is tempting to interpret the irregularities on the 30kV and 15kV distributions as indicative of the presence of the preferential absorption peaks, but it does not appear that the resolution of attenuation analysis can justify this.

The results presented in this chapter define the spectral distribution of the beryllium window X-ray tube to two different degrees of accuracy. The three component representation of 4.6. can be very useful to calculate the attenuation of X-ray beams in aluminium or to estimate small scatter corrections. The distributions in absolute units derived in 4.7.6 define the beams far more accurately and specify the

intensity of characteristic radiation present. These spectra are suitable for many calculations, e.g. mean energy of the beam, accurate scatter and transmission corrections, and secondary effects in other materials than aluminium. Use has already been made of these distributions to derive energy spectra for the use in the determination of ferrous sulphate G values (Law and Redpath, 1968).

The good agreement with theory of the results presented here is in marked contrast with the work of Norman and Greenfield (see 3.11). This confirms the importance of allowing for the characteristic radiation, and illustrates the necessity for the application of the measurements of characteristic intensity made in Chapter 3. The Laplace transform $f(x) = CK_o \{ B(x + d)^{1/2} \}$ which seems to have been ignored by previous workers has been shown to be most suitable for the analysis of attenuations curves of the type presented here. It is also apparent that the discussion in Chapter 2, which contains a more realistic treatment of target self-absorption than previous workers have attempted, leads to good agreement of theory with experiment at low energies.

Figure 36

Block diagram of pulse height analysis system

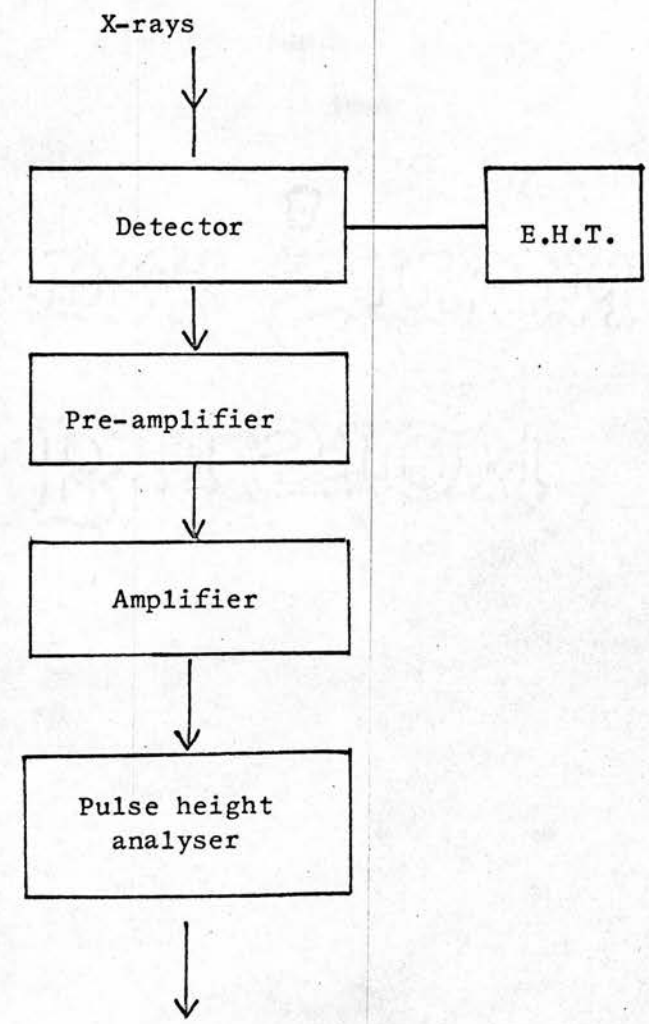

CHAPTER 5

PULSE HEIGHT ANALYSIS

5.1 Introduction

The development of multichannel pulse height analysers has made pulse height analysis a most convenient method for the determination of X-ray photon spectra. A single photon absorbed in the detection system gives rise to a voltage pulse with a height nearly proportional to the absorbed energy. These pulses are amplified and sorted in a pulse height analyser. The recorded pulse height distribution requires correction for distortions such as those caused by finite detector resolution or incomplete absorption of the incident photon energy. Various methods of undertaking these corrections are discussed in Chapters 6, 7 and 8. If the pulse height distribution is to be converted into an accurate photon spectrum, then the following three relationships must be known and must remain constant throughout the experiment.

1. The variation of pulse height with photon energy.
2. The variation of the detector resolution with photon energy.
3. The variation of the detector efficiency with photon energy.

The elements of a typical pulse height analysis system are shown in the block diagram of Fig. 36. We will examine the effect of each element on the performance and stability of the system.

5.2 Discussion of requirements for a pulse height analysis system

5.2.1 Detector

The detectors used in this study are a sodium iodide scintillation counter and an argon-methane gas flow proportional counter. The principles of their operation have been discussed in Chapter 1 and the

detectors will be described in Chapters 7 and 8. The interaction of an incident photon with the detector results in a current briefly flowing at the detector output terminals. The duration of this current is 0.25 - 1.5μs for a scintillation counter, and 0.01 - 5.0μs for a proportional counter. It is usual to integrate the current at the pre-amplifier input thus producing a voltage-mode signal for further amplification.

Corrections for backscatter, sidescatter and transmission by the detectors are most easily calculated if narrow beam geometry is used.

When using the gas flow detector it is important that the gas is dry and at constant pressure if the gain and detection efficiency are not to vary.

5.2.2 High voltage supplies

In scintillation counters the fractional change in gain for small changes in voltage varies approximately as the number of dynodes times the fractional voltage change, i.e.

$$\frac{\Delta G}{G} \simeq a \frac{\Delta V}{V} \qquad \text{where} \quad a \simeq 8$$

A similar relationship holds for proportional counters with $a \simeq 14$. A.C. ripple on the high voltage supply causes line broadening whereas long term voltage fluctuations cause a variation in the energy calibration. Hence for a gain and resolution stability of better than 1% the E.H.T. supplies must have a long term stability and A.C. ripple of less than 0.1%

5.2.3 Pre-amplifier

Signals from the detector are in the range of 10^{-15} - 10^{-10} coulombs per pulse. The pre-amplifier produces voltage pulses which are nearly proportional in height to the absorbed energy, and are of a suitable

shape for the main amplifier. To maximise signal to noise ratio the the signal charge must be integrated on a small capacitance, usually the stray capacitance between the detector and pre-amplifier, which is ~ 5 - 50pF. To ensure true integration the time constant, i.e. the product of the resistance and capacitance shunting the pre-amplifier input, must be long compared with the signal duration, e.g. for sodium iodide detectors the signal duration is ~0.5μs and the input time constant is commonly made ~1.5μs by a suitable choice of anode load resistor. To avoid distortion due to pulse pile up, count rates must then be less than 10^4 - 10^5 counts per second.

The pre-amplifier is usually an emitter follower type, since the low output impedance enables the signals to be passed along considerable lengths of cable without distortion. Its gain should be stable to better than 0.1% and it should not introduce significant noise into the system.

5.2.4 Amplifier

The measurement of continuous distributions gives rise to pulses of very different heights. It is therefore important that the amplifier possesses good overload characteristics. The same requirements of gain stability and noise apply as for the pre-amplifier..

5.2.5 Pulse height analyser

Owing to the inherent delays in sorting and storing all the pulses from the detector, multichannel pulse height analysis imposes slightly greater restrictions on the acceptable count rate than the use of a single channel system. The maximum overall count rate for a multichannel system must be less than 5 x 10^4 counts per second for a shift of less than 1% in channel number. However the overall

advantages of multichannel analysis outweight this slight disadvantage.

5.3 Method of Calibration

To convert the pulse height distribution to an intensity spectrum the energy calibration (pulse height against energy) and resolution calibration (resolution against energy) must be obtained. To do this, use can be made of the source of characteristic radiation described in Chapter 3.

At low energies the absorption of X-rays in the detectors used here is principally by the photoelectric effect. Thus the detector response to a monoenergetic X-ray beam is a Gaussian distribution, called the photopeak (see Fig. 3). The width of this distribution at half height characterises the detector resolution and the pulse height corresponding to the peak gives the photon energy calibration. Thus by recording the photopeaks due to monoenergetic beams covering the energy region of interest, two calibration curves can be obtained for each detector.

The measurement of peak position and resolution can be difficult if the peak is broad and channel width large. Zimmerman (1961) has described a method of graphical analysis which gives these parameters accurately. It uses the fact that the photopeak is a Gaussian distribution. Denoting channel number by x, a normal distribution about channel x_o is given by:-

$$y(x) = C \exp\left(-(x - x_o)^2/2\sigma^2\right) \quad \ldots\ldots\ldots \quad 5.1$$

therefore

$$\frac{y(x-1)}{y(x+1)} = \exp 2(x - x_o)/\sigma^2 = Q(x) \quad \ldots\ldots\ldots \quad 5.2$$

Hence a graph of ln Q(x) against x should give a straight line with

Figure 37

Zimmerman plot for Cu characteristic radiation

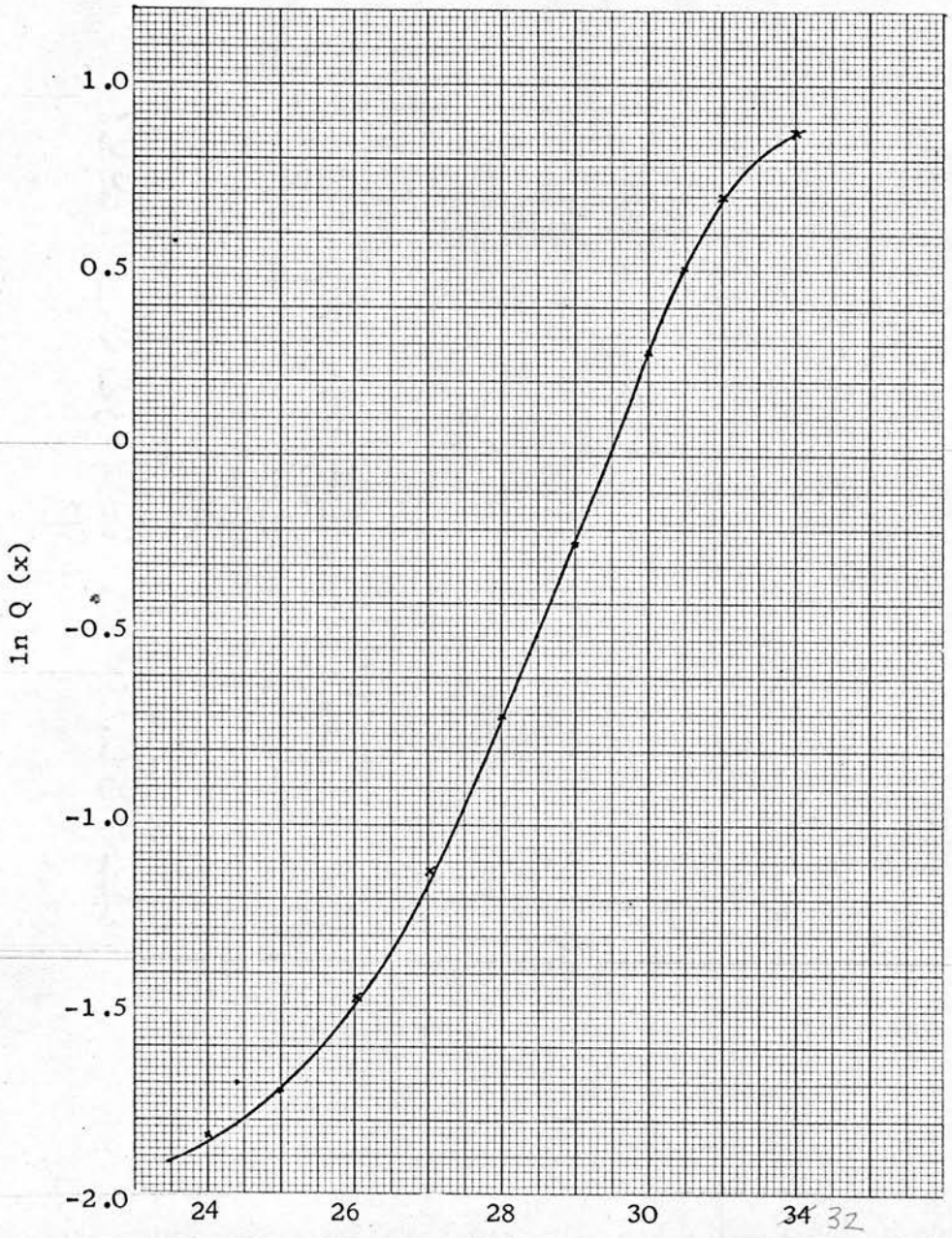

Figure 38

Copper line broadening

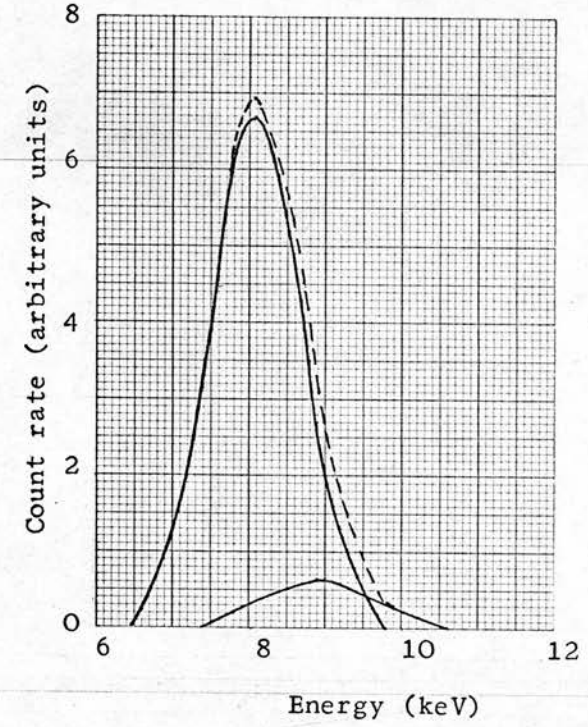

gradient $^{2}/\sigma^{2}$ which cuts the x axis at $x = x_o$. Resolution as defined in 1.3.4 is then given by $2.36\sigma/x_o$. If the number of counts is large so that there is only a small uncertainty in values of y, this method allows peak position and resolution to be measured to an accuracy of better than 1%. Fig. 37 illustrates the use of this method to analyse the photopeak of copper characteristic radiation obtained from the gas proportional counter. The shape of the photopeak can also be investigated by this method since only a normal distribution will give a straight line graph. The detector is incapable of resolving the copper K_α and K_β lines at 8.1 and 8.9keV respectively, but the resultant photopeak deviates from a normal distribution at the high energy side, and this can be seen in curvature of the graph. It is possible that the K_β radiation causes both line broadening and a shift of the photopeak, but since both effects are expected to be small we can use the resolution figures derived from Fig. 37 to investigate the effect. By constructing K_α and K_β line shapes in the appropriate intensity ratio, and allowing for any variation of detector efficiency for the α and β lines, the percentage increase in height and resolution due to the K_β radiation can be found, e.g. from Fig. 37 the resolution for copper radiation is 16.3%. Fig. 38 shows α and β line shapes constructed by use of this measurement (multiplied by $(E_\alpha/E_\beta)^{1/2}$ for the β line). The "sum" photopeak is broadened by about 2.4%. Hence the detector resolution for pure K_α radiation would be 15.9%. The peak shift due to the K_β radiation is less than 0.1keV in this case. By consideration of different radiations, a correction curve can be built up for each detector and so accurate calibrations can be obtained.

5.4 Expected count rate

The discussion in 5.2 concludes that a stable multichannel pulse height analysis system requires a total count rate of less than 5×10^4 pulses per second. Spectral distributions of the X-ray beams described in Chapter 4 are required, since these beams have been used for other measurements where a knowledge of the spectra is necessary for the application of corrections (see Law and Redpath, 1968; Greening, Randle and Redpath, 1968; Greening and Randle, 1968).

The results of Chapter 4 can be used to estimate the photon fluence expected. Graphical integration of the spectra from Fig. 35 gives this estimate. For the discussion which follows it will be most convenient to consider photons per cm^2 per second, and this conversion is simply made, taking the focus-window distance as 1.6cm. Table 38 gives the photon fluence just outside the X-ray tube window for the beams measured.

Table 38

Estimated photon fluence at X-ray tube window

Beam	Photon Fluence (photons x $10^{-13}/cm^2$-s)		
	Continuum	Characteristic	Total
30kV 25mA	1.21	1.14	2.35
25kV 25mA	1.10	0.67	1.77
20kV 25mA	0.98	0.23	1.21
15kV 30mA	0.67	0.08	0.75

Thus the flux must be reduced by a factor of about 10^9 before these beams can be measured by pulse height analysis.

5.5 Possible methods of count rate reduction

5.5.1 Reduction of tube current

This method was used by Ehrlich (1955) who operated a beryllium window X-ray tube at 50kV and about 0.01μA. However recently Epp and Weiss (1966) have found changes in spectral shape when large current reductions are made. This might be expected since the focussing of the electrons on to the target depends on the tube current. In the present study no variation in spectral distribution has been found when the current is between about 6mA and the maximum rating, so that a reduction of 4 or 5 is available.

5.5.2 Inverse square law

Ehrlich used a focus-to-detector distance of 1 metre to reduce the count rate, whilst Epp and Weiss employed a 2.1 metre air path. However a 2 metre air path attenuates 5keV X-rays by about 2×10^4 so that it would be impossible to derive the true photon distribution at the tube window by this method. To remove the air filtration objection an evacuated tube with Melinex entrance and exit windows was considered but with a maximum path length of 2.5 metres available due to room size, insufficient count rate reduction would be produced.

5.5.3 Apertures

By placing a small aperture in front of the detector, the number of incident photons can be reduced. The construction of very small diaphragms poses three problems.

(i) The diaphragm material must be sufficiently thick to attenuate all incident radiation other than that passing through the aperture.

(ii) The edges of the aperture must be smooth to prevent spectral distortion.

(iii) The radiation exit should be conical to reduce further the possibility of the production of secondary radiation.

The smallest drilled aperture satisfying all these requirements has an area of about $1 \times 10^{-3} cm^2$ giving a count rate reduction by a factor of 10^3. The method adopted by Wang et al. (1957), makes use of fine collimation to view only part of the target. However Epp and Weiss (1966) have found that the spectral distribution varies across the target and so in this investigation, since all other measurements have used the spectrum from the whole target, the fine collimation method would not have been suitable.

5.5.4 Filtration

If the beam is highly filtered before measurement the low energy part of the unfiltered spectrum cannot be recovered. An air path of 100cm transmits about 6% of 6keV and 31% of 8keV X-rays so that spectra at the tube window deduced from measurements at 100cm will be defined down to 7 or 8keV. For the 30kV spectrum obtained in Chapter 4, 100cm air filtration reduces the photon flux by a factor of 2 in addition to the reduction of 10^4 due to inverse square law.

5.5.5 Detector efficiency

The detection efficiency of the scintillation counter is nearly 100%. In Chapter 6 the detection efficiency of the proportional counter will be calculated, and will be shown to be very low at high energies. The effect of this efficiency on the air filtered 30kV spectrum derived in 5.5.4 can be calculated, and this indicates that a further count rate reduction by a factor of about 5 will occur. Due to the low detection

efficiency the spectrum will be rather ill-defined above 25keV.

5.5.6 Summary

Thus by using all the reduction techniques discussed, i.e. reduced current and a small aperture 100cm from the tube, the count rates from the proportional and scintillation counters for a 30kV beam would be about 1×10^5 and 5×10^5 pulses per second respectively.

The count rate from the proportional counter may still cause distortion but lower energy beams will give acceptable count rates. Results taken with this system are described in Chapter 7.

The scintillation detector count rate requires further reduction by a factor of at least 10. There are many ways by which this could be done, but that which will be described in the remainder of this chapter has the great advantage of allowing beams to be measured at high tube current and low air filtration, thus giving accurately defined low energy spectra of useful X-ray beams.

5.6 Survey of X-ray scattering

5.6.1 Introduction

The attenuation of low energy X-rays in any material occurs by three processes:-

(i) Photoelectric absorption.

(ii) Coherent (Rayleigh) Scattering.

(iii) Incoherent (Compton) Scattering.

Between 5 and 30keV the probability of X-ray scattering is small, and by also accepting only radiation scattered into a narrow cone about an angle θ, the detected photon flux may be very much less than that incident on the scatterer. If the initial spectrum can be deduced from the scattered

spectrum, then this provides a very effective method of dealing with high photon fluxes. Scrimger and Cormack (1963) have used this technique to measure the spectrum of Cobalt 60 by recording the spectrum scattered off a Lucite sheet. They note the importance of using a thin scattering source so that only once-scattered photons are obtained, and the correction can then be made relatively simply. The method does not appear to have been used to measure low energy X-ray spectra, but we will show that it is easily applied and introduces little more distortion than that due to the detectors.

There are two variables which must be considered when designing a scattering spectrometer:-

(i) Angle of scatter.

(ii) Scattering material.

5.6.2 Optimum angle of scatter

The probability of X-ray scattering from a free electron depends on the differential scattering cross-section $d\sigma$. By definition $d\sigma$ is the number of photons scattered at a particular angle expressed as a fraction of the number of incident photons, i.e.

$$d\sigma(\Theta) = \frac{\text{Number scattered at } \Theta}{\text{Number incident}} \qquad \ldots\ldots\ 5.1$$

($d\sigma(\Theta)$ has dimensions: $\frac{\text{number/sec-electron}}{\text{number/cm}^2\text{-sec}} = \frac{\text{cm}^2}{\text{electron}}$)

Classically it can be shown that:

$$d\sigma(\Theta) = \frac{r_o^2}{2}\,(1 + \cos^2\Theta)\,d\Omega \quad \text{cm}^2/\text{electron} \qquad \ldots\ldots\ 5.2$$

where X-rays are scattered into the solid angle $d\Omega$ at a mean angle Θ (r_o is the classical radius of the electron).

The application of wave mechanics leads to the Klein-Nishina differential cross-section:

$$d\sigma(\Theta) = d\sigma(\Theta)_{Classical} \times \left\{1 + \alpha_o(1 - \cos\Theta)\right\}^{-2} \left[1 + f(\alpha_o)\right] \ldots\ldots 5.3$$

where $\alpha_o = E_o/m_o c^2$ where E_o is the incident photon energy and $m_o c^2$ is the electron rest mass energy (= 511keV). The function $f(\alpha_o)$ is very small unless $\alpha_o > 1$. This formula reduces to the classical expression for any Θ when α_o tends to zero. In the present study the maximum value of α_o is 0.06 hence we will consider the classical case.

Defining the total scattering cross-section by σ_s, we have

$$\sigma_s = \int_o^\pi \frac{d\sigma(\Theta)}{d\Omega}\, d\Omega = \frac{r_o^2}{2} \int_o^\pi (1 + \cos^2\Theta)\, 2\pi \sin\Theta\, d\Theta$$

$$= \frac{16\pi}{3} \frac{r_o^2}{2}$$

$$\text{Therefore} \quad \frac{d\sigma(\Theta)}{d\Omega} = \frac{3\sigma_s}{16\pi} (1 + \cos^2\Theta) \ldots\ldots 5.4$$

In practice the detector will receive photons which have been scattered over a small spread of angles centred about Θ. If the angle of acceptance is small, then we can assume that $d\sigma/d\Omega$ is constant over this angle, and the initial spectrum can easily be derived from the scattered spectrum. The least error will be introduced by this assumption if the angle is chosen so that $d\sigma(\Theta)/d\Omega$ is a minimum with respect to Θ. Differentiation of equation 5.5 shows that this occurs when $\Theta = 90^\circ$. Then if N_o is the incident photon flux, equations 5.1 and 5.4 can be used to calculate $N(\Theta)$, the number of photons per electron per second scattered in a cone of small solid angle $\Delta\Omega$ at a mean angle Θ.

This is given by

$$N(\theta) = N_o \int^{\Delta\Omega} \frac{d\sigma(\theta)}{d\Omega} \, d\Omega \qquad \ldots\ldots\ldots 5.5$$

and since $d\sigma/d\Omega$ is constant over small angles when $\theta = 90^o$ this simplifies to:

$$N(90^o) = N_o \frac{3\sigma_s}{16\pi} \Delta\Omega \qquad \ldots\ldots\ldots 5.6$$

5.6.3 Choice of scattering material

To avoid characteristic radiation from the scatterer swamping the scattered spectrum, a low atomic number material with no K-edge higher than 2keV must be chosen, i.e. atomic number 14^{Si} or lower. The material must be available as a thin foil so that only single scattered photons are produced and the scattered spectrum is not appreciably absorbed by the foil.

Scrimger and Cormack (1963) used a 1/16" Lucite sheet and assumed that only single scattering was being obtained since they could produce identical spectra from scatterers of several times this thickness. In the present case two other materials have been investigated, aluminium and Melinex. Both are available in thin foils, but Melinex has a lower attenuation of the scattered spectrum.

5.6.4 Composition of the scattered radiation

The discussion in 5.6.2 was confined to scattering from free electrons where energy conservation makes Compton scattering the only allowed process. However in considering atomic scattering it is necessary to take the binding energy of the electrons into account. A full description of the process requires the use of wave mechanics, but some qualitative conclusions will be sufficient for the present discussion.

Figure 39

Energy of 90° Compton-scattered photons

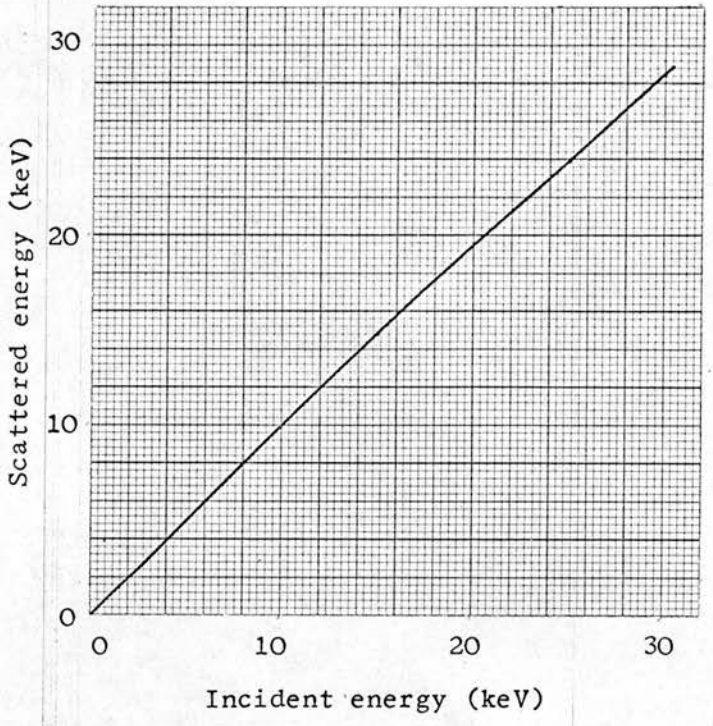

Figure 40

Spectra of silver K_α line, scattered by different elements

(from Compton and Allison, 1954)

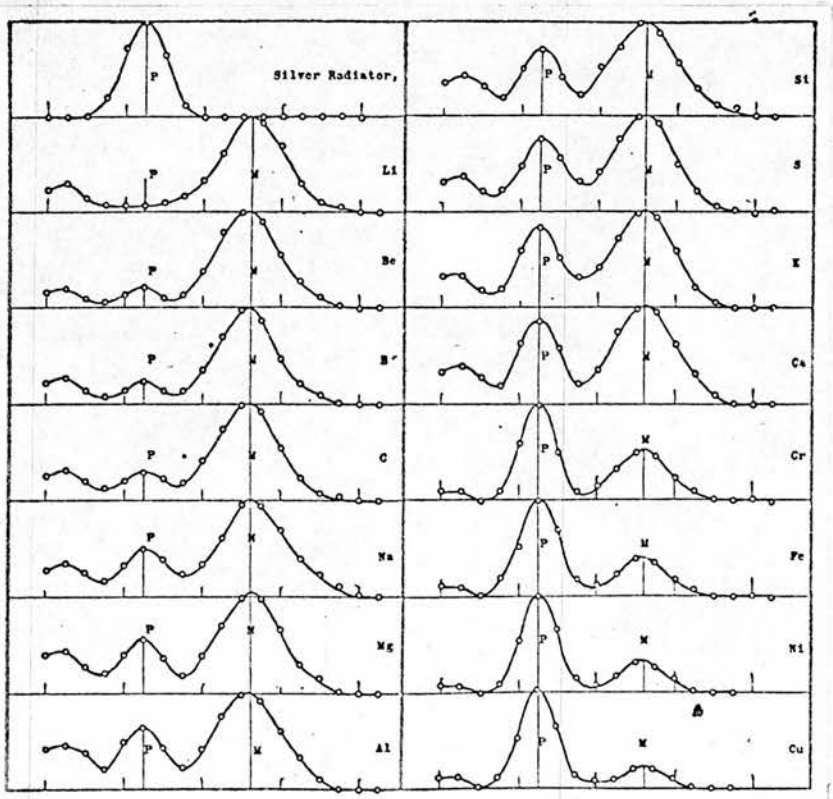

Electrons in the inner shells are tightly bound, and elastic scattering can take place from these electrons provided they do not receive enough energy to eject them from the atom. In fact there is a finite probability of elastic scattering from any bound electron, and the cross-section for all the bound electrons acting together is given by

$$\sigma_{coherent} = \sigma_{classical} \times |f(\Theta)|^2$$

where $\sigma_{classical}$ is the total classical scattering cross-section of a free electron (see 5.6.2) and $|f(\Theta)|^2$ is the atomic scattering factor. At very low energies $f(\Theta) \rightarrow Z$.

Electrons with low binding energies are virtually free, especially for the scattering of high energy photons, so that Compton scattering takes place. Hence generally there are two scattered components for an incident monoenergetic X-ray beam. The energy of the Compton scattered component is given by

$$E = \frac{E_o}{1 + \alpha_o(1 - \cos \Theta)} \qquad \ldots\ldots\ldots 5.7$$

where E_o, α_o and Θ are as defined in equation 5.3. Fig. 39 shows the variation of the energy of the Compton scattered component with the incident photon energy for 90^o scattering.

The relative intensities of the Compton and elastic scattered components vary with the atomic number of the scattering material and the energy of the incident photons. Fig. 40 which is taken from Compton and Allison (1954) shows the spectra of the silver K_α line (22keV) scattered by various elements. The increase in prominence of the coherently scattered line with increasing atomic number can be seen. Scattering

Figure 41

Mass attenuation coefficients for photons in Melinex

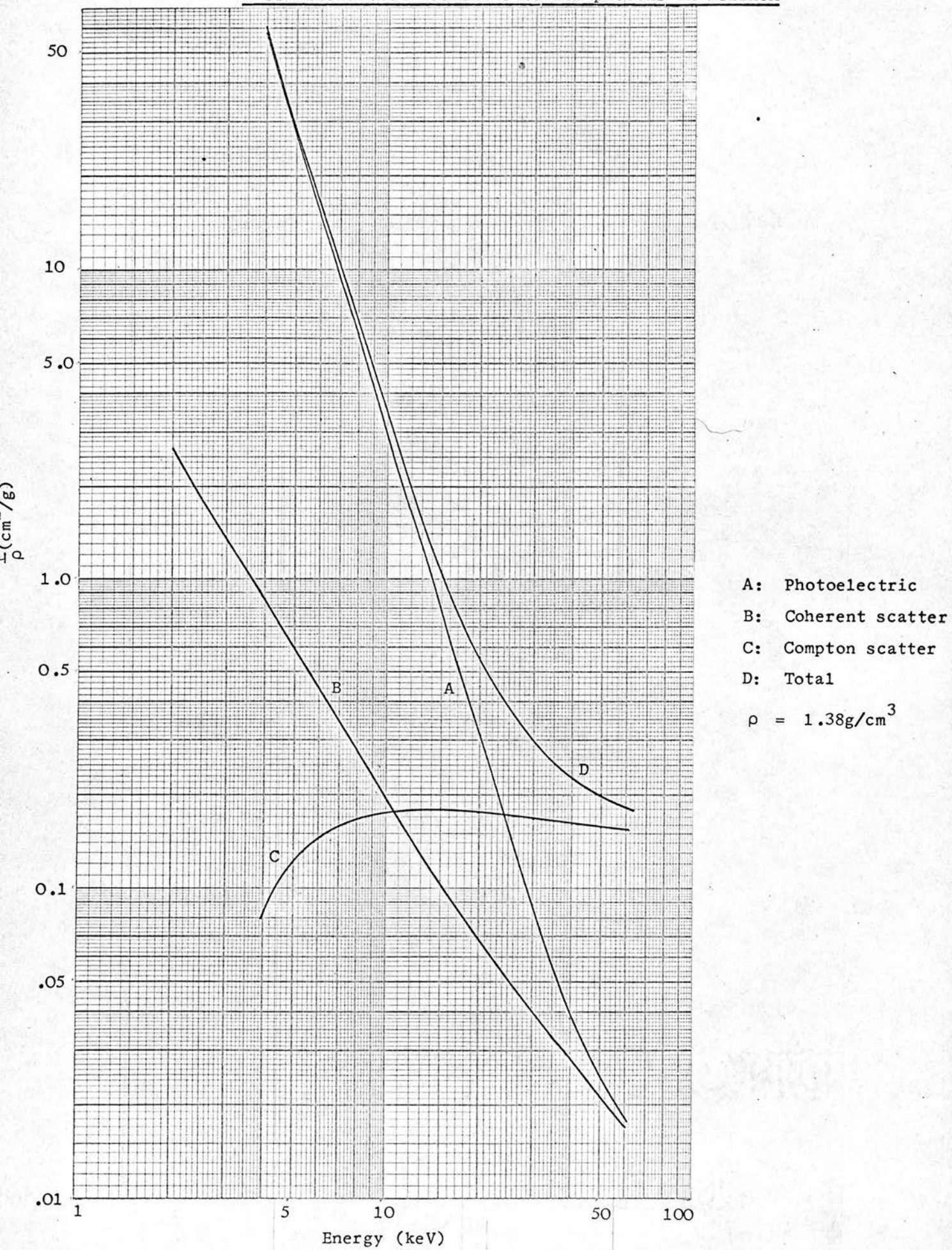

A: Photoelectric

B: Coherent scatter

C: Compton scatter

D: Total

$\rho = 1.38 g/cm^3$

Figure 42

Mass scattering coefficient for photons in Melinex

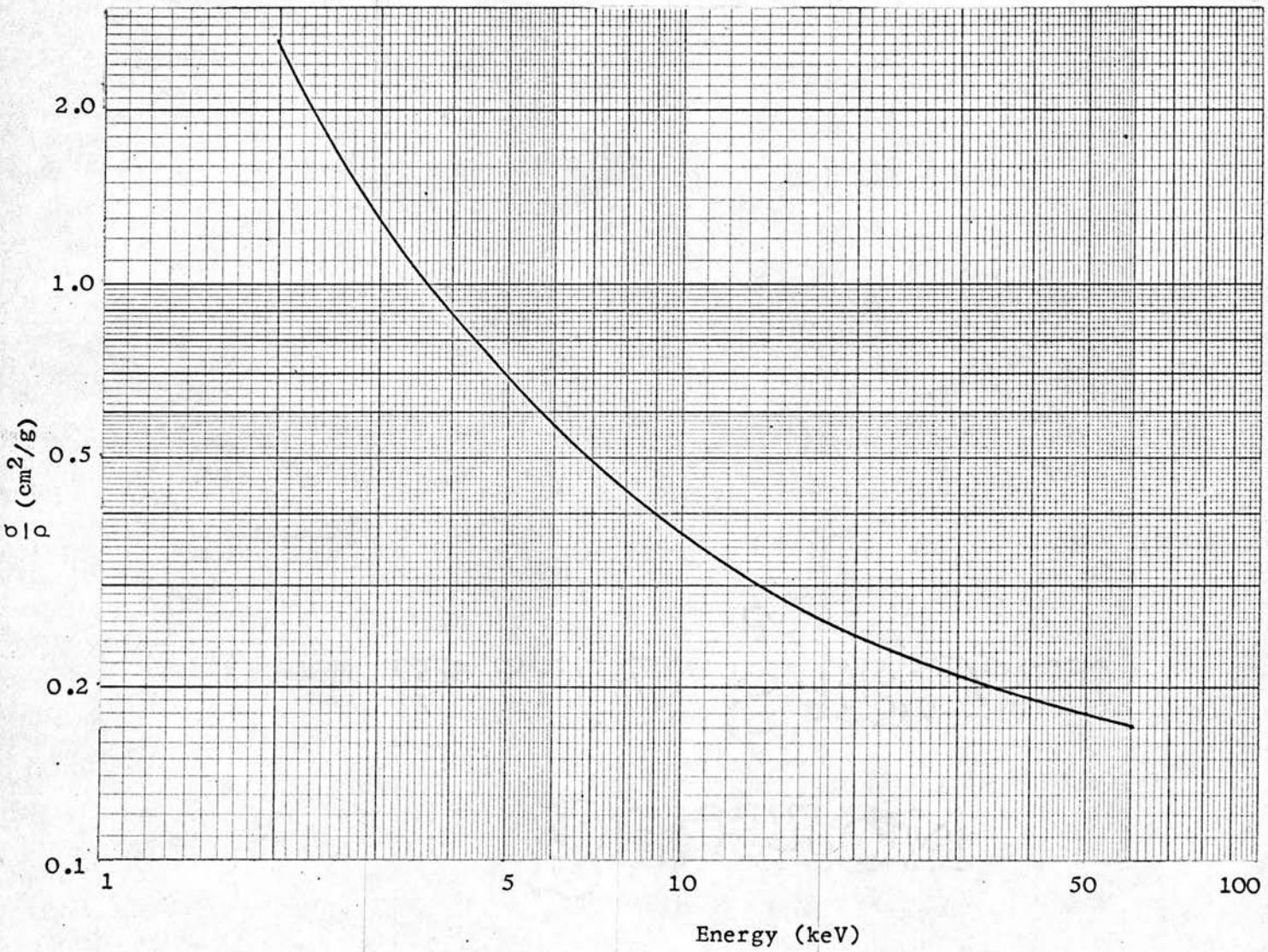

cross sections for the elements have been tabulated by McMaster et al. (1967). Melinex is polyethylene terephthalate film, containing, by weight, 62.5% carbon, 33.3% oxygen and 4.2% hydrogen. Mass attenuation coefficients for photons in Melinex have been calculated and are shown in Fig. 41. In view of the increasing use of Melinex in the construction of low energy X-ray dosemeters it is believed that this graph will be of use to other workers, since tabulations of attenuation data for Melinex do not appear to have been published elsewhere. For this reason the photoelectric component has been included. Fig. 42 shows the total (Compton plus coherent) scattering cross sections for Melinex. Since this cross section only varies by a factor of about three over the energy region 5 - 30keV a scattered spectrum will suffer much less distortion than a spectrum which has been heavily filtered by air (see 5.5.4). From Fig. 42 the variation of relative intensities of the two scattered components with energy can be deduced from the magnitude of the scattering cross sections. These are equal at about 10keV. Since the component separation is insufficient to be resolved by the scintillation counter the result of scattering will be a slight line broadening and peak shift e.g. at 10keV the two components, of energies 9.9 and 10keV, are of equal intensity, hence the sum photopeak at 9.95keV will only have been shifted by 0.5%. In Chapter 8 corrections for this shift will be discussed.

5.7 Estimation of the count rate due to a 90° scattered spectrum

Using the 30kV spectrum derived in Chapter 4 the count rate which will be received when this spectrum is scattered can be estimated. Consider the scattering from a Melinex film 6.3×10^{-4} cm thick, i.e. mass

cross-section $\rho t = 0.88$ mg/cm^2. The following assumptions will be made:-

(i) Coherent and Compton scattered components have a $(1 + \cos^2\theta)$ angular distribution.

(ii) Negligible energy loss for Compton scattered component.

(iii) Negligible air absorption or attenuation of radiation after scattering.

(iv) Small angle of acceptance by the detector.

Then the flux in the energy interval dE scattered at 90° from unit area of the film into unit solid angle is approximately given by (cf. Equation 5.6)

$$N_s(E)\,dE \simeq N_o(E)\,dE \times \frac{3\sigma_s(E)}{16\pi\rho}\,\rho t \qquad \ldots\ldots 5.8$$

where σ_s/ρ is the total mass scattering cross-section for Melinex in this case.

The use of equation 5.8 on a 30kV 25mA spectrum indicates that the scattered flux from 0.1cm^2 of the Melinex would be about 1.3×10^9 photons/sec-sterad. whereas the flux at the window of the tube is about 6.0×10^{15} photons/sec-sterad. If the detector is about 10cm from the scatterer and has an aperture of area 0.1cm^2 defining the accepted beam, then the count rate would be about 1.3×10^4 counts/sec.

This analysis has not taken into account air attenuation and it would be possible to irradiate a smaller area of Melinex, so that a further reduction of count rate by an order of magnitude would be easily possible. Hence this method reduces the count rate to a level which will not be distorted by the electronics. In addition, the low energy spectrum at the tube window can be accurately defined since the correction factors are

Figure 43

Diagram of scattering spectrometer

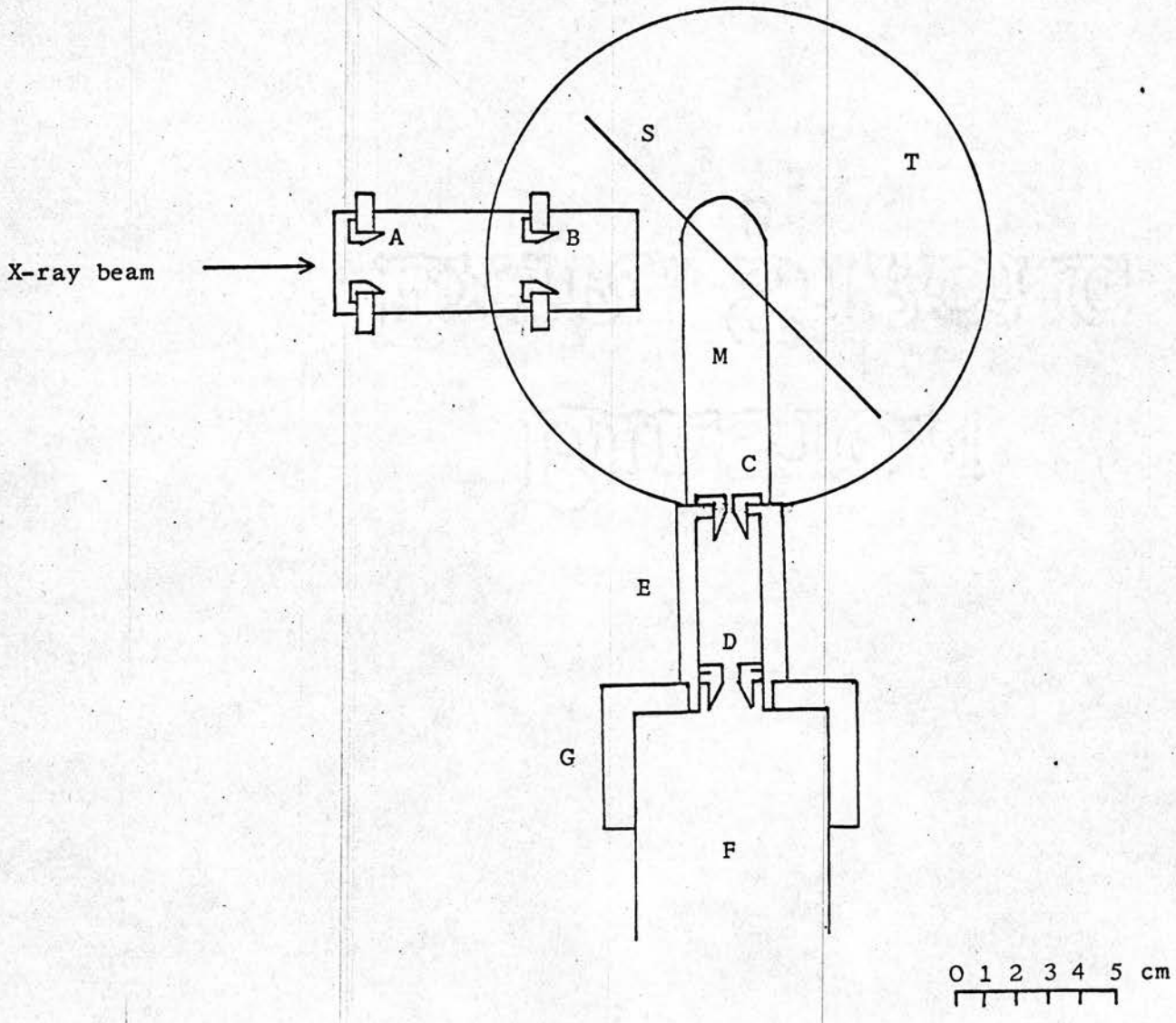

Figure 44

SCATTERING SPECTROMETER ON OPTICAL BENCH

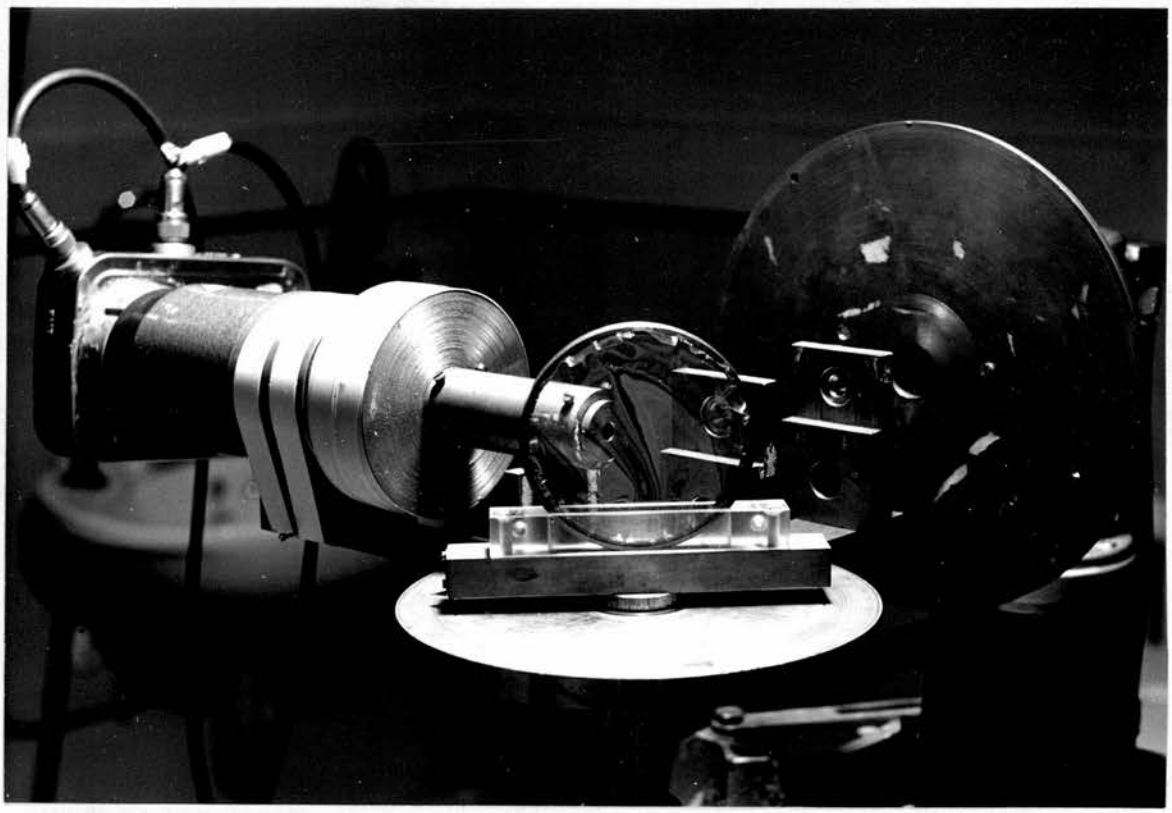

not excessively large.

5.8 Description of Scattering Spectrometer

In designing the scattering spectrometer provision has been made for a full investigation of scattering at various angles and from various materials. The apparatus, which is a modified optical spectrometer of brass construction is shown in Fig. 43. The beam received from the X-ray tube is defined by the apertures A and B. The size and separation of these apertures can be varied to produce beams of various solid angles which strike the scattering material S. For most of the work Melinex film has been used as a scatterer, and this is held under tension in a brass frame 7cm in diameter. The angle of the material to the beam can be varied to produce different effective scattering thicknesses. The scintillation counter F is mounted on a moveable arm M, the angle of which to the primary beam can be read off from graduations around the spectrometer table T. The beam accepted by the detector is defined by the collimator E which consists of a brass tube which holds two apertures C and D. These apertures have been manufactured in various sizes so that the accepted angle can be adjusted so as to include only the irradiated area of the scatterer. The collimator is fixed into a brass shield G which envelopes the front of the detector. Fig. 44 shows the spectrometer positioned in front of the X-ray tube.

5.9 Investigation of the performance of the scattering spectrometer

The optimum operating conditions for the spectrometer have been determined by a large series of experiments. The development of an analogue readout system for the multichannel analyser which gives normalised

smoothed graphs of pulse height distributions enables small changes in these distributions to be detected easily.

It is most important that the collimation system does not introduce any characteristic radiation into the X-ray beam. By using two identical sets of apertures one of brass and the other of lead construction, and utilising the high resolution of the gas proportional counter it has been confirmed that no such radiation is being produced.

By blanking off each aperture in turn, and using extra lead screening it has been shown that only radiation which has passed along the defined path is detected.

Radiation scattered from the air will also be detected. Correction for this can be made by operating the multichannel analyser in the subtract mode with no scatterer present but with the X-ray beam on for a length of time equal to the spectrum accumulation time, although this may over-estimate the correction at low energies since photons scattered from air behind the scatterer position would not be attenuated by the scatterer during the correction process. Since the ratio of the scattering cross-sections for air and Melinex is constant in the energy region 6 - 30keV, air-scattered and Melinex-scattered spectra will have the same shape. If radiation scattered from air behind the Melinex film was attenuated in the Melinex before reaching the detector, the correction for air-scatter would itself be in error, and spectra corrected for air-scatter would differ in shape from uncorrected spectra. For Melinex films of thicknesses from 6.3×10^{-4}cm up to 25×10^{-4}cm no such variation is detected, hence it is concluded that attenuation of scattered radiation in the Melinex is negligible. Similarly radiation scattered from the rear of the scattering film will be negligibly attenuated in the film before detection.

Figure 45

Scattered spectra from various materials

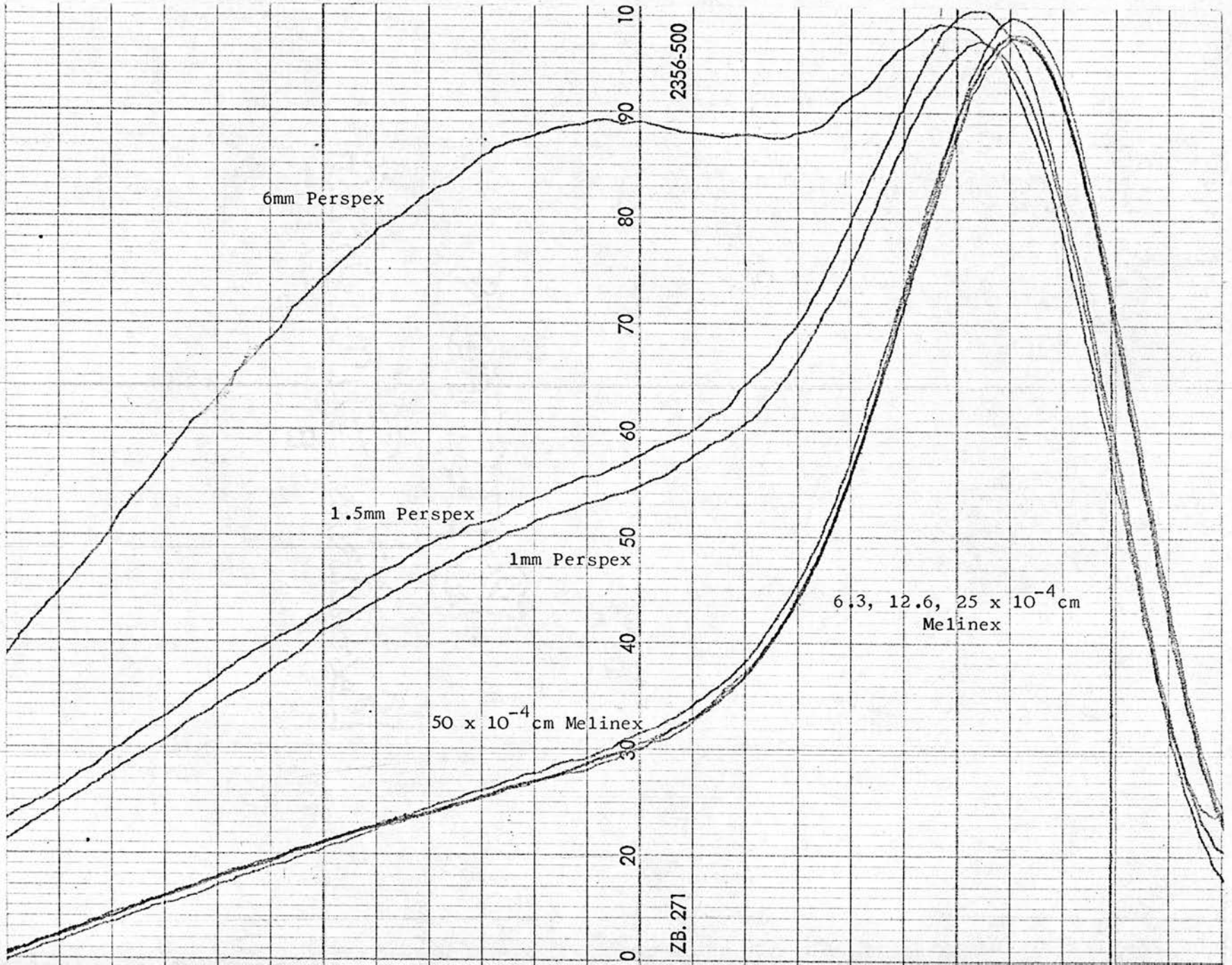

The effect of increasing the thickness of the scatterer has been investigated. Fig. 45 which shows a record obtained from the analogue readout system illustrates this for the 30kV beam. Spectra scattered from Melinex films of thicknesses 6.3, 12.6 and 25 x 10^{-4}cm all give the same normalised pulse height distribution for a given X-ray beam. When the thickness of Melinex is increased to 50 x 10^{-4}cm there is a very slight relative reduction in the distribution at low energies, showing that attenuation in the scatterer is becoming important. This becomes far more pronounced when 1, 1.5 and 6mm perspex sheets are used as scatterers. A similar investigation with the thinnest aluminium foils available showed differences between spectra scattered from foils of thickness 0.002cm and 0.003cm, and these differences must be attributed to attenuation effects. Therefore aluminium has been rejected as a suitable scatterer.

The total count rates due to a 30kV spectrum scattered from Melinex films of thicknesses 6.3, 12.6 and 25 x 10^{-4}cm are in the approximate ratio 1:2:4 when corrected for air scatter and this is in agreement with equation 5.8. Hence for all spectral measurements Melinex films of thickness less than 25 x 10^{-4}cm have been used. These results are described in Chapter 8.

5.10 Summary

Using the spectra obtained by attenuation analysis, it has been shown that very high count rates are to be expected from gas and scintillation detectors. A literature survey has led to criticism of previous pulse height analysis work on beryllium window X-ray tubes. Two acceptable methods have been put forward for determining spectra. The use of the gas

proportional counter with an air path of 100cm has the advantage of requiring the minimum apparatus and corrections, but spectra will be ill-defined below about 8keV due to air attenuation and above about 25keV due to low detector efficiency. A new method of determining the low energy X-ray spectra by scattering has been suggested, and it has been shown that this technique produces count rates which will not be distorted by the electronics. The design and testing of a scattering spectrometer have been discussed and it has been shown that no instrumental effects distort the spectrum. This new method enables spectra of X-ray beams produced at high tube currents to be measured, and because correction factors are small the spectra will be well-defined even at low energies.

CHAPTER 6

CORRECTION FOR DETECTOR RESOLUTION

6.1 Introduction

In pulse height analysis methods several sources of distortion occur, which cause measured pulse height distributions to differ from photon spectra at the X-ray tube window. The discussion in Chapter 5 shows that electronic distortion can be virtually eliminated by suitable experimental design. However other effects, not all of which necessarily cause significant distortion in the present study, cannot be avoided, and necessitate corrections. In order of occurrence these effects are:-

(i) Air attenuation between the tube window and detector.

(ii) Scattering from Melinex (scattering spectrometer measurements only).

(iii) Detector window attenuation.

(iv) Incomplete absorption in the detecting medium.

(v) Detector resolution.

Corrections to the pulse height distributions must be applied in the reverse order to the above. This chapter treats the first correction, that for resolution. The remaining corrections will be discussed in Chapters 7 and 8.

6.2 Formulation of the problem

Due to statistical processes in the detectors used in this investigation, an input of monoenergetic photons gives rise to a Gaussian distribution of pulse heights, called the photopeak (for discussion see Chapter 1 and Appendix 2). Thus there is a probability that a photon of

energy E will produce a pulse corresponding to an energy E'. If G(E',E) is the Gaussian response function defining this probability, the observed pulse height distribution f(E') and the true detected spectrum n(E) are related by the integral equation:

$$f(E') = \int_{E_{min}}^{E_{max}} G(E',E)\, n(E)\, dE \qquad \ldots\ldots\ldots\ldots 6.1$$

Correction for resolution consists of solving this equation for n.

The Gaussian response function for photons of energy E is defined by:

$$G(E',E) = \frac{K}{\sqrt{\pi}} \exp\left[- (E' - E)^2 K^2 \right] \qquad \ldots\ldots\ldots\ldots 6.2$$

where K is a characteristic of the detector related to the experimentally observable full width W(E) at half maximum height of the distribution by:

$$K = \frac{2\sqrt{\ln 2}}{W(E)} \qquad \ldots\ldots\ldots\ldots 6.3$$

Experimentally it is found that W is proportional to E^r where r depends on the detector. Resolution may therefore be expressed as

$$R = W/E = CE^{r-1} \qquad \ldots\ldots\ldots\ldots 6.4$$

and equation 6.3 becomes

$$K = \frac{2\sqrt{\ln 2}}{CE^r} \qquad \ldots\ldots\ldots\ldots 6.5$$

Hence the complete Gaussian probability function is given by:

$$G(E',E) = \frac{2\sqrt{\ln 2}}{\sqrt{\pi}\ CE^r} \exp\left[- (E' - E)^2 \frac{4 \ln 2}{C^2 E^{2r}} \right] \qquad \ldots\ldots\ldots\ldots 6.6$$

and by defining C and r from the experimental resolution calibration, the detector response to photons of any energy can be calculated.

Since multichannel analysers give data output in digital form it is convenient to express equation 6.1 in matrix notation so that corrections can easily be made. Consider an analyser with u channels, each of energy width ε, corresponding to energies $E_1 \pm \varepsilon/2$ up to $E_u \pm \varepsilon/2$. Then by analogy with equation 6.1,

$$\underline{f} = H\underline{n} \qquad \ldots\ldots\ldots 6.7$$

where $\underline{f}$ and $\underline{n}$ are u x 1 column vectors and H is the u x u response matrix. The j^{th} column of H therefore represents the response of the detector to photons of energies $E_j \pm \varepsilon/2$, and the element H_{ij} is given by:-

$$H_{ij} = \frac{2\sqrt{\ln 2}}{\sqrt{\pi}\, CE_j^{\,r}} \exp\left[-(E_i - E_j)^2 \frac{4 \ln 2}{C^2 E_j^{2r}} \right] . \varepsilon \qquad \ldots\ldots\ldots 6.8$$

This method of presentation has been adopted by Skarsgard et al. (1961), and the validity of the matrix notation has been investigated by Rand (1962).

6.3 Survey of suggested methods of resolution correction

Several methods have been suggested for the solution of equations 6.1 or 6.7 and these will be described briefly here. Discussion of the methods will follow in the literature survey (section 6.4).

6.3.1 Numerical integration

This method, first suggested in this context by Liden and Starfelt (1954), attempts to solve equation 6.1 by taking an estimate of n(E) as a starting point. This is then operated on by the Gaussian for a fixed value of E', and integration of the curve produced gives a single point on f(E'). In this way the curve f(E') is built up and can be compared with the measured distribution. An iterative method can then be used to suggest a better estimate of n(E) and the method is continued until the

calculated f(E) agrees with the experimental values. Then the estimated n(E) must be the true spectrum.

6.3.2 Matrix Inversion

Provided the response matrix H in equation 6.7 is non-singular, the solution is clearly:-

$$\underline{n} = H^{-1} \underline{f} \quad \ldots\ldots \quad 6.9$$

The inverse matrix H^{-1} can be calculated using a digital computer.

6.3.3 Matrix Iteration

Iterative methods of solving equation 6.7 avoid inversion of H. They are similar in application to numerical integration, but more easily programmed for computers. Successive approximations to $\underline{n}$ are chosen, such that

$$\underline{n}_p = \underline{n}_{p-1} + (e\, H\underline{n} - e\, H\underline{n}_{p-1}) \quad \ldots\ldots 6.10$$

where $H\underline{n}_{p-1}$ is the pulse height distribution as calculated from the previous approximation to the true spectrum, and $H\underline{n}$ is the observed pulse height distribution. The scalar e is often taken as unity.

6.3.4 Numerical Analysis

If the observed distribution f can be obtained in analytical form Dixon and Aitken (1958) have shown that the solution to equation 6.1 is:-

$$n(E) = \sum_{m=0}^{\infty} \frac{(kE)^m (-1)^m}{2^m\, m!} \left\{ f^{(2m)}(E) - k f^{(2m+1)}(E) \right\} \quad \ldots\ldots 6.11$$

where $k = \frac{c^2}{8 \ln 2}$ (see equation 6.4). This solution assumes that resolution can be expressed by $R = CE^{-1/2}$, which is usually the case, to a reasonable approximation, with the types of detector used in this study.

6.4 Literature Survey

Dixon and Aitken (1958) in an important paper have described the limitations of most of the methods described in 6.3. They show that numerical integration and matrix iteration can suffer from non-convergence and pseudosolutions, and point out that trial solutions must be restricted by a condition of smoothness. This makes it most important that the effect of characteristic radiation is subtracted before the resolution correction, a fact which only Epp and Weiss (1966) seem to have appreciated. Since numerical integration is also extremely tedious in use and not so easily adapted to computer solution, it has been rejected for use in the present study.

Dixon and Aitken also point out that matrix inversion must not be used unless it can be demonstrated that the determinant of the response matrix is non-zero, i.e. no columns of the response matrix are identical, or nearly so. This requires the matrix channel width to be comparable with the photopeak width (i.e. $\sim$ 5keV for low energy photons detected by a scintillation counter). Since the channel width of the multichannel analyser is about 0.3keV in the present study, the use of matrix inversion requires the summing of about 15 channels, with a corresponding loss of detail. However the method is useful for the correction of the high energy end of the spectrum where little detail is required. Ehrlich (1955) used this method with a channel width of about 5keV to correct 50kV spectra from a beryllium window tube. She was, however, unable to correct information below about 13keV.

Wang et al (1956) in their study of beryllium window X-ray tube spectra used numerical integration to correct their results, but give no details. They do not publish any corrected unfiltered spectra,

and it seems unlikely that their correction method would work with a large proportion of characteristic radiation in the beam. There do not appear to be any other pulse height analysis studies of spectra from beryllium window tubes.

For spectra with higher filtration, iterative methods have found the most use. The approach of Skarsgard et al (1961) appears most valid since they have used a stopping criterion for the iterative process which depends on the statistical accuracy of the data. The method of Hettinger and Starfelt (1958) where data is smoothed by hand between each iteration seems rather subjective. Almost all published studies have used a matrix channel width of 5 - 10keV (e.g. Peaple and Burt, 1968; Cormack and Burke, 1960) since small widths tend to produce oscillations in the solution (discussed by Burrus, 1960, and Rand, 1962).

The method of Dixon and Aitken does not appear to have been used by any others. However, it has the advantage of using all the data in fitting a smooth function f(E) to all the experimental points, and this can easily be done using readily available computer routines. We will show later that this allows spectra to be corrected at lower energies than has previously been possible.

In view of the lack of guidance available, three computer programmes have been written in Atlas Autocode and tested on an English Electric KDF 9 computer. These programmes use the methods of matrix inversion, iteration, and numerical analysis. It is clearly desirable to use the smallest channel width possible to correct experimental data, and ideally the same channel width should be used as that in which the data was collected. Consequently the programmes have all been designed

to allow the effect of variable channel width to be investigated. This enables the validity of the corrections to be checked by comparing two solutions with similar channel widths so that pseudosolutions can be eliminated.

6.5 Descriptions of computer programmes for resolution correction

6.5.1 Matrix Inversion

The programme can be divided into four distinct routines:-

(i) Energy calibration,
(ii) Response matrix generation,
(iii) Matrix inversion,
(iv) Graphical display.

Energy data consisting of points picked at 1keV intervals from the graph of channel versus energy are fed into the computer. The calibration routine linearly interpolates between these points to calculate the energy corresponding to each analyser channel. The response matrix H is calculated using equation 6.8 and values of C and n defined by experiment. The inverse matrix H^{-1} is calculated using a sub-routine which is available in the computer compiler and has been tested on a wide variety of matrices. The product $H^{-1}\,\underline{f}$ (see equation 6.9) is displayed graphically and numerically. Larger channel widths can be formed by adding any number of adjacent rows and columns of the matrices, and the inversion and display routines can be used to find the minimum channel width which gives a true solution, i.e. a solution which does not tend to oscillate when channel width is slightly increased or decreased.

Dixon and Aitken have pointed out that if the determinant of the response matrix is very small, the inverse matrix is unlikely to exist.

Figure 46

25kV spectrum corrected by matrix inversion

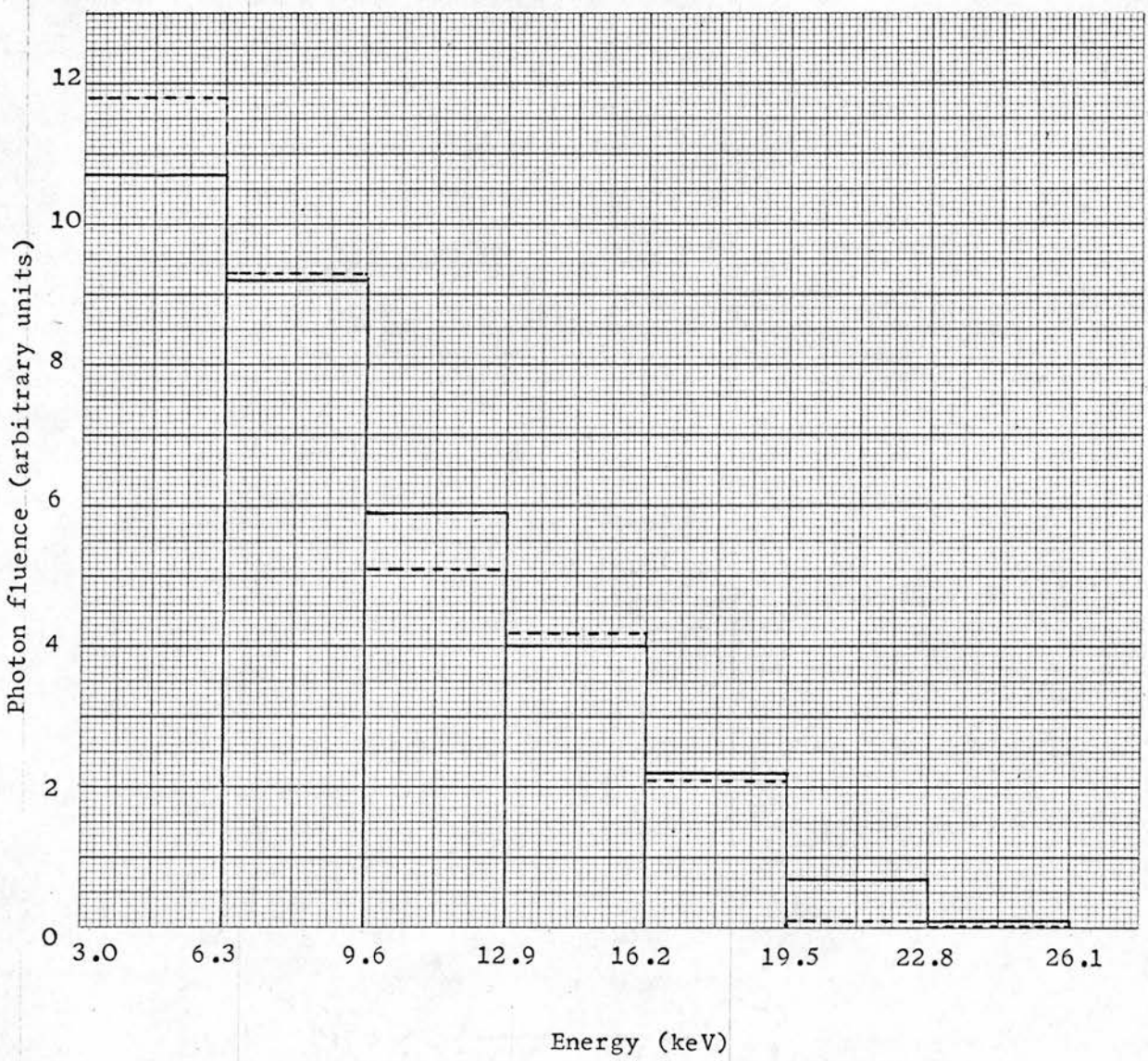

In the present study, the determinant of a 35 x 35 scintillation counter response matrix with a channel width of 0.7keV is less than 10^{-40} so that it appears impossible to use such a narrow channel. When, however, the matrix is reduced to 7 x 7, of channel width 3.5keV, the determinant is about 10^{4} and the inverse matrix is easily calculated. Fig. 46 shows the raw and corrected data for a 25kV spectrum treated in this way. The sharpening of the high energy end of the spectrum is apparent, but it can also be seen that the method is incapable of producing detail at low energies unless a smaller channel width can be used. Attempts have been made to improve the accuracy of the inversion process by methods suggested by Faddeeva (1959) but without success, and it appears that a channel width of about 3.5keV is the minimum which can be used for the response matrix of the scintillation counter used in this study.

6.5.2 Iteration

A programme which follows the approach of Skarsgard et al. (1961) has been written. This corrects data by the use of equation 6.10. However, non-convergence and oscillation occur when the channel width is less than about 5keV. Faddeeva (1959) has described improvements which increase the rate of convergence of the iterative process and remove rounding errors, and these have been written into the programme, but it is still not possible to use a smaller channel width. The method therefore has no advantage over matrix inversion and uses more computer time, so has not been used to correct final results.

6.5.3 Numerical Analysis

I am very grateful to Mr. H. M. Moores of the Edinburgh Regional Computer Centre for his assistance in writing and testing a programme which

Figure 47

15kV spectrum corrected by numerical analysis

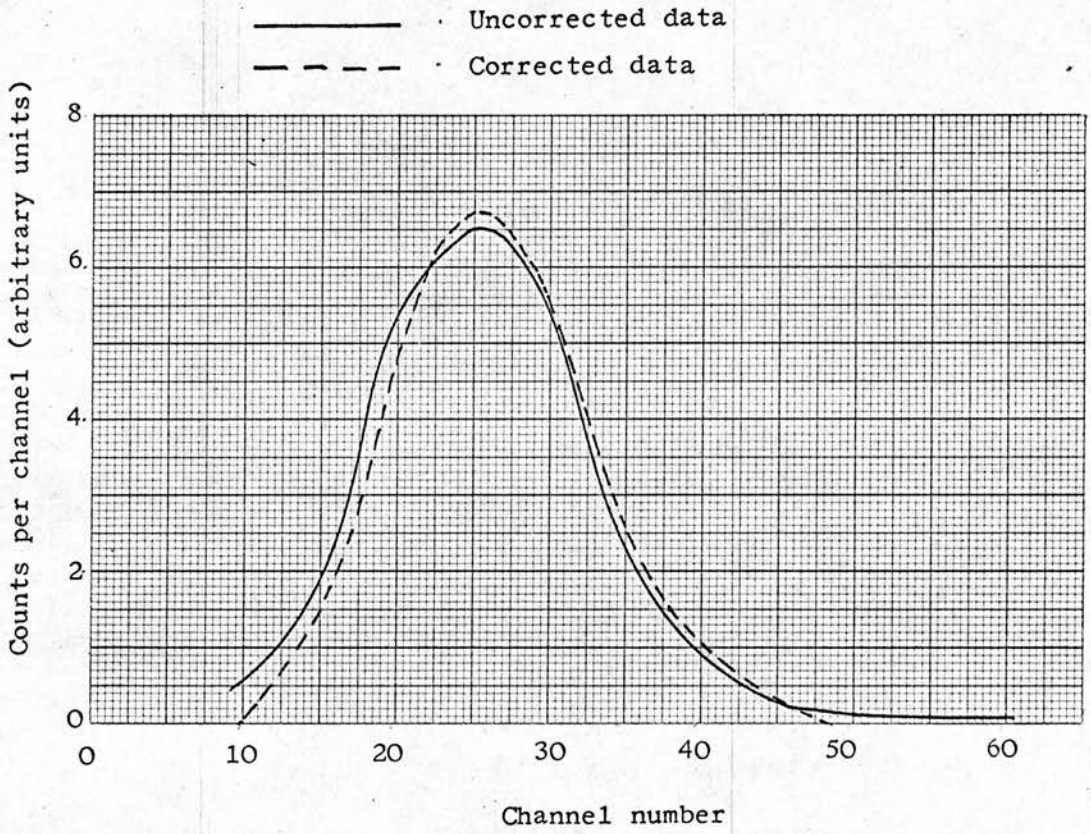

corrects pulse height distributions by Dixon and Aitken's numerical analysis method (equation 6.11). The programme undertakes the energy calibration by the same routine used in the inversion programme. A polynomial is then fitted to f(E) and derivatives are easily found thus enabling n(E) to be calculated. Provided that characteristic radiation is subtracted before undertaking the correction, a fourth power polynomial will usually fit the data well. Fig. 47 shows the effect of the correction on a 15kV spectrum obtained using the proportional counter. The long tail of pulses at high energies is eliminated, and the low energy side of the spectrum is considerably sharpened, whilst, as might be expected, the peak is not appreciably shifted.

This programme has been used to correct all the proportional counter results. In treating scintillation counter results the low energy side of the spectra is corrected well and the peak is not shifted but convergence does not occur at the high energy side. This may be due to statistical uncertainties in the data in this region, or to the approximation in equation 6.11 that resolution is proportional to $E^{-1/2}$. However, since this non-convergence only affects the last 2 - 3keV of the distributions where the photon flux is a very small percentage of the total flux, no significant error is introduced by using the results of matrix inversion to give smooth distributions with a sharp high energy cut-off.

6.6 Conclusion

Four methods for making resolution corrections have been discussed and criticised. Most previous work has required the use of large channel widths to ensure convergence and non-oscillation. Such an approach does

not make best use of the resolving potential of multichannel analysers, and does not enable the low energy side of a spectrum to be corrected. A computer programme using the method of Dixon and Aitken (1958) has been written and enables spectra measured by the proportional counter to be corrected with no loss of detail. Spectra from the scintillation counter require the use of a matrix inversion programme to correct for resolution at high energies, but at low energies numerical analysis yields the solution.

Methods developed here enable spectra to be defined at lower energies than have previously been possible. Corrected results will be described in Chapters 7 and 8.

CHAPTER 7

MEASUREMENTS OF X-RAY SPECTRA USING THE PROPORTIONAL COUNTER

7.1 Introduction

In this chapter, measurements of the spectra of X-ray beams produced at potentials between 15 and 30kV are described. Resolution corrections are made by the numerical analysis method, and corrections for counter efficiency and air attenuation are then applied. A new experimental technique to estimate the proportion of characteristic radiation in the X-ray beams is described.

7.2 Detection System

The operation of gas proportional counters has been discussed in Chapter 1. The counter chosen for this study is of the gas flow type with side entrance and exit windows[1]. The windows are aluminised Melinex of thickness 6.3×10^{-4}cm and diameter 1.9cm. Dried argon-methane gas (90% argon, 10% methane) flows at about 25cc/min at atmospheric pressure. Output pulses are fed into a Dynatron pulse amplifier system, type 1430A, which incorporates a high impedance head amplifier and non-overloading main amplifier, giving positive going pulses over a range 0-10V peak. These pulses are then sorted by a 100 channel pulse height analyser[2]. E.H.T. supplies from a Dynatron 1082B power unit are monitored potentiometrically to ensure a stability of better than $\pm$ 0.1%. The linearity and stability of the system have

---

1. Telsec Instruments, type FA 3223 E.
2. T.M.C. Gammascope, Model 101.

Figure 48

Energy and resolution calibration of gas proportional counter

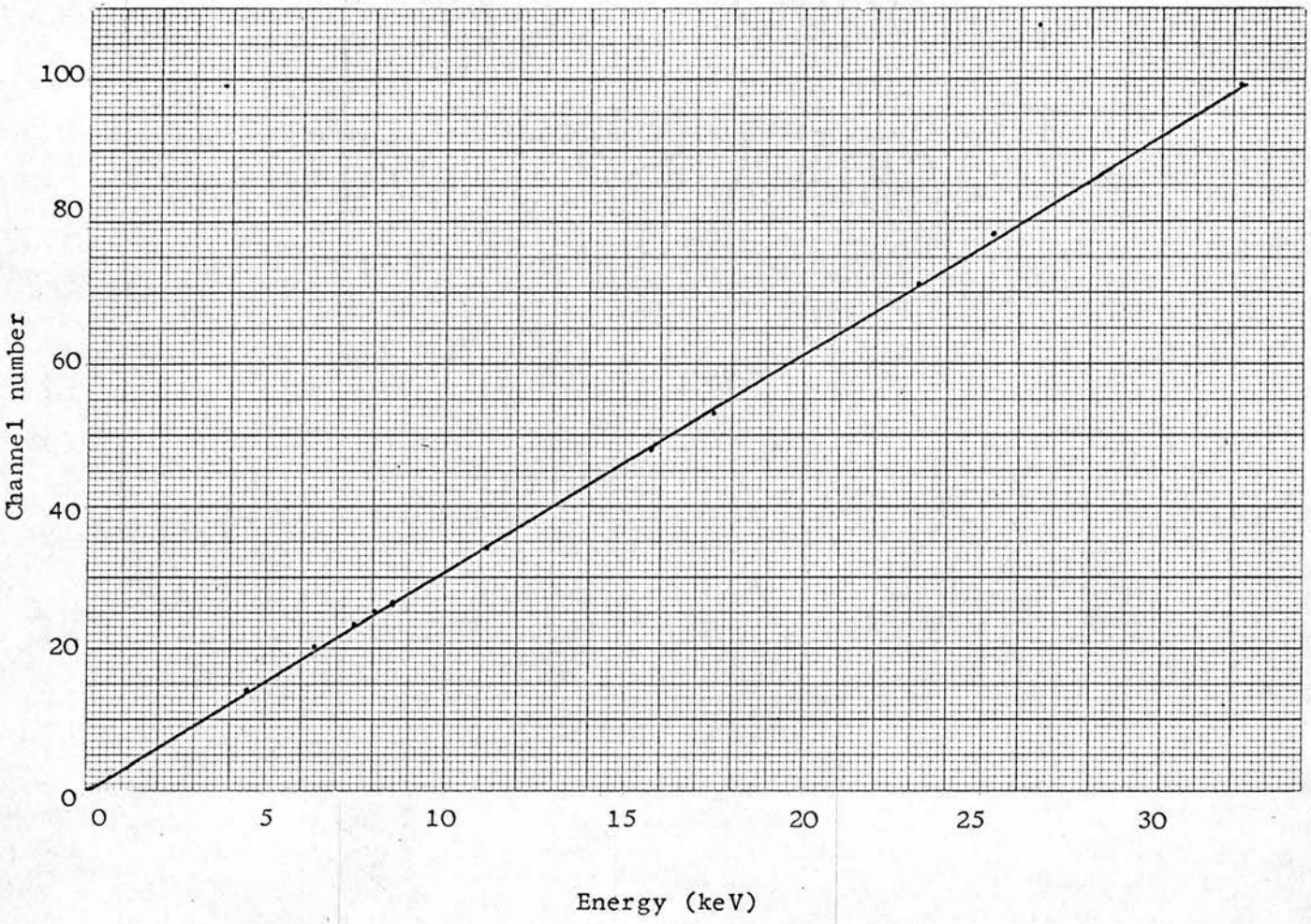

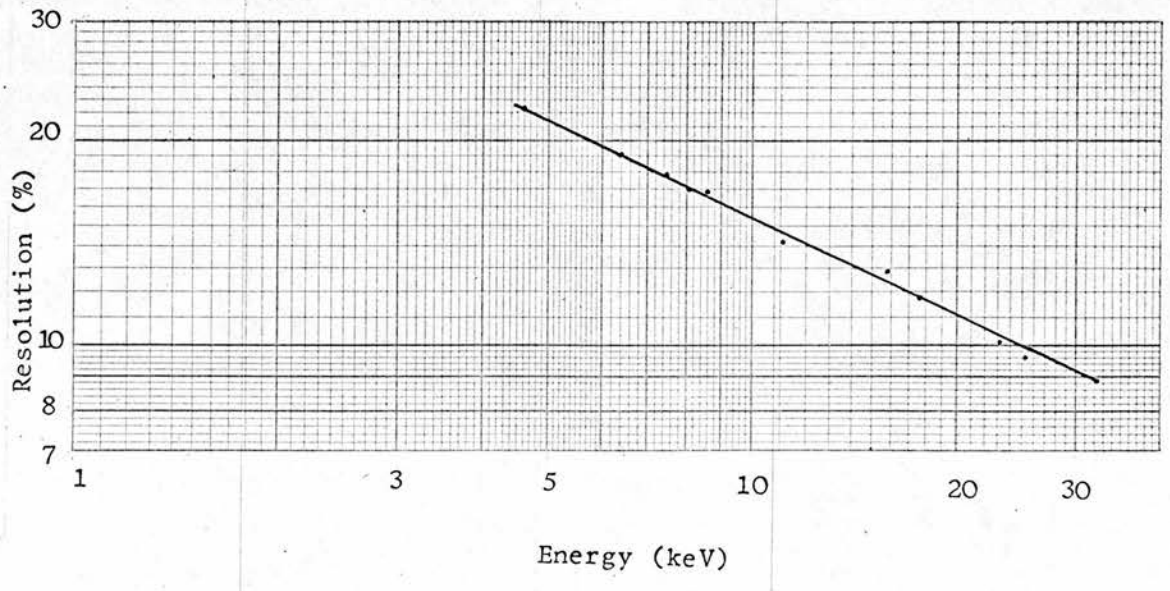

been checked using a pulse generator.

7.3 Experimental situation

The detector is operated with an air path of 100cm. The beam is defined by a collimator identical to that described in 5.8. An aperture of area $1.0 \times 10^{-3} cm^2$ immediately in front of the entrance window limits the flux received. The second aperture of diameter 0.16cm limits the amount of scattered radiation which can be received, but is sufficiently large to ensure that the total target is being viewed. The exit window is screened with aluminium to prevent the detection of scattered radiation. Investigation has shown that this does not distort the detected spectrum.

7.4 Calibration

Calibration is carried out using the fluorescent sources as described in 5.3. The low intensity of the characteristic radiation results in inconveniently long collection times if calibration is carried out under the same experimental conditions as those used for beam measurement. In addition the 100cm air path increases the relative intensity of the K_β radiation, causing greater line broadening. Experiment has shown that larger beams can be accepted without loss of resolution provided they do not impinge on the counter walls, and so calibration is carried out closer to the fluorescent sources using apertures of 0.16cm and 0.32cm in the collimator. The resultant photopeaks are analysed by Zimmerman's method and corrected for the slight broadening and peak shift caused by K_β radiation (see 5.3). Fig. 48 shows the corrected pulse height and resolution calibration curves for the proportional counter for gain

conditions chosen to give optimum resolution and a convenient energy scale. The sources used for this calibration are listed in Table 39.

Table 39

Sources of Characteristic Radiation used for Calibration

Element	K_α Energy (keV)	Form
Ti	4.51	Pure element, sheet
Fe	6.40	Pure element, sheet
Ni	7.48	Pure element, sheet
Cu	8.05	Pure element, sheet
Zn	8.64	Pure element, sheet
Se	11.2	Pure element, powder
Zr	15.8	Pure element, sheet
Mo	17.5	Pure element, sheet
Cd	23.2	Pure element, sheet
Sn	25.3	Pure element, sheet
Ba	32.2	$BaCO_3$, powder

When the material is only available in powder form, several methods of preparation of sources have been tested. The least background scatter is produced if the powder is enclosed between 6×10^{-4} cm Melinex sheets in a shallow perspex annulus.

The experimental results for percentage resolution, R, can be fitted by the expression $R = CE^{r-1}$ with $C = 49.2$ and $r = 0.51$.

7.5 Quantum Efficiency of the Detector

Photons incident on the detector window can remain wholly or partially undetected due to four effects:-

a) Attenuation in the Melinex entrance window

b) Transmission through the gas

Figure 49

Quantum counting efficiency of proportional counter

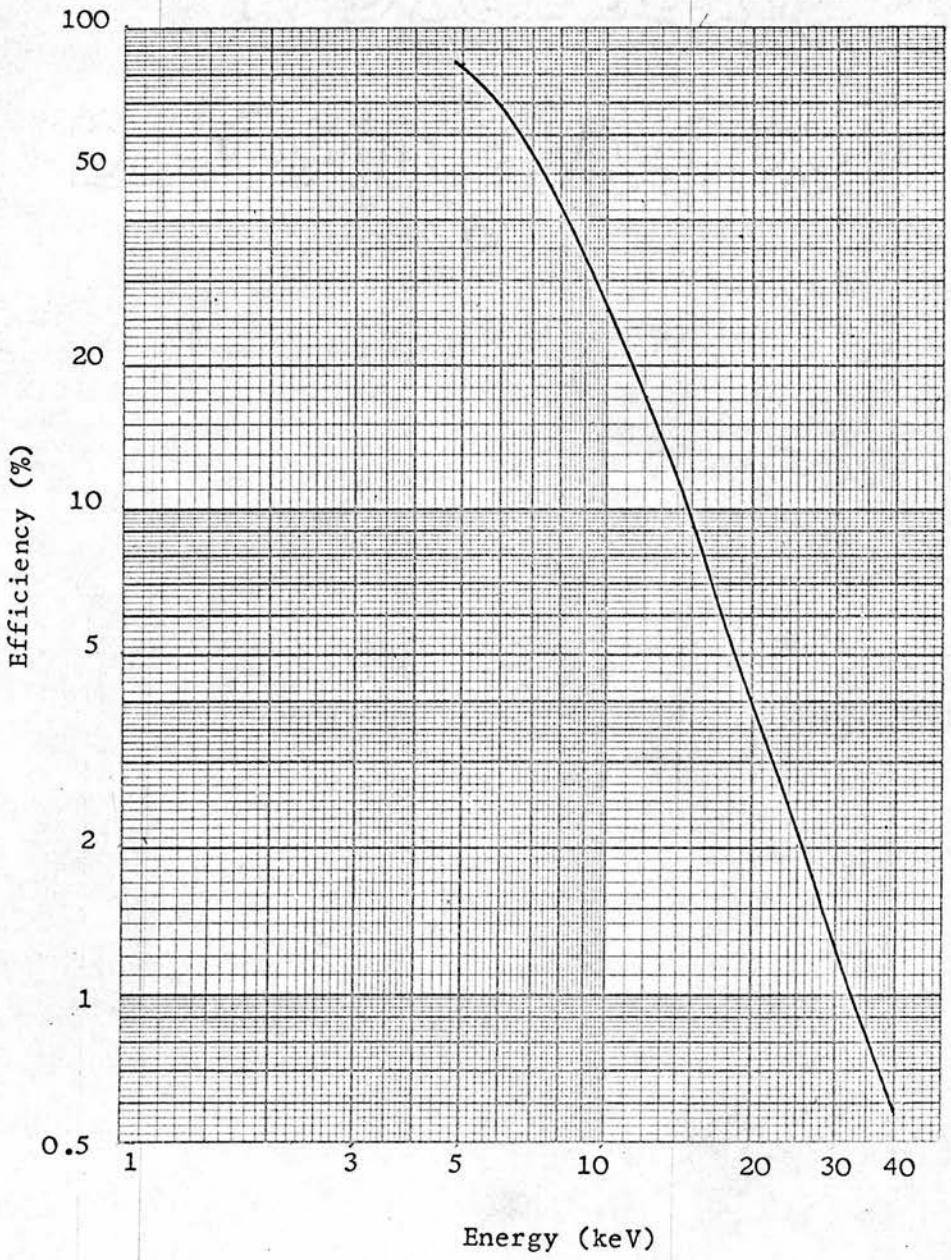

c) Backscatter from the gas

d) Escape of argon fluorescent radiation.

Backscatter calculations similar to those described in Appendix 1 show that less than 1% of 4 - 30keV photons will be lost in this way. This correction has been neglected. The escape of argon K-characteristic photons results in pulses being produced which correspond to energies 3.2keV less than that of the incident photons. The K fluorescent yield of argon is less than 0.10, so that this effect produces only slight distortion of the continuous distributions. Such distortion would be most noticeable at low energies. However, due to the large air path, measured distributions are ill-defined at low energies, so that no further loss of accuracy will be introduced by neglecting the argon escape correction.

This method of approach, by neglecting backscatter and escape, has been adopted by Taylor and Parrish (1955) who have calculated the quantum efficiency of various detectors. They define quantum efficiency Q by:-

$$Q = f_W f_A \qquad \ldots\ldots\ 7.1$$

where f_W is the fraction of radiation transmitted through the window and f_A is the fraction absorbed by the argon. Using this definition the quantum efficiency of the detector has been calculated for a gas pressure of 76cm Hg and temperature of 20°C. This is shown in Fig. 49. Attenuation coefficients for argon from McMaster et al., (1967) and Melinex from Fig. 41 have been used. The attenuation of the aluminium coating on the Melinex is negligible for energies above 5keV (Heroux et al., 1962). Some verification of the efficiency curve has been obtained

experimentally, by measuring the transmission of characteristic radiation through the proportional counter. The total absorption ionization chamber (described in Chapter 4) has been used as a detector of the transmitted beams. Owing to the need to use a narrow radiation beam, giving low intensity, measurements have a rather large experimental uncertainty and cannot be made at energies where the proportional counter absorption is very high or very low. However, experimentally determined efficiencies of 58% at 6.4keV and 43% at 8.1keV agree within experimental error with the calculated values of 61% and 42% respectively.

7.6 Air Attenuation

Correction for attenuation due to the 100cm air path is made using attenuation coefficients for air tabulated by McGinnies, (1959).

7.7 Estimation of proportion of Tungsten L radiation

It has been noted in Chapter 6 that the contribution of characteristic radiation must be subtracted from pulse height distributions before the correction for detector broadening can be made. To do this, the detector response to the characteristic radiation must be known. Previous studies involving the subtraction of characteristic radiation from a continuous distribution (e.g. Epp and Weiss, 1966; Tothill, 1964) have relied on graphical methods, subtracting manually various proportions of characteristic radiation and searching for a smooth continuum. Such methods however usually need to use theoretical values of the relative line intensities to calculate the detector response. In addition the methods are tedious and may be rather subjective.

In the present study, by using the source of tungsten characteristic

Figure 50

Estimation of proportion of characteristic radiation in 30kV beam

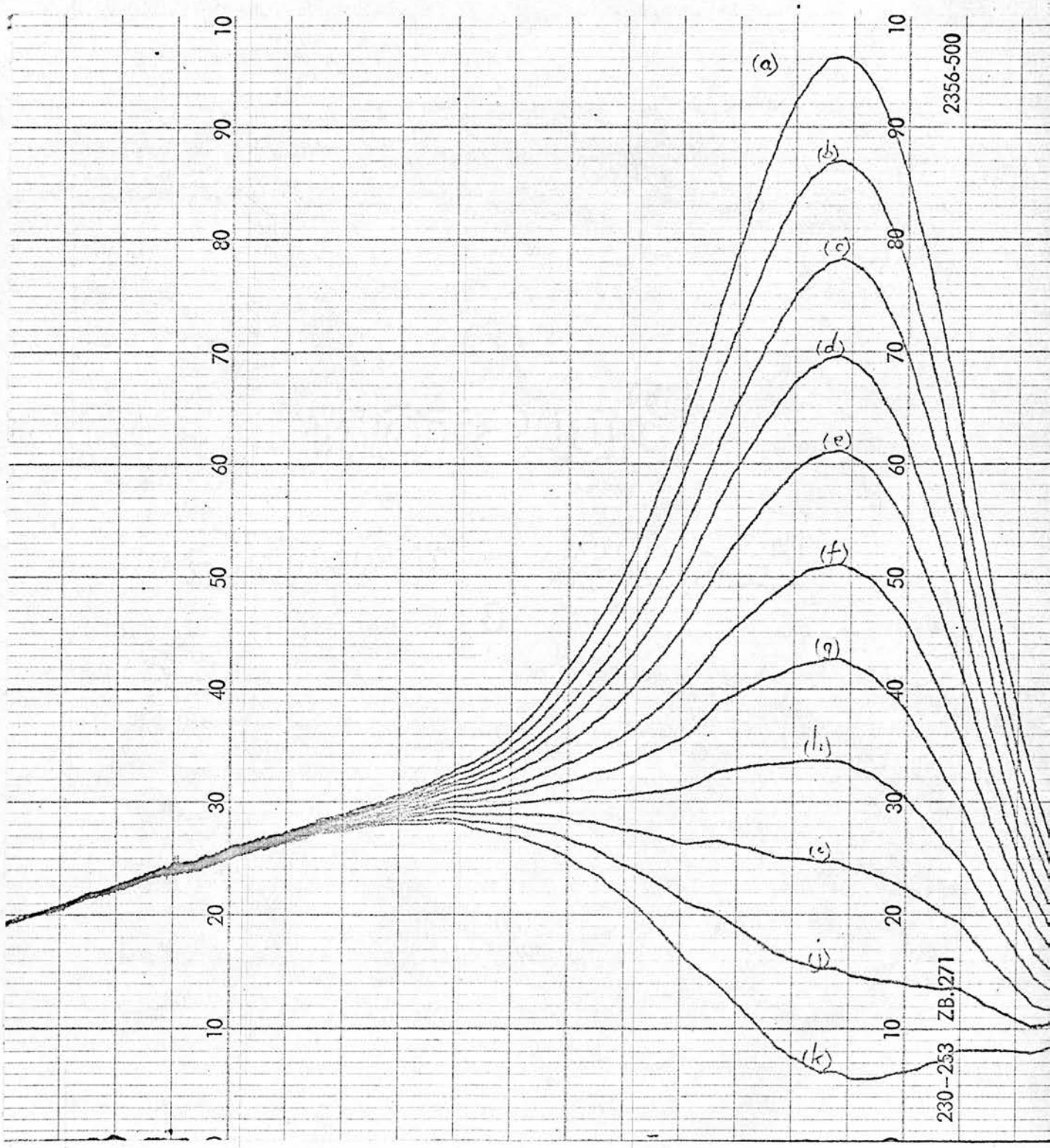

Count rate (arbitrary units)

← Pulse height

radiation, subtractions have been made experimentally using the subtract mode on the pulse height analyser. It is important that the relative intensities of the L_α, β and γ components are the same for the accumulation and subtraction processes. Since excitation of this radiation is by electrons in the first process and photons in the second, this condition is difficult to fully satisfy. However, in the subtraction process the relative intensities can be adjusted to some extent by varying the kilovoltage of the exciting beam and adjusting the air path. The optimum conditions can be found by utilising the good resolution of the proportional counter, and aiming to achieve as smooth a final distribution as possible. The method is equally useful for scintillation and proportional counter measurements.

An illustration of the subtraction method is shown in Fig. 50, which is a reproduction of an experimental record. Curve (a) is the pulse height distribution due to a 30kV X-ray beam. A sheet of tungsten placed in the box described in Chapter 3 is then used to provide a source of characteristic radiation. With the pulse height analyser in the subtract mode, various proportions of this radiation are subtracted from curve (a) to give the distributions (b), (c), ... (k). The smooth continuum occurs in the region of (h), (i) or (j). The need for some estimate of the shape of the continuum, if subjectivity is to be avoided, can be seen. Such an estimate can be provided from the results of the attenuation analysis work, when suitable corrections for air attenuation and detector efficiency are made.

The spectra illustrated were measured with a scintillation counter

Figure 51

Subtaction of characteristic radiation from 25kV distribution

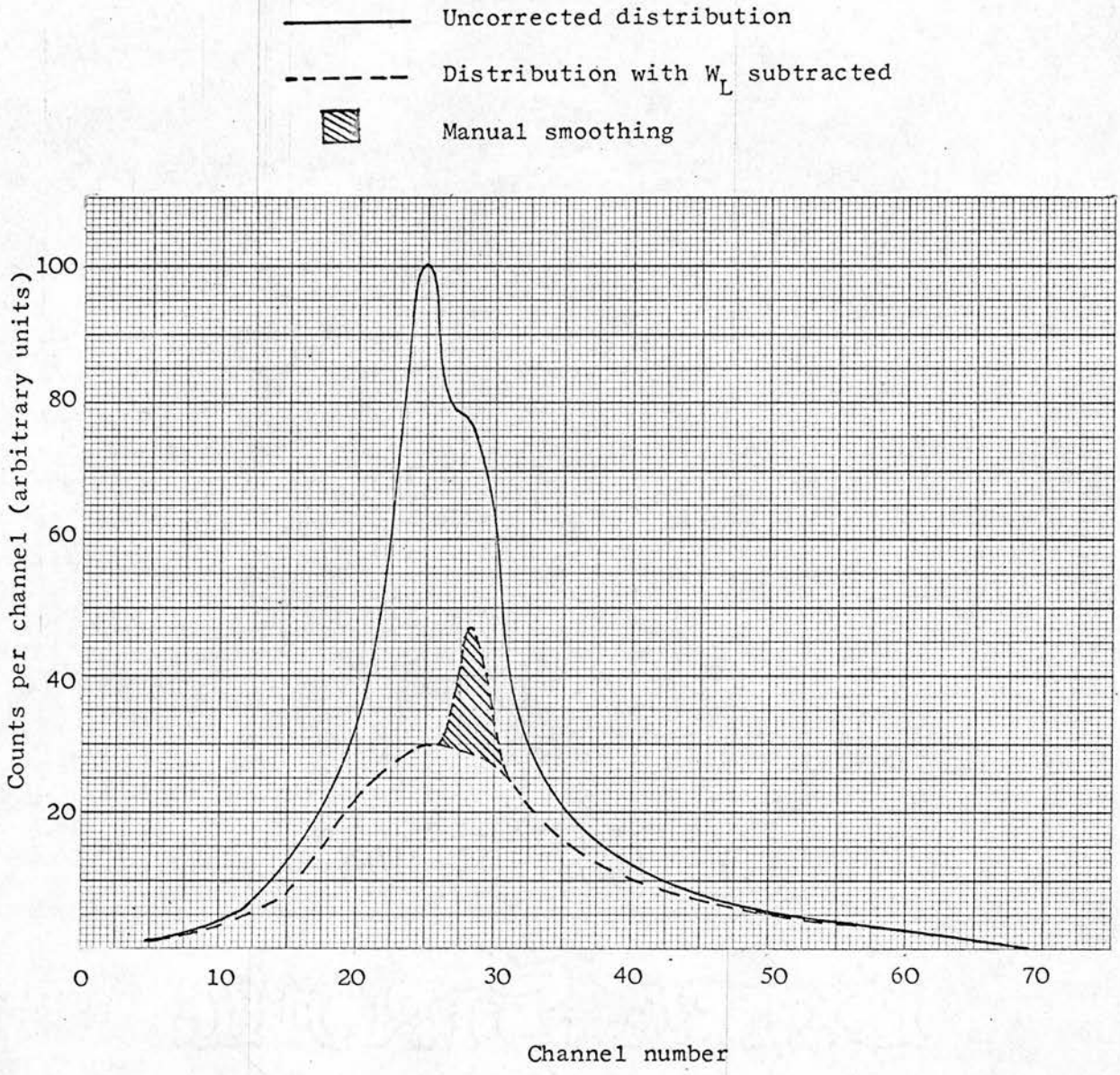

since the experimental record is clearer and the correction process essentially the same for both types of detector. The better resolution of the proportional counter shows up any slight discrepancies in the relative intensities of the characteristic lines between the accumulation and subtraction processes, and a small amount of smoothing by hand is necessary on the 20, 25 and 30kV distributions to correct for this. However at least 90% of the subtracted counts can first be removed experimentally, so that the continuum is well defined before manual smoothing. Fig. 51 illustrates this for the 25kV results.

After tungsten L radiation has been subtracted experimentally, the shaded peak stands out clearly from the otherwise smooth distribution. This is due to the difficulty in obtaining the correct relative intensities for the L_α and β lines. The peak is removed by choosing a smooth curve by eye to fit the shape of the continuum. It is clear that the uncertainty introduced by this smoothing is very slight.

The use of the experimental subtraction method, which does not appear to have been reported previously, allows a more full investigation of the proportion of characteristic radiation in X-ray beams to be made than would be feasible by graphical methods.

7.8 Corrected spectral distributions

Pulse height distributions due to X-ray beams produced at 15, 20, 25 and 30kV have been measured. Tungsten L radiation has been subtracted as described in 7.7. Correction for detector broadening is made by the method of numerical analysis described in Chapter 6. When corrections for detector efficiency and air attenuation have been made, the results represent the continuous distributions at the X-ray tube

Figure 52

30, 25, 20 and 15kV Intensity distributions

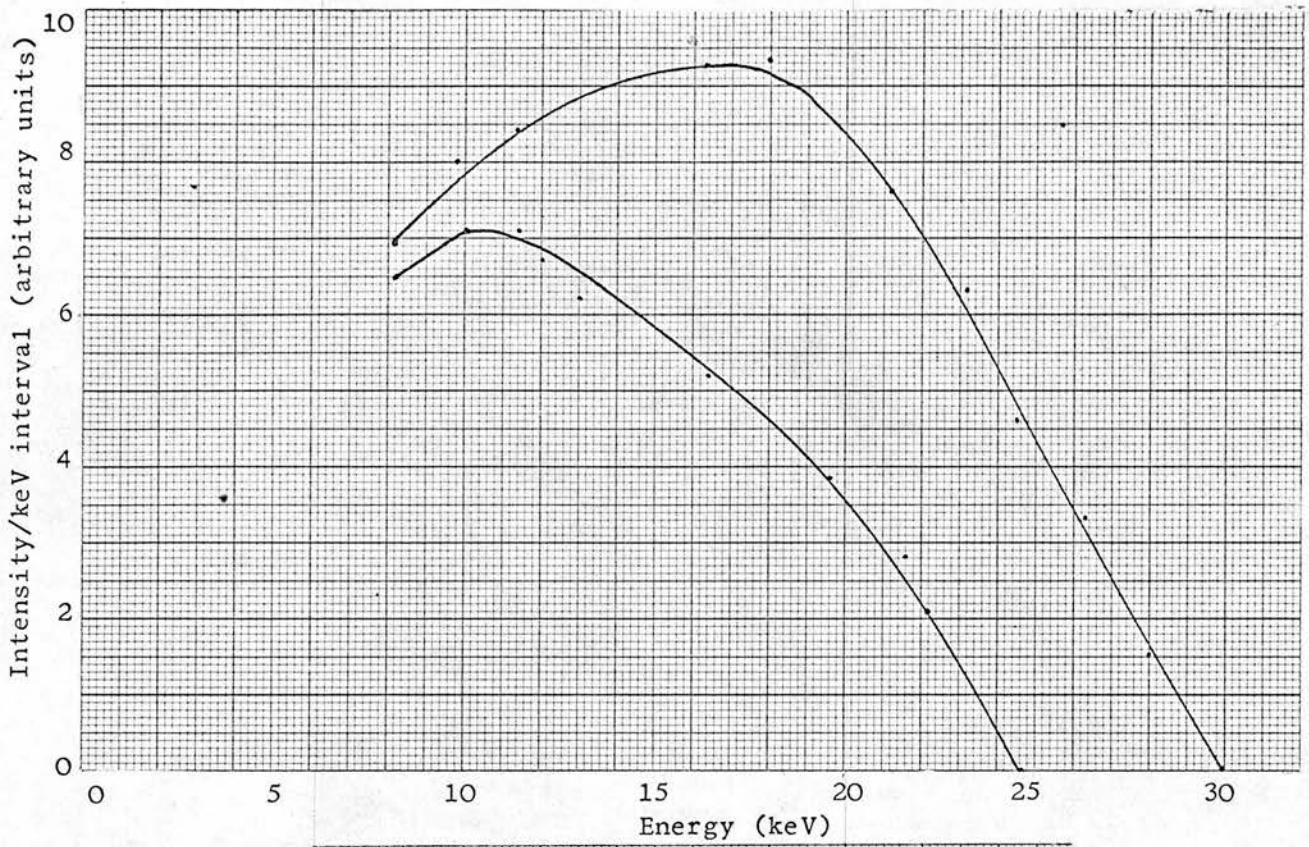

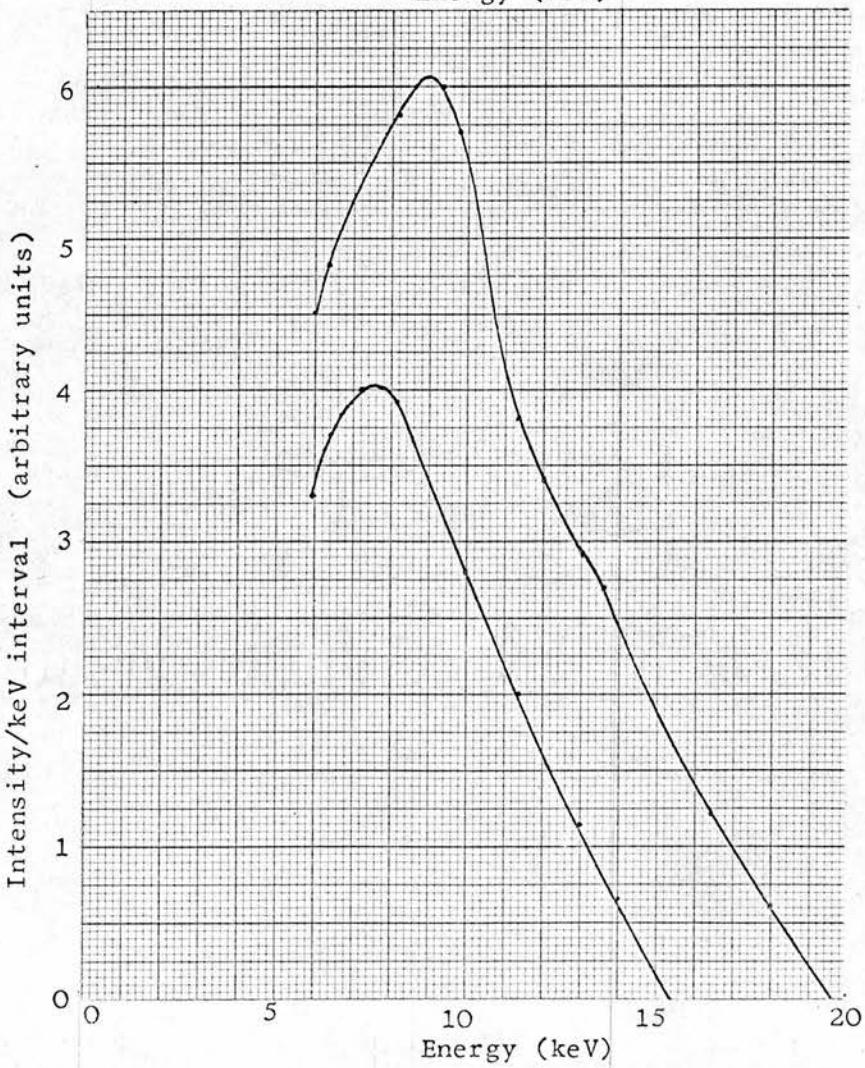

window. These are shown as intensity distributions in Fig. 52. They are defined down to energies of about 8keV, a considerable improvement in low energy definition over any previously published pulse height analysis studies. Below 8keV, the spectra are uncertain due to the large amount of air attenuation.

From a knowledge of the number of characteristic photons subtracted from each distribution to give the smooth continuum, the percentage of the total energy fluence at the tube window which is due to characteristic radiation can also be calculated. This is shown for each measured beam in Table 40.

Table 40

Percentage of total energy fluence due to characteristic radiation

Beam (kV)	Characteristic Radiation (% total energy fluence)
30	35
25	35
20	21
15	17

Corrections to the characteristic radiation are rather large, and the results shown in Table 40 have an uncertainty of about $\pm$ 20%. In Chapter 9, the spectra obtained in this chapter will be compared with experimental spectra determined by attenuation analysis (Chapter 4) and scattering spectrometry (to be described in Chapter 8). Comparisons will also be made with theoretical spectra (Chapter 2) and the results of other workers.

7.9 Summary

A measurement system using a gas flow proportional counter has been described. This system views the whole target and allows quite large (5 - 10mA) tube currents to be used, thus avoiding sources of error noted in previous studies (see 5.5.2). Calculations of counter efficiency and air attenuation have been made.

An experimental method of stripping the tungsten characteristic radiation has been developed, which is more direct than graphical methods used by previous workers. The importance of using estimates of the continuous distributions has been noted, and the results of Chapter 4 have been used for this purpose. By using these estimates as a guide, reproducible smooth pulse height distributions can be obtained. Distributions corrected for resolution, detector efficiency and air attenuation have been plotted in Fig. 52 as energy spectra, the most generally useful form of display. The percentage of the total energy fluence due to characteristic radiation has been tabulated.

The definition of the spectra presented here is considerably better at low energies than that achieved in previous pulse-height analysis studies. The measurements of the proportion of characteristic radiation by a new experimental method give further information which has not previously been available.

CHAPTER 8

MEASUREMENTS OF X-RAY BEAMS BY SCATTERING SPECTROMETRY

8.1 Introduction

Measurements made with the scattering spectrometer (Chapter 5) are described in this chapter. Resolution corrections by the methods developed in Chapter 6 are made, and further corrections are discussed and applied. The proportion of tungsten L radiation in the X-ray beams is estimated by the experimental method used in Chapter 7.

8.2 Detection system

In Appendix 2 the factors governing scintillation counter resolution have been discussed. A commercially available sodium iodide-photomultiplier assembly[1] has been modified[2] to incorporate improvements suggested in this appendix, and the resultant system has very good resolution. The 1" diameter by 3mm deep crystal, specially selected to give optimum resolution at low energies, is placed directly on to the face of a 2" diameter photomultiplier tube, thus reducing statistical broadening due to optical coupling losses and photocathode non-uniformity. The photomultiplier has been selected for high sensitivity and low noise current and permits pulses corresponding to energy as low as 3.5keV to be resolved easily. The detector window of 0.20mm beryllium causes little attenuation of photons above 4keV.

A preamplifier[3] giving a voltage gain of 20 is used, and the pulse

---

1. Nuclear Enterprises, type IA-HG-2.
2. I am grateful to the Research Department of Nuclear Enterprises for carrying out these modifications, and for much helpful advice.
3. Nuclear Enterprises, type NE 5282.

Figure 53

Energy and resolution calibration of scintillation counter

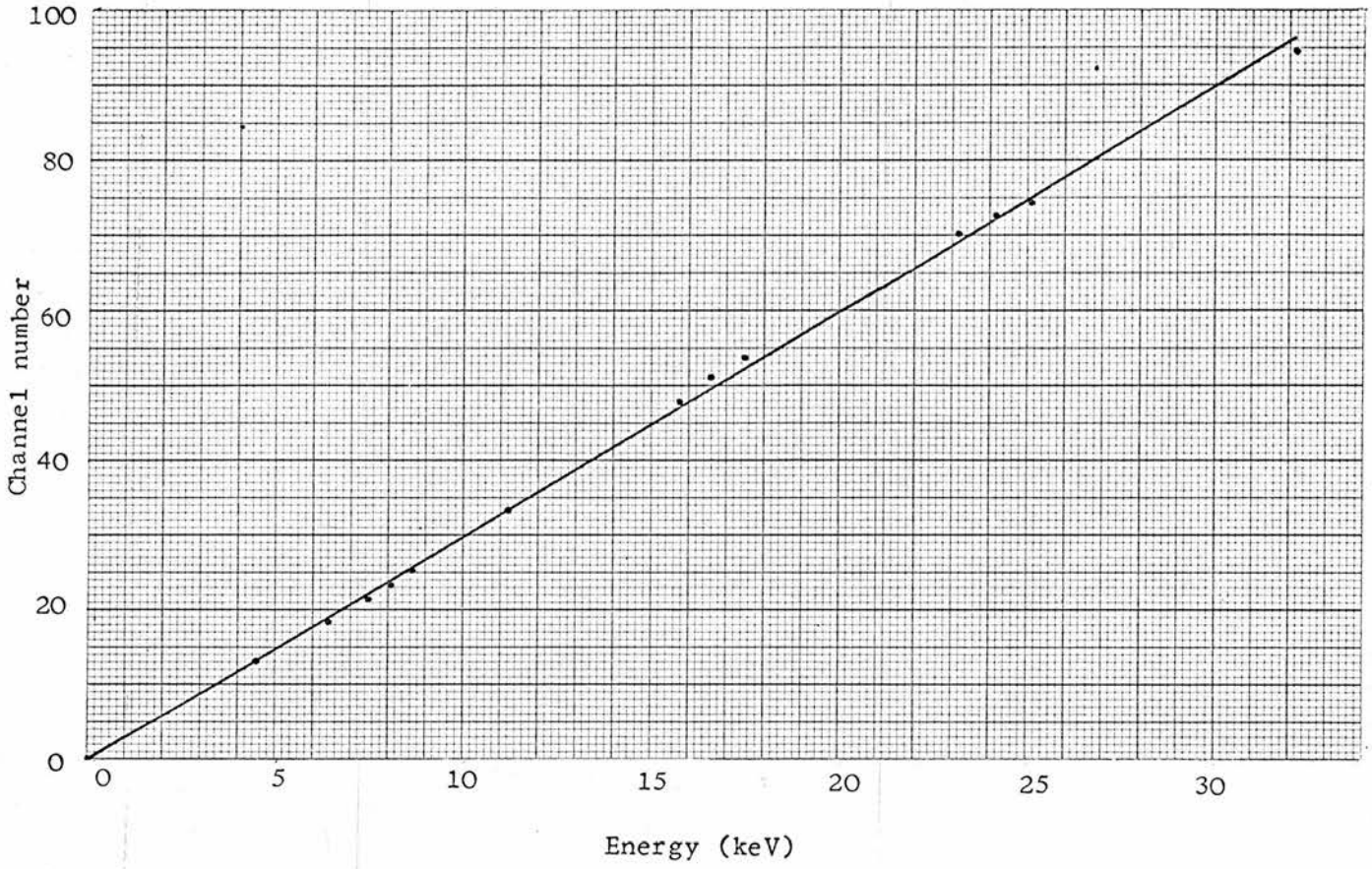

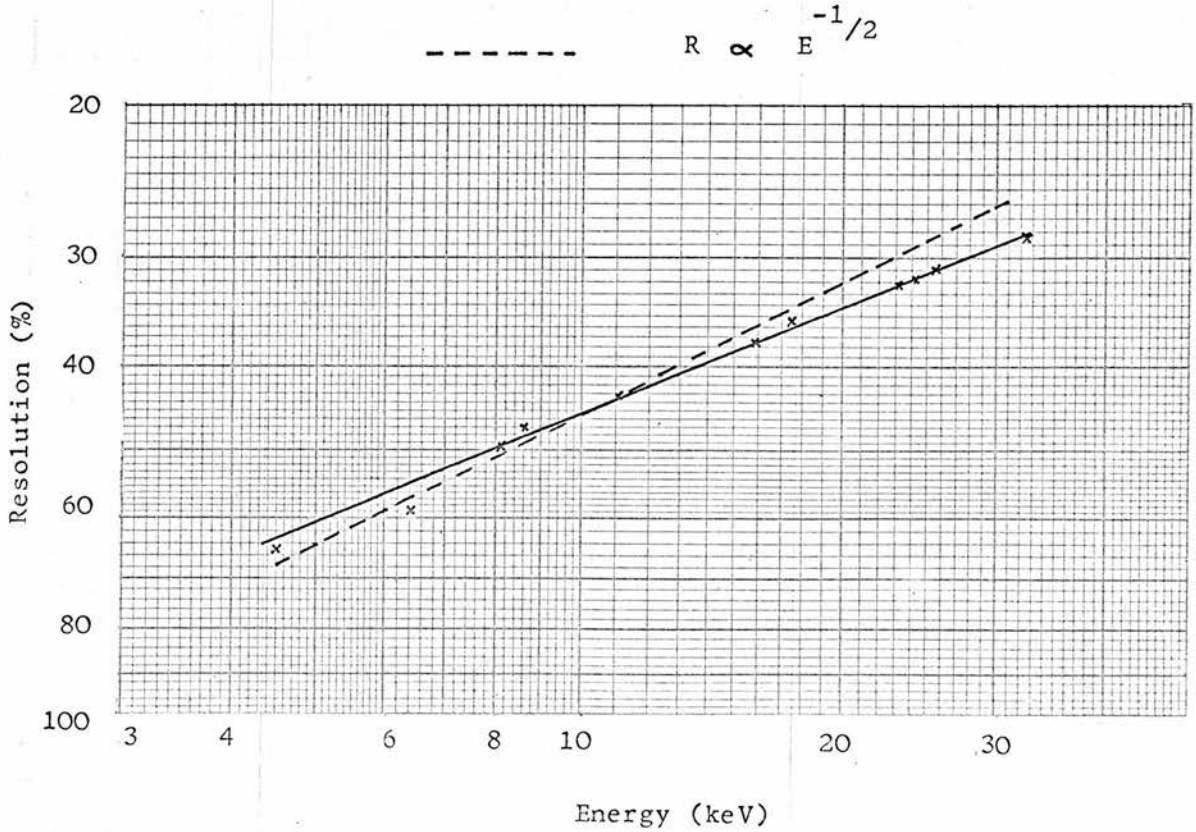

height analyser and E.H.T. unit are the same as used in the proportional counter measurements.

8.3 Experimental situation

A Melinex film of thickness 12.6×10^{-4}cm is used as a scatterer in the spectrometer described in Chapter 5 (Figs. 43, 44). The primary beam is defined by two 0.48cm apertures on the scattering spectrometer. The detector collimator contains a 0.16cm aperture close to the detector window and a 0.32cm aperture to reduce the detection of air scattered radiation. The total air path from tube window to detector window is 27.6cm.

8.4 Calibration

Calibration was carried out as described in Chapter 7. Gain and E.H.T. were chosen to give optimum resolution. The corrected energy and resolution calibration curves are shown in Fig. 53. The percentage resolution results are best fitted by $R = CE^{r-1}$, with C = 102 and r = 0.58. However the numerical analysis method of resolution correction assumes that resolution varies as $E^{-1/2}$, i.e. r = 0.5. The function $R = CE^{-1/2}$ with C = 144 is also shown in Fig. 53, and, within the accuracy of the experiment is a reasonable fit to the data at energies below 20keV. Disagreement at higher energies may account for the non-convergence difficulties discussed in Chapter 6.

8.5 Measurement of spectra

Spectra of 15, 20, 25 and 30kV X-ray beams have been measured. The experimental technique of subtracting characteristic radiation, as described in Chapter 7 has been used. An estimate of the shape of the

scattered continuous distribution can be obtained from the results of the attenuation analysis measurements, suitably adjusted for variation of scattering cross section and air attenuation with energy. Ideally a 90^{o} scattered tungsten L spectrum should be subtracted, but the low intensity of the characteristic radiation makes this a very long process. However a comparison of direct and 90^{o} scattered tungsten L spectra shows no detectable differences in the pulse height distributions, so that no error is introduced by subtracting direct tungsten L radiation as described in Chapter 7.

Resolution corrections to the continuous distributions have been made as described in Chapter 6.

8.6 Further corrections

Several further corrections to the pulse height distributions must be applied to derive spectra at the X-ray tube window. The discussion in Appendix 1 shows that losses due to transmission and scatter from the scintillation crystal are negligible over the energy region of interest. Attenuation in the detector window can be calculated from the tables of McMaster et al. (1967). Air attenuation is only significant below 10keV. Consequently, correction for this attenuation over the two separate air paths (X-ray tube to Melinex, and Melinex to detector) can be made in one step, neglecting the very small energy change in the scattered beam at low energies. At higher energies, correction for energy change on scattering has been made by assuming that the energy of the scattered radiation is given by the weighted mean of the energies of the Compton and coherent components, taking the respective scattering cross sections as weights. The correction for the variation of Melinex scattering cross section with energy can then be made.

Figure 54

30, 25, 20 and 15kV Intensity distributions by scattering spectrometry

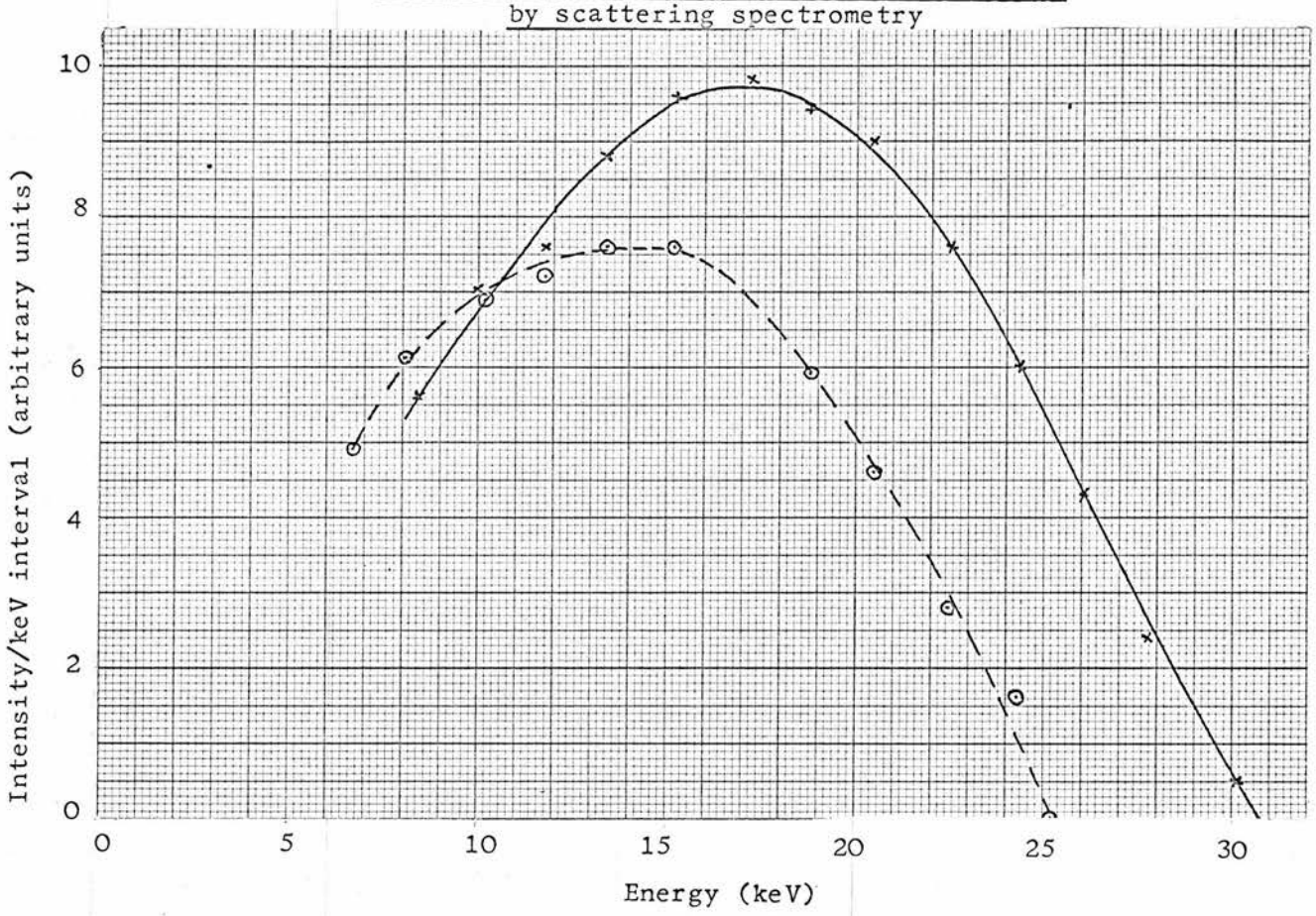

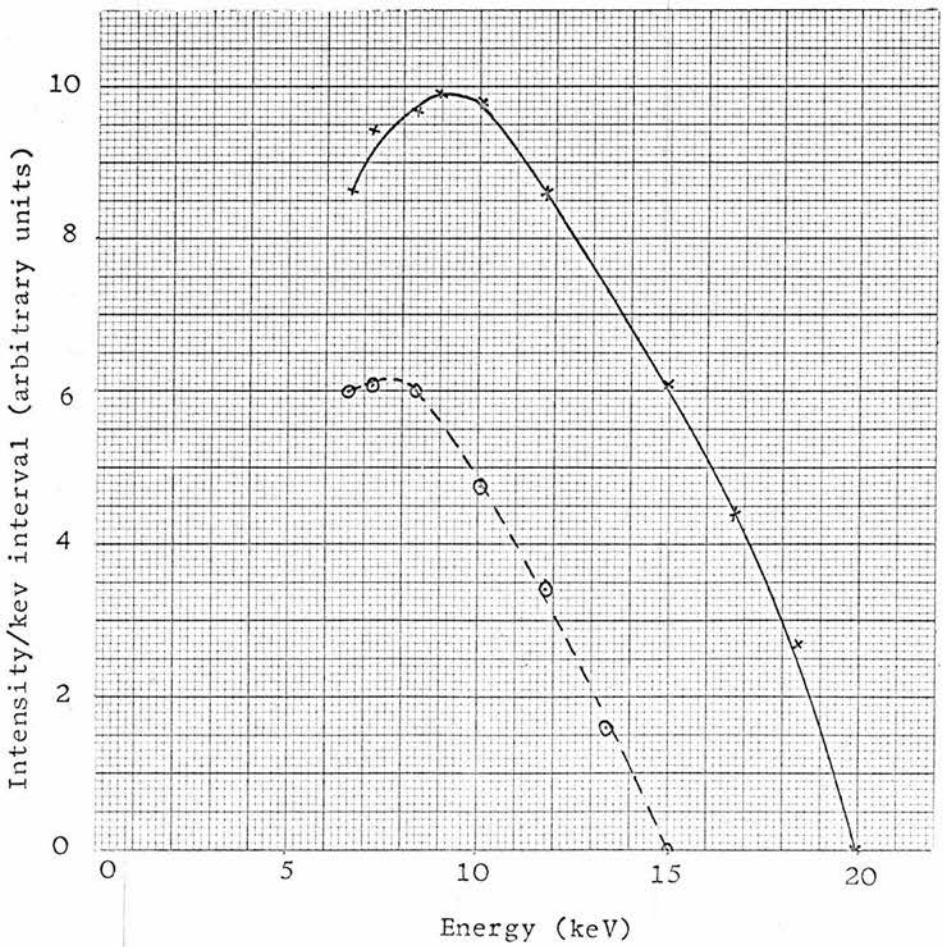

Fig. 54 shows fully corrected intensity distributions at the X-ray tube window.

The proportion of characteristic radiation subtracted from each raw distribution can also be corrected and is expressed as a percentage of the total energy fluence at the X-ray tube window in Table 41.

Table 41

Percentage of total energy fluence due to Characteristic Radiation

Beam (kV)	Characteristic Radiation (% total energy fluence)
30	37
25	41
20	21
15	16

Due to the large number of corrections the results in Table 41 are probably only reliable to $\pm$ 20%. In Chapter 9 the spectra obtained by the various methods used in this study will be compared and discussed.

8.7 Summary

Spectra measured by a new scattering method are presented, and corrections have been discussed and applied. The proportion of characteristic radiation in each beam has been determined experimentally. The use of the scattering method enables spectra to be measured with a much shorter air path than that used for the proportional counter measurements. Consequently the spectra are defined at even lower energies than in previous work.

Figure 57

25kV Intensity distribution by:

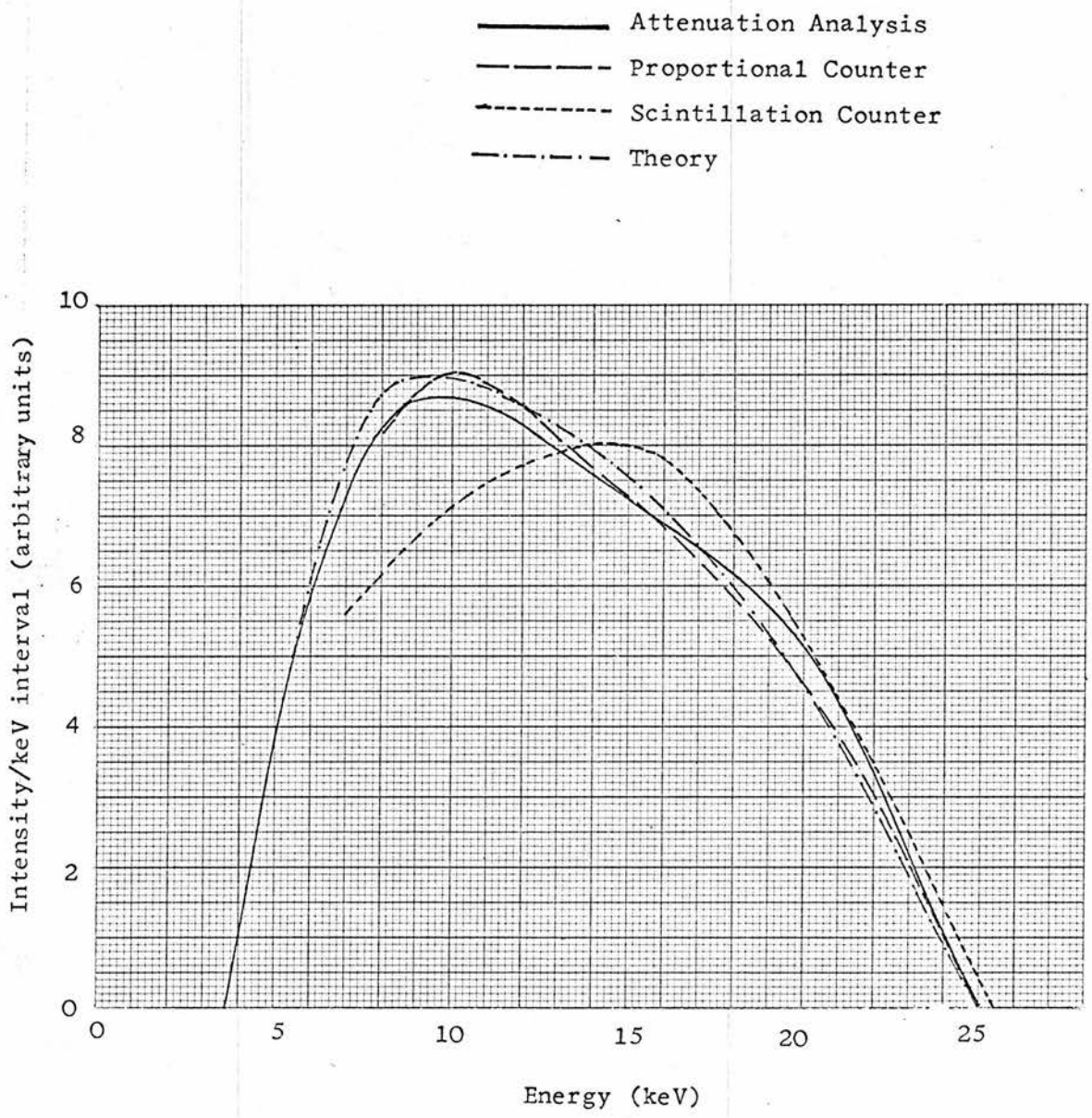

Figure 55

15kV Intensity distribution by:

——— Attenuation Analysis

— — — — Proportional Counter

---------- Scintillation Counter

—·—·—·— Theory

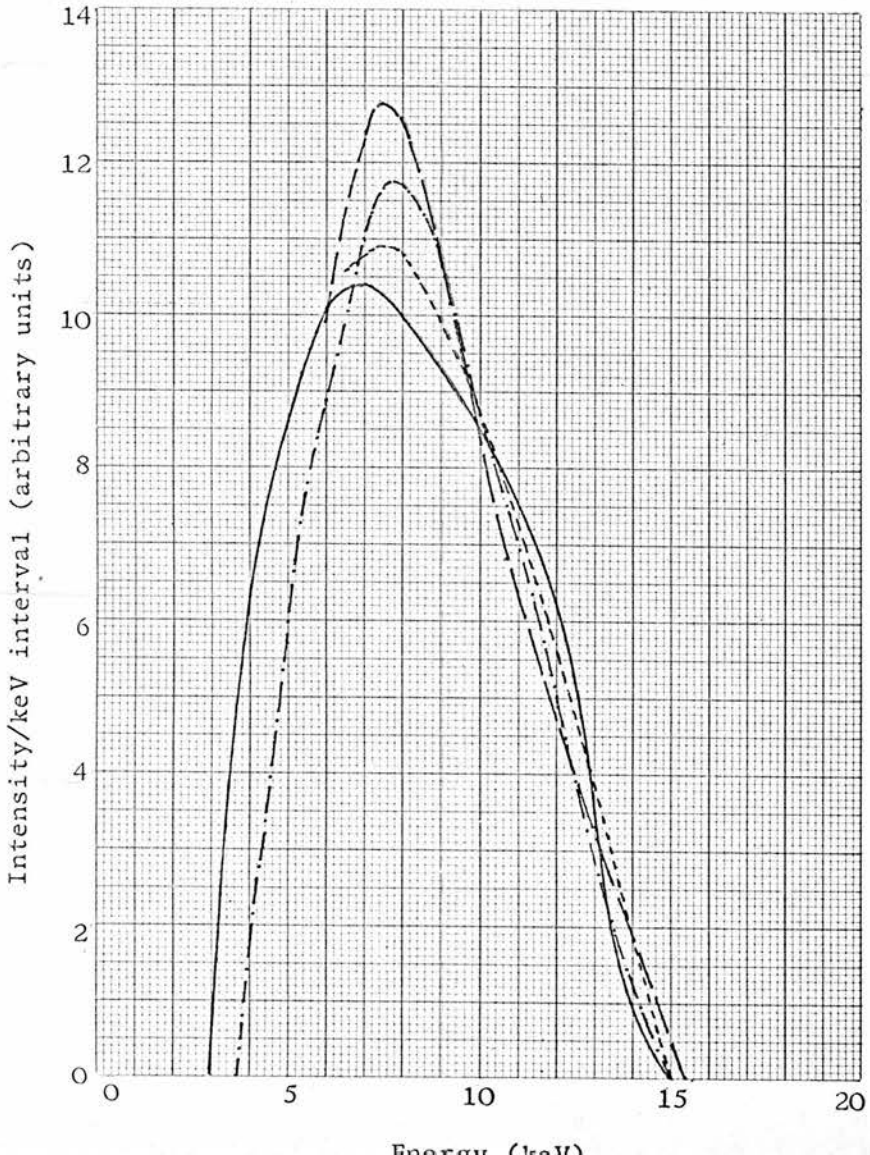

Figure 56

20kV Intensity distribution by:

——— Attenuation Analysis

— — — — Proportional Counter

---------- Scintillation Counter

—·—·—·— Theory

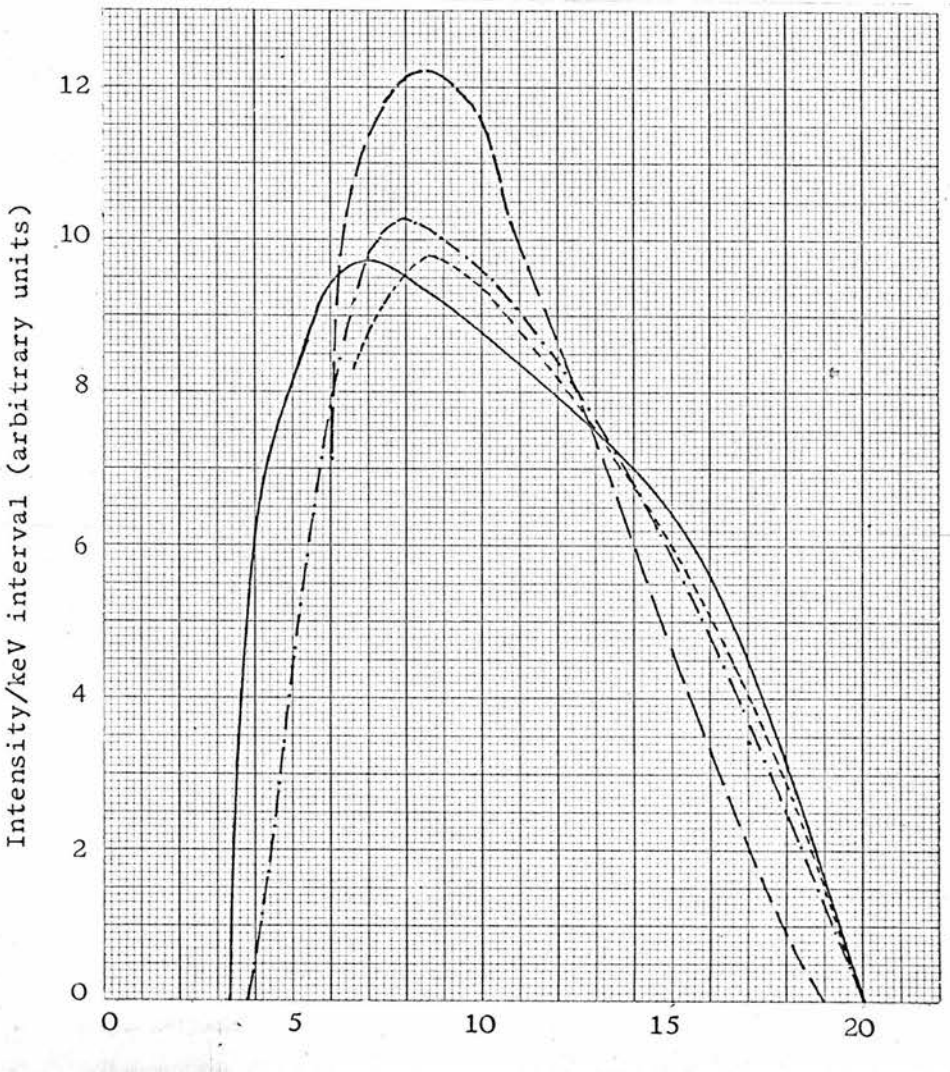

Figure 58

30kV Intensity distribution by:

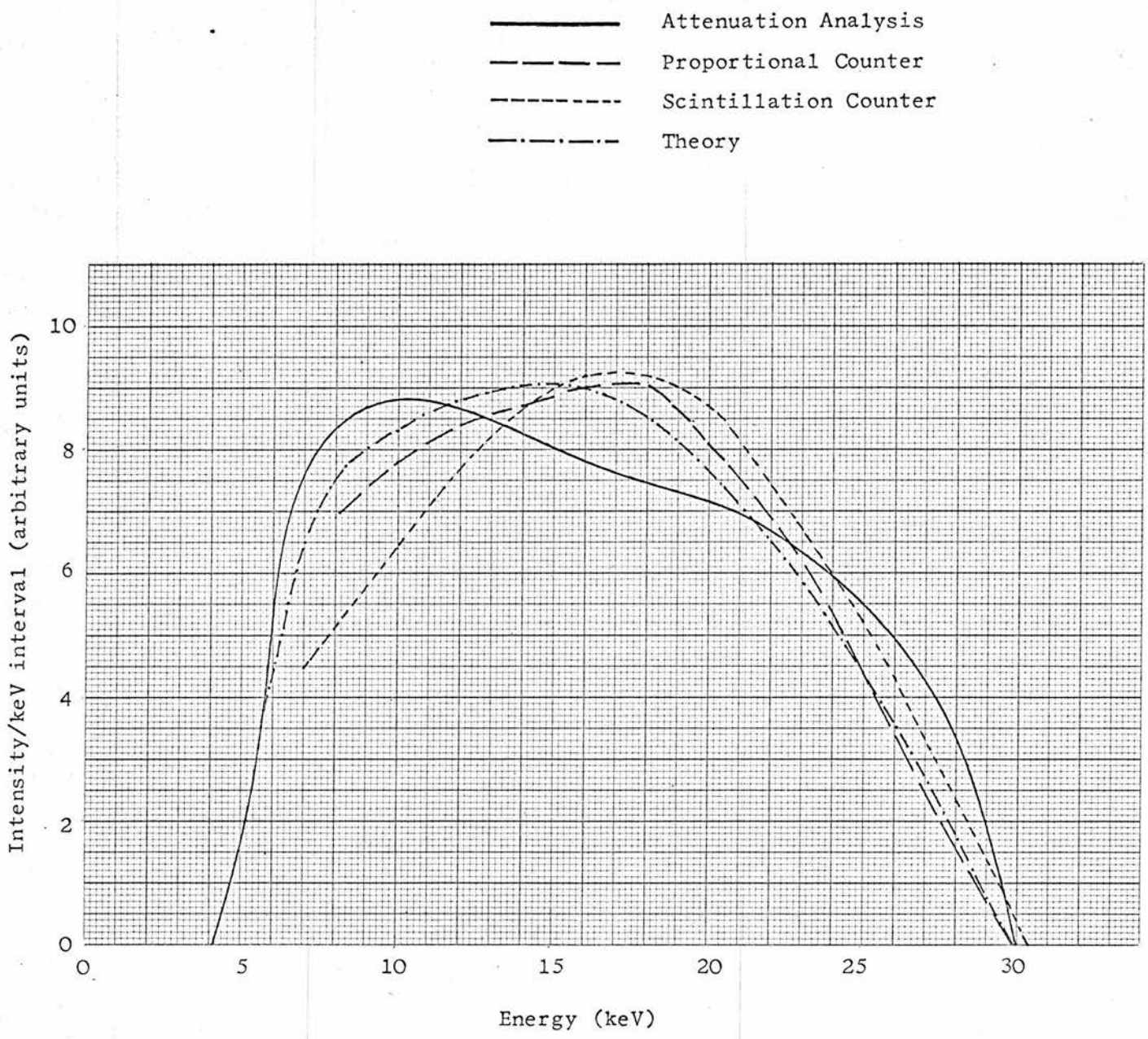

Table 42

Percentage of total intensity due to characteristic radiation

Beam kV	Characteristic intensity (percentage of total intensity)				
	Theory	Ross filters	Attenuation Analysis	Proportional Counter	Scintillation Counter
30	36 ± 6	29 ± 6	40 ± 6	35 ± 6	37 ± 6
25	39 ± 5	28 ± 6	35 ± 6	35 ± 6	41 ± 6
20	40 ± 4	28 ± 6	21 ± 5	21 ± 5	21 ± 5
15	34 ± 2	22 ± 3	16 ± 4	17 ± 5	16 ± 5

CHAPTER 9

COMPARISON AND DISCUSSION OF RESULTS AND METHODS

9.1 Introduction

In the present study, continuous spectra of X-ray beams have been measured by three experimental methods, and have also been calculated theoretically. The proportion of characteristic radiation in the beams has been determined by four experimental methods in addition to theoretical calculations. All these results will now be presented for comparison and discussion. Weighted mean continuous distributions and proportions of characteristic radiation will be derived and discussed, and comparisons with the work of other authors will be made.

9.2 Comparison and discussion of results

Figs. 55, 56, 57 and 58 show the continuous distributions of 15, 20, 25 and 30kV X-ray beams measured by attenuation analysis, gas proportional counting, and scintillation spectrometry. Theoretical distributions calculated in Chapter 2 are also shown. For the purpose of comparison, each set of spectra has been normalised to contain equal intensity above 8keV, the minimum energy above which all four curves are well defined.

Table 42 summarises the the measurements of the percentages of the total beam intensities which are due to characteristic radiation. The methods used in attenuation analysis and pulse height analysis to estimate this percentage depend on the choice of a smooth continuum, and are not very sensitive. The uncertainties shown in Table 42 are estimates of the

total range of the measurements.

Pulse height analysis and attenuation analysis techniques cannot distinguish true characteristic radiation from pseudo-characteristic radiation (as defined in Chapter 2). However theoretical spectra separate the two types of radiation and the intensity of pseudo-characteristic radiation must be estimated by choosing a smooth curve by eye. Many possible curves can be drawn, and the uncertainties in the "Theory" column of Table 42 reflect this problem. The minimum figure for each beam would apply to the case where virtually all the pseudo-characteristic discontinuities were contained within the smooth continuum envelope (see e.g. Fig. 12 and discussion).

Similar considerations apply to the results of the Ross filter experiment, since theoretical continuous distributions were used to estimate the contribution of the continuum to the pass-band intensity. Hence the rather large uncertainties shown in Table 42 apply. The theoretical spectra shown in Figs. 55 - 58 have been visually smoothed to enable comparisons with experimentally determined spectra to be made.

The agreement between each set of continuous distributions is, in general, very good, supporting the validity of the different methods of measurements used in this study. Where disagreement does occur it is most noticeable over the energy region 6 - 10keV, and is probably due to small differences in the proportions of characteristic radiation subtracted. The results in Table 42 are not inconsistent with this suggestion, but due to their large uncertainties they cannot fully prove it. However, in the 25 and 30kV spectra, the scintillation counter results lie rather low below 12keV, and the proportion of characteristic radiation subtracted is larger than that subtracted from the proportional

counter results.

It would be expected that disagreement between different methods would be most noticeable for the 25 and 30kV spectra, since the subtracted intensity is large, and the choice of a smooth continuum becomes somewhat arbitrary. Because these distributions are rather broad, a small change in the proportion of characteristic radiation subtracted can move the continuum peak considerably. In view of this difficulty, the agreement obtained seems very satisfactory. It may also be noted that spectra obtained by simple theoretical considerations and by attenuation analysis agree well with those measured by more direct pulse height analysis methods which need quite sophisticated equipment.

Apart from the theoretical predictions for the 15 and 20kV beams, measurements shown in Table 42 of the proportion of characteristic radiation in the beams agree within the limits of experimental error. It has been noted in 3.9 that the theoretical results may be in doubt at low energies, due to the possible breakdown of validity of the Thomson-Whiddington energy loss formula, and, more likely, due to inaccuracy of the approximations of Spielberg (1959) used in deriving the characteristic intensity.

Since attenuation analysis spectra were used to give estimates of the shape of the continuum after the subtraction of characteristic radiation in proportional and scintillation counter measurement, the percentage of characteristic radiation measured by these latter two methods is dependent, to some extent, on the attenuation analysis results.

9.3 Discussion of the merits of methods used

In discussing the relative merits of the methods used in this study, it is necessary to consider the accuracy to which the spectra are required.

If accurate measurements of the intensity of characteristic radiation are required, then the Ross filter method is most suitable since measurements of the pass-band intensity can be made very accurately with the detectors described. However it is still necessary to define the continuous distribution so that its contribution to the pass-band intensity can be subtracted. The results presented in this chapter show that theoretically derived continuous distributions agree well with experiment provided that target filtration is taken into account, and hence these theoretical results may be used for the pass-band correction. Since only the tungsten L_α line falls within the pass-band, it is necessary to use relative intensity measurements by other workers to deduce the intensity of the L_β and L_γ lines, but this introduces little error.

If experimental measurements of the continuum are required, then the scattering spectrometry method developed in this thesis gives the greatest accuracy. This has advantages over the gas proportional counting method of only requiring a small correction for air attenuation and also of using a detector with a high quantum counting efficiency at all energies. The poorer resolution of the scintillation counter has proved no great problem due to the development of a computer programme capable of correcting for detector broadening with no loss of low energy detail. It is however fundamentally desirable to use a detector giving optimum resolution to minimise the correction necessary to derive the true spectrum.

The new experimental technique for subtracting characteristic radiation is most convenient in use, but is not very sensitive due to the difficulty of defining the smooth continuum (see Fig. 50). However any errors in the subtraction process result either in part of the continuous distribution at about 8 - 9keV being regarded as characteristic radiation, or vice versa. The majority of applications of spectra use both the continuous and characteristic radiation (e.g. calculation of scatter corrections) and any uncertainty will not seriously affect the results. In such cases, scattering spectrometry with experimental subtraction of characteristic radiation provides a good representation of the X-ray spectrum.

Attenuation analysis, using a previously untried Laplace transform, has been shown to produce spectra in good agreement with those obtained by pulse-height analysis. The method has the advantage of requiring very little apparatus, but the analysis of results requires more time than is needed for more direct methods. If a large number of spectra were to be measured the development of a computer programme to perform this analysis would be useful. A further advantage of attenuation analysis in the present study is that spectra are obtained directly in absolute units, and these have been shown to give good agreement with theory. If attenuation analysis is used to measure spectra, a Ross filter experiment should be undertaken to measure the proportion of characteristic radiation present, since the method of Greening (1947) is not accurate, and may not be valid. The Ross filter experiment would, of course, require an estimate of the continuum, and theoretical continuous distributions calculated as described in Chapter 2 are useful for this purpose. It would also be possible to use simpler modifications of Kramers' theory, such as those suggested by

Figure 59

Percentage of total beam intensity due to L-characteristic radiation

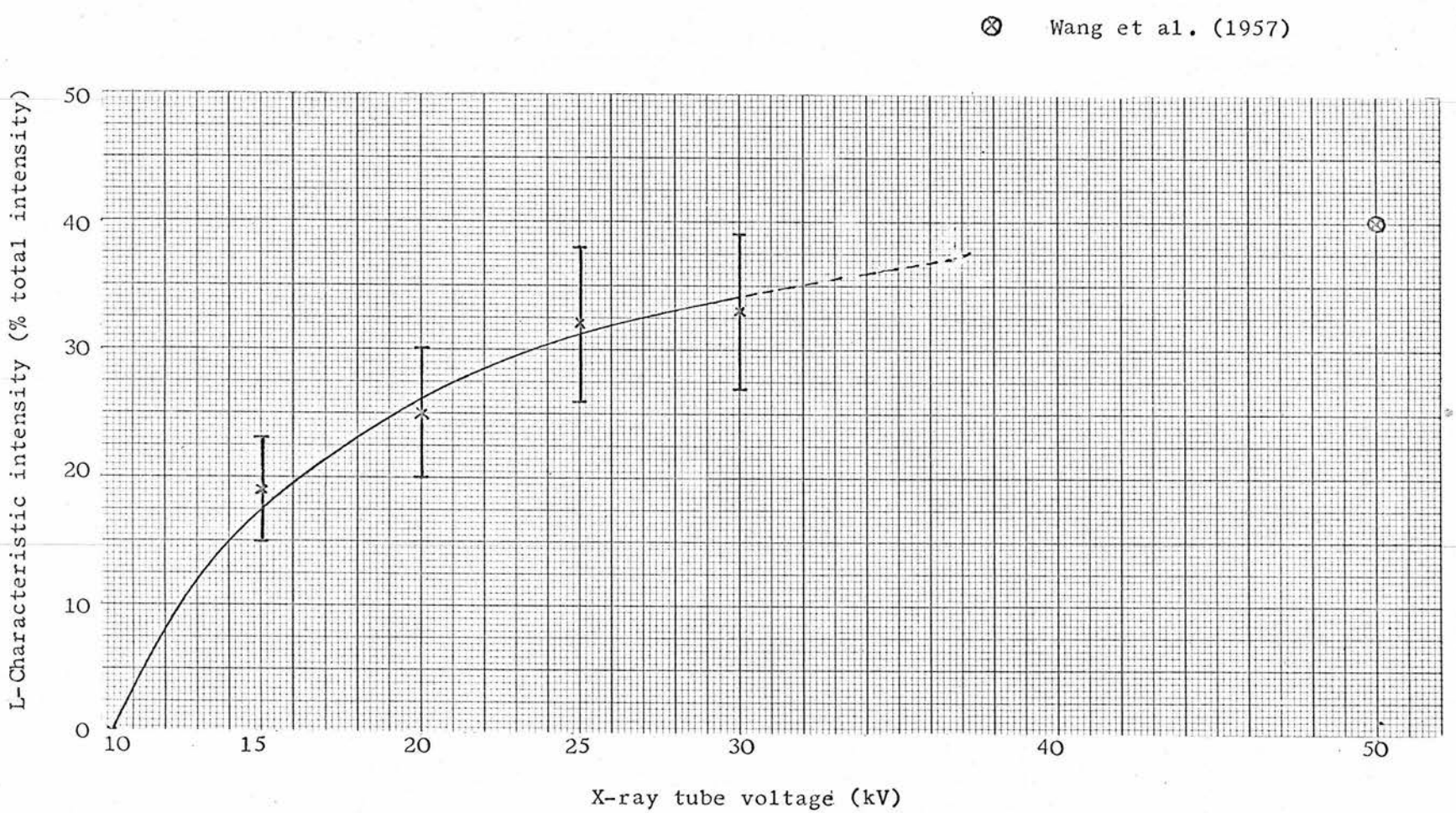

Jennings (1953). In this case, since target filtration would not be fully taken into account, an iterative method of finding the proportion of characteristic radiation present would be most applicable.

Theoretical calculations of characteristic radiation intensity do not agree with experimental measurements at low energies. It appears likely that more rigorous theoretical studies are necessary, especially in the definition of electron paths in tungsten and in the calculation of L-shell ionization cross-sections.

9.4 Weighted mean spectra

A considerable number of results, obtained by various methods, have been presented and discussed in this study. It is advantageous to derive weighted mean spectra from these, since this enables the maximum amount of information to be extracted from the results and presents them in the most useful form for applications by other users.

9.4.1 Characteristic radiation

It has already been noted that the pulse height analysis measurements of characteristic radiation are dependent on the attenuation analysis results. For this reason, in the calculation of weighted means, the proportional counter, scintillation counter and attenuation analysis results have each been given a weight of 1/3 and the Ross filter results have been given a weight of 1. The purely theoretical predictions have been ignored in view of the discussion in 9.2. Fig. 59 shows the weighted mean results of the percentage of the total X-ray beam intensity which is due to characteristic radiation. Uncertainties shown represent the spread of experimental measurements.

The results appear to lie on a smooth curve, although the uncertainty

Figure 60

Normalised weighted mean spectra

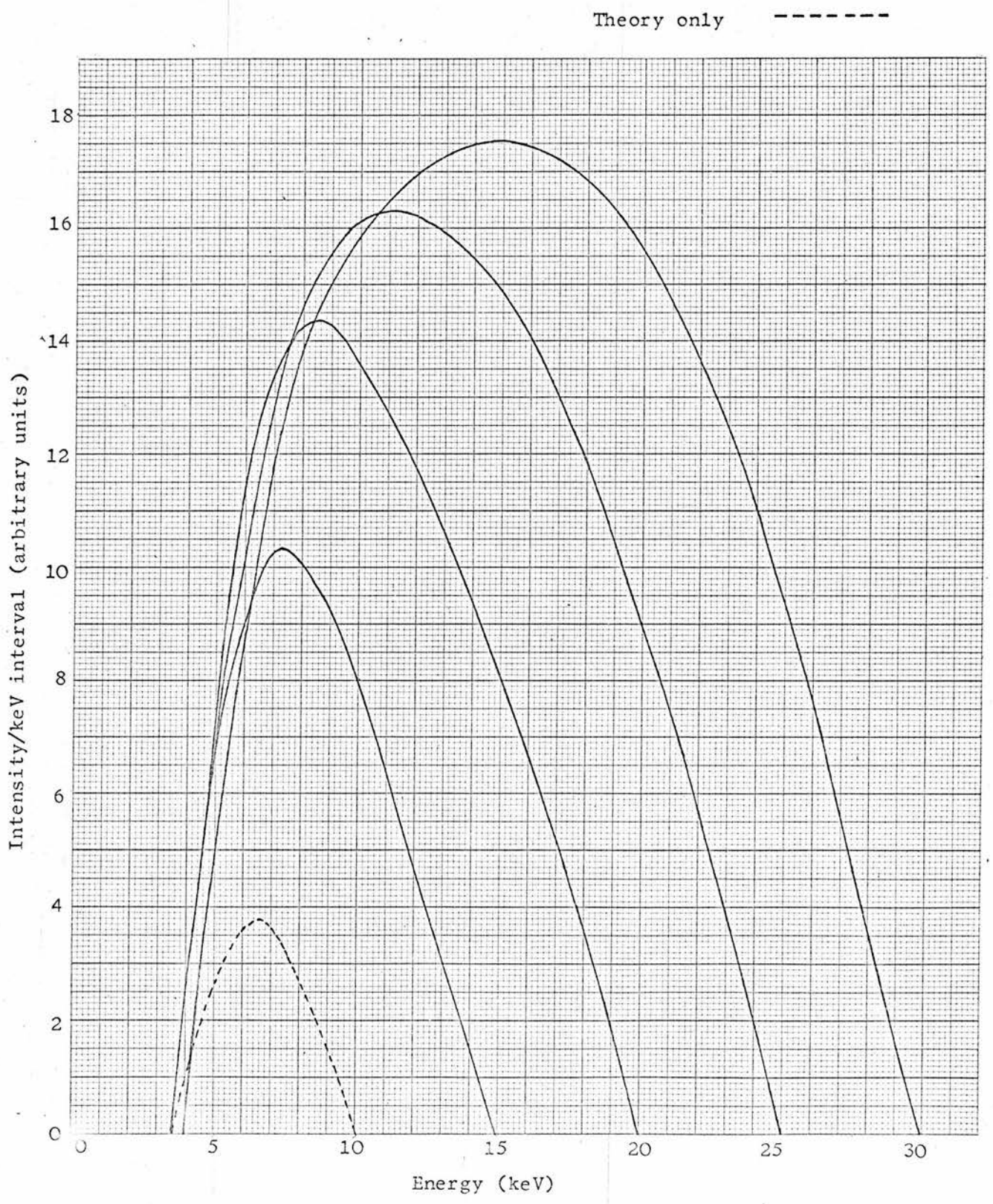

of individual measurements is large. It is interesting to note that Wang et al. (1957) in their attenuation analysis measurements of a 50kVp beryllium window X-ray beam estimated that 40% of the total intensity was due to characteristic radiation, ~~and this appears consistent with the results presented here~~.

The general shape of the curve, rising sharply and then becoming fairly flat, is very similar to that reported by Tothill (1964) for the K radiation from tungsten target tubes under conditions of light filtration. Although the emission of L radiation is complicated by the three L absorption edges, the physical similarity between K and L emission processes suggests that such agreement would be expected.

9.4.2 Continuous distributions

Theoretical studies have shown that, due to target filtration, continuous distributions are not, in fact, smooth curves. The discontinuities however cannot be seen by any low resolution spectrometry methods and are lost in the high characteristic intensity. It is therefore reasonable to represent the averaged continuous distributions by smooth curves since very little error will be introduced by this assumption in any subsequent calculations.

Fig. 60shows weighted mean continuous distributions. In deriving these, each of the four curves in Figs. 55 - 58 has been given equal weight, since it is not felt that the theoretical curve is any more accurate than the three experimental curves which may not be wholly independent (see 9.4.1). By averaging in this way the effect of any systematic errors will be reduced. The 10kV theoretical distribution has been included to give a full set of spectra. Although this spectrum has not been confirmed by experimental measurements, the good agreement of the 15 and 20kV

distributions with experiment suggests that the 10kV spectrum is accurate.

Distributions have been normalised by using the theoretical total beam intensity results shown in Table 15. These have been shown to give good agreement with experimental measurements of energy fluence. The intensity due to characteristic radiation, defined from Fig. 59, is subtracted from the total intensity, leaving the intensity due to the continuum. The areas under the curves in Fig. 60 have been made proportional to the continuum intensities.

The distributions form a consistent set, as would be expected on physical grounds. Theoretical formulae and experimental results from tubes with higher inherent filtration indicate that when the tube potential is increased, the intensity at all energies should increase, but this does not occur at low energies in the spectra presented here. This may be due to uncertainty in the low energy definition of these spectra. It is, however, also possible that this effect is due to target filtration. The 30kV beam has the greatest effective production depth of the beams measured, so that low energy radiation is more heavily filtered than with other beams. This would account for the relative lack of low energy intensity in this distribution. It is unfortunate that there have not been any other accurate measurements of the spectra of similar X-ray tubes extending to sufficiently low energies to test this suggestion. The best method of investigating the very low energy portions of the spectra would be high resolution spectrometry using crystal diffraction apparatus, or possibly a semiconductor proportional counter. An alternative approach would be the use of balanced filters to isolate

Figure 61

Variation of characteristic intensity with $E - E_L$

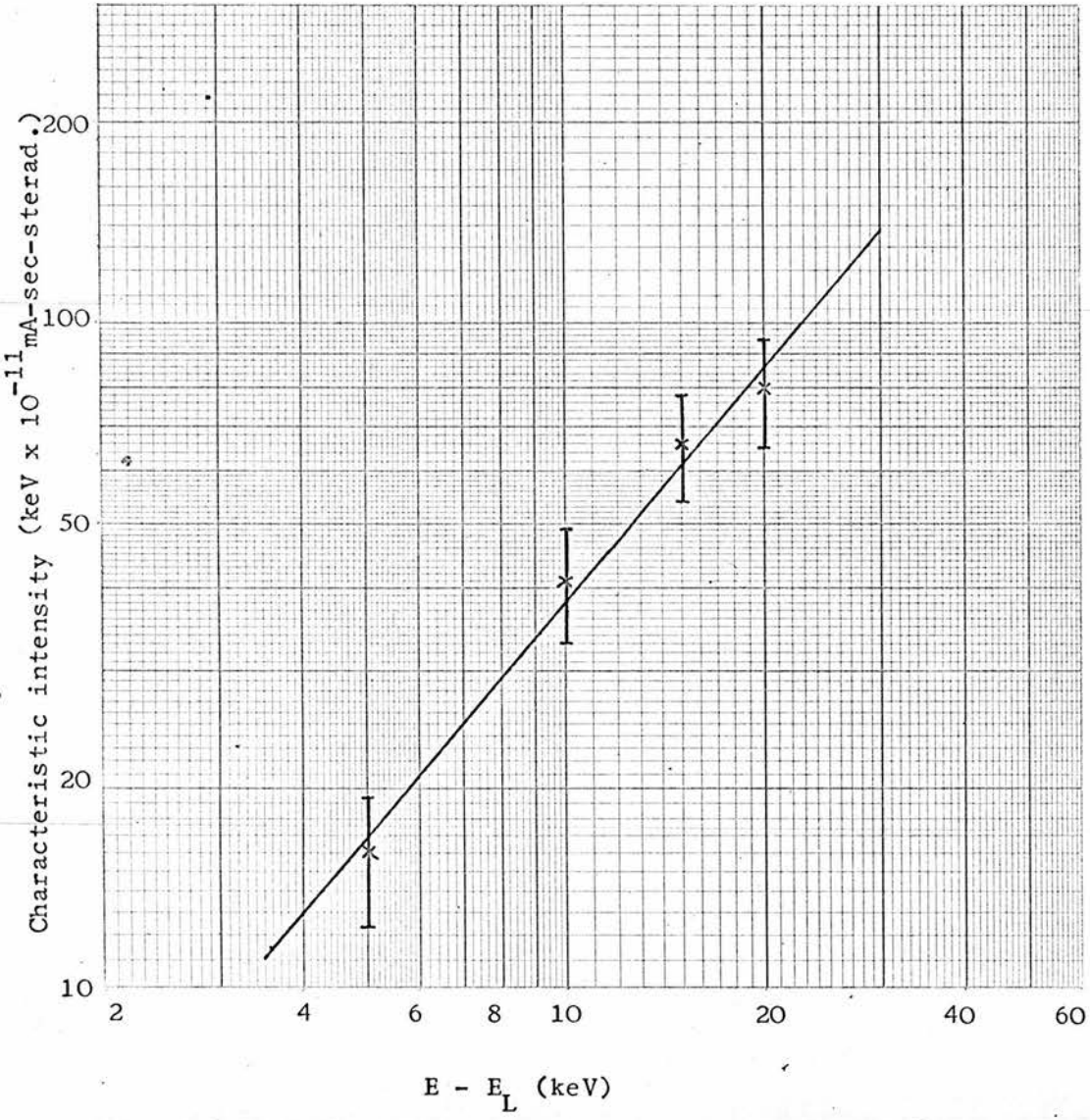

Figure 62

Variation of total intensity with tube voltage

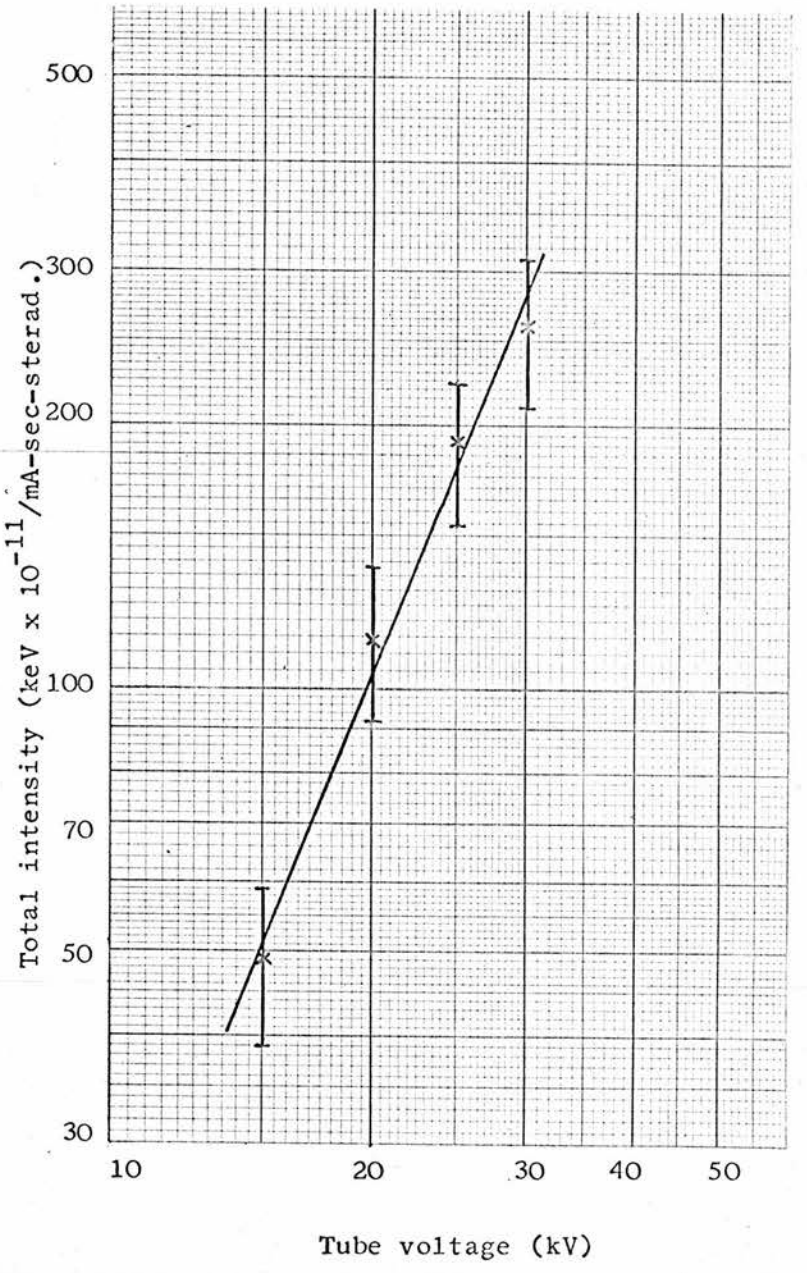

different bands of the spectra and to measure the percentage of the total intensity falling within each pass-band. Results could then be compared with those predicted by areal measurements from the curves in Fig. 60.

9.4.3 Variation of the intensity of characteristic and continuous radiation with tube voltage

Many workers have found that the variation of the intensity, I, of characteristic radiation with tube voltage, E_o, can be expressed in the form $I = A(E_o - E_q)^n$ where A and n are empirical constants, and E_q is the excitation potential of characteristic radiation.

Using the weighted mean values from Fig. 59, of the percentage of L characteristic intensity in X-ray beams, and theoretical results (which are in excellent agreement with experiment) for the total beam intensities, the intensities due to L radiation can be found. These are plotted in Fig. 61, against $(E_o - E_L)$, taking E_L = 10keV, and the results satisfy the power law, with $n = 1.2 \pm 0.1$.

Similarly the total intensities can be plotted on logarithmic scales against tube voltage E_o, and this is shown in Fig. 62. In this case, the total intensity varies as tube voltage to the power 2.4 ± 0.1.

Hence the variation of the ratio R of characteristic intensity to total intensity is given by an expression of the form:-

$$R = \frac{B(E_o - E_L)^n}{E_o^m} \qquad \ldots\ldots 9.1$$

In the present study, expressing the ratio as a percentage and energies in keV, we find: $B = 28 \times 10^2 \pm 4 \times 10^2$, $n = 1.2 \pm 0.1$, and $m = 2.4 \pm 0.1$.

9.5 Comparison with the results of other workers

There is very little published experimental work with which to compare the results obtained here. Only Burke and Pettit (1958) give 20 and 30kVp spectra from a beryllium window tube. These were measured by attenuation analysis only and are discussed in Chapters 3 and 4. However, their X-ray tube was operated from a full-wave-rectified generator so that their spectra would be expected to differ from those measured at constant potential. Their estimates of the proportions of characteristic radiation present are rather lower than the measurements made here, but it has been noted in 3.11 that their method, which does not allow for the effects of target filtration, appears very inaccurate and may not be valid. Their continuous distributions do not contain quite as much energy at high energies as those presented here, and this would be expected in view of the waveform. The peaks of their intensity distributions occur at about 8 and 12keV for the 20 and 30kVp spectra respectively, and this is in reasonable agreement with the spectra in Fig. 60.

There has been no previous accurate investigation of the proportion of tungsten L radiation in beams from a commercial beryllium window X-ray tube. Equation 9.1 indicates that, at 50kV, 20% of the total beam intensity would be due to tungsten L radiation. ~~This is in reasonable agreement with the previously noted (9.4.1) estimate of 40%, made by Wang et al. (1957).~~

Hink (1965), whose work is discussed in 2.5, found empirically that the intensity of directly produced tungsten L characteristic radiation varied as $(E_o - E_L)^{1.44}$. However his measurements were taken using a

special transmission target and so are not directly comparable with the present case. The small difference between his result and that of 1.2 ± 0.1 obtained here may be due to different filtration in the target.

It is interesting to compare the results for L radiation with those obtained by Tothill (1964) for tungsten K radiation. He found that, for unfiltered radiation, the characteristic exposure rate varied as $(E_o - E_k)^n$ where n lay between 1.2 and 1.4. This is in excellent agreement with the L radiation result. Tothill suggests that the discrepancy between his value of n and that of 1.65 proposed by Compton and Allison (1954) may be due to the attenuation of K radiation by the high atomic number target. This theory is supported by these results for L radiation where target filtration is very important.

9.6 Summary

Continuous distributions and relative characteristic radiation intensities have been derived by combining results from all the experimental measurements. These results define completely the spectra of 10 - 30kV X-ray beams. The continuous distributions indicate that, at low energies, intensity does not increase with tube voltage. This may be due to filtration by the target, and cannot be seen in previously published spectra since it is only apparent below about 10keV.

Using the weighted mean results, the variation of the intensity of characteristic and continuous radiation with X-ray tube voltage has been investigated. An analytical expression for the proportion of L characteristic radiation in X-ray beams has been derived.

Comparison has been made with other published work. Agreement is

good although few results are available. Some comparisons with investigations of tungsten K radiation have been drawn, and similarities have been discussed.

9.7 Points for further study

The results of the present work show that L characteristic radiation forms a large proportion of the total energy output of beryllium window X-ray tubes. Although Kramers' formula gives good theoretical representations of continuous X-ray distributions provided that target filtration is taken into account, a similar approach in calculating the intensities of characteristic radiation does not appear suitable at low energies. A more thorough theoretical treatment appears necessary to investigate this discrepancy. In addition further measurements of the balanced filter type would be desirable to investigate the variation of characteristic intensity at higher tube voltages. This would require the development of new detector systems giving total absorption at higher energies.

It would also be instructive to extend the range of the new scattering spectrometry method to enable spectra produced at higher tube potentials to be measured. This would entail the development of a computer programme to undertake the correction for the escape of iodine fluorescent radiation from the sodium iodide detector. This becomes significant above 33keV.

It would be highly desirable if a simple method could be found of specifying the quality of low filtration X-ray beams for which the usual parameters of half value layer and homogeneity coefficient cease to be useful concepts (see e.g. I.C.R.U., 1964). A further analysis of the

attenuation of low energy X-ray beams, in conjunction with the knowledge of the proportion of characteristic radiation in such beams obtained from the present study, may yield a valid method of specifying X-ray beam quality in this energy region.

APPENDIX 1

ESTIMATION OF ENERGY LOSSES FROM DETECTORS

A1.1 Introduction

Low energy X-rays can undergo three types of interaction with the detectors used in this study, photoelectric absorption, Compton scatter and Classical scatter. After each of these processes it is possible that photons may escape from the detector and consequently part of the total incident energy will not be recorded. The following is a brief discussion of the energy losses from each detector. Full details of the calculations have been given by Redpath (1967) and Greening and Randle (1968).

A1.2 General theory

Consider a pencil beam of monoenergetic X-rays incident axially upon a cylinder of length 1 and radius a. Losses which may be significant are:-

(i) Backscatter (photoelectric, Compton and Classical) from the front face of the cylinder.

(ii) Sidescatter (photoelectric, Compton and Classical) through the cylinder walls.

(iii) Transmission along the cylinder axis.

Calculations of backscatter are simplified by assuming that the front face of the cylinder is an infinite plane surface, and that transmission of the X-ray beam can be neglected. It can then be shown that the number of photons N', escaping by photoelectric backscatter is given by:-

$$N' = \frac{N\omega\tau}{2\mu}\left[1 - \left(\frac{\mu'}{\mu}\right) \ln\left(1 + \frac{\mu}{\mu'}\right)\right] \quad \ldots\ldots\ldots \text{A1.1}$$

where N is the number of incident photons, ω is the fluorescent yield, μ is the linear attenuation coefficient for primary radiation, made up of photoelectric and scatter cross sections. τ and σ_T respectively and μ' is the linear attenuation coefficient for fluorescent radiation.

In calculations of losses due to Compton and classical backscatter, additional assumptions can be made. To a first approximation the energy loss of the Compton scattered photons can be neglected, and a classical $(1 + \cos^2\phi)$ distribution of scattered radiation can be assumed. It can then be shown that the number of photons N' escaping by Compton and classical backscatter is given by:

$$N' = \frac{3\,N\,\sigma_T}{8\,\mu} \int_0^{\pi/2} \sin\phi\,(1 + \cos^2\phi)\left[1 + (1/\cos\phi)\right]^{-1} d\phi \quad \ldots\ldots \text{A1.2}$$

and, by analytical integration,

$$N' = 0.168\,\frac{N\,\sigma_T}{\mu} \quad \ldots\ldots\ldots \text{A1.3}$$

Similarly, by assuming infinite absorber length it can be shown that the total number, N'', of photons lost by sidescatter is given by:-

$$N'' = \frac{N}{\mu}\left[\omega\,\tau\,g\,(\mu' a) + \sigma_T\,g'\,(\mu' a)\right] \quad \ldots\ldots\ldots \text{A1.4}$$

where $$g\,(\mu' a) = \frac{1}{2}\int_0^{\pi} \sin\phi\,\exp(-\mu' a/\sin\phi)\,d\phi \quad \ldots\ldots\ldots \text{A1.5}$$

and $$g'\,(\mu' a) = \frac{3}{8}\int_0^{\pi} \sin\phi\,(1 + \cos^2\phi)\,\exp(-\mu' a/\sin\phi)\,d\phi \quad \ldots\ldots \text{A1.6}$$

Figure A1.4

Total percentage energy loss, $\delta\varepsilon$,
from Argon at 2.99kg/cm^2 pressure

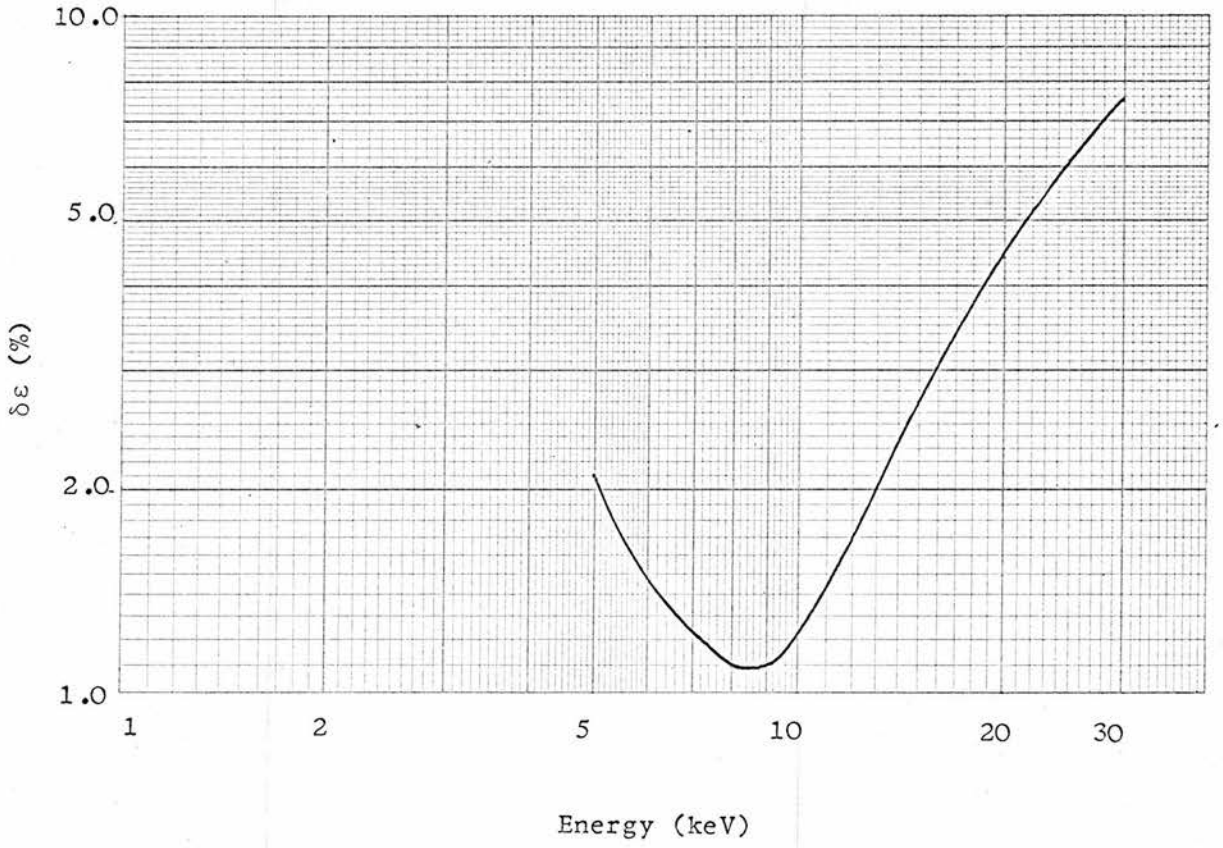

Figure A1.3

Total percentage energy loss, $\delta\varepsilon$, from Gold

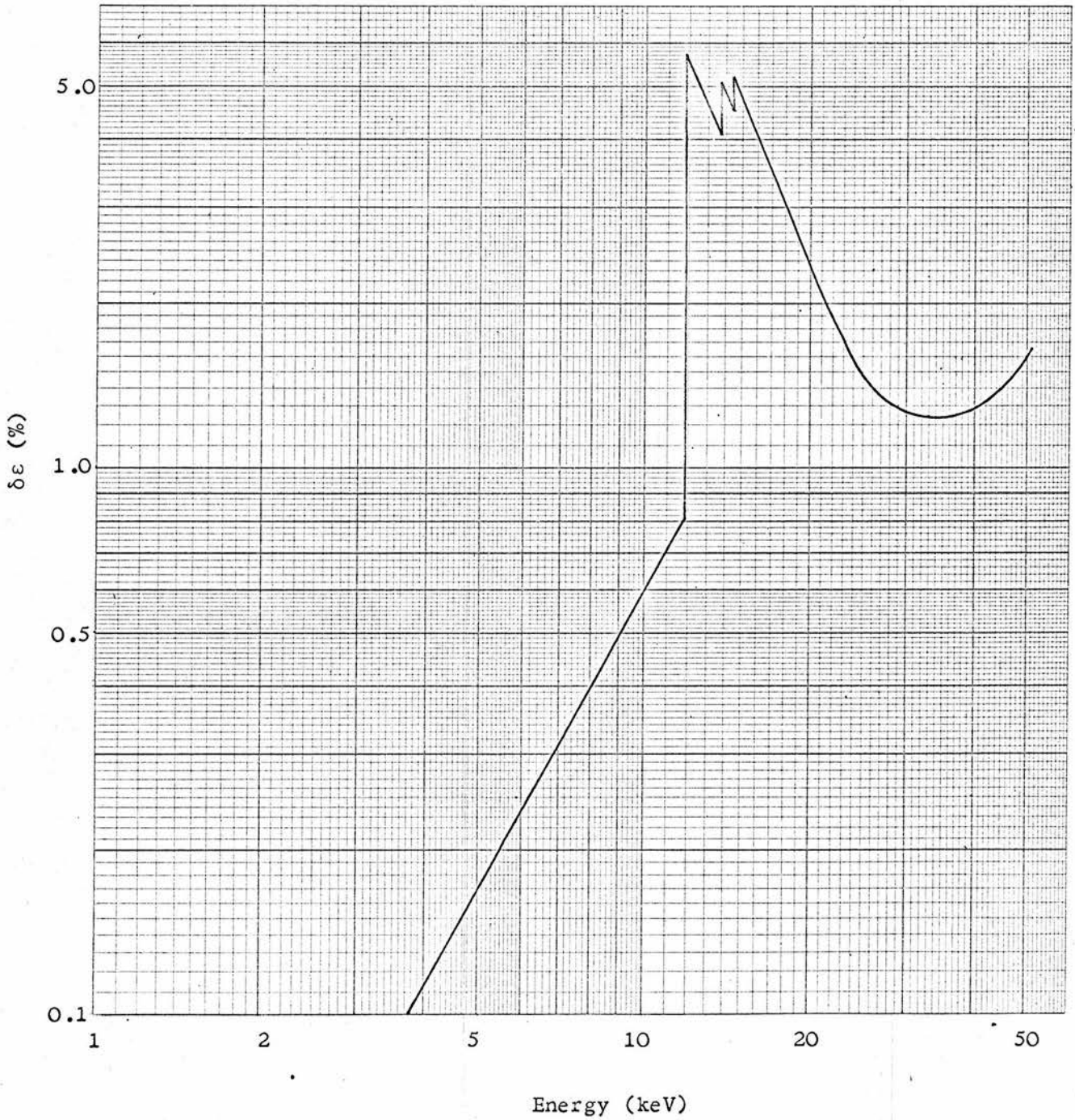

Figure A1.2

Total percentage energy loss, $\delta\varepsilon$, from Sodium Iodide

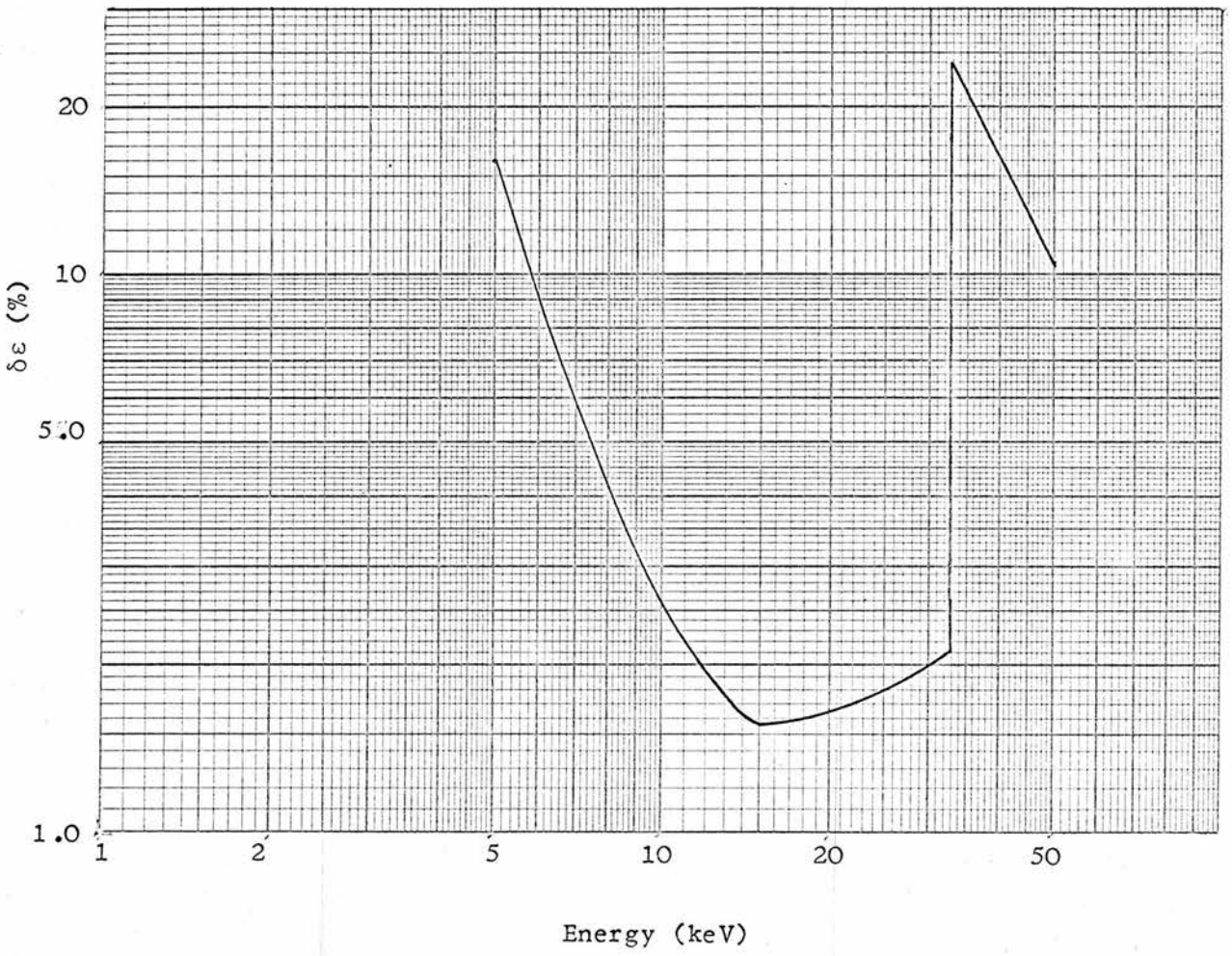

Figure A1.1

Percentage energy loss, $\delta\varepsilon$ against energy for Sodium Iodide

—·—·— · Beryllium window attenuation

– – – – · Photoelectric backscatter

——— · Coherent and incoherent backscatter

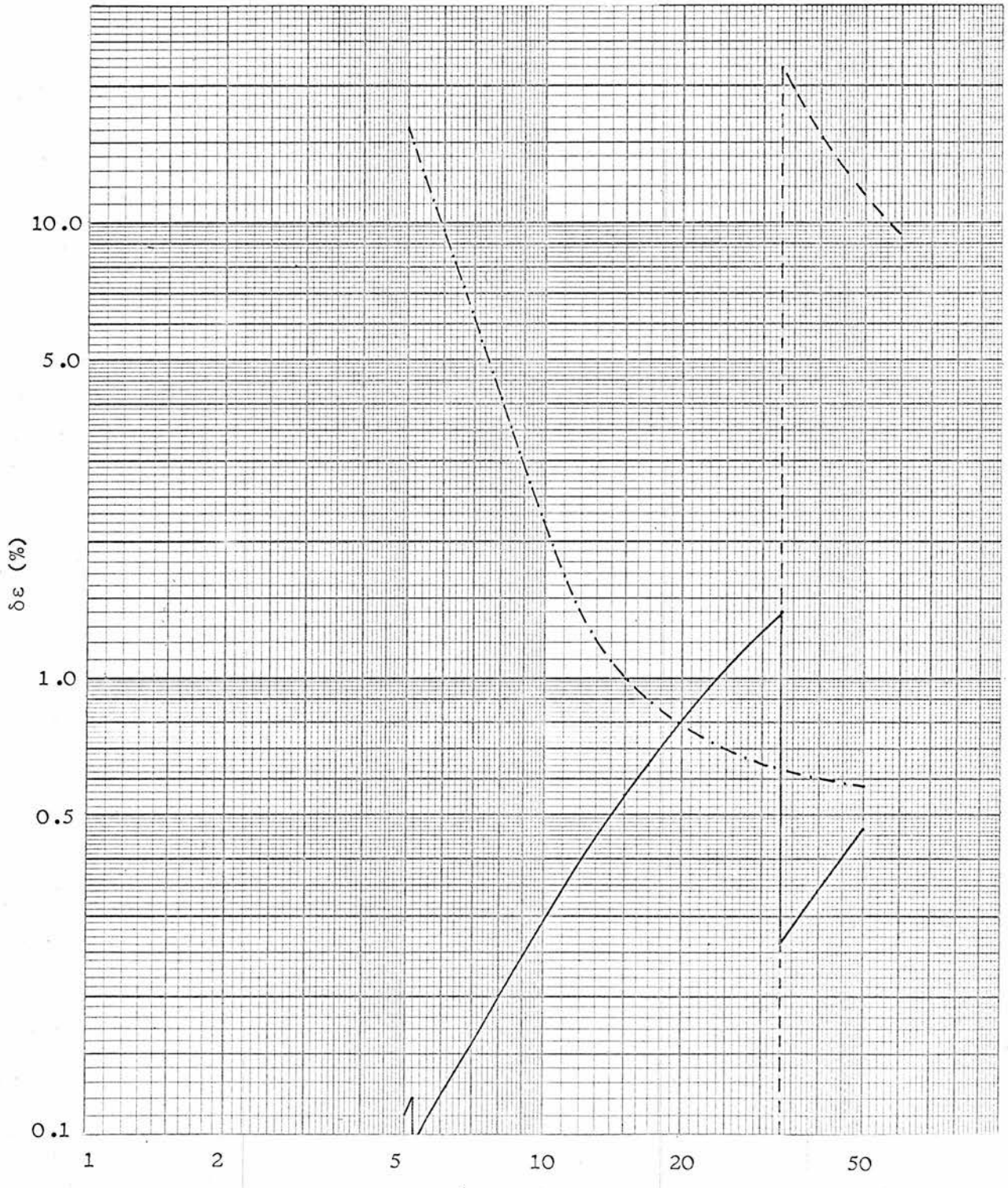

Figure A1.5

Total percentage energy loss, $\delta\varepsilon$, from Silicon

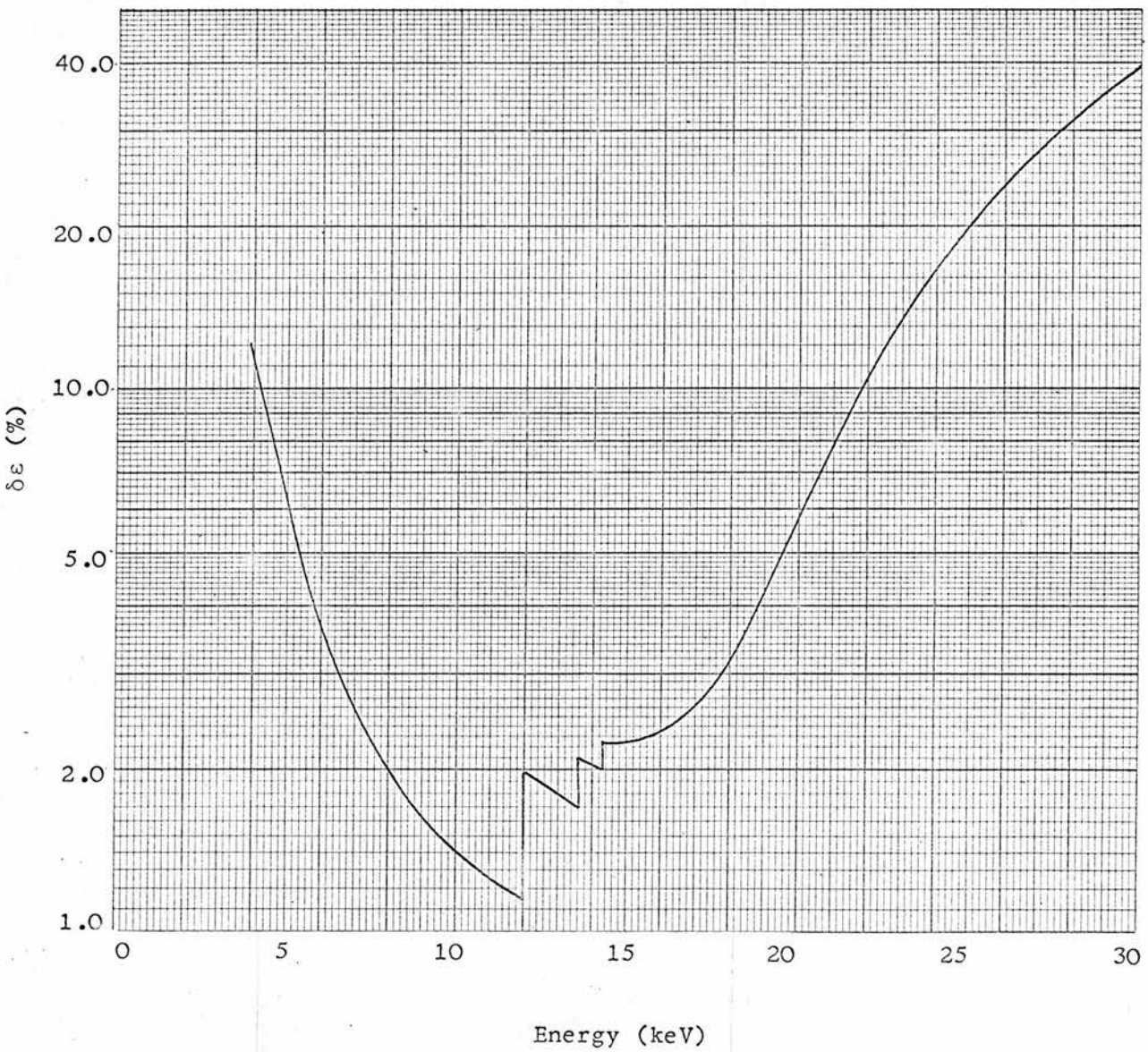

Values of g and g' have been tabulated by Greening and Randle (1968). By analogy with equations A1.1 and A1.3 it will be seen that the first expression in equation A1.4 gives losses due to photoelectric sidescatter, and the second gives Compton and classical sidescatter losses.

Corrections for lack of linear total absorption are easily made, using attenuation coefficients from McMaster et al (1967).

Equations A1.1, A1.3 and A1.4 enable the variation with energy of the total intensity lost by scattering from each detector to be calculated. The contributions of the various components will be shown in detail for sodium iodide. Losses from the other detectors will be briefly summarised since they have been fully described by Redpath (1967) and Greening and Randle (1968).

A1.3 Energy losses from the sodium iodide detector

The crystal used is 3mm deep and 2.5cm in diameter, so that transmission is negligible below 50keV, and, since narrow beams have been used for all measurements, sidescatter is also negligible. Above 33keV losses due to iodine photoelectric backscatter become very large. At low energies the 37 mg/cm^2 beryllium window has significant attenuation. Figure A1.1 shows the variation with energy of the percentage of energy, $\delta\varepsilon$, lost by the detector due to each process. The variation of the total percentage of energy lost is shown in Fig. A1.2.

A1.4 Energy losses from other detectors

The total percentage of energy lost from the calorimeter, ionization chamber and solid state detector is shown in Figs. A1.3, A1.4 and A1.5 respectively. Figs. A1.3 and A1.4 are based on calculations made by

Redpath (1967) and Fig. A1.5 uses the results of Greening and Randle (1968).

Below 14keV the principal loss in the calorimeter is due to Compton and classical backscatter from the gold absorber. Above 14keV losses due to the escape of gold L radiation are important, and above 30keV transmission losses become large.

Energy losses from the ion-chamber for a total argon pressure of 2.99 kg/cm^2, that used for all measurements, are shown. Between 5 and 8keV photoelectric sidescatter dominates. Between 8 and 20keV Compton sidescatter is important, and above 20keV transmission losses become a serious problem.

Losses from the silicon surface barrier detector are shown in Fig. A1.5. For energies above 5keV, the principal scattering loss is due to Compton backscatter, although the attenuation of the 80$\mu g/cm^2$ gold window dominates up to 15keV. However the most serious limitation of this detector is transmission loss, which increases very rapidly above 15keV.

APPENDIX 2

STATISTICAL CONSIDERATIONS GOVERNING THE RESOLUTION OF SCINTILLATION SPECTROMETERS

A2.1 Introduction

In a scintillation spectrometer, each stage in the conversion process, from an input of X-ray photons to an output of electrical pulses, is governed by the laws of probability. This causes a spread of pulse heights to be produced by an input of monoenergetic photons. We will assume normal distributions throughout the process. For the purpose of defining the total broadening of a monoenergetic line, a scintillation system can be considered in two sections:-

(i) The crystal assembly

(ii) The photomultiplier

An excellent discussion by Crouthamel (1960) suggests many techniques for optimising detector resolution. Those useful in the present study will be summarised here, together with a more full discussion of photomultiplier broadening than is generally available.

A2.2 Statistical definitions

The following is a summary of a comprehensive survey by Berks (1964) of statistics relevant to scintillation counting.

The absolute standard deviation σ, of a normal Poisson distribution about a mean $\bar{x}$ is given by:-

$$\sigma = \sqrt{\bar{x}} \qquad \ldots\ldots\ldots \text{A2.1}$$

Relative variance V, is defined by:-

$$V = \frac{\sigma^2}{\bar{x}^2} = \frac{1}{\bar{x}} \qquad \ldots\ldots\ldots \text{A2.2}$$

For a cascade of s events, it can be shown that

$$\bar{X} = \bar{x}_1 \bar{x}_2 \bar{x}_3 \ldots \bar{x}_s \qquad \ldots\ldots\ldots \text{A2.3}$$

$$V(X) = V(x_1) + \frac{V(x_2)}{\bar{x}_1} + \ldots \frac{V(x_s)}{\bar{x}_1 \bar{x}_2 .. \bar{x}_{s-1}} \qquad \ldots\ldots\ldots \text{A2.4}$$

In a practical scintillation counter, the number of light photons produced in the scintillator is very large, and the observed pulse height distribution due to mono-energetic photons approximates closely to a Gaussian distribution. In this case the resolution R (as defined in Chapter 1) of the distribution about the mean, $\bar{x}$, is the most convenient measure of line broadening, and it can be shown that

$$R = 2\sqrt{2 \ln 2}\ \frac{\sigma}{\bar{x}} = 2.36\ V^{1/2} \qquad \ldots\ldots\ldots \text{A2.5}$$

A2.3 Crystal package

To produce minimum line broadening, a scintillation crystal must first convert incident X-ray energy to light quanta with high efficiency and then transfer as much of this light as possible to the photocathode of the photomultiplier tube. Thallium doped sodium iodide is generally chosen as the scintillator for X-ray spectrometry because it has the highest conversion efficiency of X-ray energy to light quanta at room temperature. Usually crystals are surrounded with reflecting material to increase their light transfer efficiency, but this is not possible for low energy work since the reflector attenuation would be too great. Instead, it is an advantage to roughen the crystal walls to increase the probability of internal reflection of light. Commercial systems usually fix the crystal to a Pyrex glass face-plate with silicone fluid, and then fix the face-

plate to the photomultiplier tube, again with silicone fluid. However, Crouthamel (1960) suggests that an improvement in resolution of up to 10% can be obtained by dispensing with the face-plate and fixing the crystal directly to the tube using silicone fluid to reduce light losses due to large differences in refractive indices.

It is possible to define a total crystal resolution R_c which takes into account the line broadening introduced by the processes discussed above. The work of Bisi and Zappa (1958) indicates that, for low energy X-rays, this resolution is independent of energy, and they find that for a good crystal package, $R_c = 6.7\%$

A2.4 The photomultiplier tube

The broadening introduced by the photomultiplier tube will be shown to be of great importance for low energy X-ray spectrometry.

If $\bar{f}$ is the average energy transfer efficiency from the crystal package to the photocathode, then the incident energy on the photocathode is $\bar{f}E$. Owing to non-uniformity of the photocathode, only a mean fraction $\bar{F}$ of this energy is available to produce photoelectrons. If the mean photocathode sensitivity is $\bar{\varepsilon}$, then the average number of photoelectrons produced is:-

$$\bar{n}_e = \bar{\varepsilon}\bar{F}\,\bar{f}E = \bar{F}\,\frac{E}{\bar{w}}$$

where $\bar{w} \equiv \frac{1}{\bar{\varepsilon}\,\bar{f}}$ is the average incident energy required to produce one photoelectron.

Only an average fraction $\bar{P}$ of the photoelectrons are collected at the first dynode. Hence the relative variance at the first dynode is:-

$$V_1 = \frac{1}{\bar{P}\,\bar{n}_e} = \left(\frac{\bar{P}\,\bar{F}\,E}{\bar{w}}\right)^{-1} \qquad \ldots\ldots \text{A2.6}$$

At the first dynode electron multiplication takes place with an average gain $\bar{M}_1$. Hence, from equation A2.4, the contribution of this process to the total variance is:-

$$\frac{V_2}{\bar{P}\,\bar{n}_e} = \frac{1}{\bar{P}\,\bar{n}_e\bar{M}_1} = \left(\frac{\bar{P}\,\bar{F}\,\bar{E}}{\bar{w}}\right)^{-1} \frac{1}{\bar{M}_1} \qquad \ldots\ldots\ldots \text{A2.7}$$

For each subsequent stage the average gain is generally made equal, and denoting this by $\bar{M}$, the contribution of all the subsequent stages to the total variance is:-

$$\frac{V_3}{\bar{P}\,\bar{n}_e\,\bar{M}_1} + \frac{V_4}{\bar{P}\,\bar{n}_e\,\bar{M}_1\,\bar{M}} \cdots = \frac{1}{\bar{P}\,\bar{n}_e\,\bar{M}_1\,\bar{M}}\left[1 + \frac{1}{\bar{M}} + \frac{1}{\bar{M}^2} \cdots \frac{1}{\bar{M}^r}\right]$$

$$= \left(\frac{\bar{P}\,\bar{F}\,E}{\bar{w}}\right)^{-1} \frac{1}{\bar{M}_1\,\bar{M}}\left[1 + \frac{1}{\bar{M}} + \frac{1}{\bar{M}^2} \cdots \frac{1}{\bar{M}^r}\right]$$

$\ldots\ldots\ldots$ A2.8

where r = (Number of tube stages) - 3.

From equation A2.4 the total variance V_M due to the photomultiplier is therefore:-

$$V_M = V_1 + \frac{V_2}{\bar{P}\,\bar{n}_e} + \frac{V_3}{\bar{P}\,\bar{n}_e\,\bar{M}_1} + \cdots\cdots$$

$$= \left(\frac{\bar{P}\,\bar{F}\,E}{\bar{w}}\right)^{-1}\left[1 + \frac{1}{\bar{M}_1} + \frac{1}{\bar{M}_1\,\bar{M}}\left(1 + \frac{1}{\bar{M}} + \frac{1}{\bar{M}^2} \ldots + \frac{1}{\bar{M}^r}\right)\right]$$

$$= \left(\frac{\bar{P}\,\bar{F}\,E}{\bar{w}}\right)^{-1}\left[1 + \frac{1}{\bar{M}_1} + \frac{1}{\bar{M}_1\,\bar{M}}\left(\frac{\bar{M}^r + 1 - 1}{(\bar{M} - 1)\,\bar{M}^r}\right)\right] \ldots\ldots\ldots \text{A2.9}$$

and since $\bar{M}^{r+1} \gg 1$

$$V_M = \left(\frac{\bar{P}\,\bar{F}\,E}{\bar{w}}\right)^{-1}\left[1 + \frac{1}{\bar{M}_1} + \frac{1}{\bar{M}_1\,(\bar{M} - 1)}\right] \qquad \ldots\ldots\ldots \text{A2.10}$$

Thus theory predicts that the variance due to the photomultiplier should be proportional to E^{-1}, i.e. resolution is proportional to $E^{-1/2}$. Bisi and Zappa's results (1958) support this conclusion. Factors which are directly under our control are:-

1. Choice of photomultiplier sensitivity $\bar{\varepsilon}$ $(\alpha \frac{1}{\bar{w}})$
2. Choice of first dynode gain, by varying cathode to first dynode voltage.

We can substitute some typical figures into equation A2.10, to investigate the variation of resolution with photomultiplier sensitivity. A typical E.M.I. tube has the following values:-

$\bar{P}\,\bar{F} \simeq 0.9$

$\bar{M}_1 \simeq 6$

$\bar{M} \simeq 4$

$\bar{w} \simeq$ 250eV/photoelectron (For NaI), corresponding to $\bar{\varepsilon}$ = 80μA/lumen.

Assuming that $\bar{f}$ does not alter for different tubes, values of $\bar{w}$ can be calculated for various photocathode sensitivities, and hence the resolution due to the photomultiplier can be calculated as in Table A2.1.

A2.5 System resolution: Comparison of theory with experiment

The total variance of the scintillation spectrometer is then given by:-

$$V_s = V_c + V_M$$

or

$$R_s^2 = R_c^2 + R_M^2$$

and since crystal resolution does not vary with energy,

$$R_s^2 = \alpha + \beta/E$$

Figure A2.1

Resolution of 60keV X-rays versus photocathode sensitivity

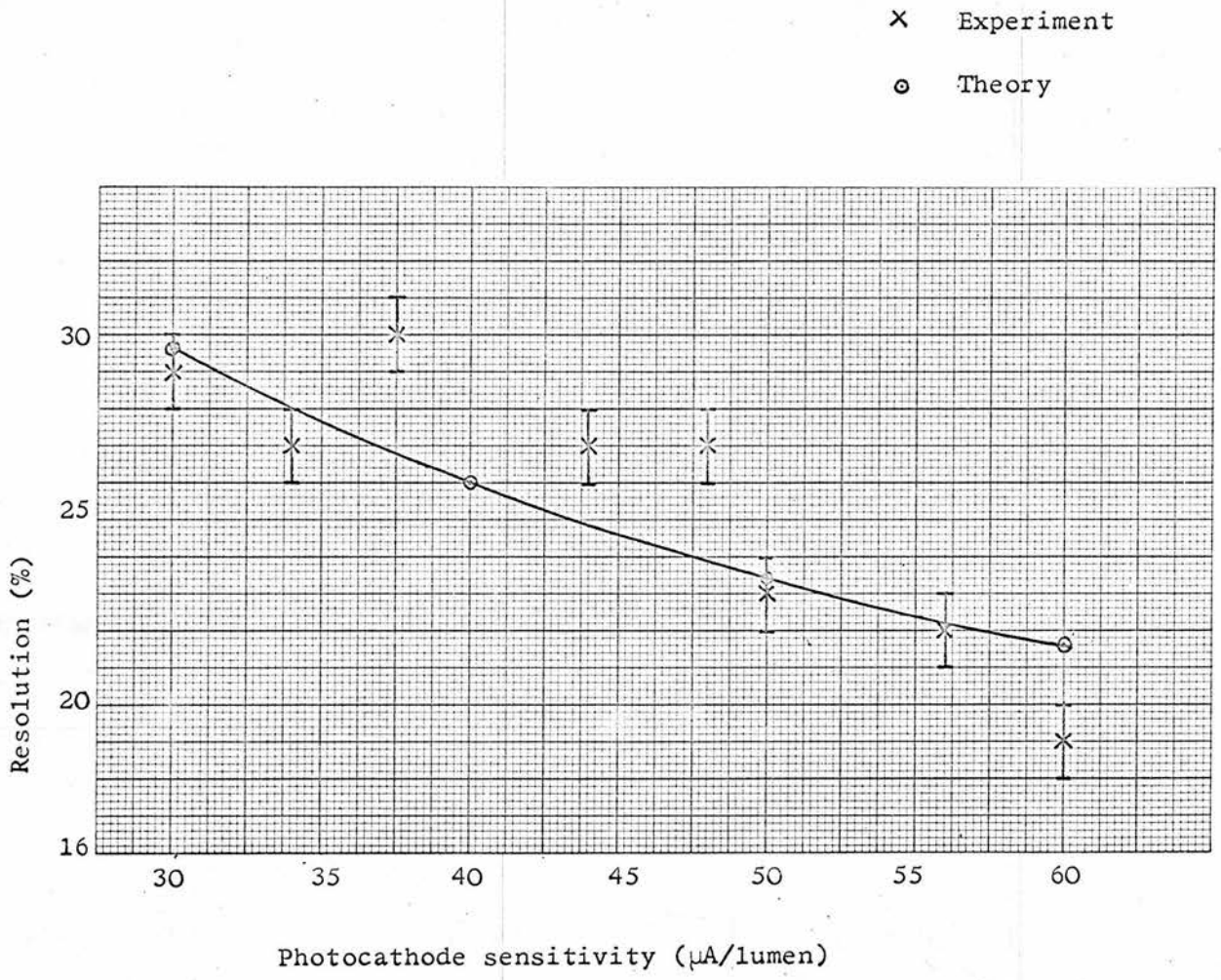

Assuming a crystal resolution of 6.7% the variation of system resolution with photomultiplier sensitivity can be calculated. This is shown in Table A2.1 for photons of energy 60keV.

Table A2.1

Contributions of photomultiplier and crystal to system resolution at 60kV

Photomultiplier Efficiency (μA/lumen)	Photomultiplier Resolution %	Crystal Resolution %	System Resolution %
80	17.7	6.7	19.0
70	19.0	6.7	20.1
60	20.5	6.7	21.6
50	22.4	6.7	23.4
40	25.1	6.7	26.0
30	29.0	6.7	29.7

In calculating these values it has been assumed that there are no variations in photocathode uniformity or first dynode collection efficiency. The validity of this depends of course on the quality of manufacture of the tubes. It has been possible to test the predictions of theory by using eight EMI 9524 S tubes of various nominal sensitivities in conjunction with a 1" sodium iodide crystal assembly. The crystal was fixed onto the tube under test with silicone fluid and measurements were taken under conditions of good geometry, in a light tight box, using the 60keV X-rays of Americium 241. Results are shown in Fig. A2.1. In view of the assumptions made, the agreement with the theoretical curve seems good.

With this experimental set up, it was also possible to investigate the optimum cathode - first dynode potential. For the tubes tested this was not found to be extremely critical, the resolution being least when the

potential was between 100 - 150 volts.

A2.6 Discussion

The results of Table A2.1 indicate that it should be possible to obtain a resolution of less than 20% for 60keV photons if a high resolution tube and good crystal areavailable. There are very few published results where the resolution is as good as this, but Bisi and Zappa (1958) and Epp and Weiss (1966) have both obtained figures of less than 20%.

The preceding calculations indicate that the most important component of a low resolution scintillation spectrometer for use at low energy is the photomultiplier. This should have a sensitivity of at least 80μA/lumen, and in addition should have a uniform photocathode. The crystal should be fixed directly on to the photomultiplier tube face. It was found most useful here to have several identical crystals made, and to choose the one that gave the best resolution with a given tube. With the advent of more sensitive photocathodes it is likely that further improvements of resolution will become possible.

By using the suggestions incorporated in this Appendix, a high resolution scintillation spectrometer has been obtained, and is described in Chapter 8. The optimum resolution obtainable for 60keV photons with this system is 16%.

A C K N O W L E D G E M E N T S

I am very grateful to my supervisor, Professor J. R. Greening, Director of the Department of Medical Physics, University of Edinburgh, for his advice and encouragement throughout the period of this investigation.

I should also like to thank:-

Dr. J. Law, Dr. K. J. Randle and Dr. A. T. Redpath for many helpful discussions.

My wife for her assistance in preparing the diagrams for this thesis.

The Medical Research Council for a Scholarship covering the period of study.

REFERENCES

Bell, G. E., 1936. Brit. J. Radiol. 9, 680.

Bendit, E. G., 1958. Brit. J. Appl. Phys. 9, 312.

Berger, M. and Seltzer, S., 1964. NASA (U.S.) Rept. SP-3012.

Birks, J. B., 1964. The theory and practice of scintillation counting, Pergamon Press.

Bisi, A. and Zappa, L., 1958. Nucl. Inst. 3, 17.

Blokhin, M. A., 1961. The Physics of X-rays, USAEC-tr-4502.

Bowen, P. J., Norman, K., Pounds, K. A., Sanford, P.W. and Willmore, A. P., 1964. Proc. Roy. Soc. 281, 538.

Bowman, H. R., 1966. Science 151, 562.

Burhop, E. H. S., 1940. Proc. Camb. Phil. Soc. 36, 43.

Burke, E. A. and Pettit, R. M., 1958. A.F.C.R.C.(U.S.), Report - TR-58-362.

Burke, E. A. and Pettit, R. M., 1960. Rad. Res. 13, 271.

Burrus, W.R., 1960. I.R.E. Trans. Nucl. Sci. 7, 102.

Compton, A. H. and Allison, S. K., 1954. X-rays in Theory and Experiment Van Nostrand, 11th edition.

Cormack, D. V. and Burke, D. G., 1960. Radiology, 74, 743.

Crouthamel, C.E., 1960. Applied Gamma-ray Spectrometry, Pergamon Press.

Dearnaley, G., 1966. J. Sci. Inst. 43, 869.

Dixon, W. R. and Aitken, J. H., 1958. Canad. J. Phys. 36, 1624.

Dyson, N. A., 1959. Proc. Phys. Soc. 73, 924.

Ehrlich, M., 1955. J. Res. N.B.S.(U.S.) 54, 107.

Engelkemeir, D., 1956. Rev. Sci. Inst. 27, 589.

Epp, E. R. and Weiss, H., 1966. Phys. Med. Biol. 11, 225.

Faddeeva, V. N., 1959. Computational Methods in Linear Algebra, Dover.

Fano, U., 1946. Phys. Rev. 70, 44.

Fano, U., 1947. Phys. Rev. 72, 26.

Farr, R. F., 1955. Brit. J. Radiol. 28, 364.

Flügge, W., 1954. Tables of Trancendental Functions, Pergamon Press.

Green, M., 1963. Proc. Phys. Soc. 82, 204.

Green, M. and Cosslett, V. E., 1961. Proc. Phys. Soc. 78, 1206.

Greenfield, M.A., Specht, R.D., Kratz, P. M. and Hand, K., 1952. J. Opt. Soc. Am. 42, 6.

Greening, J. R., 1947. Brit. J. Radiol. 20, 71.

Greening, J. R., 1950. Proc. Phys. Soc. 63, 1227.

Greening, J. R., 1952. J. Opt. Soc. Am. 42, 685.

Greening, J. R., 1963. Brit. J. Radiol. 36, 363.

Greening, J. R. and Randle, K. J., 1968. Phys. Med. Biol. 13, 159.

Greening, J. R., Randle, K. J. and Redpath, A. T., 1968. Phys. Med. Biol. 13, 359.

Gunnersen, E. M., 1967. Rep. Prog. Phys. 30 , 1, 27.

Heroux, L., Manson, J. E. and Smith, R., 1962. A.F.C.R.L.(U.S.) Rept. 1105.

Hink, W., 1964. Z. Phys. 177, 424.

Hink, W., 1965. Z. Phys. 182, 227.

I.C.R.U., 1964. Physical aspects of irradiation, N.B.S.(U.S.) Handbook 85.

Jager, W. F. and Soole, B. W., 1965. Admiralty Res. Lab. Report C/R18.

Jennings, W. A., 1953. Brit. J. Radiol. 26, 193.

Jones, D. E. A., 1940. Brit. J. Radiol. 13, 95.

Jönsson, A., 1926. Z. Phys. 36, 426.

Kirkpatrick, P., 1939. Rev. Sci. Inst. 10, 186.

Kirkpatrick, P., 1944. Rev. Sci. Inst. 15, 223.

Kramers, H. A., 1923. Phil. Mag. 46, 836.

Kuhlenkampff, H., 1922. Ann. Phys. 69, 548.

Law, J. Private communication, Dept. of Medical Phys. Univ. of Edinburgh.

Law, J. and Redpath, A. T. 1968. Phys. Med. Biol. 13, 371.

Liden, K. and Starfelt, N. 1954. Arkiv. For Fysik 7, 427.

Lukirskii, A. P., Ershov, O. A. and Brytov, I. A. 1966. Izv. AN SSSR, Ser fiz. 27, 330. (Trans. Bulletin 26, 798.)

Macey, H. H., 1948. J. Sci. Inst. 25, 251.

McGinnies, R. T., 1959. Supplement to N.B.S. Circular 583.

McMaster, W. H., Kerr Del Grande, N., Mallet, J. H., Scofield, N. E., Cahill, R. and Hubbell, J. H., 1967. Compilation of X-ray Cross-sections U.C.R.L. (U.S.) Rept. 50174, Section 2.

Metchnik, V., 1963. Proc. Phys. Soc. 82, 515.

Mulvey, T. and Campbell, A. J., 1958. Brit. J. Appl. Phys. 9, 406.

Norman, A. and Greenfield, M. A., 1955. Rad. Res. 3, 407.

Peaple, L. H. J. and Burt, A. K., 1968. AERE Rept. R.5687.

Rand, R. E., 1962. Nucl. Inst. 17, 65.

Rawson, E. G. and Cormack, D. V., 1958. Nucleonics, October issue.

Redpath, A. T., 1967. Ph.D. Thesis, University of Edinburgh.

Ross, P. A., 1926. Phys. Rev. 28, 425.

Ross, P. A., 1928. Rev. Sci. Inst. 16, 433.

Silberstein, L., 1933. Phil. Mag. 15, 375.

Spielberg, N., 1959. Philips Res. Rept. 14, 215.

Spiers, F. W., 1946. Brit. J. Radiol. 19, 52.

Stoddard, K. B., 1935. Phys. Rev. 48, 43.

Taylor, J. and Parrish, W., 1955. Rev. Sci. Inst. 26, 367.

T.M.C., 1967. Specification of photon spectrometer, model 334.

Tothill, P., 1964. Ph.D. Thesis, University of Edinburgh.

Ulrey, C. T., 1919. Phys. Rev. 11, 401.

Wang, P. K. S., Raridon, R. J. and Tidwell, M., 1957. Brit. J. Radiol. 30, 153.

Worthington, C. R. and Tomlin, S. G., 1956. Proc. Phys. Soc. 69, 401.

Zedler, R. E., 1964. Oak Ridge Nuclear Lab. Rept. 1203.